



TECHNISCHE
UNIVERSITÄT
DARMSTADT

Nanocarbon Devices and Sensors

**Zur Erlangung des akademischen Grades eines
Doktor der Naturwissenschaften
von der Fakultät für Material und Geowissenschaften
des Technischen Universität, Darmstadt**

genehmigte

Dissertation

Von

**M.Sc. Sandeep Kumar
aus Bokaro in India**

Referrant: Prof. Dr. Ralph Krupke
Koreferrant: Prof. Dr. Jan Philipp Hofmann

Darmstadt 2021

Kumar, Sandeep : Nanocarbon Devices and Sensors

Darmstadt, Technische Universität Darmstadt

Year thesis published in TUpriints 2022

Date of viva voce: 08.12.2021

Published under CC BY-SA 4.0 International

<https://creativecommons.org/licenses/>

*This thesis is dedicated
to my beloved family*

Table of Contents

1	Introduction	1-1
1.1	Scope of thesis	1-1
1.2	Outline of thesis	1-4
2	Materials and Properties	2-5
2.1	Nanocarbon materials.....	2-5
2.1.1	Graphene.....	2-5
2.1.2	Carbon nanotubes.....	2-11
2.1.3	Nanocrystalline graphene	2-21
2.2	Properties of carbon nano-systems	2-29
2.2.1	Raman spectroscopy	2-29
2.3	Support layers and coatings.....	2-34
2.3.1	Boron Nitride.....	2-34
2.3.2	Ultra-thin glass	2-35
2.3.3	Teflon AF 2400	2-37
2.3.4	Metal-organic frameworks (MOFs).....	2-38
3	Experimental Methods	3-41
3.1	Device fabrication	3-41
3.1.1	Synthesis of h-BN and NCG	3-41
3.1.2	Patterning with EBL.....	3-43
3.1.3	Deposition of CNTs with dielectrophoresis.....	3-43
3.2	Characterization tools	3-44
3.2.1	Electrical measurement	3-44
3.2.2	Raman Microscopy.....	3-46
3.2.3	Piezoresistance setup.....	3-48
3.2.4	Gas sensing setup.....	3-51
4	Vanishing Hysteresis in CNT Transistors	4-53
4.1	Synthesis and characterization of Boron Nitride	4-53
4.2	Device fabrication	4-58

4.3	Results and discussions	4-60
4.4	Summary	4-68
5	Graphene-SURMOF Molecule Sensor	5-71
5.1	GFET Device Fabrication.....	5-73
5.2	SURMOF synthesis.....	5-74
5.3	Characterization parameters.....	5-75
5.4	Results and discussions	5-77
5.5	Summary	5-92
6	NCG for Sensing Applications.....	6-93
6.1	Low-temperature NCG synthesis	6-93
6.2	Patterning and graphitization of PMMA	6-97
6.3	Transfer process	6-99
6.4	Dependence of sheet resistance of NCG on temperature	6-103
6.5	Strain dependent measurements.....	6-107
6.5.1	Strain calculation	6-108
6.5.2	Piezoresistance in NCG.....	6-109
6.5.3	Raman spectroscopy measured under strain.....	6-114
6.6	NCG field-effect transistors as a humidity sensor.....	6-119
6.7	Summary	6-122
7	Conclusion and Outlook	7-123
8	List of abbreviations	8-127
9	List of Figures.....	9-129
10	List of Tables.....	10-133
11	Bibliography.....	11-135

Abstract

Nanocarbon materials have the potential to substitute the silicon in devices that are needed to further improve in terms of scalability, speed of operation, and performance. Therefore, carbon nanotubes and graphene - allotropes with outstanding properties have been intensively explored over the years. This thesis contributes to the synthesis of nanocarbon materials and its use as sensing and transistor material by focusing on the topics: hysteresis in carbon nanotube field-effect transistors, selective molecule sensing with graphene field-effect transistors, and sensing applications in nanocrystalline graphene. Hysteresis in carbon nanotube transistors has limited its utility in large-scale device implementation. The issue of hysteresis in such device structures is addressed. A hysteresis-free device operation is achieved by packaging the carbon nanotube field-effect transistors between hexagonal boron nitride and a hydrophobic polymer Teflon. The findings indicate that hysteresis is eradicated only if the metal-carbon nanotube contacts along with the tubes are completely encapsulated with Teflon. The time dependence of reducing hysteresis for encapsulated devices indicates out-diffusion of water molecules adsorbed at the metal-nanotube contacts. Graphene field-effect transistors suffer the issue of selectivity applications. A novel sensor based on graphene field-effect transistor and surface-mounted metal-organic frameworks is demonstrated. The sensor shows sensitivity and selectivity to ethanol molecules by the shift in Dirac voltage of graphene and is insensitive to other alcohols like methanol and isopropanol, and molecules like CO₂, H₂O, H₂. The device performance shows a detection limit of 100 ppm levels. This class of sensors is tailorable and opens up a completely new range of sensors. Nanocrystalline graphene is an interesting material for several sensing applications like strain sensing, moisture sensing, gas sensing, etc. In order to be investigated as strain sensor, thin films should be either grown or transferred on flexible substrates. This motivated the study of the low-temperature synthesis (600°C) process using a metal capping layer over a carbon source. Raman spectroscopy is used to characterize the grown films. The results indicate this technique promising for a low-temperature NCG synthesis. Next, thin-film transfer technique on flexible substrate is studied. The quality of transferred films on different substrates is confirmed by atomic force microscopy. Next, influence of temperature on conductivity of thin films of NCG is investigated. Piezoresistive property of nanocrystalline graphene is explored based on changes in sheet resistance of the film and Raman spectroscopy. Finally, a potential application is demonstrated where a top (ionic liquid) gate field effect configuration of NCG works as a moisture sensor.

Declaration

I, hereby declare that, this thesis is an outcome of my work. Contents from collaborations are acknowledged. I certify that this thesis has not been submitted elsewhere. Additionally, care has been taken to ensure that the work is original and material included in the thesis previously published is cited congruously.

Date

Signature

List of conference and publications

The following research articles and conference contributions includes research performed by author during his course of study.

Research Articles:

1. Sandeep Kumar, Daghan Dagli, Simone Dehm, Chittaranjan Das, Li Wei, Yuan Chen, Frank Hennrich and Ralph Krupke. Vanishing hysteresis in carbon nanotube transistors embedded in boron nitride/polytetrafluoroethylene heterolayers. *Phys. status solidi – Rapid Res. Lett.* **2020**, 14, 2000193.
2. Sandeep Kumar, Yohanes Pramudya, Kai Müller, Abhinav Chandresh, Simone Dehm, Shahriar Heidrich, Artem Fediai, Devang Parmar, Delwin Perera, Manuel Rommel, Lars Heinke, Wolfgang Wenzel, Christof Wöll and Ralph Krupke. Sensing molecules with metal-organic framework functionalised graphene transistors. *Adv. Mater.* **2021**, 2103316.

Conferences Contributions:

1. Sandeep Kumar, Adnan Riaz, Simone Dehm and Ralph Krupke. Conversion of nanocrystalline graphene to hexagonal boron nitride. *Annual meeting of GDR-I, Sete, France*, **October 15-19, 2018**, Poster.
 2. Sandeep Kumar, Kai Müller, Simone Dehm, Artem Fediai, Devang Parmar, Manuel Rommel, Lars Heinke, Wolfgang Wenzel, Christof Wöll and Ralph Krupke. Ethanol sensing with surface mounted metal-organic framework functionalised graphene transistors. *International Conference on the Science and Application of Nanotubes and Low-Dimensional Materials*, **July 21 -26, 2019**, Wuerzburg, Germany, Poster.
 3. Sandeep Kumar, Kai Müller, Simone Dehm, Artem Fediai, Devang Parmar, Manuel Rommel, Lars Heinke, Wolfgang Wenzel, Christof Wöll and Ralph Krupke. Ethanol sensing with surface mounted metal-organic framework functionalised
-

graphene transistors. *Annual meeting of GDR-I*, **October 27-30 2019**, Bad Herrenalb, Germany, Poster.

4. Sandeep Kumar, Simone Dehm, Li Wei, Yuan Chen, Frank Hennrich and Ralph Krupke. Hysteresis free carbon nanotube transistors embedded in boron nitride and polytetrafluorethylene heterolayers. *International Winterschool on Electronic Properties of Novel Materials*, **March 7-14 2020**, Kirchberg in Tirol, Austria, Poster.
-

Curriculum Vitae

Personal Information

Name	Sandeep Kumar
Date of Birth	04 September 1992

Educational Background

09/2017 – Current	Doctoral student in Department of Materials and geosciences	<i>Technical University Darmstadt, Germany</i>
06/2011 – 06/2016	M.Tech - B.Tech Dual degree, Materials science and engineering.	<i>Indian Institute of Technology Kanpur, India</i>

Research Background

05/2015 – 08/2015	Internship	<i>Applied Materials Mumbai, India</i>
07/2016 – 06/2017	Research Assistant	<i>National centre for flexible electronics IIT Kanpur, India</i>

1 Introduction

1.1 Scope of thesis

In 1965, Gordon Moore predicted that the number of transistors on a computer chip doubles approximately every two years. However, around the year 2000, the silicon semiconductor industry started suffering due to physical limits. Hence, radical approaches were required to utilize and apply nanotechnology. This motivated the research on high mobility materials such as carbon nanotubes (CNTs) and graphene. These carbon nanomaterials have the potential to improve the semiconductor device performance in terms of operation speed, and size. Therefore, in the past two decades, interest has increased towards this class of material as can be seen by a plot of the number of publications vs year in figure 1.1.

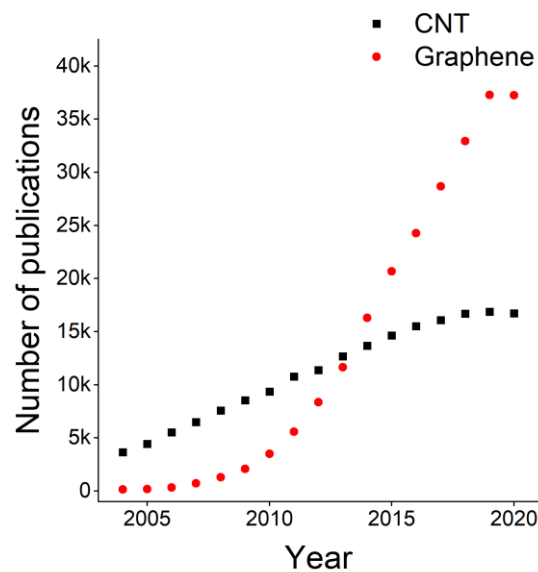


Figure 1.1: Number of publications per year in the field of CNTs and graphene. (Source: web of science)

Carbon is a chemical element with atomic number 6. With a valency of four, it can form four covalent bonds. It can also bond with itself to create different allotropes like diamond, graphite, and fullerenes. Each of the allotropes inherits distinguished properties depending on the chemical bonds formed with the neighboring carbon

atoms. For example, in diamond, sp^3 hybridised carbon atoms form four covalent σ bonds in a tetrahedral configuration. Due to the strong σ bonds, it is one of the hardest materials. On the other hand, in graphite, sp^2 carbon forms three σ bonds, and one electron is delocalized in π bond. Carbon arranges in flat layers of hexagonal structure, between which the extra electrons prevail, and are held together by Van der Waals forces. A monolayer of graphite is known as graphene with electron cloud residing on its surface and a continuous energy-momentum (E-K) space. Rolling up the 2D graphene film gives CNTs, a 1D system, and quantized energy-momentum (E-K) space^[1]. Nanocrystalline graphene (NCG) is another form of graphene possessing large defect density in form of grain boundaries (GBs) and triple junctions (TJs)^[2] and crystallite size in nanometers.

The motivation of this thesis was to improve the performance and control the functionality of nanocarbon devices by engineering the interfaces between the material and the environment, and the GBs. This gave rise to three research topics utilizing nanocarbon materials: hysteresis in CNT field-effect transistors (FETs), molecule sensing with graphene FETs, and NCG for sensing applications. These three topics have been covered in the thesis.

Semiconducting single-walled CNTs (SWCNTs) are touted as an attractive material for the semiconductor industry. With a high on/off ratio, excellent charge carrier mobility, and heat conductivity, SWCNTs are ideally suited as the channel material for FETs. The wide-ranging applications involving CNT-FETs include hydrogen sensing, light emission, and light detection^{[3][4][5]}. Nevertheless, hysteresis in CNT-FETs is an underlying problem and is often undesirable. It hampers the FET device operation by making it difficult to achieve a steady-state current at a fixed gate voltage^{[6][7]}. Several studies were reported in the literature to understand and limit the origin of hysteresis in CNT-FETs^{[8][9]}. Hexagonal boron nitride (h-BN), on the other hand, has proven to be an excellent dielectric for graphene FET^[10] to counter hysteresis. In this thesis, an attempt to eliminate hysteresis in CNT-FETs is explored by using a h-BN/SiO₂/Si substrate. A direct growth method of h-BN on the dielectric substrate (SiO₂/Si), contrary to the well-established technique of synthesis on the metal substrate is followed, thus avoiding the transfer step^[11,12]. CNT-FETs are then fabricated on the grown h-BN on top of SiO₂/Si substrate. Next, the role and significance of a top hydrophobic encapsulating layer are studied. Here, Teflon is used as the hydrophobic film to seal the CNTs from the adsorption of water molecules. Effectively, the carbon nanotubes are sandwiched between the top Teflon layer and the bottom h-BN layer. Time-dependent reduction of hysteresis after encapsulation with Teflon indicates an out-diffusion of water molecules

at the metal-CNT contacts. Finally, a hysteresis-free operation and stable device performance are demonstrated with the encapsulated CNT devices.

Electrically, graphene is a semimetal. The conduction and valence bands meet at K points where the charge carriers behave as massless fermions resulting in a ballistic transport^[13]. It has π electrons delocalised on the surface creating a 2D electron gas (2DEG). These charge carriers can have high mobility up to $200,000 \text{ cm}^2\text{V}^{-1}\text{s}^{-1}$ ^[14] based on the device and environmental conditions^[15]. High thermal conductivity in graphene up to $5,300 \text{ WmK}^{-1}$ is attributed to the weak interaction between electron and acoustic phonon^[16]. The absence of slip planes and high C-C bond strength leads to a high breaking strength of 42 Nm^{-1} and Young's modulus of 1 TPa ^[17]. Furthermore, the large surface area to volume ratio and high mobility of charge carriers^[13] makes it a suitable candidate for sensing molecules. A molecular gas sensor based on a graphene field-effect (GFET) transistor was first demonstrated by Schedin et al.^[18] Over the years several reports depicting the sensitivity of graphene gas sensors for sensing gases such as NH_3 , CO , O_2 , SO_2 , H_2S , etc.^[19–21] were reported. Alcohol detection was studied^[22] as well. However, the graphene sensors lack selectivity in detecting specific molecular species. Alternatively, surface-mounted metal-organic frameworks (SURMOFs), when integrated with GFET, lead to the detection of specific molecules. In this thesis, a novel concept of sensor based on the combination of GFET and SURMOF, tailored for the detection of ethanol is exhibited. The fabrication steps of GFETs are discussed. Next, the sensitivity and selectivity to ethanol are demonstrated from the shifts in Dirac voltage of the transconductance measurement. Subsequently, a resetting scheme for fast regeneration was explored via current annealing. A detection limit of 100 ppm was achieved for the GFET/SURMOF sensor which is comparable to the commercially available sensors. The combination of SURMOF and GFET to achieve selectivity and sensitivity, respectively, can open a new class of tailorable molecule sensors.

Only a few reports (~ 150 in 2020) on NCG, compared to graphene and CNTs, suggest the need for further exploration of this nanocarbon material. Due to a high defect density, NCG suffers from reduced carrier mobility and mechanical strength^[2]. However, despite the limitations, NCG has found applications in gas sensing^[23], strain sensing^[24], and photodetectors^[25]. The primary advantage of NCG lies in its synthesis simplicity, as NCG can be grown directly on a dielectric substrate with a predefined thickness. However, the high synthesis temperature (1000°C) limits its use to only a few substrates. For strain sensing applications, thin films should be either grown directly or transferred on flexible substrates. Therefore, in this thesis, a low temperature (600°C) synthesis route is explored by utilizing the catalytic activity of the metal capping layer on the carbon source. Next, the thin-film transfer technique is discussed, and a route for achieving a

wrinkle-free film is studied. Devices are fabricated using the NCG films and are then investigated under temperature and strain by sheet resistance measurements and Raman spectroscopy. Finally, an application of NCG-FET is demonstrated where the top-gated (using ionic liquid) channel displays sensitivity towards moisture and can act as a potential moisture sensor.

1.2 Outline of thesis

This thesis describes the performance and applications of devices based on carbon materials. The materials studied are graphene, carbon nanotubes, and NCG. In Chapter 2, a general overview of material studied in the thesis and their properties are discussed.

In Chapter 3, experimental methods used in the thesis are explained. Gas sensing and piezoresistance setup built in-house is explained in detail.

In Chapter 4, experiments and results on achieving hysteresis-free CNT-FETs are discussed. In the first section, the h-BN synthesis technique and characterization are described. The second section includes the device fabrication and electrical characterization. Lastly, the mechanism of achieving hysteresis-free operation is explained and the performance of the fabricated device is demonstrated.

In Chapter 5, a detailed study is described on SURMOF/GFET. The fabrication process is explained in detail. Next, different characterization techniques used are described. In the last part of the chapter, the results of SURMOF/GFET device sensing with selectivity to ethanol molecules are described. Raman measurements are shown to visualize the selectivity. Device performance is then studied confirming sensitivity down to 100 ppm levels.

In Chapter 6, NCG as a material is studied. First, the advantages of using a metal encapsulant layer for a low temperature (600°C) are demonstrated. Next, the transfer technique for thin-film transfer is discussed. Finally, the characterization of NCG film is done based on temperature and strain. As an example, a prospective application of NCG-FET as a moisture sensor is demonstrated.

In Chapter 7, the work in the thesis is summarized and prospects for further improvements are included.

2 Materials and Properties

2.1 Nanocarbon materials

2.1.1 Graphene

Graphene is an atomic monolayer of graphite. It was experimentally isolated from graphite in 2004 by Novoselov and Geim using an adhesive tape. The research article published in Science showed an application of graphene as a FET^[26]. Since then, graphene has sparked a fascination in the research community which led to several studies and applications of this material^[18,27].

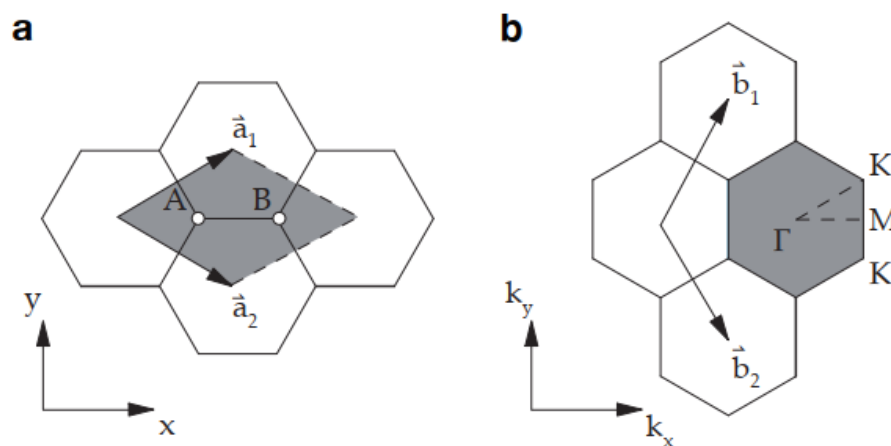


Figure 2.1: a) Unit cell of graphene in real space with a_1 and a_2 unit vectors and two carbon atoms A and B b) Reciprocal space with lattice vectors b_1 and b_2 and the Brillouin zone with K and K' points^[28].

Graphene has a hexagonal honeycomb structure with sp^2 hybridized carbon atoms. Each carbon is bound to 3 neighboring in-plane carbon atoms with a bond angle of 120° . The C-C bonds in graphene are covalent bonded with 3 σ bonds and 1 π bond. The σ bonds give immense mechanical strength as these bonds are stable and difficult to break. However, the electrons in π bonds are mobile and impart enhanced conductivity.

Graphene unit cell has unit vectors a_1 and a_2 (figure 2.1a) spanning an angle of 60° . It encloses two carbon atoms sitting at $1/3(a_1 + a_2)$ and $2/3(a_1 + a_2)$. The unit vectors a_1

and a_2 are the base to derive reciprocal lattice by Fourier transform and Brillouin zone (figure 2.1b)^[28].

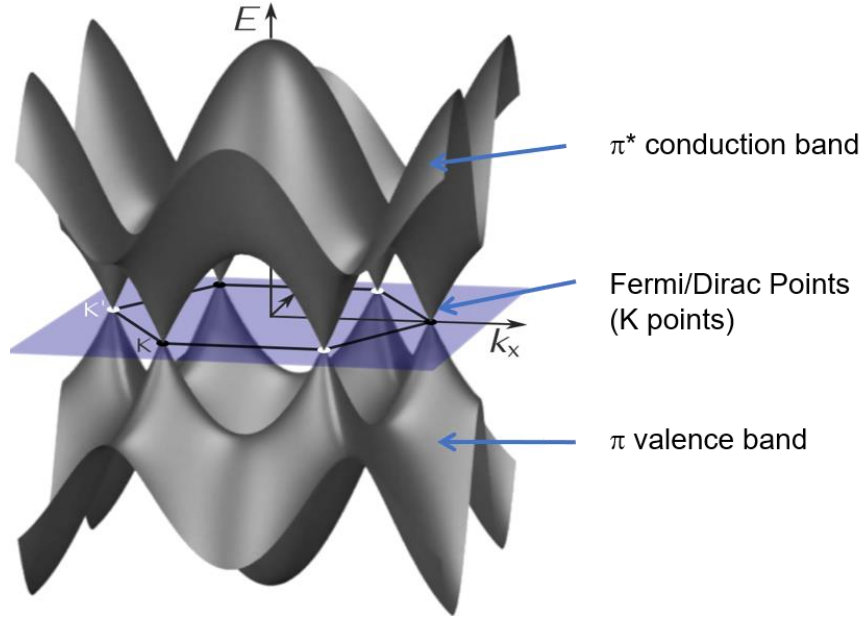


Figure 2.2: Conduction and valence band of graphene meeting each other at six symmetrical K points at the Fermi level^[29].

Using the wave function from the molecular orbital theory for π electrons in graphene and tight-binding calculations the energy dispersion relation can be derived^[30].

$$E(k) = \frac{\epsilon_{2p} \pm tw(k)}{1 \pm sw(k)} \quad (2.1)$$

$$w(k) = \sqrt{1 + 4\cos\frac{\sqrt{3}k_x a}{2} \cos\frac{k_y}{a} + 4\left\{\cos\frac{k_y a}{2}\right\}^2} \quad (2.2)$$

Here, ϵ_{2p} is the energy of an electron in $2p_z$ orbital, s , and t are overlap integrals and have identical values for all the nearest neighbor carbon atoms. $w(k)$ accounts for the phase change in the electron wave function from carbon atom A to B. There have been many theoretical approaches to calculate the values of the three unknowns. To setup zero energy point at the Fermi level $\epsilon_{2p} = 0$ is used. $t = -3.033$ eV and $s = 0.129$ have been calculated theoretically before the discovery of graphene^[31]. Hence, using equation 2.1 the energy dispersion relation can be plotted as shown in figure 2.2. In the energy dispersion relation, the conduction band and valence band meet at a point named K point. This makes graphene a zero band-gap semiconductor.

At the K point, $w(k)$ and s have small values. Therefore, using binomial expansion of the equation 2.1, energy dispersion relation at K point can be written with good approximation as ^[30]

$$E(k) = \pm tw(k) \quad (2.3)$$

The positive and negative signs correspond to conduction (anti-bonding orbital) and valence bands (bonding orbital) respectively. The bonding orbital is fully occupied by two electrons with opposite spins contributed by each carbon atom. The anti-bonding orbital is empty. However, the bands meet at the K point and electrons in valence bands have adequate energy to move to the conduction band at non-zero temperature. For the electrons held in strong σ bonds, energy >10 eV is required to excite electrons to conduction bands^[32]. Therefore, mostly electrons in π bonds contribute to the conductivity of graphene closer to the K points.

At the K point, the energy dispersion is linear. Due to this linear relation, electrons can be regarded as massless ($E = \hbar k v_F$) and have constant velocity (Fermi velocity) $v_F = 10^6 \text{ ms}^{-1}$ ^[31,32].

2.1.1.1 Graphene field-effect transistors

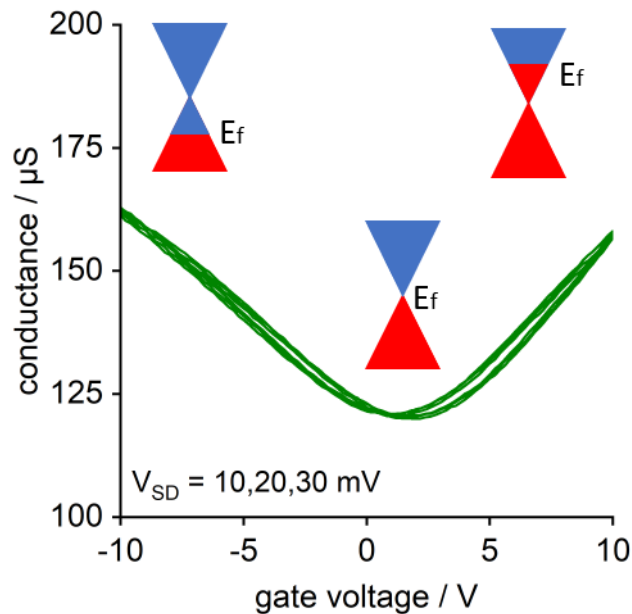


Figure 2.3: Transconductance curve of a GFET showing Fermi levels at different gate voltages. Red and blue color corresponds to electrons and holes.

The transconductance in an FET is an important parameter for device applications. It gives information about the carrier mobility in the channel, doping levels, and intrinsic charge carrier concentration. A transconductance curve is shown in figure 2.3 for a GFET. The back gate modulates the position of Fermi energy in the Dirac cone. Depending on the potential applied to the back gate, the majority of charge carriers can be electrons (red) or holes (blue) as shown in figure 2.3. There exists a minimum in the conductance. The voltage at which the minimum of conductance occurs is called the Dirac voltage and indicates the location of the Fermi energy at the K -point where the valence band and conduction band touch each other. For p-doped (n-doped) graphene, the Dirac voltage can shift to positive (negative) voltage.

2.1.1.2 Charge carrier density in graphene

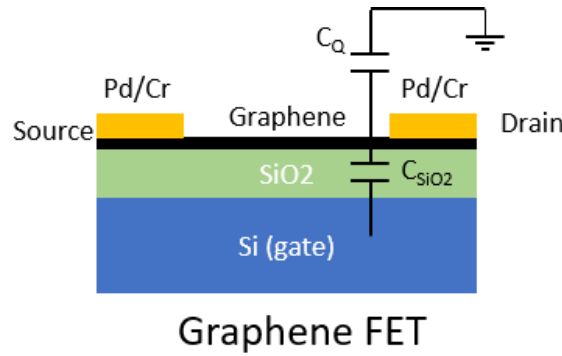


Figure 2.4: Schematic of GFET with equivalent capacitance circuit (adapted from ref ^[33]).

Kim et al.^[34] had studied mono and bi-layer graphene charge carrier density. Here, few excerpts are adapted from Kim's work. In a transistor configuration, the back gate (V_{BG}) can be used to modulate the charge carrier density (n) in the graphene. Considering a parallel capacitance model, shown in figure 2.4, the charge carrier density can be given as

$$V_{BG} = \frac{en}{C_{BG}} \quad (2.4)$$

Important to note here is that the work function of graphene is equal to Si back gate and the charge neutrality point of graphene is at $V_{BG} = 0$ V^[35]. Due to a limited density of states and Pauli's exclusion principle, for a given electron density, the Fermi energy has to be increased to occupy all the electrons in higher energy states. Hence, the Fermi energy term should be included in equation 2.4.

$$V_{BG} - \frac{E_F}{e} = \frac{en}{C_{BG}} \quad (2.5)$$

E_F/e term is the surface potential of graphene due to the electric field not being screened by graphene. This phenomenon is termed quantum capacitance and is used to determine the surface potential at a fixed charge carrier density^[36]. The equation for the quantum capacitance and density of states is given as

$$C_Q = e^2 D(E) \quad (2.6)$$

$$D(E) = \frac{2}{\pi(\hbar v_F)^2} E = \frac{2}{\hbar v_F \sqrt{\pi}} \sqrt{n} \quad (2.7)$$

$$C_Q = \frac{2e^2}{\hbar v_F \sqrt{\pi}} \sqrt{n} \quad (2.8)$$

Using the series configuration of parallel plate capacitances yields

$$V_{BG} = \left(\left(\frac{1}{C_Q} \right) + \left(\frac{1}{C_{BG}} \right) \right) en \quad (2.9)$$

The integration gives the equivalent quantum capacitance $C_{Q,Eq} = (1/2)C_Q$

$$C_{Q,Eq} = \frac{e^2}{\hbar v_F \sqrt{\pi}} \sqrt{n} \quad (2.10)$$

The quantum capacitance C_Q contribution to overall capacitance is insignificant when C_Q is larger than the geometrical capacitance C_{BG} . At the charge neutrality point, n is minimum and therefore C_Q is minimum. Hence, the contribution of quantum capacitance is maximum at the Dirac voltage and reduces with higher charge density.

The charge density can be now calculated based on the back gate voltage V_{BG} ^[33]. Using equations 2.9 and $E_F = \hbar v_F \sqrt{\pi n}$

$$n(V_{BG}) = \left[\left(\sqrt{\left(\frac{\hbar v_F \sqrt{\pi} C_{BG}}{2e^2} \right)^2 + \frac{C_{BG}}{e} V_{BG}} - \frac{\hbar v_F \sqrt{\pi} C_{BG}}{2e^2} \right) \right]^2 \quad (2.11)$$

Using the following equation 2.12

$$\rho = \frac{1}{\sqrt{n^2 + n_o^2} e \mu} \quad (2.12)$$

the resistivity of graphene can be then calculated. Here, n_o is the residual carrier density and μ is the mobility.

Now the total resistance of the device can be written as

$$R_{total} = R_{contact} + \frac{L}{W\sqrt{n^2 + n_o^2}e\mu} \quad (2.13)$$

Here L and W are the length and width of the channel. The experimental transconductance curve can be fitted to equation 2.13 and the parameters $R_{contact}$, mobility, and residual charge carrier density can be extracted^[37].

2.1.1.3 Literature

Since the discovery of graphene, this 2-D material has been extensively studied for different applications based on its high mobility, conductivity, and large surface area to volume ratio^[38]. One of the many applications is its use as a sensing material. It can detect slight changes surrounding its environment and give corresponding output, electrically or optically^[39]. Graphene has also found its way into biological applications for monitoring human health and water quality^[40]. Some reports on these sensors are discussed below.

- **Gas/Vapor sensors:** Graphene-based sensors have increased exponentially in the last decade. There are different device structures used. These can be chemiresistor, FET, capacitance sensor, surface work function change transistor, surface acoustic wave (SAW) change transistor^[41]. Chemiresistor is simple in fabrication and convenient in application and is the most commonly used sensor structure. A bias is applied across a channel/sensing material and a change in the surrounding is then detected by a change in the current values. A few of the reports are briefly described below:
 1. **Ammonia Sensor:** Using gold nanoparticles on chemical vapor deposited (CVD) graphene the ammonia sensing and regeneration time have been enhanced^[42]. Yavari et al. displayed room temperature sensing ammonia at ppb levels^[43]. Inkjet-printed graphene-PEDOT: PSS composite film sensed ammonia concentration low to 25 ppm. This device structure is capable of mass production and can be realized in flexible electronics^[44].
 2. **Nitrogen dioxide sensor:** Choi et al. fabricated gas sensor on a flexible substrate with multi-layered CVD graphene showing a detection limit at low ppm levels^[45]. Monolayer graphene FET has been also used for detection limit to 2.5 ppm but had a long response time^[46].

3. **Carbon dioxide sensor:** Nemade et al. used electrochemically exfoliated few-layer graphene to fabricate CO₂ sensor with excellent performance^[47]. Yoon et al. used mechanically cleaved graphene to fabricate a chemiresistor for sensing carbon dioxide to 10 ppm levels^[48].
- **pH sensor:** Fu et al. used the shift in Dirac point of graphene transconductance curve to detect the change in pH. They show that the GFET itself is not highly sensitive and a few nm of aluminum oxide is needed for increasing the sensitivity^[49]. Vivaldi et al. fabricated a pH sensor based on reduced graphene oxide on paper^[40].
- **Strain sensor:** Graphene inherently does not possess piezoresistivity with a low gauge factor (GF) of 1.9 reported by Huang et al.^[50] Hence, the engineering of graphene is required to achieve a higher GF. Introducing grain boundaries, defects can improve GFs as high as 151 in graphene^[51]. Kim et al. demonstrated interconnected micro-sheets of graphene as a channel material for strain sensing^[52]. It can detect strain by changing the resistance when stretched or compressed due to the change in the overlap of neighboring sheets.
- **Optical sensors:** Surface-enhanced Raman scattering (SERS) sensors have also been implemented in various fields based on graphene^{[53][54]}. SERS is an attractive tool due to its enhanced detection of sensitivity. Graphene quenches the fluorescence background and with certain nanometals can be a potential substrate for SERS^[55]. Ling et al. showed graphene enhances the Raman signal for molecules adsorbed onto its surface^[56]. Ye et al. displayed polarization-dependent optical absorption in graphene^[57]. This property was then used by Xing et al. to develop high sensitivity detection of cancer cells^[58].

2.1.2 Carbon nanotubes

CNTs are a rolled-up structure of a graphene sheet. Hence, an additional boundary condition is imposed. The $\vec{k}_{||}$ vector parallel to the CNT axis is continuous but \vec{k}_{\perp} is quantized due to the rolled-up structure^[1]. The rolling up of the graphene can be done in numerous ways by superposing multiples of the primitive lattice vectors a_1 and a_2 forming a chiral vector, shown in figure 2.5.

$$C_h = na_1 + ma_2, m \leq n \quad (2.14)$$

Due to the hexagonal symmetry, $m \leq n$ should be only considered. Here n, m belongs to the natural number and are called chiral indices and unique for a CNT. The translation

vector T is defined as the vector normal to the chiral vector and parallel to the nanotube axis. Using the indices, the diameter d of the CNTs can be given as

$$d = \frac{|C_h|}{\pi} = \frac{a}{\pi} \sqrt{n^2 + nm + m^2}, a = \sqrt{3}a_c = 0.246 \text{ nm} \quad (2.15)$$

The angle between na_1 and ma_2 is the chiral angle and given by the equation 2.16 ^[59]

$$\theta = \arctan \left(\frac{\sqrt{3}m}{2n + m} \right) \quad (2.16)$$

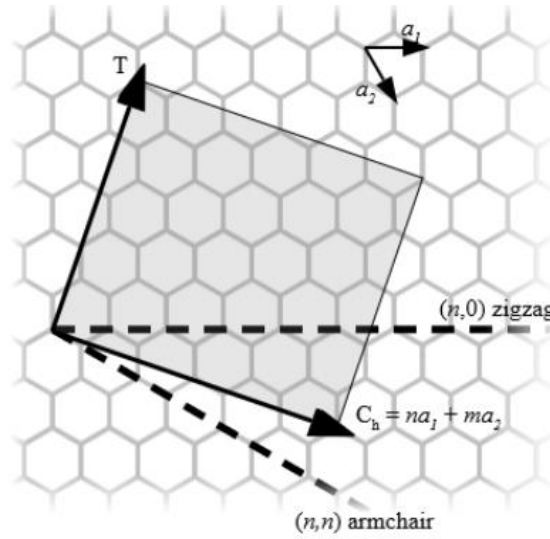


Figure 2.5: Graphene sheet rolling to a carbon nanotube. T is the translation vector along the axis and C_h is the chiral vector^[60].

Due to hexagonal symmetry, $0 \leq \theta \leq 30^\circ$. CNTs with $(n, 0)$ indices and chiral angle of 0° are called zig-zag CNTs and (n, n) with the chiral angle of 30° , armchair CNTs. They are metallic or semiconducting depending on the chiral indices (n, m) . The condition $3i = (n - m)$, where i is an integer, denotes all the tubes that have metallic behavior ^[61]. All the others have semiconducting properties. The band structure of a CNT is calculated by a zone-folding approximation based on the tight-binding calculation of graphene. Due to multiple 1D parabolic bands, the density of states is marked by van Hove singularities and $\frac{1}{\sqrt{E}}$ energy dependence is given by ^[59],

$$\rho(E) = \frac{2a}{\pi t |C_h|} \sum_{i=1}^{2n} \sum_{s=\pm} \frac{|E_i^s(k)|}{\sqrt{E_i^s(k)^2 - \epsilon_{is}^2}} \quad (2.17)$$

Here i iterates over the different bands and s is the spin state. The band gap in semiconducting CNTs is calculated by the energy gap between the first two van Hove singularities. Figure 2.6 shows the band diagram of a semiconducting and a metallic CNT.

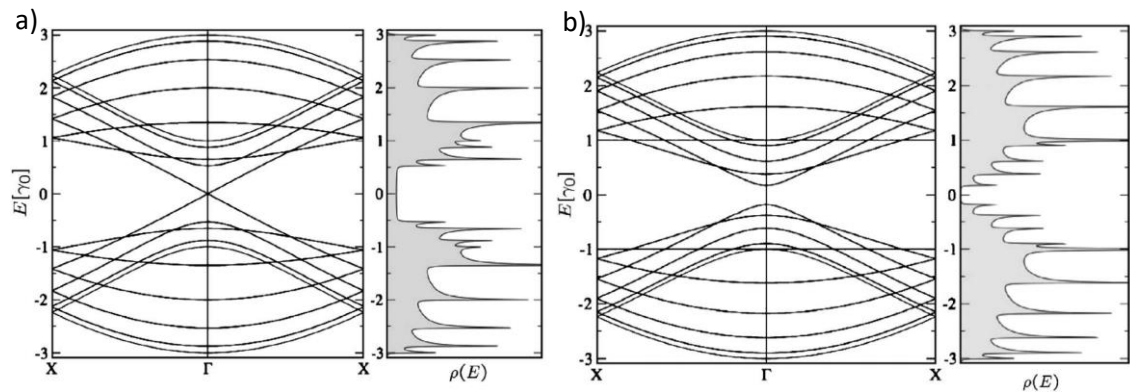


Figure 2.6: a) (9,0) metallic zig-zag carbon nanotube b) (10,0) semiconducting zigzag carbon nanotube (adapted from ref^[59]).

2.1.2.1 Carbon nanotubes field-effect transistors

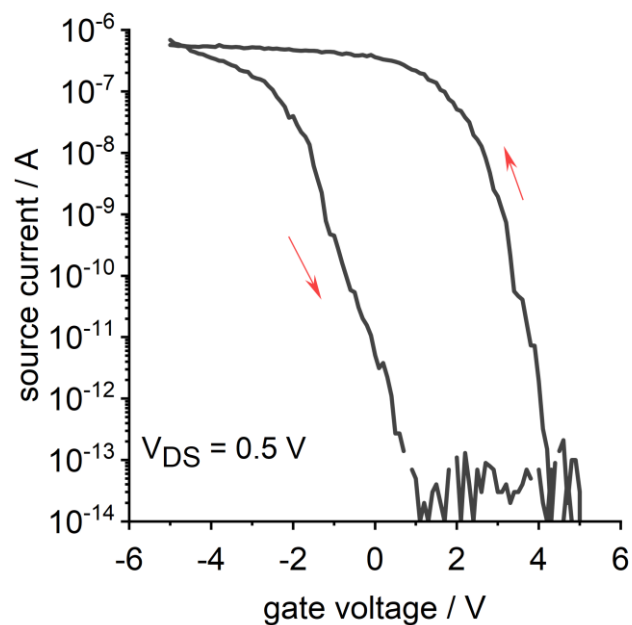


Figure 2.7: Transconductance curve of a CNT-FET fabricated on h-BN/SiO₂/Si. Red arrows indicate the sweep direction.

Carbon nanotubes can be utilized as a channel material to fabricate FETs. The transconductance curve of p-type CNTs on h-BN and SiO₂ as gate dielectrics is shown in figure 2.7. The channel conducts only holes (at negative gate voltage) and not electrons. The red arrows indicate the sweep direction. The source current is not equal in forward and reverse sweeps. This can happen if hysteresis exists in the system. Hysteresis in these types of field-effect transistors is always present and is discussed in the next section. Important parameters to understand the performance of such transistors are field-effect mobility, on-off ratio, and sub threshold slope which are also discussed in next section.

2.1.2.2 Hysteresis

2.1.2.2.1 Causes of hysteresis

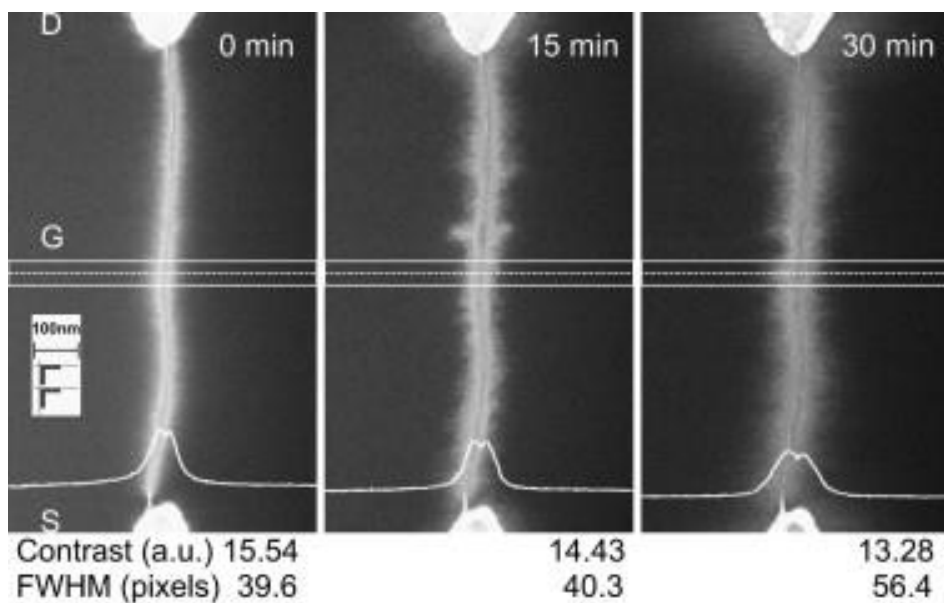


Figure 2.8: Time-dependent voltage contrast SEM images for a metallic nanotube at 20 V gate bias. At 0 min charges are injected in the nanotube and it appears brighter than the substrate. At 15 mins of charging, dielectric around the nanotube is populated with charges visible by high contrast area around the tube. At 30 mins the nanotube is itself darker but the substrate around is brighter (adapted from ref ^[62]).

- a) **Charge traps in dielectric:** Vijayraghavan et al.^[62] used voltage-contrast scanning electron microscopy (VC-SEM) to study and image the charging and discharging of charge traps present in the dielectric layer. The concept is based on the fact that charges from nanotube would be injected into the dielectric (SiO₂) which contributes to surface potential and consequently to secondary electrons yield

which then can be used to image the charge injection and redistribution. For gate bias of +20 V, images were recorded at three timestamps (figure 2.8). At $t = 0$, the nanotube appears brighter and the substrate darker because of the charging of the nanotube. With time, electrons start getting injected from the nanotube into the substrate which is visible at $t = 15$ min as a brighter area growing around the tube. At time $t = 30$ min, the nanotube itself remains dark and the substrate becomes brighter because of zero potential to nanotube but the negative potential to the substrate because of charge injection.

- b) **Water molecules:** Kim et al. ^[63] have shown how water molecules in the environment affect device performance and hysteresis. They infer that the main contributors are water molecules, especially SiO_2 surface-bound, which cannot be removed even in an inert atmosphere.

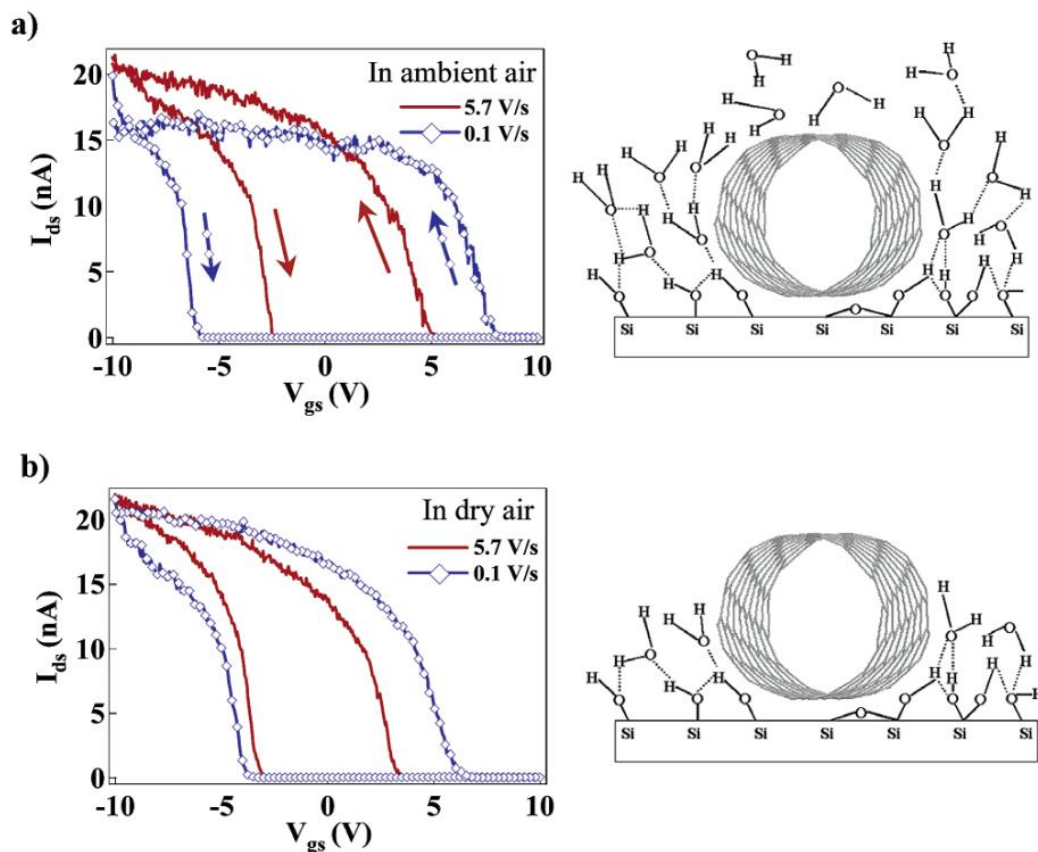


Figure 2.9: a) In ambient air, water molecules and water adsorbed on silicon oxide can interact with nanotubes and give rise to larger hysteresis compared to b) dry air, where only water molecules on the substrate contribute towards hysteresis (adapted from ref ^[63]).

Water on CNTs can also act as slow charge traps, and while gate sweeping, charging, and discharging do not occur on the same time scale. This in turn can lead to hysteresis (figure 2.9).

- c) **Surface hydroxyl groups:** Jin et al. [64] studied the interface of CNTs and the substrate SiO_2 . Surface-hydroxyl groups present on SiO_2 surface due to adsorption of water molecules are one of the prime contributors to hysteresis^[65,66]. Charging and discharging of hydroxyl (-OH) group can electrostatically modulate and thereby change the conductivity of the SWCNTs. With a positive bias on the gate, -OH groups can trap electrons. For a p-type SWCNT-FET, this causes the threshold voltage to shift in the positive direction to counter-balance electron charges trapped. The density of physisorbed water molecules at the interface affects the magnitude of this effect^[67,68].

2.1.2.2.2 Mechanism of hysteresis

To understand the mechanism of hysteresis, charge redistribution at the dielectric-nanotube interface during gate bias needs to be realized. Figure 2.10e illustrates a transconductance curve measured for (9,8) p-type SWCNT transistor on SiO_2/Si substrate under ambient conditions. The complete gate voltage sweep (forward and reverse) is explained by showing charge redistribution in the oxide layer using figures 2.10a-d. The sweep range is -5 V to 5 V with a scan rate of 0.1 Vs^{-1} . Initially, $V_g = -5 \text{ V}$ is applied depicted in figure 2.10a. Subsequently, positive charges appear on the dielectric surface (SiO_2) which p dopes CNT channel and source-drain current ($\sim \text{nA}$) is measured. The channel is in the on-state (regime a). Due to charge traps present in the dielectric, even after removal of bias ($V_g = 0 \text{ V}$), the dielectric surface remains positively charged and starts to n dope channel as shown in figure 2.10b. Electrons do not contribute as charge carriers because the Schottky barrier is very large for electrons and low for holes. Therefore, the channel is in off-state (regime b). At positive gate bias ($V_g > 0 \text{ V}$), mirror charges (negative charges for positive gate bias) appear on oxide surface and n dopes the channel shown in figure 2.10c. Source-drain current in the order of fA flows through the channel and the channel is still in off-state (regime c). During the reverse sweep (at $V_g = 0 \text{ V}$), charges trapped in the dielectric are negative which p dopes the CNT channel (figure 2.10d). A finite value ($\sim 1 \text{ nA}$) of current flows from source to drain and the channel is in on-state (regime d). To summarize, in forward bias at $V_g = 0 \text{ V}$, the source-drain current is zero, but in the reverse sweep at $V_g = 0 \text{ V}$, the source-drain current has a non-zero value. Therefore, the history and present conditions of gate voltage play a role if the channel would behave as off or on in a transistor. Although the reasons are discussed in the previous section, it is important to note that charge traps in the

dielectric can induce a condition of hysteresis in CNT transistors, and different time scales of charging and discharging of these charge traps lead to this phenomenon. Charge traps can also be formed at metal-CNT contacts due to the adsorption of water molecules on the metal ^[70] for devices with CNT on top of metal contacts. For devices with metal on top of CNT contacts, water adsorbed charge traps on metal do not play any role in the hysteresis. After understanding the mechanism, one can ponder over possible solutions.

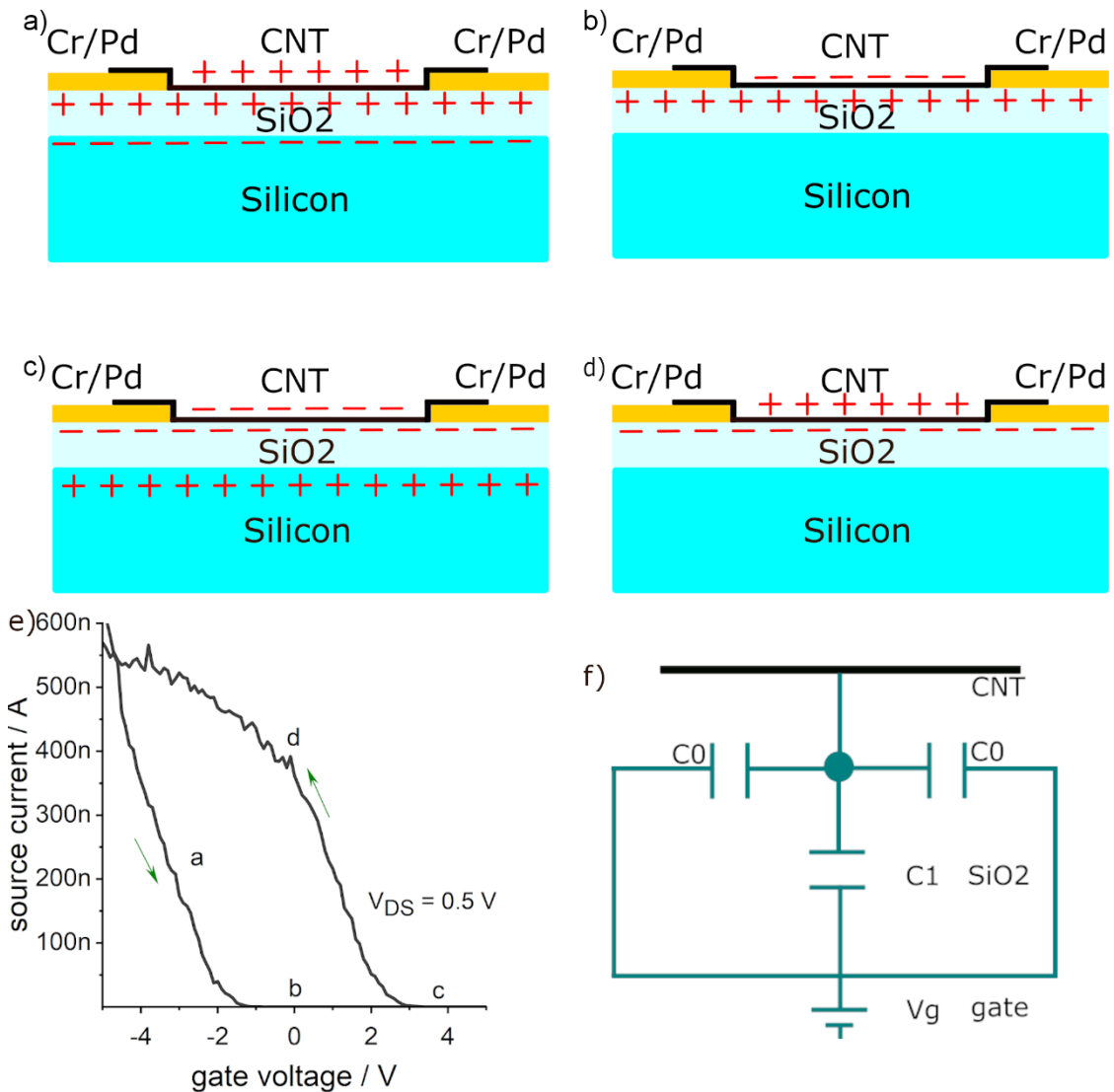


Figure 2.10: a) Schematic of hysteresis surface charging and discharging. a) At the start of gate sweep with negative gate voltage ($V_g < 0$). b) At $V_g = 0$ V. c) At positive gate bias ($V_g > 0$). d) At $V_g = 0$ V in a reverse sweep. e) Transconductance curve of (9,8) SWCNTs on SiO₂ measured under ambient conditions, green arrows indicate sweep direction. f) Equivalent circuit of hysteresis model. C1 is silicon oxide capacitor and C0 is the surface leaky capacitors where charge redistribution takes place (modified from ref ^[69]).

2.1.2.2.3 Solutions to hysteresis

The key to hysteresis-free SWCNT transistors is to form an environment for the nanotubes free from charge traps and water molecules. Some of the reported studies are briefly described below.

a) Passivation of substrate:

- a. Functionalization of SiO₂/Si using silanes^[71].
- b. Making the substrate hydrophobic by polymers like parylene^[72] or PTFE^[73].
- c. Self-assembled monolayer on metal gate oxide which is used as gate dielectric^[74]

b) Using top gate structure: Many oxides like TiO₂^[75], self-grown Aluminum dioxide^[76] have been used as top-gate dielectric which can remove the effects of SiO₂ charge traps and can also act as an encapsulant.

c) Encapsulation of the nanotubes: To inhibit any interaction of water molecules from the environment, SWCNTs should also be encapsulated.

- a. Oxide coating, for example, aluminum dioxide^[77]
- b. Polymer coating like methyl siloxanes or polymethylmethacrylate (PMMA) ^{[63][64][78][79][80][81]}

d) Creating inert atmosphere:

- a. Suspending carbon nanotubes and exposing them to high vacuum^[69]
- b. Cooling down to 4 K^[5].

2.1.2.3 Charge traps

Carbon nanotube transistors on h-BN and SiO₂ can be considered in the capacitance model shown in figure 2.11. The capacitance of the system was calculated using CNT as a cylinder on top of the parallel plate Si shown in figure 2.11. The capacitance of such a system is^[69]

$$c_g = C/L = \frac{2\pi\epsilon}{\ln\left(\frac{4h}{d}\right)} \quad (2.18)$$

Here L is the length of the CNT channel, d is nanotube diameter and h is the distance between CNT and silicon.

$\epsilon = \epsilon_o \epsilon_{eq}$, (ϵ_o is the permittivity in free space).

$h = 300 \text{ nm (SiO}_2\text{)} + 80 \text{ nm (h-BN)} = 380 \text{ nm}$

$$\varepsilon_{h-BN} = 3.29, \varepsilon_{SiO_2} = 3.9$$

For CNT transistors on top of the SiO_2

$$C_{g,SiO_2} = 0.302 \text{ pF cm}^{-1}$$

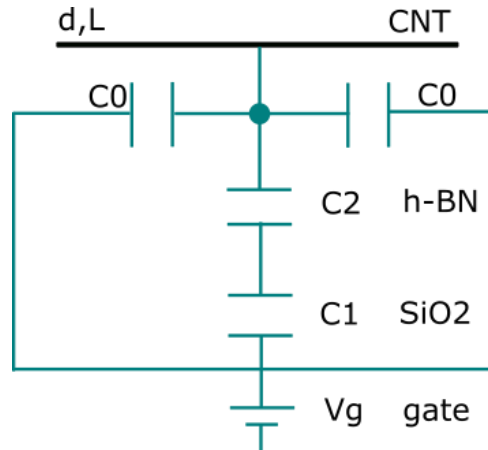


Figure 2.11: Capacitance system of nanotubes on h-BN and SiO_2/Si .

For 80 nm of h-BN on top of 300 nm of SiO_2 , two dielectrics are in series, and therefore the equivalent dielectric constant of the system has to be calculated using two capacitors in series. The equivalent dielectric constant of the system is then

$$\varepsilon_{eq} = \frac{(d_{h-BN} + d_{SiO_2})\varepsilon_{SiO_2} \varepsilon_{h-BN}}{d_{h-BN}\varepsilon_{SiO_2} + d_{SiO_2}\varepsilon_{h-BN}} \quad (2.19)$$

which is calculated $\varepsilon_{eq} = 3.75$

Calculating C_g gives the value

$$C = 0.290 \text{ pF cm}^{-1}$$

For calculating the number of charge traps for devices ^[63], an absolute value of threshold voltage for forward and reverse sweeps are required (hysteresis). Utilizing the capacitance value, charge traps can be calculated by using $Q = C V$ where V is the value of hysteresis in volts.

2.1.2.4 Field-effect mobility

Mobility for a nanotube device is given by:

$$\mu = \sigma/q \quad (2.20)$$

Charge density per unit length q is given by

$$q = c_g(V_t - V_g) \quad (2.21)$$

For channel length greater than the thickness of the dielectric, mobility is given by

$$\mu = \frac{L}{c_g} \frac{G}{(V_t - V_g)} \quad (2.22)$$

Due to ambiguity in determining the threshold voltage V_t for field-effect transistors, mobility is expressed in terms of field-effect mobility^[82]:

$$\mu_{FE} = \frac{L}{c_g} \frac{\delta G}{\delta V_g} \quad (2.23)$$

Field-effect mobility is device-specific and not material-specific. It depends on contact resistance, surface effects, etc.^[82].

The device performance can also be measured in terms of field-effect mobility values. Higher values are required for better performance of transistors.

2.1.2.5 Sub threshold slope

The subthreshold slope is one of the parameters on which a transistor performance is characterized. In the subthreshold region of the device's transport, current in the channel decays exponentially controlled by the gate, similar to a forward-biased diode. The subthreshold slope is the reciprocal value of subthreshold swing and is given by the following equation^[82]:

$$S = (d(\ln G)/dV_g)^{-1} \quad (2.24)$$

The theoretical limit of subthreshold slope known as the thermionic limit is 60 mV dec⁻¹ at room temperature, and experimentally ~ 70 mV dec⁻¹, slightly degraded due to parasitic capacitances^[83]. Smaller values imply a faster switching rate and therefore better performance of a transistor.

2.1.2.6 Literature

CNTs have been employed in several device applications and shown promising performance in diodes^[84], quantum light sources^[85], and sensors^[3]. Few reports are discussed below:

- **Memory devices:** CNTs based memories have advantages due to high stability, high thermal conductivity, and small sizes^[86]. Fuhrer et al. reported the first application of carbon nanotube transistors as a non-volatile memory^[87]. Cai et al. reported excellent charge storage capability at room temperature^[88]. Derycke et al. fabricated a voltage inverter by using n-type and p-type carbon nanotubes^[89]. Yang et al. showed non-volatile memory based on semiconducting CNTs with large retention capacity^[90].
- **Gas Sensors:** The ability to detect changes in its surroundings, doping, and large on/off ratio makes CNTs an ideal candidate for sensing application. When interacted with a foreign molecule, the electrical conductivity of the CNTs changes due to charge transfer. Kong et al. first displayed this principle in 2000 where the conductivity increased or decreased when exposed to NO₂ or NH₃ molecules^[91]. Huang et al. fabricated a three-terminal device N₂ sensor based on vertically aligned CNTs^[92]. Ganzhorn et al. demonstrated a hydrogen sensor based on carbon nanotubes, where the change in the work function of Pd was the sensing principle^[3].
- **Photo sensors:** A photon with energy higher than the band gap of CNTs generates electron-hole pair, which is then separated by built-in electric potential and measured as photocurrent. This photocurrent can be utilized for photo sensing. The potential is created by either a p-n junction^[93] or a Schottky barrier^[94].

2.1.3 Nanocrystalline graphene

2.1.3.1 Synthesis

Nanocrystalline graphene (NCG), is another form of graphene with crystal size in nanometers. Several synthesis routes are reported in the literature. Zhang et al. graphitized the spin-coated photoresist under high vacuum at higher temperatures (~1000°C) with a controlled flow of H₂/Ar^[95]. Turchanin et al. used aromatic self-assembled monolayer (SAM) to grow NCG. The SAM was first cross-linked using a high dose of electron irradiation and subsequently vacuum annealed to form graphene^[96]. Zhao et al. reported an ultrafast technique of NCG synthesis. A platinum foil was heated at high temperature (~900°C) and thereafter quenched in ethanol at room temperature, resulting in the synthesis of NCG in few seconds^[97]. Yekani et al.^[98] synthesized NCG on germanium substrate using a similar process reported by Riaz et al^[99].

The CVD technique can also be utilized to synthesize NCG. Noll et al. reported the fabrication of NCG for ammonia detection by using an additional layer of PMMA as a carbon source other than the CH_4/H_2 precursor^[100]. Plasma-enhanced CVD allows the synthesis at lower temperatures (750-900°C) as the precursors can be dissociated using plasma^[101]. Oliveira et al. reported NCG fabrication using molecular beam epitaxy (MBE) on sapphire substrates^[102] where HOPG filament as a carbon source is heated at extremely high temperatures (2200-2400°C) in ultra-high vacuum.

2.1.3.2 Electrical properties

In graphene, resistance can be given as ^{[103][104]}

$$R_{total} = R_{grains} + R_{GB} \quad (2.25)$$

The GBs have a diminished conductivity for electron and hole-type charge carriers and may act as an electrical potential barrier for charge transport and enhance intervalley scattering^[105]. Scanning tunneling microscope (STM) studies have shown an inclination of GBs towards n-type behavior when compared with the grains in bulk graphene^[106]. It is independent of temperature and can range from few to hundreds of kΩ. The charge transport in graphene is controlled by scattering at GBs and scattering in grains. In a polycrystalline graphene sample, average GB resistivity can be calculated using the scaling law

$$R_s = R_s^0 + \frac{\rho_{GB}}{l_G} \quad (2.26)$$

Here, R_s is the sheet resistance of polycrystalline graphene, R_s^0 is the sheet resistance within grains and l_G is the average size of the grain^[107]. For larger grain size (>10 μm), the first term is dominated and the sheet resistance is equivalent to the resistance of the individual grains and the contribution from GBs does not play an important role^[108]. However, for nanocrystalline graphene (grain size 2-5 nm), resistance is dominated by scattering at GBs. Therefore, the conductivity in NCG can be described as a framework where the electron conduction occurs within grains and tunnels through the grain boundaries. It is based on tunneling conduction theory. Simmons gave a generalized formula by studying conduction between two electrodes separated by a thin insulating film^[109]. Considering two grains separated by GB, based on the Simmons formula, charge transfer from one grain to another occurs through tunneling, and the conductance is given by^[110]

$$G_{ij} = G_f \exp \left(-2\chi S_{ij} - \frac{E_{ij}}{kT} \right) \quad (2.27)$$

$$E_{ij} = \frac{1}{2} (|E_i - E_j| + |E_j - E_i|) \quad (2.28)$$

Here χ is the tunneling parameter, E_i and E_j are the electron energies at the grains i and j . S_{ij} is the tunneling distance between the center of the grains.

Few studies reported on the values of sheet resistance of NCG thin films. The sheet resistance primarily depends on the thickness and crystallite size. Riaz et al. studied the sheet resistance based on thickness which varied from 20 k Ω sq $^{-1}$ (6nm) to 80k Ω sq $^{-1}$ (1nm)^[99]. Zhang et al. reported 30 k Ω sq $^{-1}$ for 1 nm thick NCG films^[111]. Turchanin et al. were able to tune the crystal size with temperature and had values of sheet resistance from 10 to 100 k Ω sq $^{-1}$ for crystal sizes 25 to 8 nm^[96]. Zhao et al. achieved 33.7 k Ω sq $^{-1}$ (10.3 nm) and 180 k Ω sq $^{-1}$ (3.6 nm) sheet resistance values^[97].

2.1.3.3 NCG field-effect transistor

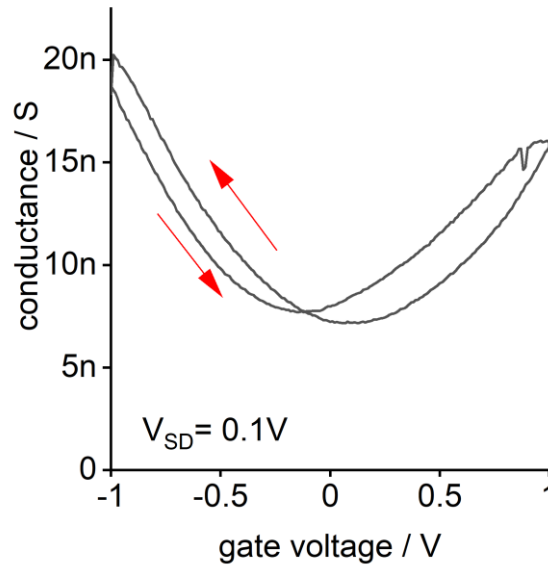


Figure 2.12: Transconductance curve of an ionic liquid gated NCG field-effect transistor. The red arrows indicate the sweep direction.

Figure 2.12 shows a transconductance curve of an NCG-FET with a top ionic liquid gate. The curve is similar to graphene field-effect transistors and shows hole (negative gate voltage) and electron (positive gate voltage) conduction regimes. The conductance minima occur close to zero gate voltage indicating small doping levels.

2.1.3.4 Mechanical properties

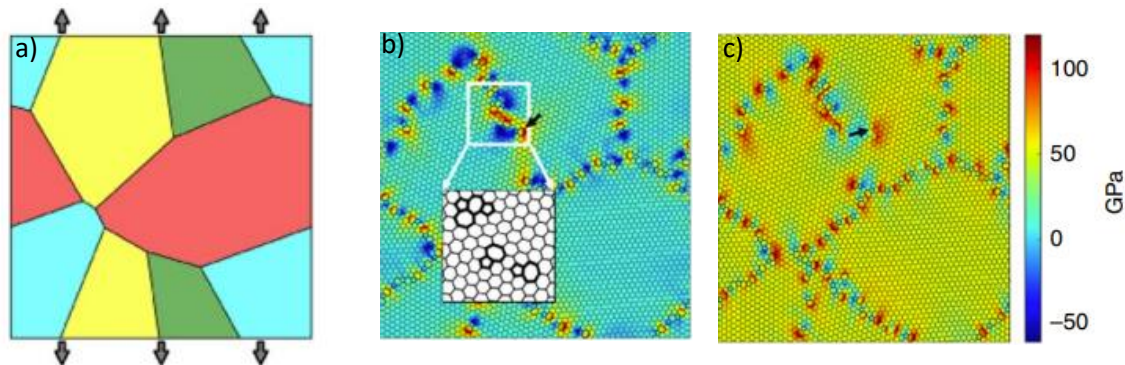


Figure 2.13: a) Schematic of randomly oriented grains in a polycrystalline graphene under tensile stress b) Residual stress showing the grain boundaries have higher concentration of strains (black arrow) compared to grains c) Stress in the grains and grain boundaries just before fracture of the film (adapted from ref ^[15]).

Lee et al. were the first to report on the mechanical properties of graphene specifying excellent mechanical strength with young's modulus of 340 N m^{-1} ^[17]. NCG, however, has a large density of defects present in the form of GBs and TJs which comprises heptagon and pentagon defects in an otherwise hexagonal structure. This affects the mechanical and electrical properties in comparison to graphene^[112,113]. Shekhawat et al. showed that these defects can act as stress concentrators^[2]. In figure 2.13a, simulation is shown where a polycrystalline graphene sample is subjected to tensile stress. Figure 2.13b-c show two instances of zero external stress and the peak stress at failure. In figure 2.13c it is depicted that the origin of fracture occurs at one of the GBs and then propagates through the crystals. The GBs are however already under higher stress compared to the crystals even before the application of any external stress. Zhao et al. showed that as the size of the crystals moves down to 3.8 nm, the fracture strength of graphene reduces by 40%^[97]. GBs are a low elastic modulus region in NCG because of the long bond length in GBs compared to inside grains^[114]. According to the Hall-Petch effect, nanocrystalline materials are primely harder compared to their microcrystalline counterparts^[115]. However, NCG GBs have stable covalent sp^2 bonds and hence no slip occurs between two grains. Therefore, under externally applied stress, brittle breakage of these covalent bonds occurs and the origin of fracture is always at a defect site (GBs or TJs). Fracture propagation could be intergranular or intragranular^[2].

2.1.3.5 Piezoresistance principle in NCG

Piezoresistance exists in many metals like iron and semiconductors like silicon. It was first studied by William Thomson in iron and copper back in 1856^[116]. He observed a

change in resistance by elongating the metals using a Wheatstone bridge. In 1935 the term “Piezoresistance” was coined by Cookson^[117]. The first experimental proof of piezoresistance on semiconductors was shown in 1954^[118]. Since then, silicon has been used in various strain gauges to measure mechanical quantities like force, torque, etc.^[119,120]. Consequently, this led to the emergence of the MEMS technology in 1982^[121].

The resistance (R) of material with a current (direction indicated by orange arrow) passing through an area A and length l (figure 2.14) is given by



Figure 2.14: Resistance of a block of material with length l and cross-section area A .

$$R = \frac{\rho l}{A} \quad (2.29)$$

Here, ρ is the resistivity of a material.

Resistance can change due to the application of external strain. The change occurs either due to a change in resistivity of material or change in geometry or both. GF is the ratio of fractional change in resistance and applied strain ε . It is expressed as

$$GF = \frac{\Delta R}{R \varepsilon} \quad (2.30)$$

Taking into consideration the geometrical factor $(1+2\nu)$ and the resistivity change^[122]

$$\frac{\Delta R}{R} = (1 + 2\nu)\varepsilon + \frac{\Delta\rho}{\rho} \quad (2.31)$$

Here ν is the Poisson's ratio. The value for most metals' ranges from 0.2 to 0.35. Silicon, as an anisotropic material, the Poisson's ratio depends on the direction of the crystal structure and the value ranges from 0.06 to 0.36^[123]. The limits of ν for an isotropic material are -1 to 0.5^[124].

Metals have a very small GF due to the small change in resistivities, whereas, silicon and germanium experience large changes in resistivity in a certain direction of crystal structure and strain due to anisotropic behavior. Semiconductors have a directional dependence of piezoresistivity in terms of directions of load applied (stress) and fields

such as current or potentials. In semiconductors, the explanation of piezoresistance is in how electrons and holes move in the crystals under strain. Mobilities and effective mass of charge carriers change under applied strain^[125]. The two types, n- and p-type semiconductors behave inversely. The reason for the change in mobility is attributed to band bending and non-uniformity in the density of states^[118].

There have been few studies that have reported on NCG as a piezoresistance material. Riaz et al. demonstrated a proof of concept of NCG strain sensor with a GF of 23^[99]. Zhao et al. achieved GF of ~300 based on nanographene films. They used the charge tunneling model to explain their findings^[126] until small strain values of 0.3%. In another report by the same group, a tunable piezoresistive strain sensor was fabricated with GF up to 500. The tunability of resistance and GF was gained by controlling the domain size of NCG films. The piezoresistance behavior beyond 0.3% strain follows the tunneling and destruction model^[24].

2.1.3.5.1 Piezoresistance model

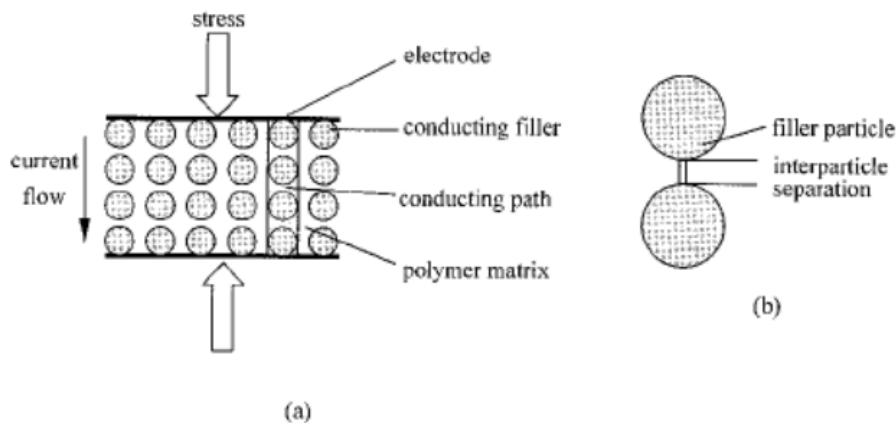


Figure 2.15: Schematic of a) the stress applied on a conductor-filled polymer composite and b) two conductive particles with an interparticle separation (adapted from ref^[127]).

NCG film displays the inherent property of piezoresistance. To explain this, researchers take into account the charge tunneling model given by Simmons^[109] where the tunneling of charged carriers occurs between adjacent electrodes separated by a distance. Zhang et al.^[127] studied a conductor-filled polymer composite as a piezoresistance system which can be mimicked for piezoresistance in NCG. The same model was also applied by Zhao et al.^[24]. Grains of NCG can be considered as conductive fillers in a composite of polymer separated by a tunneling distance similar to GBs. In this section, the derivation of the model is discussed briefly.

In the polymer conductor composite, resistance is contributed by resistance through each conductor particle and the polymer matrix. Figure 2.15a-b shows a polymer conductor composite where the conductor particles are separated by a distance. Resistance can be given by ^[128]

$$R = \frac{L(R_m + R_c)}{N} \quad (2.32)$$

Here L is the number of particles forming a conducting path, R_m and R_c are the resistances of matrix and conductor and N is the number of conducting paths. An assumption of constant resistance of the matrix is made, and therefore, several conducting paths perpendicular to the current flow is ignored. At small distances between the conductor, tunneling current can flow^[129] which can be given by Simmon's function at low bias as ^[109]

$$J = \frac{3\sqrt{2m\phi}}{2s} \left(\frac{e}{h}\right)^2 V \exp\left(-\frac{4\pi s}{h}\sqrt{2m\phi}\right) \quad (2.33)$$

Here, e, m is the electron charge and mass, h is Plank's constant, V is the bias applied and s is the thickness of the insulating film and ϕ is the difference in work functions of conductor and polymer. Assuming all the electrons tunnel within a small surface area a^2 and at the least distance s between particles ^[130]. Resistance of the matrix can now be expressed as

$$R_m = \frac{V}{a^2 J} = \frac{8\pi h s}{3a^2 \gamma e^2} \exp(\gamma s) \quad (2.34)$$

Here $\gamma = \sqrt{2m\phi} \frac{4\pi}{h}$

Using equating 2.34 in equation 2.32, the total resistance can be expressed as

$$R = \frac{L}{N} \left(\frac{8\pi h s}{3a^2 \gamma e^2} \exp(\gamma s) \right) \quad (2.35)$$

After establishing the relation between the resistance and the tunneling distance, the rate of change of resistance with original tunneling distance s_0 can be derived (for strain values $< 0.3\%$) using equation 2.35 as

$$\ln \frac{R}{R_0} = \ln(1 + \varepsilon) + \gamma s_0 \varepsilon \quad (2.36)$$

$$GF = \frac{\Delta R}{R_0} / \varepsilon = \frac{1}{\varepsilon + \varepsilon^2} \exp(\gamma \Delta s) - \frac{1}{\varepsilon} \quad (2.37)$$

From equation 2.37, for the same strain values, higher sensitivity can be achieved if the change in tunneling distance, Δs , is larger. As strain is equivalent to $\Delta s/s_0$, Zhao et al. reported that films with similar sheet resistance have different GFs because of different initial tunneling distances [24]. For higher tunneling distance, higher GFs were achieved. Therefore, the initial tunneling distance should be the prime focus to achieve a higher GF piezoresistor. From the slope of $\ln(R/R_0)$ vs ε curve, the initial tunneling distance s_0 can be calculated, considering $\gamma = 10 \text{ nm}^{-1}$ [131].

For strain $> 0.35\%$, tunneling and destruction model is applied, where the number of conductive path N is reduced exponentially with increasing strain, and given by [132]

$$N = N_0 \exp[-(\alpha \varepsilon + \beta \varepsilon^2 + \gamma \varepsilon^3 + \lambda \varepsilon^4)] \quad (2.38)$$

and [24]

$$\ln \frac{R}{R_0} = \ln(1 + \varepsilon) + \alpha \varepsilon + \beta \varepsilon^2 + \gamma \varepsilon^3 + \lambda \varepsilon^4 \quad (2.39)$$

Here $\alpha = \gamma s_0$.

2.1.3.6 Literature

NCG has been employed in several applications. A few of the reports are mentioned below:

- **Sensors:** NCG with conductive domains, and a high density of GBs makes it a suitable candidate for sensing. The conductivity of the material changes if gas molecules get adsorbed on the GBs or if the distance between the grains is changed. Noll et al. fabricated an ammonia sensor using NCG-FET with detection limits of 100 ppb [100]. Zhao et al. fabricated a tunable strain sensor based on NCG and explain the dependence of tunneling distance on the sensitivity of strain sensing [24]. Yasei et al. demonstrated a 300 times higher sensitivity to the gases for NCG compared to mono-crystalline graphene [133].
- **Photodetectors:** NCG on Si/SiO₂ has shown promising application as Schottky junction photodetectors [134] [25] owing to high transparency, ~80-90% in the visible and IR region [99].
- **Gas separation:** Fishlock et al. utilized PECVD grown NCG films for the separation of gases based on molecular sizes [135]. The cut-off barrier of separation was ~0.34

nm, which is equivalent to the interlayer distance. This suggests that the flow of the gases for separation is interlayer and not through the defects in the layer.

2.2 Properties of carbon nano-systems

2.2.1 Raman spectroscopy

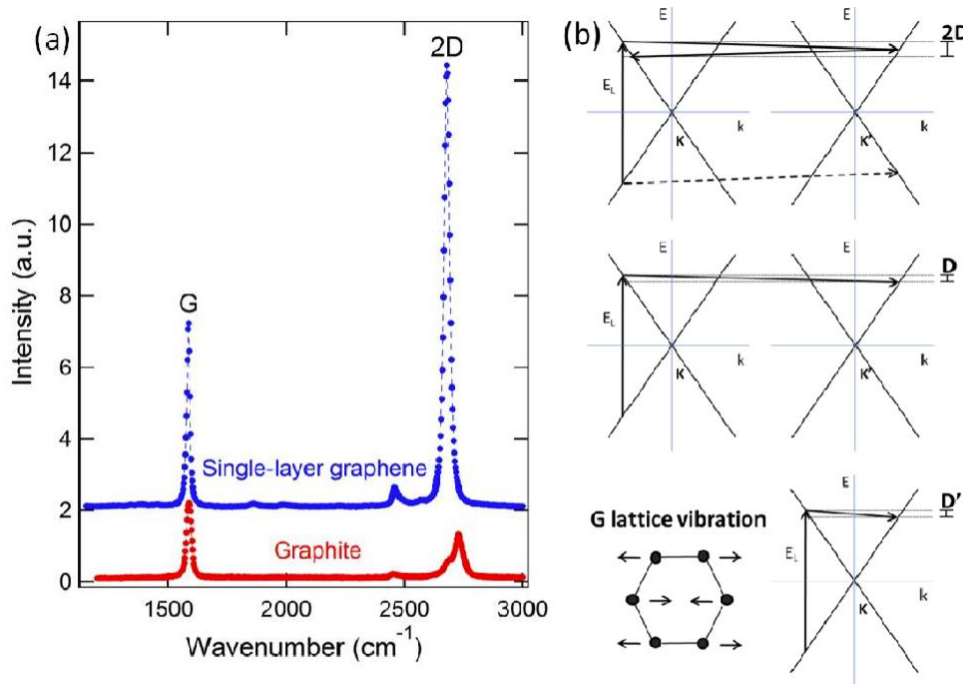


Figure 2.16: a) Raman spectra of graphene (blue) and graphite (red) by a 532 nm excitation laser b) Phonon scattering processes for different Raman peaks in graphene. D and D' peaks only occur in graphene films with defects (adapted from ref^[136]).

Raman spectroscopy is a widely used technique to study carbon nano systems such as graphene, carbon nanotubes, and nanocrystalline graphene. Raman spectra of a graphite crystal have a G band located at 1580 cm^{-1} and a 2D band at 2680 cm^{-1} (figure 2.16a). It is a non-destructive tool to study graphene in many different aspects, for example, number of layers, level of doping, and strain, etc. The G peak at 1580 cm^{-1} comes from the doubly degenerate zone-center E_{2g} phonon mode (figure 2.16b). Graphene is a monolayer of graphite and has additional peaks depending on defects. Some of the defects like GBs could break the symmetry and a defect band called the D band appears at 1350 cm^{-1} . The 2D mode at 2700 cm^{-1} is caused by the double resonant

Raman scattering with two phonon emissions (figure 2.16b)^[137]. The 2D band intensity is insensitive to defects but is sensitive to the number of layers of graphene. The G and 2D mode peak positions or the intensity ratio, both are sensitive to the doping level and charge carrier density due to electron-phonon coupling^[138]. Temperature and the levels of strain can also be determined by the shifts in graphene's Raman G and 2D peaks^{[139][140]}. Tunistra and K oenig used Raman to calculated the crystallite size of a graphitic material^[141]. Although, many pieces of information can be extracted from Raman spectroscopy of graphene, in this chapter the discussion is limited to the level of doping and crystallite size.

2.2.1.1 Doping and Strain

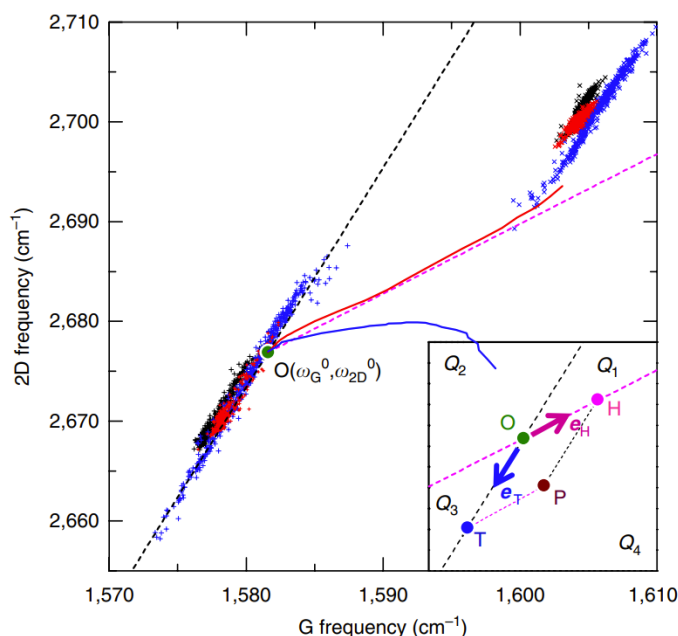


Figure 2.17: Three graphene samples were studied (red, blue, and black). The green dot is a reference point unaffected by any strain and doping. Magenta color dashed line depicts strain-free graphene with varying density of holes. The black dashed line depicts undoped graphene with varying strain. Red and blue solid lines represent holes and electron doping trajectories respectively. Inset: Decomposition of OP vector into e_T (strain axis) and e_H (doping axis) and the four quadrants Q_{1-4} (adapted from ref^[145]).

Numerous reports have studied the strain and doping level based on Raman peak positions of graphene^[142–144]. One of the reports on studying strain and hole doping is discussed which is used in chapter 5 to understand the results. Lee et al.^[145] characterized graphene doping and strain levels based on shifts and position of graphene Raman G and 2D peaks. Two vectors based on tensile strain (e_T) and hole (e_H) doping were established in ω_G - ω_{2D} space. Any vector OP (inset of figure 2.17) can be

deconvoluted into two components as $a\omega_{\text{T}} + b\omega_{\text{H}}$ and the level of doping and strain can be derived from the Raman peak frequencies.

The green dot is the G (ω_{G}^0) and 2D (ω_{2D}^0) frequencies of free-standing graphene which is undoped and unstrained. Red and blue solid lines represent varying holes and electron doping in the graphene film respectively. The space is divided into four parts by the vectors e_{T} and e_{H} . As the strain varies, the values move along the black dashed line (e_{T}) from O and with varying doping levels along the magenta line (e_{H}). The quadrants Q_2 and Q_3 are prohibited because the doping of electrons or hole should increase the G frequency. Q_4 and Q_1 is attributed to tensile and compressive strain respectively in combination with the doping.

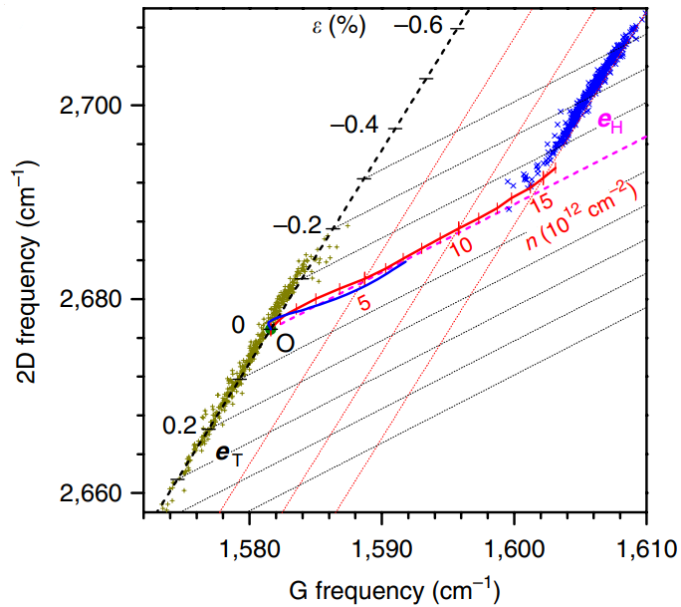


Figure 2.18: The parallel red dashed lines represent the different hole doping levels and the parallel black dashed lines represent the strain level. Step size of hole doping is $5 \times 10^{12} \text{ cm}^{-2}$ and of strain is 0.1% (adapted from ref ^[145]).

The assumption for the constant slopes of the line $\frac{\Delta\omega_{\text{2D}}}{\Delta\omega_{\text{G}}}$ is valid for a wide frequency range. At lower charge density, ($|n| \sim 10^{12} \text{ cm}^{-2}$) because of anomalous softening of G phonon, the variation of ω_{G} with n becomes non-linear and the slope is non-linear. The red solid line in figure 2.18 (theoretical) and the blue solid line (experimental) agree with each other and are represented by e_{H} lines. The uniaxial strain sensitivity, $\frac{\Delta\omega_{\text{G}}}{\Delta\varepsilon} = 23.5 \text{ cm}^{-1} \text{ \%}^{-1}$ was calculated from Yoon et al. Each tick mark on e_{T} corresponds to 0.1% strain. The slope of the e_{T} lines $\frac{\Delta\omega_{\text{2D}}}{\Delta\omega_{\text{G}}} = 2.2 \pm 0.2$ was determined experimentally. For the effect

of hole doping, an average of two results were used which is the slope of the line $e_H = \frac{\Delta\omega_{2D}}{\Delta\omega_G} = 0.7 \pm 0.05$. Each tick mark on the e_H line corresponds to $5 \times 10^{12} \text{ cm}^{-2}$. A point on the ω_G - ω_{2D} space can disentangle the amount of strain and doping levels in the graphene film using Raman shifts.

2.2.1.2 Crystallite size

Next, the crystal size can be estimated based on the intensities of the D and G peaks. This method is more beneficial for graphene which has crystal sizes in nm scale similar to nanocrystalline graphene or polycrystalline graphene. Tuinstra and Koenig concluded that the intensity ratio of D and G peak $\frac{I_D}{I_G}$ is inversely proportional to the crystallite size L_a of the measured sample^[141]. Mernagh et al.^[146] showed that the laser excitation wavelength also plays a crucial role in determining the crystallite size. Concado et al.^[147] derived a general relation to calculate the crystallite size for any excitation wavelength in the visible region. The ratio of intensities was plotted against the crystallite sizes obtained by x-ray diffraction profiles for each excitation wavelength. The plot was fitted by different powers of excitation wavelength as shown in figure 2.19a to converge at one point of L_a . The best fit was obtained for fourth power of excitation energy.

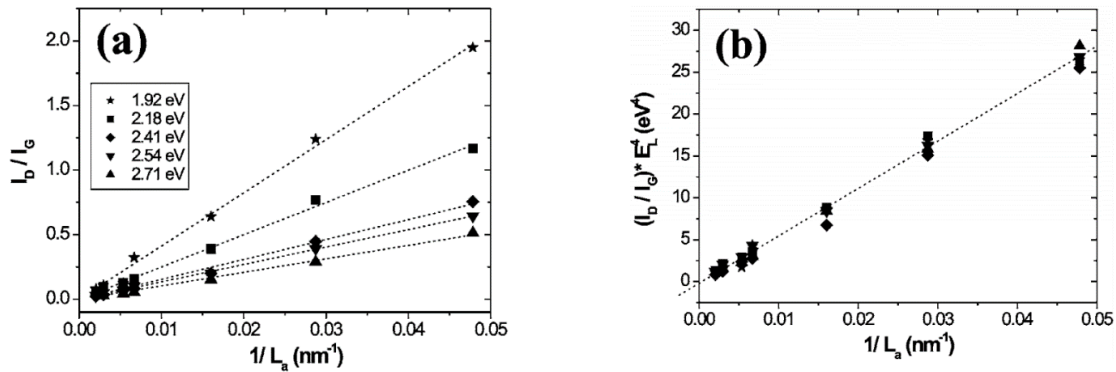


Figure 2.19: a) Ratio of integrated intensities vs inverse of crystallite sizes for different excitation lasers. b) Points fall in same straight line for E^4 dependence (adapted from ref ^[32]).

Next, the fourth power data is then fitted (figure 2.19b) to obtain a general relation for crystallite size calculation in terms of the wavelength of excitation wavelength in nm as follows

$$L_a(\text{nm}) = 2.4 \times 10^{-10} \times \lambda^4 \left(\frac{I_D}{I_G} \right)^{-1} \quad (2.40)$$

In other work by Concado et al.^[148], the full width at half maximum (FWHM) of Raman D and G peaks were used to calculate the crystallite size in nanographites.

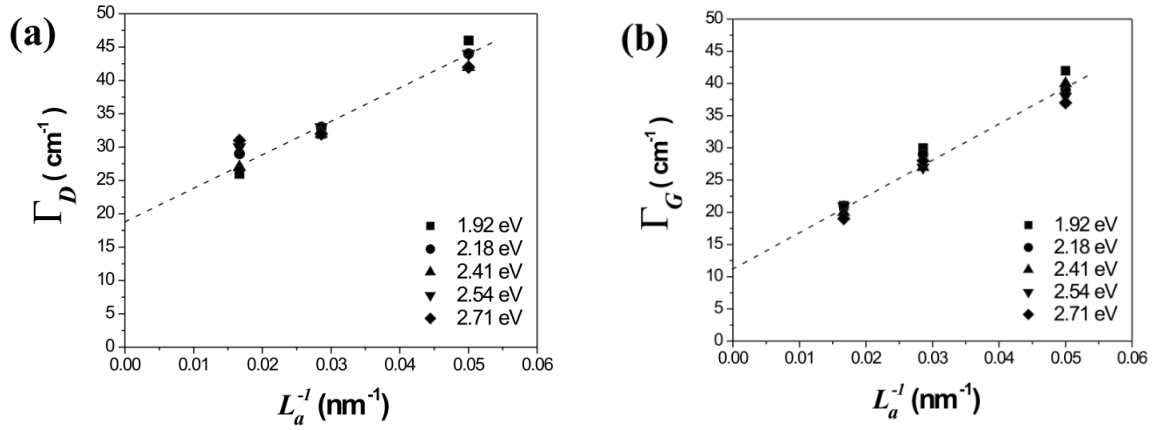


Figure 2.20: FWHM of a) D and b) G peak vs inverse of crystallite size for different excitation energies (adapted from ref^[33]).

From the linear fit in figure 2.20a-b, it is clear that FWHM of D and G peaks is inversely proportional to crystallite size and independent of the excitation wavelength. This fit can be expressed as

$$FWHM = A + \frac{B}{L_a} \quad (2.41)$$

FWHM in Raman peaks is linked to the lifetime of the phonons and is inversely proportional to it. For crystallite sizes smaller than the phonon mean free path, the phonon lifetime is proportional to the crystallite size. Hence, *FWHM* is inversely proportional to L_a . The lifetime reduces due to phonon scattering at the defect sites^[149]. Therefore, broader D, G, and 2D peaks are obtained for nanographites as they have smaller crystal size (in nanometer) compared to graphene which has sharper G and 2D peaks and larger crystal size (in micrometer). For different peaks, *A* and *B* values were calculated from the fit parameters and are tabulated in table 2.1.

Table 2.1: Linear fit parameters for D and G peaks obtained experimentally^[148]

Using equation 2.41 and values of *A* and *B* from table 2.1 crystallite size can be

Peak	A (cm^{-1})	B ($\text{cm}^{-1} \text{ nm}$)
D	19	500
G	11	560

calculated.

2.3 Support layers and coatings

2.3.1 Boron Nitride

Boron nitride, or white graphene, has been used as a ceramic for almost seven decades and integrated into graphene devices for almost a decade. Song et al. have reported an elastic modulus of 0.334 TPa and intrinsic strength of 26.3 GPa for h-BN^[150]. It has a melting point of 2973°C and a thermal expansion coefficient higher than diamond. It is stable in the air till 1000°C confirming its chemical stability^[151]. With a thermal conductivity of $\sim 2000 \text{ W mK}^{-1}$, it can conduct heat equivalent to graphene. Therefore, with such versatile properties, boron nitride is applied in different applications since its discovery^[10].

h-BN can boost charge carrier mobility in other 2D materials like graphene^[10,152] if used as the gate dielectric. Minimized Coulomb scattering, smooth surface with an absence of dangling bonds, and prevention from being contaminated are the key advantages allowing 2D materials to exhibit outstanding performance on h-BN^[151]. Boron nitride has sp^2 hybridized, equally spaced, boron and nitrogen atoms with a structure analogous to graphene honeycomb structure. It has lattice parameters, $a = 0.25 \text{ nm}$ and $c = 0.67 \text{ nm}$ and interlayer spacing of 0.33 nm. The in-plane bonds are covalent and highly polarised. Interlayer, van der Waal bonds play a major role. It has a band-gap of $\sim 6 \text{ eV}$ owing to large asymmetry in sublattices. The close lattice parameters of graphene and h-BN with slight lattice mismatch of $\sim 1.7\%$ ^[153] allow excellent interaction and opens possibilities for various device applications.

2D h-BN is an insulator and transparent that can work as a gate dielectric as well as an encapsulant with excellent chemical degradation resistance. Despite remarkable properties from the applications point of view, the following challenges persist:

- Large-scale synthesis and transfer techniques
- Combination with other nanomaterials

Recently progresses have been made to address these challenges.

Exfoliation of h-BN crystal gives the best quality, contamination-free thin films. The adhesive force of tape is used to physically cleave out boron nitride films^[154]. Another exfoliation pathway is using chemical reactions achieved by Han et al^[155]. Scalability is an issue in both processes and limits its industrial applications. CVD process is promising as it allows large-area synthesis and can be controlled for monolayer or multi-layered

growth. Precursors for CVD growth that have been extensively used in past times for h-BN synthesis are borazine^{[150][11][156]} and ammonia borane^{[157][158]}. Lower temperature (<1500°C) synthesis requires a catalyst to activate the precursor, discussed later in chapter 4. The drawback of h-BN synthesis on a catalyst surface is the requirement for the transfer process after synthesis. This makes the process complicated and can potentially lead to many defects such as wrinkles, film breaking, and contamination. Therefore, for a clean and easy process, catalyst substrate should be avoided. Growing h-BN thin films directly on a dielectric substrate is a better alternative for transistor applications^[156].

Integrating h-BN with other nanomaterials is the next challenge that has been addressed by the research community. The pioneering study of graphene and h-BN heterostructure was a water-based transfer process^[10]. Recently, the dry transfer method by using polypropylene carbonate (PPC) polymer on a polydimethylsiloxane (PDMS) elastomer stamp^[159–161] was demonstrated. Okada et al. used CVD to grow Tungsten disulfide (WS₂) directly onto h-BN/SiO₂^[162]. h-BN in combination with CNTs has proved to be an interesting material to study photonics^[163] as well. Baumgartner et al. reported carbon nanotubes quantum dots on flakes of h-BN^[164]. Huang et al. reported a better current carrying capacity for CNT devices embedded in h-BN flakes^[165]. Thus, it can be concluded that h-BN is a promising substrate for a variety of nanoscale electronics.

Although not implemented by the CNT community, integration of h-BN as a gate dielectric can eliminate one of the detrimental problems for CNT transistors that is hysteresis. This work captures insights into the synthesis process of h-BN using borazine and aims to address the long-standing issue of hysteresis in the CNT transistors.

2.3.2 Ultra-thin glass

Ultra-thin glass is a type of glass that has thicknesses in hundreds of microns. Many companies like Schott and Corning already developed technologies to fabricate glasses as thin as 30 microns. The technology used by Schott is called as down draw method. In this work, AF 32 eco thin glass was used which was acquired from Schott. Some of the important properties are mentioned in a tabular form below in table 2.2.

Table 2.2: Important properties of ultra-thin glass source: Schott.de

Properties	Values
Surface roughness	< 1 nm
Thickness	0.05 mm
Glass transition temperature	714°C
Luminous transmittance	91.9%

The low roughness and high transmittance make it an excellent choice for the fabrication of transparent strain sensors. Some of the advantages of this substrate are:

- The coefficient of thermal expansion is similar to silicon
- Temperature resistance up to 600°C

2.3.2.1 Stress in two-point bending of ultra-thin glass

There are various ways to impart stress to a thin film on a flexible substrate. Two-point, three-point, or four-point bending fixtures are the prominent ones. Gulati et al. in their work studied the stress distribution of two-point bending fixtures in ultra-thin glass^[166]. Prominent advantages for the use of ultra-thin flexible glass are:

- Ease of building and operation of the setup
- Uniform stress across the width substrate
- Bending without contacting the surface of the substrate

The stress in the ultra-thin glass in a two-point bending setup is at maximum at the mid-length and is given by ^[167]

$$\sigma_{max} = 1.198 \frac{Et}{(D - t)} \quad (2.42)$$

Here E is the young's modulus, t is the thickness and D is the distance between the two bending plates. The value decreases with moving to either side, based on the angle between the tangent and the normal at the center as shown in figure 2.21 and is given by the following equation 2.43

$$\sigma = \sigma_{max} \sqrt{\sin \theta} \quad (2.43)$$

For substrates (<5mm), the angle ψ between the substrate and the plates comes into account:

$$\sigma_{max} = 1.198 \frac{Et}{(D - t)} \sqrt{\cos\psi} \quad (2.44)$$

$$\sigma = \sigma_{max} \sqrt{\sin\theta} \sqrt{\cos\psi} \quad (2.45)$$

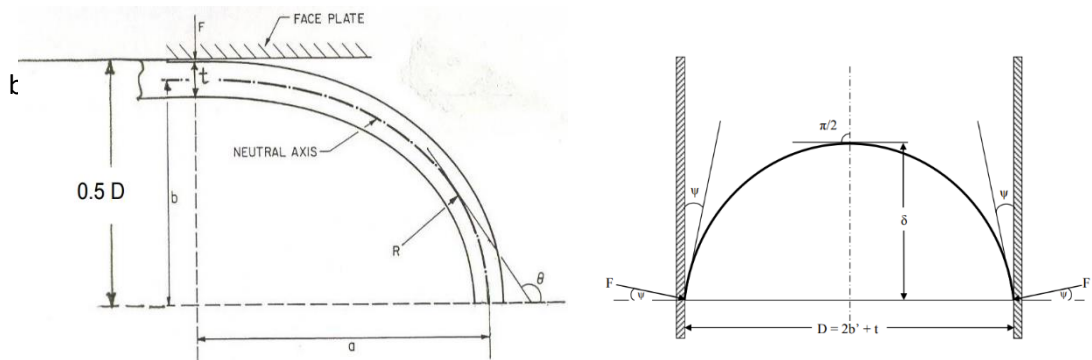


Figure 2.21: a) Schematic of two-point bending test b) A short glass substrate with angle ψ at the contacts (adapted from ref^[47]).

Finite element method (FEM) simulations show that the stress in ultra-thin glass in a

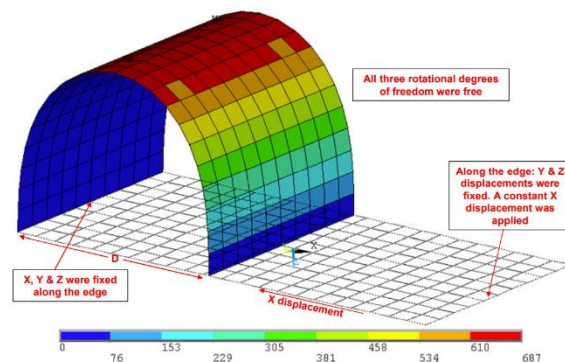


Figure 2.22: Stress profile in ultra-thin glass film under two point bending calculated by finite element analysis (adapted from ref^[47]).

two-point bending fixture is maximum at the middle area of the substrate (figure 2.22). The stress then reduces to a minimum value at the ends^[166].

2.3.3 Teflon AF 2400

Teflon, the chemical name of PTFE, commercial name Teflon AF 2400, is a family of amorphous fluoroplastics. It is an insulator, chemical resistant, and withstands higher

temperatures. It has a high gas permeability, high creep resistance, and very low thermal conductivity. Among fluoroplastics, Teflon has the lowest dielectric constant and refractive index^[168]. Some of its properties have been tabulated below in table 2.3.

Table 2.3: Properties of Teflon AF2400. Important barrier properties are marked blue.

Properties	Values
Dielectric constant	1.9 kV/0.1 mm
Optical transmission	>95%
Refractive index	1.29
Yield strength (MPa)	26.4 @ 25°C 8.7 @ 220°C
Tensile modulus (GPa)	1.6
Contact angle with water (°)	105
Gas permeability (Barrer)	H ₂ O = 4026 N ₂ = 490 O ₂ = 990 CO ₂ = 2800
Water absorption	<0.01 %
Glass transition temperature (T _g) (°C)	240

2.3.4 Metal-organic frameworks (MOFs)

MOFs is a group of crystalline materials consisting of metal nodes and organic ligands (linkers) connected by coordination bonds. Nano-porous structures with a controlled environment are the key advantages of using this class of material. These enable a wide range of practical applications in different physical or chemical environments^[169].

Virtually, an infinite number of MOFs are possible based on different combinations of the organic linker and metal nodes. A detailed review was published in 2017^[170]. MOFs have up to 90% of free volume and a large surface area makes them an ideal candidate for gas storage for example hydrogen and methane, and aid for separation^{[171][172]}. The pore sizes can be tuned along with the surface properties allowing to tether the requirements based on MOFs.

MOFs possess a range of interesting properties. For instance, they can be an insulator or a semiconductor^[173]. They can also be magnetic or find applications in photonics^{[174][175]}. Therefore, to understand the versatility of this material few reports on its properties are briefly discussed below.

- **Electrical properties:** Normally, MOFs are electrical insulators, but there have been recent reports on semiconductor MOFs. The first conclusive result on semiconductor property in MOFs was on $\text{Cu}[\text{Ni}(\text{PDT})_2]$ with p-type majority charge carriers and optical band gap of 2 eV^[176]. Another example is poly(Ni 1,1,2,2-ethenetetrathiolate), a nonporous MOF with n-type semiconductor properties^[170]. There are three charge transport mechanisms reported: bond-conduction, space conduction, and through guest molecules. Discussion about these mechanisms is beyond the scope of this thesis.
- **Conduction of ions:** The nano-porous structure allows the separation and transfer of ions easily. Most reports in MOFs are focused on proton conduction. The proton transfer occurs by “vehicle mechanism” wherein hydrogen bonds play an important role in aqueous media^[177,178]. Few studies have focused on Li^{+1} transfer as a prospective application in Li-ion batteries. MOFs are also advantageous for large-sized and multivalent metal ion transfer because of their permanent porous structure^[179].
- **Light emission and energy harvesting:** The organic-inorganic combinations of MOFs allow tunability of light emission and detection. The guest molecules in pores, organic linkers, and metal nodes can all act as a light-harvesting tool. They have been implemented in photovoltaics. The concept to use in photovoltaics is that the MOFs act as electron donor-acceptor and guest molecules in the pores for hole transfer^[180]. The application to light-emitting devices has been realized as well, where the engineering of different components of MOF can be done based on required applications. For example, a luminescent guest molecule can be infiltrated into the pores according to the wavelength of interest^[181]. Long et al. reported on capturing carbon dioxide for clean energy and the environment^[182] and Chen et al. demonstrated the prospect of storing hydrogen and methane^[183].

3 Experimental Methods

This chapter is divided into two parts. The first part describes the different experimental methods used in the thesis. The second part explains few characterization tools. Making of in-house built piezoresistance setup is explained including the dimensions of building blocks.

3.1 Device fabrication

3.1.1 Synthesis of h-BN and NCG

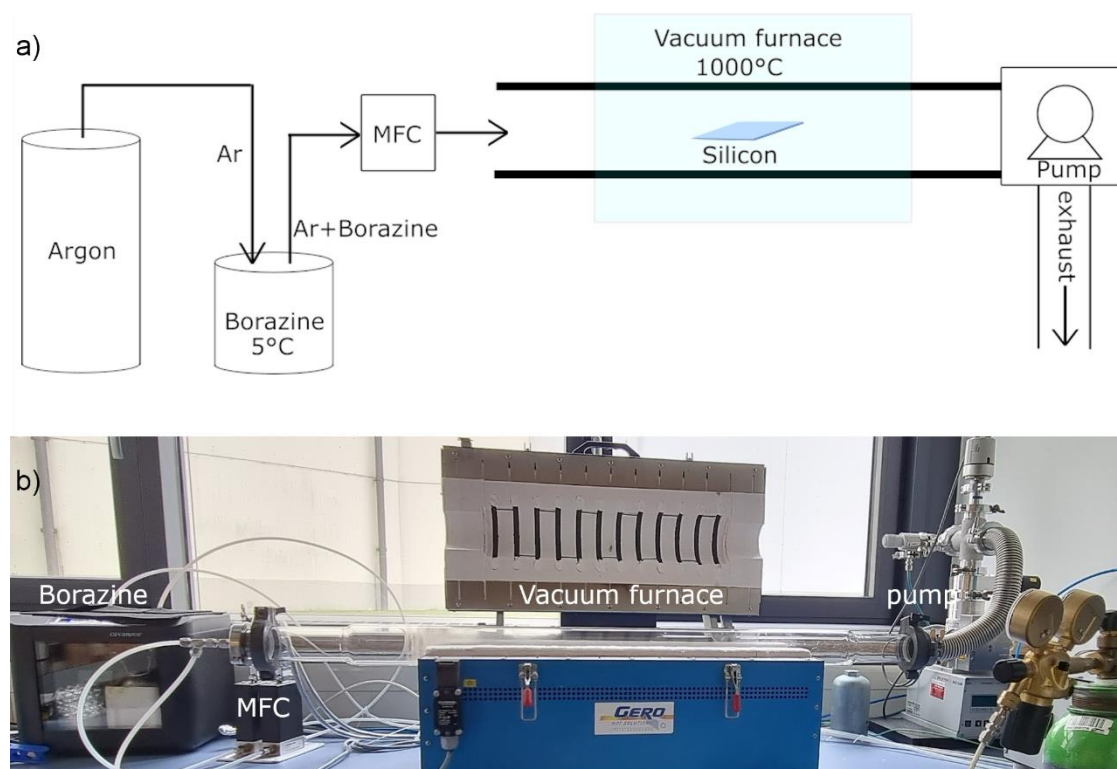


Figure 3.1: a) Schematic of the experimental setup, and b) corresponding image.

The experimental setup requires an inert atmosphere or vacuum for the synthesis of h-BN and NCG thin films. A cylindrical vacuum furnace that can be heated up to 1000°C was used. A stainless-steel bubbler (100 ml) filled with borazine (5 g) (Katchem, Czech

Republic) was connected to an Ar gas bottle (Linde, purity 5N), and to the high-vacuum oven (Gero, heating zone diameter: 7 cm, length: 65 cm) via a mass flow controller (MKS 1179B). The process parameters which can be controlled are pressure, temperature, and flow rate of borazine. Figure 3.1 shows the schematic and actual experimental setup used for h-BN synthesis.

3.1.1.1 Calculations on the mass flow rate of borazine for h-BN synthesis

A mass flow controller (MFC) was used to limit the total mass of a gas flowing through it at a certain temperature and pressure. It is calibrated for standard temperature and pressure (STP) conditions (0°C and 1 atm.). Mass flow is a dynamic quantity and is measured in g/min. At different working conditions than STP, the actual mass flow will be different for the same volumetric flow. Hence calculations for sccm measurements for an MFC must be done for mass flow rate rather than volumetric flow rate.

For 1 sccm flow rate of nitrogen (N₂), volume flow rate \dot{V} is:

$$\dot{V} = 1 \text{ sccm} = 1 \text{ cm}^3 \text{ min}^{-1}$$

$$\text{Density } (\rho) \text{ of N}_2 = 1.251 \text{ g l}^{-1}$$

$$\text{Mass in 1 mole (m) of N}_2 = 28 \text{ g}$$

$$\text{Number of moles (n)} = 1$$

$$\text{Pressure (P)} = 1 \text{ atm}$$

$$\text{Gas constant (R)} = 82.1 \text{ cm}^3 \text{ atm mole}^{-1} \text{ K}^{-1}$$

$$\text{Temperature (T)} = 273.15 \text{ K}$$

$$\text{Mass flow of nitrogen} =$$

$$\dot{m} = \dot{V} \frac{mp}{nRT} \quad (3.1)$$

$$\dot{m} = 1.2 \times 10^{-3} \text{ g min}^{-1}$$

Borazine was carried from the bubbler to the reaction chamber using nitrogen as a carrier gas.

Assuming equilibria conditions, the vapor pressure at 273.25 K can be calculated:

$$\log p(\text{mm}) = 6.39278 - (919.131) / (T-67.198)$$

$$p = 84.4 \text{ mm Hg} = 84.4 / 760 \text{ atm} = 0.11 \text{ atm}$$

Therefore, inside the bubbler nitrogen will be at 1 atm pressure and borazine at 0.11 atm pressure. Considering Dalton's law of partial pressure, for 1 sccm total flow, 0.11 sccm is the flow of borazine.

$$\dot{V} = 0.11 \text{ sccm}$$

$$\text{Mass in 1 mole of borazine} = 80.4 \text{ g}$$

$$\begin{aligned} \text{Hence, using equation 3.1, mass flow rate} &= \dot{m} = 0.11 \times (80.4 \times 1) / (1 \times 82.1 \times 273.15) \\ &= 4 \times 10^{-4} \text{ g min}^{-1} \end{aligned}$$

3.1.2 Patterning with EBL

Electron beam lithography (EBL) is a device fabrication technique to pattern structures in nanometer scale. A beam of the electron is focused on a material that is electron sensitive (resist) which changes the property of the resist which affects its solubility. One of the prominent e-beam resists is PMMA which was discovered by Hatzakis in 1969^[184]. The SEM is modified to be used for EBL. The difference between an SEM and EBL is a pattern generator. In EBL, the pattern generator scans the beam onto the resist coated sample following the instructions fed into the pattern generator.

For the devices fabricated in this work, PMMA 950k A4.5 from Microresist was used. After spin-coating PMMA, a post-annealing step of 3 min at 150°C was done. The patterning step was performed at 30 kV acceleration voltage and 1.8 mm working distance.

3.1.3 Deposition of CNTs with dielectrophoresis

Force exerted on dielectric particles under a non-uniform electric field is known as dielectrophoresis (DEP). This process can be used to deposit aligned SWCNTs onto the electrodes. The imbalanced forces exerted on induced dipoles of CNTs can result in their movement under the applied electric field^[185]. A recent study on DEP principles has been reported by Li et al.^[186] The magnitude of the force experienced by the nanotubes is proportional to the difference between the dielectric constants of nanotubes and the dispersion medium^[187]. The force also depends on the parameters like length and diameter of the tube^[187]. With the high dielectric constant of metallic tubes compared to semiconducting nanotubes, they have a larger affinity to move towards the applied

electric field. Krupke et al. used this technique to separate metallic and semiconducting nanotubes^[188]. Details about the parameters for SWCNT deposition in thesis is included in chapter 4.

3.2 Characterization tools

3.2.1 Electrical measurement

3.2.1.1 Transport measurement

All the transport measurements were conducted using an Agilent 4155C semiconductor parameter analyzer and a probe station with TRIAX probes and a current detection limit of 30 fA. The transport was measured by sweeping silicon back gate (Chapter 4 and 5), and ionic liquid top gate (Chapter 6). The gate windows for measuring CNT-FET transport were kept between -5 V to 5 V and for the ionic liquid top gate NCG-FET between -1 V to 1 V. For GFETs, the transport measurement gate window was kept -10 V to 100 V. Calculations of parameters from transport measurements, for example mobility, is explained in Chapter 2.

3.2.1.2 Sheet resistance measurement

3.2.1.2.1 Two-point probe

Current is applied by two probes and the same probes are used to read the potential drop across the device under test. This measurement can be used to determine the contact resistance between metal and the channel using the scaling law. The y-intercept of the plot of resistance vs channel length gives the value of contact resistance.

3.2.1.2.2 Four-point probe

Separate pairs of probes are used to apply current and sense voltage drops. This method is more accurate than the conventional two-terminal measurements because it eliminates the role of contact resistances.

A simple approach to measuring sheet resistance using four-point is fabricating a structure where the direction of flow of current is fixed. The following figure 3.2 demonstrates it.

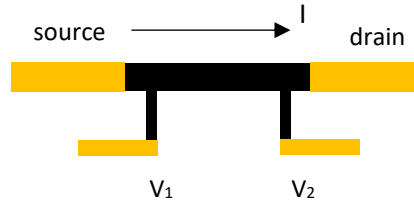


Figure 3.2: Device structure for four-point sheet resistance measurement.

The current flows between the outer two electrodes (main lines) and voltage drops are measured between the inner two electrodes (sense lines). Using $R = \frac{V}{I}$, resistance and the resistivity of the thin film are calculated. Sheet resistance is then given by the formula $R_s = \rho/t$, where t is the thickness of the film.

3.2.1.2.3 Van der Pauw method:

This technique can be used to measure the sheet resistance of thin films independent of their shape. Montgomery method is an extension of the Van der Pauw method for measuring the sheet resistance of anisotropic materials^[185].

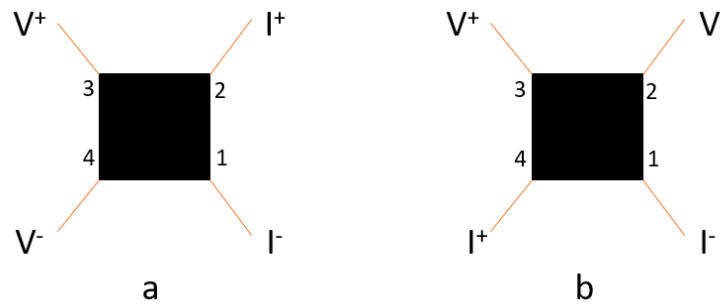


Figure 3.3: Measurement configurations a and b in the Van-der Pauw method.

Sample must have a homogeneous surface; contacts should have a small area of contact. The resistivity of the film is then calculated using the equation

$$\rho = R_s \times t \quad (3.2)$$

As an example, a square structure demonstrating two configuration schemes is shown in figure 3.3. For configuration a, a current is flown through one edge of the device structure (I_{12}) and the voltage drop is measured along the opposite edge (V_{34}). The voltage drop value is utilized to calculate the resistance R_{1234} . Similar measurements are repeated in configuration b to calculate R_{4123} . Sheet resistance is then calculated by the Van-der Pauw equation

$$e^{\frac{\pi R_{1234}}{R_s}} + e^{\frac{\pi R_{4123}}{R_s}} = 1 \quad (3.3)$$

Iterations are needed to solve equation 3.3. Therefore, for ease of calculation, a symmetrical structure, where $R_{horizontal} = R_{vertical} = R$, can be used which reduces the Van der Pauw equation to

$$R_s = \pi R / \ln 2 \quad (3.4)$$

3.2.2 Raman Microscopy

Raman spectroscopy was first observed by the physicist C.V. Raman in 1928^[189]. The technique uses vibrational modes of the materials as its fingerprint. Inelastic scattering of photons is known as Raman scattering. It can be classified into a Stokes (longer wavelength) or an Anti-stokes (shorter wavelength) line. This increase or decrease in the wavelength of the scattered radiation is attributed to the vibrational energy state of the system under test (figure 3.4).

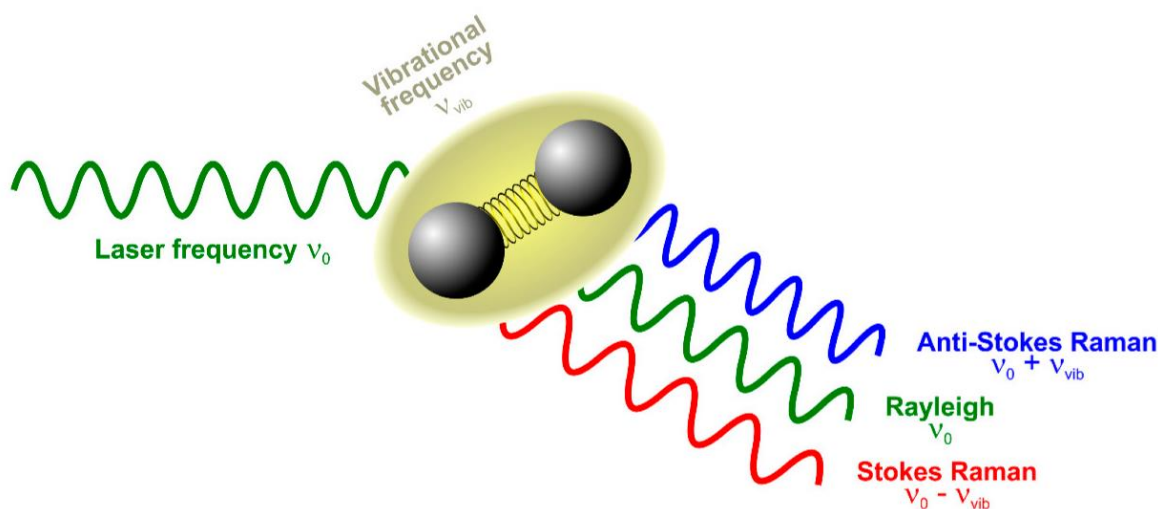


Figure 3.4: An excitation laser beam (ν_0) interacts with a molecule with vibrational frequency ν_{vib} generating a Rayleigh scattered light (ν_0), Stokes Raman scattering ($\nu_0 - \nu_{vib}$), and an Anti-Stokes Raman scattered light ($\nu_0 + \nu_{vib}$) (adapted from ref ^[189]).

The Stokes and Anti-stokes spectra are spaced equally from the Rayleigh (elastic) scattering line because one quantum of energy is gained (Anti-stokes) or lost (Stokes). The intensity of the Anti-stokes scattering is weaker than Stokes because only the molecules in the excited vibrational energy states can give rise to Anti-stokes. Rayleigh scattering has the highest intensity.

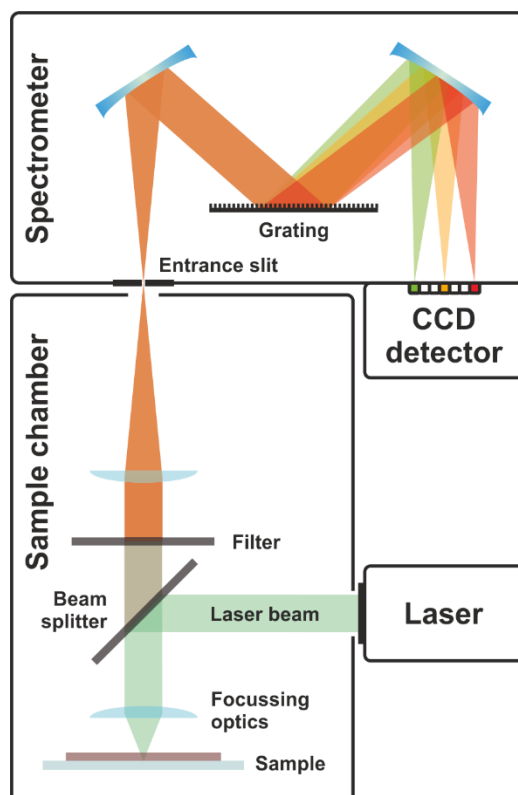


Figure 3.5: Schematic of a Raman microscope (adapted from ref ^[189]).

In figure 3.5, a schematic of a basic setup of Raman spectroscopy is shown. The laser light is passed through a beam splitter and focused onto the sample using the microscope objective which is also used to collect the scattered light from the sample. The filter allows only Raman scattered photons to reach the spectrometer and removes Rayleigh scattered photons. The spectrometer consists of a grating and CCD detector. The Raman scattered light falls on the grating which disperses each wavelength of light to a different angle. The dispersed light is then detected by a CCD detector. Higher grooves per mm are required for a higher resolution of detection. Gratings are “blazed” for a certain wavelength such that the efficiency of diffraction can reach up to 80%.

Raman spectroscopy gives results in intensity vs Raman shift. Raman shifts are usually reported in wavenumbers in the units of cm^{-1} .

$$\Delta\nu = \frac{1}{\lambda_0} - \frac{1}{\lambda_1} \quad (3.5)$$

Here λ_0 is the excitation wavelength and λ_1 is the Raman scattered light wavelength. Raman spectroscopy conducted in the thesis was measured by Renishaw inVia Raman

microscope. The measurements conditions are included within the experimental chapters.

3.2.3 Piezoresistance setup

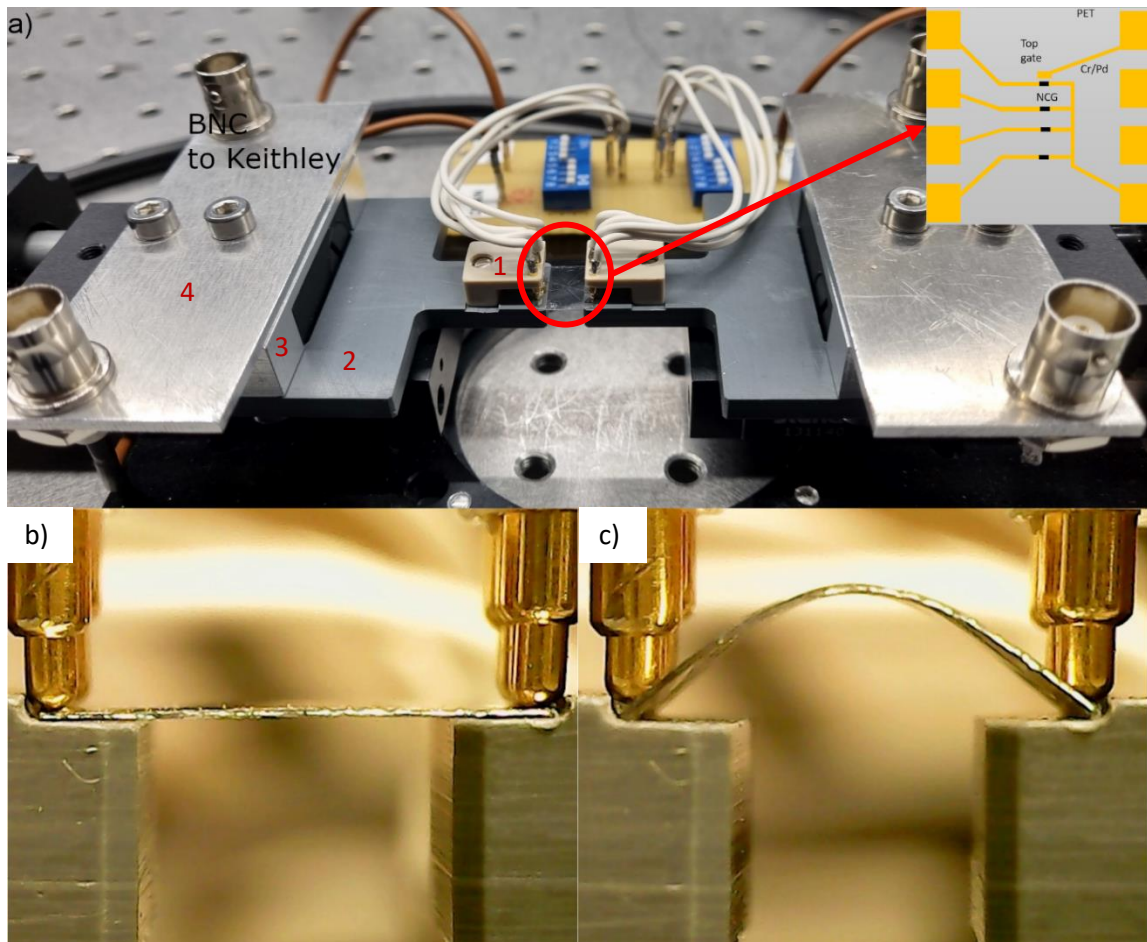


Figure 3.6: a) Piezoresistance setup with sample loaded (red circle) and the inset shows device structure b) Side view of the substrate and the spring contacts at zero stress and c) at a finite stress value.

Table 3.1: Few Parameters of Standa 8MT173-20 translation stage.

Travel range	20 mm
Lead Screw pitch	0.25 mm
Resolution in full step	1.25 μm
Maximum speed	5 mm/s

This setup was built in-house using two commercially bought stepper motors and a source measure unit (SMU). The motorized translation stage 8MT173-20 was acquired

from Standa Inc for the x-axis movement control. A Keithley 2636A was used as the SMU. Some of the important configurations of the stand stepper motor are given in table 3.1.

The setup is shown in figure 3.6. A flexible substrate with structure is shown in the inset and marked in the red circle (figure 3.6a). The strain was imparted in steps by moving the stepper motor. Each step of the motor provides an x-movement of 1.25 μm . The x-movement was then converted to a strain value (shown in the calculation in chapter 6). The parts built by the mechanical workshop are marked as 1, 2, 3, and 4. Diagrams of them are shown below. All dimensions marked are in mm.

Part number 1: Contact holder

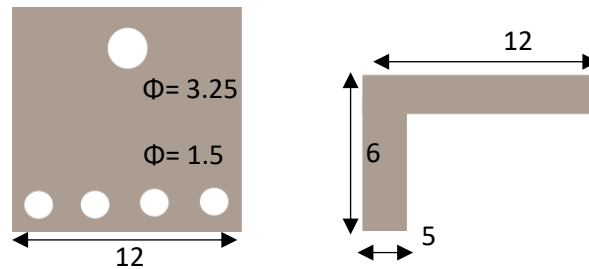


Figure 3.7: Schematic of the top (left) and side (right) view of the contact holder with dimensions in mm.

Part number 1 is the contact holder made from polyether ether ketone (PEEK). It has four holes in the front with a diameter equivalent to gold-coated spring contacts. Four spring contacts were inserted into these holes, where the frictional force inhibited the movement of spring contacts. The front end of the gold contacts touches the metal electrodes on the structure as shown in figure 3.6a. As the strain is applied on the substrate, the spring moves back keeping the contacts intact as shown in figures 3.6b and 3.6c.

Part number 2: Substrate holder

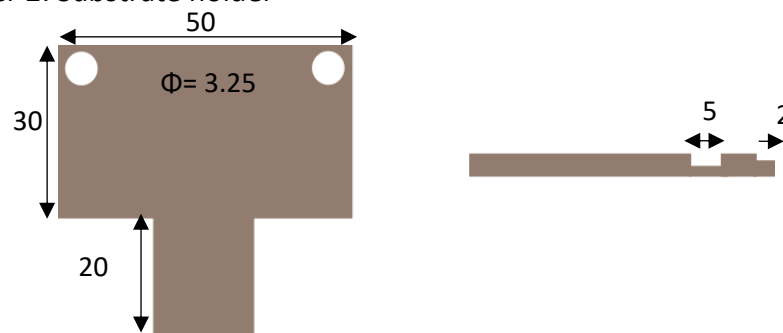


Figure 3.8: Schematic of the top (left) and side (right) view of the substrate holder with dimensions in mm.

The substrate holder has an undercut of 2mm at the front to place the sample. The 5mm undercut fixes the contact holder and inhibit its movement. The holder was made of polyvinyl chloride (PVC) to keep the structure lightweight and the undercut low in roughness. Low roughness keeps the stress on the edge of the substrate uniformly distributed and prevents premature fracture of the glass substrate.

Part number 3: Motor connector

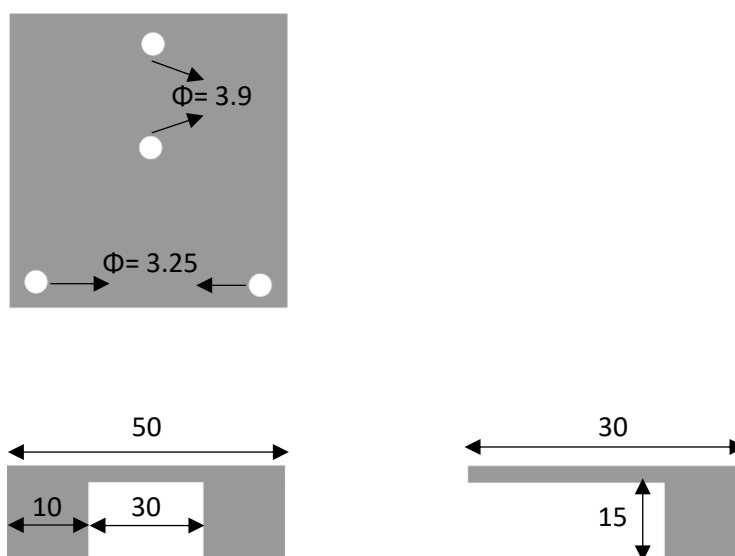


Figure 3.9: Schematic of the top (top left), front (bottom left), and the side (bottom right) view of the motor connector with dimensions in mm.

This part attaches the substrate holder to the stepper motor. The substrate holder was kept as low as possible by using the motor connector. This allows a microscope objective (FTIR and Raman) to fit at the top of the substrate. The setup with Raman measurement is shown in chapter 6. The material used for its fabrication was aluminum.

Part number 4: BNC connector holder:

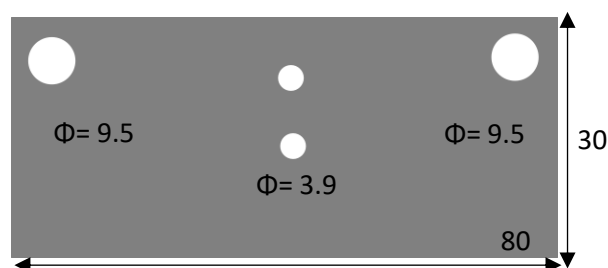


Figure 3.10: Schematic of the top view of BNC connector holder.

This part holds the BNC connectors on its top as shown in figure 3.6a. Metal electrodes on the substrate are connected to switchboards via copper wires for source, drain, and gate. The switchboards are soldered to BNC connectors placed on the holder. Connections to Keithley 2636A was made using these BNC connectors. Steel was used for the fabrication of this part.

The python code to control the Piezoresistance setup and Keithley is included in <https://github.com/krupke-group>.

3.2.4 Gas sensing setup

The setup was originally built by Marc Ganzhorn^[3]. A modified version was used for the gas sensing experiments. The explanation and images are adapted from his diploma thesis work.

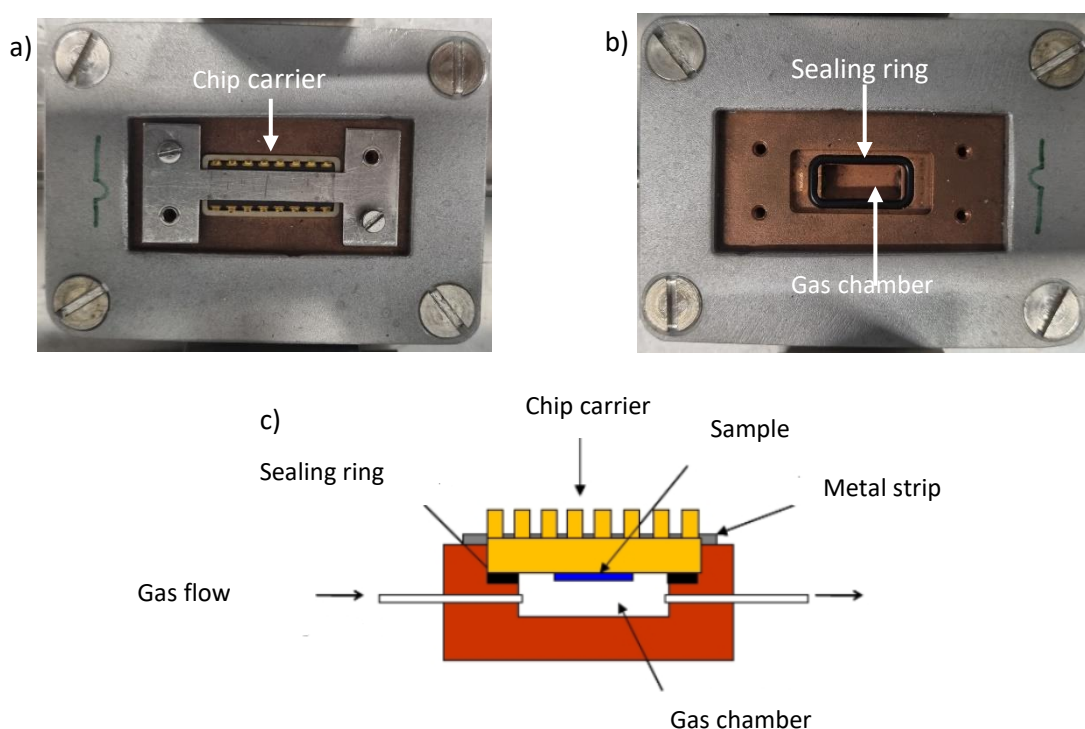


Figure 3.11 a) Sample holder bond wired into the chip carrier and loaded in the gas chamber upside down b) Gas chamber and the sealing ring c) schematic of the gas chamber with the device.

In figure 3.11a, a sample loaded into the gas chamber is shown. The sample is bond wired onto a chip carrier and loaded upside down in the gas chamber. The sealing ring prevents any leakage of gas from the gas chamber (figure 3.11b). The schematic in figure 3.11c shows the gas flow direction with the sample loaded into the gas chamber.

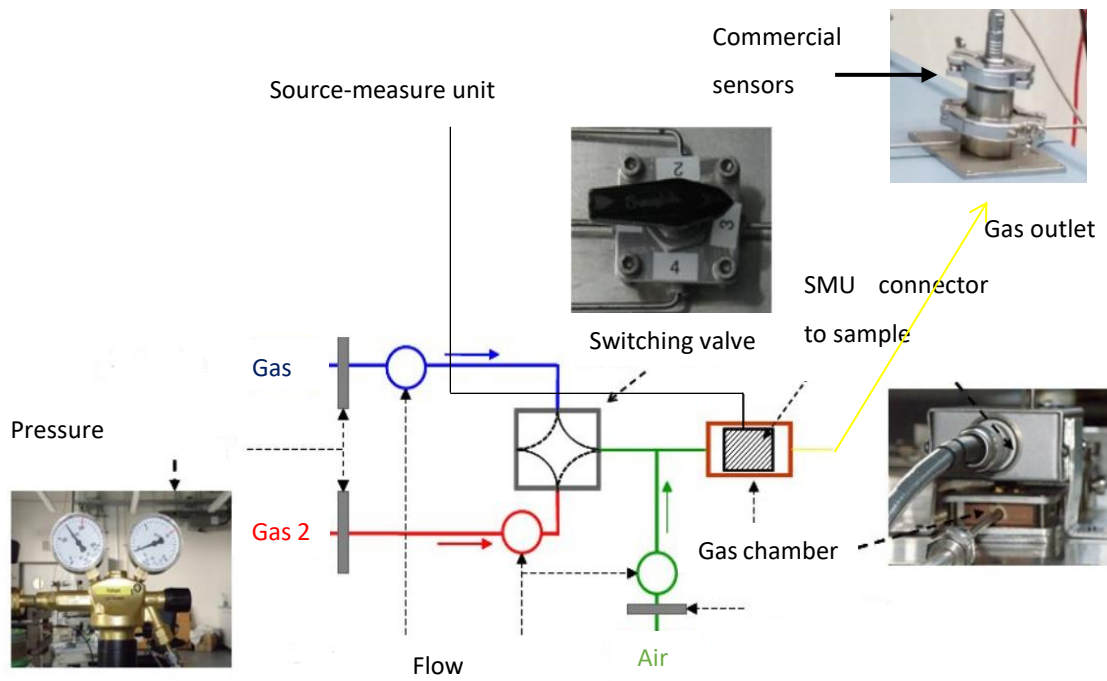


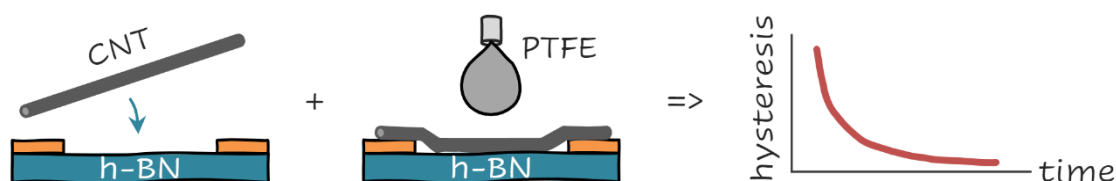
Figure 3.12: Schematic of the connection diagram of the gas sensing setup.

Figure 3.12 shows a schematic of the gas sensing setup. Gas 1 and Gas 2 flow through flowmeters which control the amount of gas flowing through the gas line. The pressure of the gas flow is controlled by a pressure controller. The electrical readout as sensing response is taken from the chip carrier on which the sample is wire bonded. The chip carrier is connected to a SMU. The gas outlet passes through another chamber which contains alcohol (MQ3) and moisture (BME280) sensors to read out as reference readings.

4 Vanishing Hysteresis in CNT Transistors

This chapter includes content from a research article that has been published^[190].

The chapter has been divided into two parts. The first part introduces the synthesis of h-BN on a dielectric substrate. The role of pressure and metal catalyst in the synthesis process was studied. The second part demonstrates a novel approach to incorporate the grown h-BN film into CNT transistors to achieve hysteresis-free operation. It is described how the bottom h-BN reduces hysteresis (charge traps) and that a top coating of the hydrophobic polymer PTFE film (or Teflon in this case) was needed to encapsulate CNTs as well as metal-CNT contacts to eliminate hysteresis. The schematic below captures the complete vision of the chapter.



4.1 Synthesis and characterization of Boron Nitride

The synthesis of large-area h-BN has been demonstrated in previous works by decomposition of ammonia borane or borazine on metal foils^{[11][150][156][191][192]}, dielectric surface^{[193][194]}, and by chemical conversion of graphene to h-BN^[195]. In this work, to avoid any transfer process, h-BN was grown by allowing borazine to polymerize on SiO₂ substrate. Borazine was chosen because of its 1:1 stoichiometric ratio and high vapor pressure at 5°C, and high chemical reactivity^{[11][156][196]}. The process schematic is shown in figure 4.5a. The bubbler was cooled to 5°C to inhibit the premature decomposition of borazine. Boron doped silicon wafers (resistance < 0.005 Ω cm, Active Business Company) with 300 nm thermal oxide were cut into 10 x 10 mm² pieces, loaded into the center of a quartz tube (Aachener Glass, 2inch diameter, 50cm long), evacuated to 10⁻⁷ mbar and ramped up to 1000°C at a rate of 10°C min⁻¹. Argon (2 sccm) was flown through the borazine-filled bubbler into a heated quartz tube for 10-60 min, depending on targeted h-BN thickness. It has been assumed that Ar uptakes borazine at equilibrium partial pressure of 144 mbar (5°C) when streaming through the bubbler at 1 bar pressure. The calculation has been shown later in the chapter. The amount of borazine

was calculated to approximately 1 mg min^{-1} at 2 sccm Ar flow, as shown in calculations later in the chapter. During growth, a pressure of 5 mbar was maintained. After terminating the gas flow, the sample was kept in a vacuum at 1000°C for 1 hr to improve crystallinity and to promote further dehydrogenation. Finally, the furnace was cooled to room temperature at a rate of $< 7^\circ\text{C min}^{-1}$.

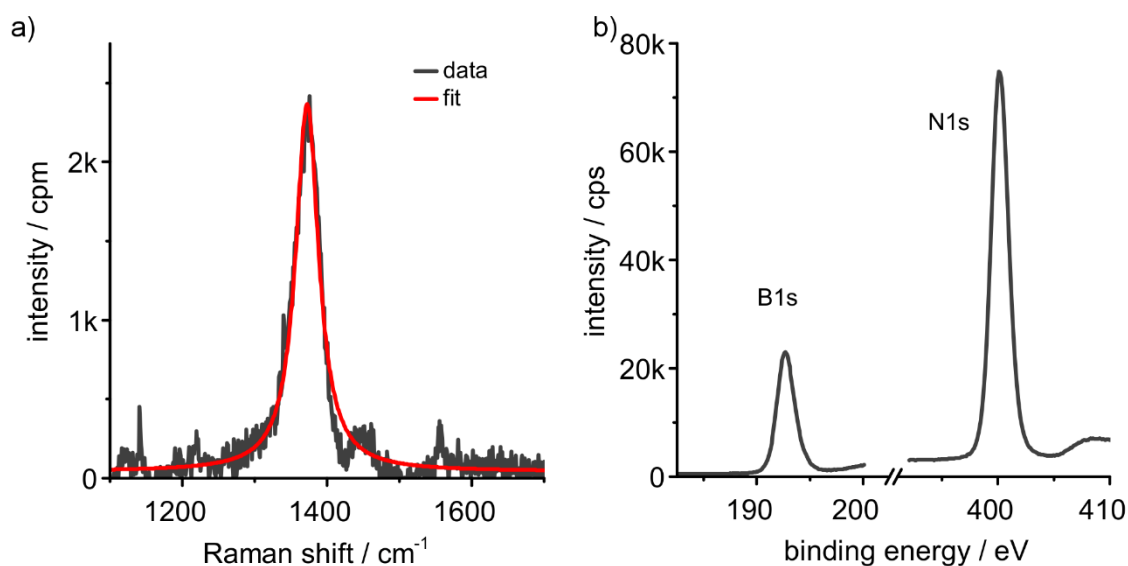


Figure 4.1: a) Raman data of high pressure grown h-BN on SiO_2/Si , background subtracted and fitted to a Lorentzian (peak 1372.5 cm^{-1} , linewidth 38.7 cm^{-1}). b) XPS of the h-BN film with the peak binding energies for B1s and N1s at 192 eV and 399.5 eV, respectively^[190].

To avoid premature polymerization of borazine to polyborazylene^[197], it was ensured to keep the gas temperature in gas pipes below 70°C . Borazine undergoes polymerization to form polyborazylene around 70°C . Between temperatures $125\text{--}300^\circ\text{C}$ cross-linking of B-H and N-H occurs resulting in loss of hydrogen. The second stage of dehydrogenation occurs between 700°C - 1000°C to ultimately form boron nitride^{[197][198]}.

Raman spectroscopy was used to confirm the presence of h-BN film (Renishaw inVia Raman spectroscopy) shown in figure 4.1a. 532nm excitation wavelength at 100x magnification with 3mW laser power was used as parameters with an integration time of 60 s for all Raman measurements on h-BN thin films. X-ray photoelectron spectroscopy (XPS) measurements were done using a Thermo Fisher's K-alpha machine. The samples were excited with a monochromatized Al K-alpha source (1486.6 eV) with an X-ray spot size of $400 \mu\text{m}$. The ejected photoelectrons were collected using a hemispherical 180° double focus analyzer with a 128-channel detector. Measurements were done without

the use of a charge compensation mechanism (figure 4.1b). Figures 4.2a and 4.2b show optical and atomic force micrographs of the grown film respectively. Figure 4.3 shows corresponding scanning electron micrographs.

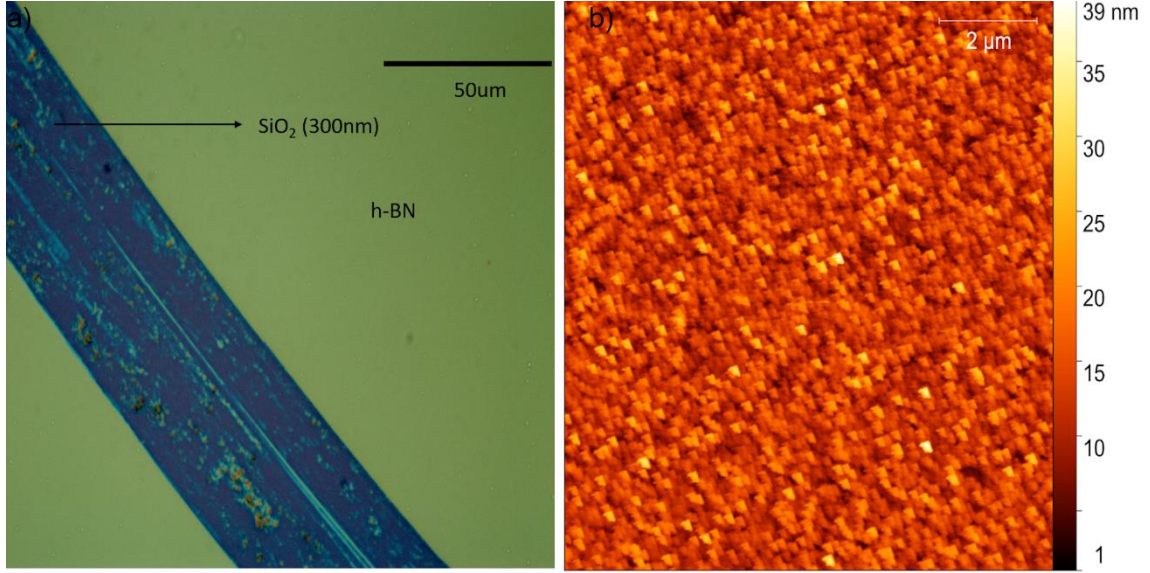
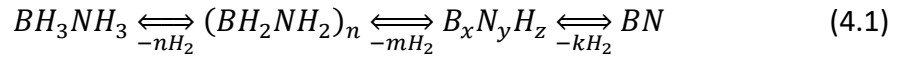


Figure 4.2: a) Optical image (100x) showing a scratch on h-BN film. b) Atomic force micrograph of the grown h-BN film.^[190]



Koepke et al.^[199] have discussed the role of pressure in growing h-BN. They concluded that beyond 2 Torr (1.33 mbar) pressure the growth of h-BN on Cu is increasingly amorphous and the growth rate is uncontrolled. Behura et al. have used the same pressure range (5-10 Torr) to grow h-BN on dielectric substrates^[200]. The growth temperature must be above 1170°C for a crystalline growth and can be lowered down to 1000°C in presence of transition metal catalysts^[201]. Borazine undergoes dehydrogenation process twice to form the final product as h-BN. The electron pair is delocalized on nitrogen and it can act as a Lewis base in presence of a Lewis acid. The first stage of dehydrogenation (polymerization) is the rate-determining step (RDS) in the complete process of h-BN formation^[202] (equation 4.1). Transition metals are a good Lewis acid as they have vacant d-orbitals to accept electron pairs and form complexes which therefore reduces the activation energy for polymerization. The reaction in the absence of a metal catalyst needs higher activation energy and proceeds slowly. Hence, at low pressure (10⁻⁶ mbar), no growth was detected on SiO₂/Si substrates (shown as the yellow line in figure 4.4). It can be inferred that the residence time of the precursor

is small enough to not allow the reaction to pass the RDS, and therefore no Raman signature of growth is measured. Increasing pressure (5-10 mbar), and repeating the experiment gives a clear Raman signature of h-BN film at $\sim 1370 \text{ cm}^{-1}$ (shown as the black line in figure 4.4). The increasing background is due to photoluminescence for h-BN on 300nm SiO_2 .

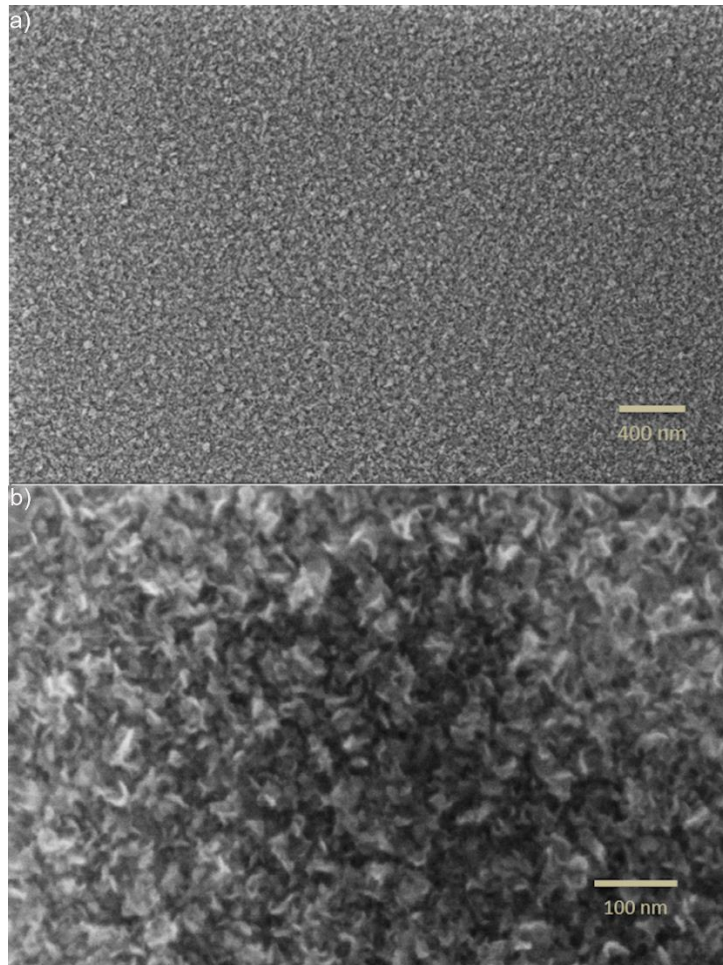


Figure 4.3: Scanning electron micrographs of h-BN film at different magnifications. The grown h-BN film is grainier in texture^[190].

As already known from the literature, at 1000°C , a larger crystal size is only possible in the presence of the catalyst^[156]. This is also confirmed by the line width of Raman E_{2g} which is broader (figure 4.1a, linewidth 38.7 cm^{-1}) compared to Raman peaks of monocrystalline h-BN (15.5 cm^{-1} for bulk)^[150]. In this work, no catalyst was used and therefore can be concluded that in absence of catalyst nanometer domain size film is synthesized. At higher pressures, the growth rate becomes uncontrolled, and the film is

increasingly amorphous, disordered, and sp^3 -hybridised^[199] which leads to the roughness of the film confirmed by AFM (figure 4.2b) and SEM images (figure 4.3).

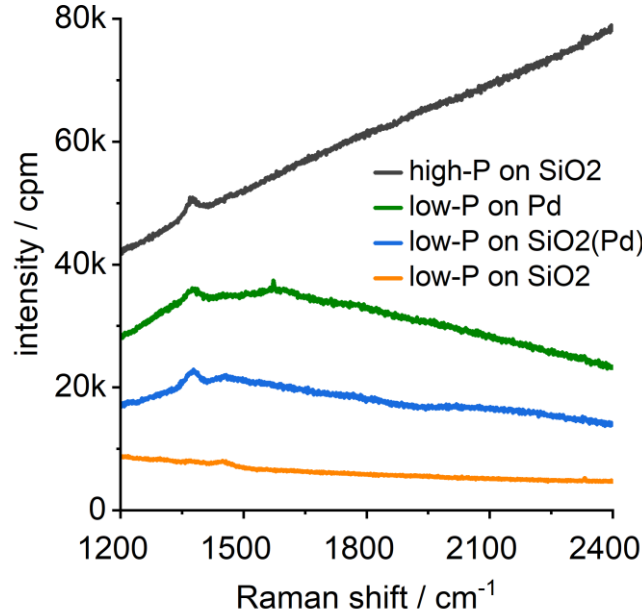


Figure 4.4: Raman spectra recorded after CVD. The E_{2g} Raman peak of h-BN at $\sim 1370 \text{ cm}^{-1}$ is visible on bare SiO_2/Si substrates when synthesized at high pressure (5-10 mbar, black line). Synthesis at low pressure (10^{-6} mbar) yields h-BN only in the presence of Pd electrodes: on top of Pd (green line) and nearby Pd (blue line), not on bare substrates (yellow)^[190].

After establishing that the h-BN film on dielectrics can be formed at high pressures (5-10 mbar), the role of the metal as a catalyst for growth on dielectric at lower pressure was studied. Therefore, the Si/SiO_2 substrate with square patches of palladium metal was fabricated. With similar conditions of fabrication, but at low pressure (10^{-6} mbar), the experiment was repeated. In this case, a Raman signal was observed on the complete dielectric surface and the metal surface (shown as blue and green curves in figure 4.4). Here, the RDS was faster because of the presence of palladium metal catalyst leading to the successful synthesis of h-BN at low pressure.

4.2 Device fabrication

The parts included in device fabrication, and results and discussion sections have been published in a research article^[190].

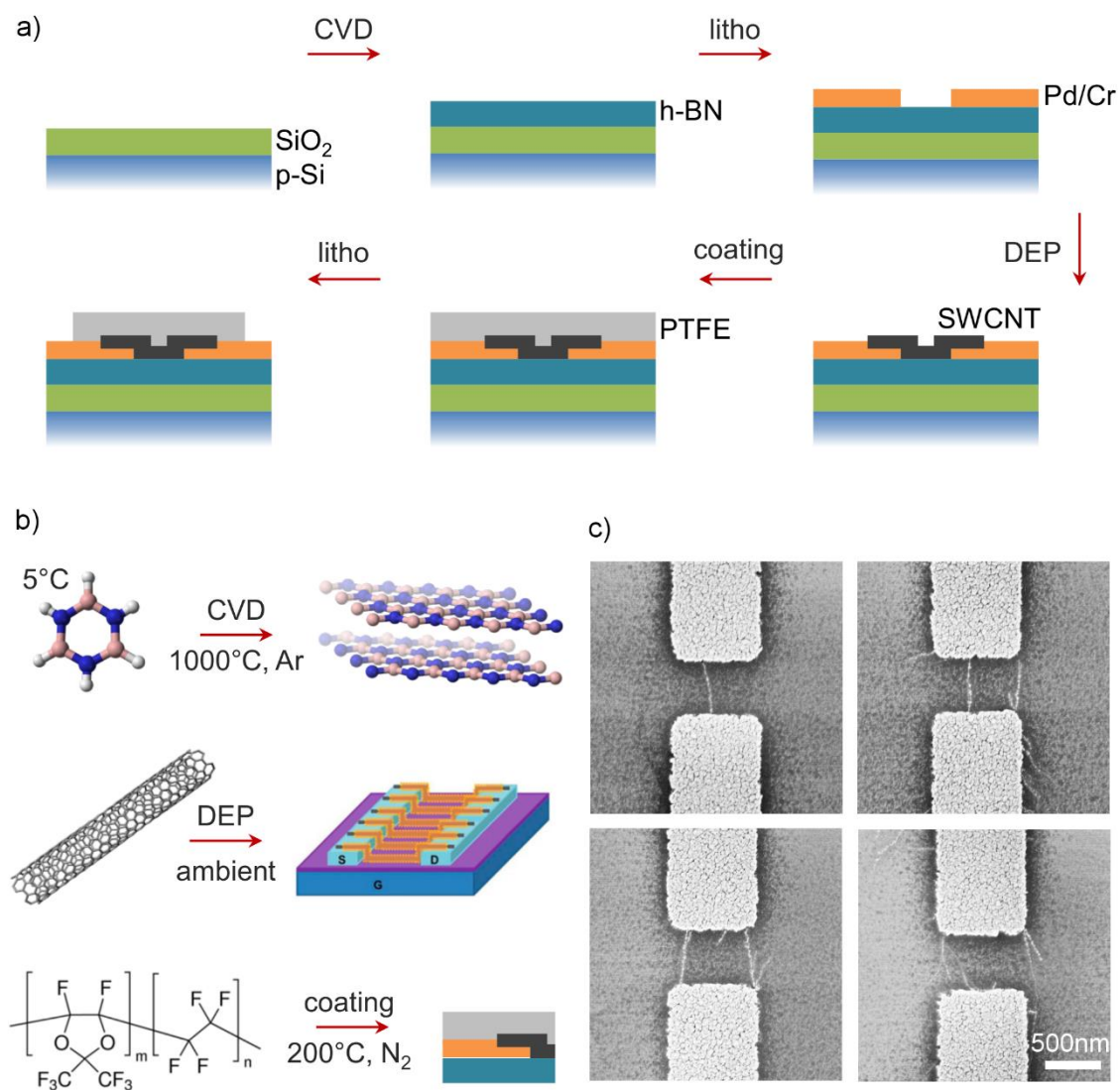


Figure 4.5: a) Process flow comprising CVD synthesis of h-BN, deposition of SWCNTs by dielectrophoresis (DEP), spin coating of Teflon AF2400 (PTFE), and lithographic patterning of metal contacts and Teflon layer. b) Schematic on the deposition processes and conditions. c) Scanning electron micrographs of devices after deposition of (9,8)-SWCNTs and before Teflon coating. The SiO₂/Si substrate was overgrown with 80 nm h-BN.^[190]

The graphene community has realized that packaging graphene into flakes of h-BN eliminates doping and hysteresis, and boosts mobility, provided the h-BN layer is tens of nanometers thick^[10]. The Bockrath group has similarly encapsulated SWCNT devices in h-BN flakes and reported superior current carrying capability^[165]. However, the integrated nanotubes were metallic, and transistor behavior was not observed. Similarly, not for SWCNTs grown on h-BN flakes^[164]. Here in this work, the target was to achieve a wafer-scalable fabrication of hysteresis-free SWCNTs transistors via encapsulation into the h-BN bottom layer and a PTFE top layer.

80nm h-BN was first overgrown on 300nm SiO₂/Si substrates. 45 nm thick Pd/Cr source-drain electrodes with 600 nm gap size were fabricated on h-BN coated substrates by standard electron-beam lithography and metallization. (9,8) semiconducting SWCNTs were produced by selective catalyst CVD^{[203][204]} dispersed in toluene by wrapping in poly(9,9-di-n-dodecylfluorenyl- 2,7-diyl) (PFD) and purified and length sorted by gel filtration^[205]. The SWCNTs were deposited simultaneously onto 6-7 devices per chip by electric field-assisted deposition (DEP). For details regarding synthesis, purification, optical characterization, and deposition of (9,8) SWCNTs please refer to Gaulke et al^[5]. Devices were then annealed at 400°C and 10⁻⁷ mbar vacuum for 4 h. Electrical characterization was conducted first without PTFE top layer under ambient conditions, with an Agilent 4155C semiconductor parameter analyzer and a probe station with TRIAX probes with a current detection limit of 30 fA. Transfer characteristics were measured with back gate voltage sweeps from -5 to +5 V (step size 100 mV, scan rate 0.5 V s⁻¹) using source-drain voltages of 0.5 V. For coating PTFE, the devices were loaded into a nitrogen glove box with a spin-coater and hotplate and annealed at 150°C for 1 h. A solution of poly[4,5-difluoro-2,2-bis(trifluoromethyl)-1,3-dioxole-co-tetrafluoroethylene] (1 g) (Teflon AF-2400, Sigma-Aldrich) dissolved in Fluorinert FC-40 (100 ml) (Sigma-Aldrich) was prepared by stirring the solution for 2 weeks at 60°C. Residual nanometer-sized PTFE particles were removed by ultracentrifugation for 1 h at 40000 rpm. The devices were loaded to the spin-coater and the purified 1 % PTFE solution (10 µl) was drop-casted onto the sample surface. For 30 and 45 nm thick PTFE layers, samples were rotated for 60 s at 3000 and 1000 rpm, respectively. A thickness of 80 nm was obtained by spin-casting two times, at 3000 and 1000 rpm for 60 s each. The samples were then heated, still in nitrogen atmosphere, at 100°C for 5 min, 150°C for 5min, and 200°C for 10h. Finally, the samples were cooled down to room temperature and unloaded from the glovebox. PTFE was removed from the metal contact pads by direct electron beam patterning using an exposure dose of 10 mC cm⁻² at 10 keV beam energy^[206]. Subsequent electrical characterizations were done under conditions outlined before. At the end of the fabrication process the SWCNT devices were

encapsulated between the h-BN bottom and PTFE top layer (Figure 4.5a). SWCNTs within completed devices cannot be imaged due to the PTFE coating, therefore shown in figure 4.5c are scanning electron micrographs of 4 representative SWCNT devices without PTFE coating. The images were recorded after nanotube dielectrophoresis. Typically, 1-5 SWCNTs are contacted and visible in the gap region. The underlying h-BN layer was characterized by Raman spectroscopy after CVD synthesis. Figures 4.6a-b show an overview of the fabricated device structure at 50x and 100x optical magnifications respectively.

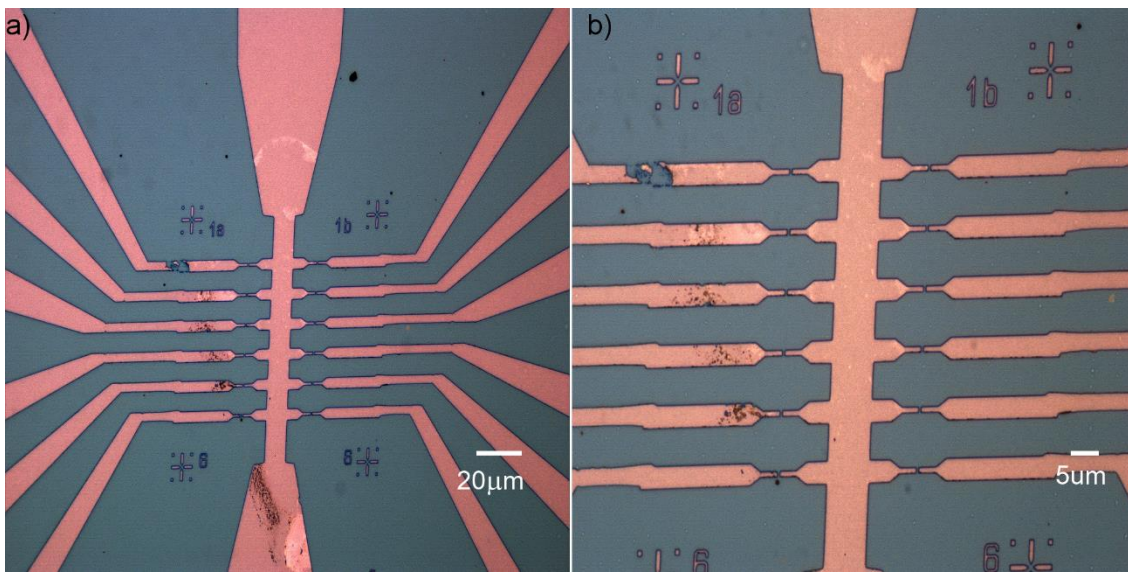


Figure 4.6: Optical microscopy images of fabricated device structure showing metal pads at (a) 50x and (b) 100x magnifications. The channel length is 600nm. Device 1 metal damaged while measurements.

4.3 Results and discussions

The complete stack of PTFE/h-BN/SiO₂/Si was characterized by reflectance spectroscopy to analyze the thicknesses of individual layers via the transfer matrix method, as shown in figure 4.7. Refractive indices of PTFE AF-2400^[207] and h-BN^[208], and respective nominal thicknesses of the layers were used as starting values in the fitting procedure. The h-BN layers are homogenous over large areas, as shown in the optical image in figure 4.2a. However, the layers are not single crystalline but have a grainy structure, which gives rise to a broader linewidth of the Raman E_{2g} peak (38.7 cm⁻¹) as compared to monocrystalline h-BN (15.5 cm⁻¹ for bulk) and is visible in the scanning electron micrographs (figure 4.3) and atomic force micrographs (figure 4.2b). The gate-voltage hysteresis observed in the transconductance curves of h-BN/SiO₂/Si supported devices

before and after Teflon coating is now discussed. (9,8) SWCNTs were embedded in three combinations of layer thicknesses: 30nm Teflon / 40nm h-BN, 45nm Teflon / 40 nm h-BN, and 80 nm Teflon / 80nm h-BN.

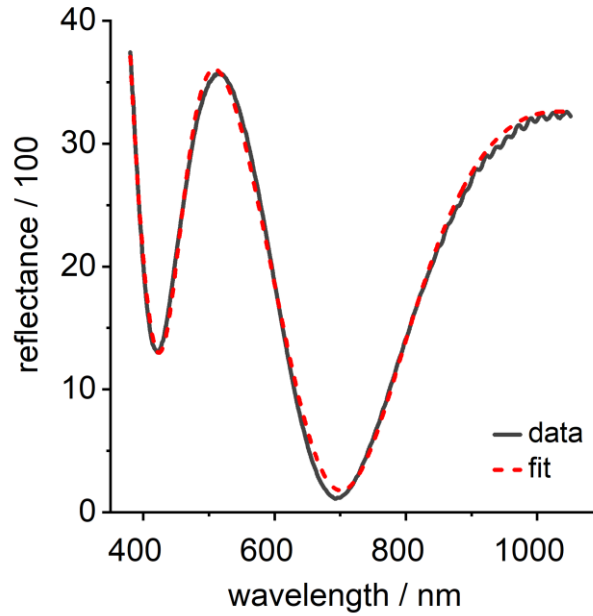


Figure 4.7: Reflectance spectra of a complete stack of 30nm Teflon / 40nm h-BN / 300nm SiO₂ / Si determined by fitting with the transfer matrix method^[190].

Figure 4.8a summarizes the temporal evolution of hysteresis in a total of 21 devices. The largest hysteresis values among all layer combinations were observed prior to Teflon (on h-BN) deposition at $t = -2$ days ranging between 2-4.5 V. This is significantly smaller than 4.5-6 V range for SWCNT devices fabricated on bare Si/SiO₂ (figure 4.11) and shows that h-BN without Teflon coating yields devices with a reduced hysteresis. This conclusion is supported by a quantitative comparison of the number of charge traps at the end of the chapter. An additional reduction of hysteresis to 1-3 V was then observed after Teflon AF coating at $t = 0$, as was expected due to the water-repelling nature of Teflon. However, an unexpected further significant reduction was observed over a timescale of days to weeks, in particular for 45 nm and 80 nm thick Teflon layers. Depending on the waiting time and layer combination, hysteresis becomes eventually smaller than 1 V. A direct comparison of the transconductance curves for representative devices of three layers combinations is given in Figure 4.8b-d. The results resemble a similarity to Ha et al.^[8] work, where a vanishing hysteresis was obtained after Teflon AF coating of SWCNTs on an amino-acid functionalized substrate. Teflon layers required a thickness larger than 10 nm to be effective, however, the reduction in hysteresis was instantaneous and did

not show a time dependence, likewise for a complete encapsulation in Teflon AF as shown by Lefebvre et al^[73].

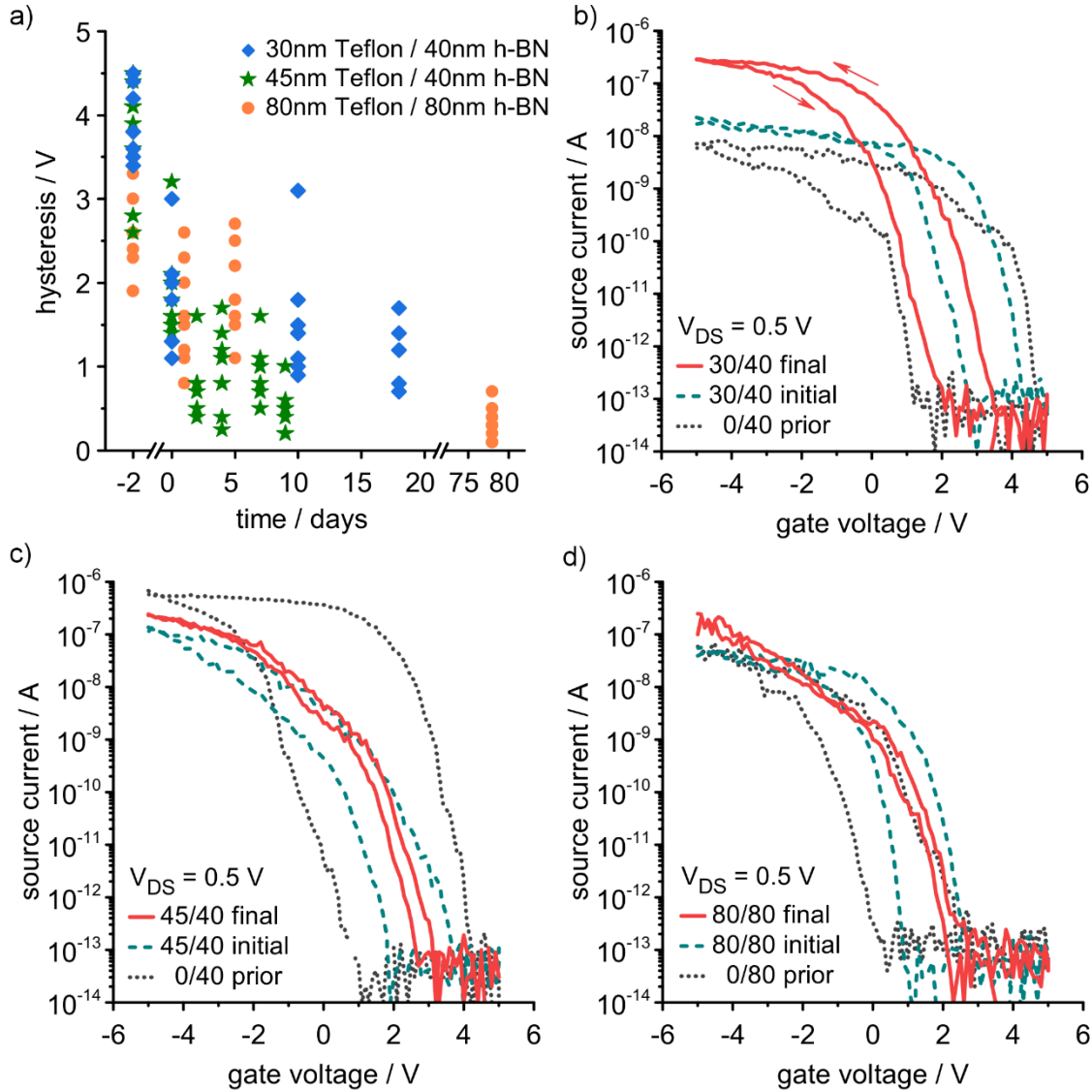


Figure 4.8: a) Temporal evolution of hysteresis in transconductance curves for 21 devices. The SWCNT devices were encapsulated in three combinations of Teflon and h-BN layer thicknesses, as indicated. Also shown are results taken 2 days before the Teflon deposition at $t=0$. (b-c) Corresponding transconductance curves of representative devices, taken before Teflon deposition (prior), directly after Teflon deposition (initial), and after a week of storage under ambient conditions (final). Current detection limit is 30 fA^[190].

Here in this work, a minimum Teflon thickness of 45 nm is required to coat not only the SWCNTs segment lying flat on the h-BN surface but also the nanotube segment on the top of metal electrodes. Concerning the origin of the temporal evolution of hysteresis,

it is the long-timescale that points to a diffusion process – likely of water molecules. Interestingly, transconductance traces show that the threshold voltage is stable during the hysteresis reduction; however, the on-state hole current systematically increases with time after Teflon coating. This shows that the Schottky barrier reduction for holes is correlated with the reduction of hysteresis, possibly via surface dipoles trapped in the contact area between Pd electrodes and SWCNTs. Indeed, an obvious difference to previous works is that in this work SWCNTs were deposited on top of the Pd electrodes and hence the contact interface was inevitably exposed to humidity. Since water molecules are known to adsorb on Pd surfaces^[70] and desorption of water from Pd surfaces is slow below 450°C^[209], it can be speculated that slow repelling of water molecules from the contact area is causing the time dependence.

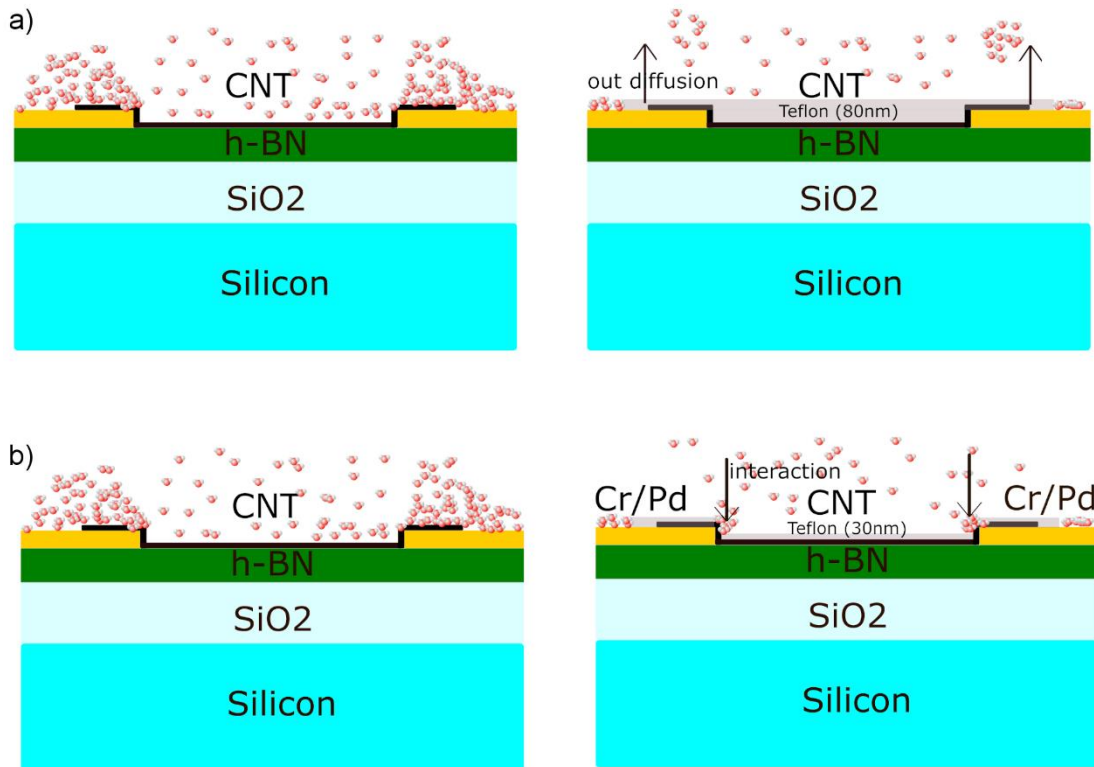


Figure 4.9: a), b) Left image shows the initial condition of the fabricated device in terms of water adsorption. The water molecules are heavily adsorbed onto the metal and CNT contacts as well onto the CNTs. a) Right image shows an encapsulated CNTs by 80 nm Teflon and bottom h-BN. As the thickness of Teflon (80 nm) is larger than electrodes (45 nm), interaction is completely cut-off and the trapped water molecules diffuse out through Teflon. b) Right image shows a thickness of Teflon (30 nm) less than the electrodes, which leaves some area on the contacts for water interaction to the contacts and in turn contributes to hysteresis.

To gain further understanding, the mechanism schematic is shown in figure 4.9. Initially, without the Teflon coating, water molecules are adsorbed on nanotubes as well as on the metal electrodes (left figures in figure 4.9a and b), but not on the h-BN surface because of the absence of dangling bonds and charge traps. After a Teflon coating of 80 nm, the interaction of water with the nanotubes is completely cut off, however, adsorbed water onto the metal electrode, and nanotubes get trapped. This contributes towards hysteresis shown in transconductance curves at $t = 0$ (in figure 4.8b-d). Teflon is a good permeable membrane that allows water trapped to diffuse out, and due to its extremely good hydrophobicity doesn't allow re-adsorption of water molecules on CNTs and metal-CNT contacts, known as the lotus effect in Teflon^[210]. The out-diffusion of water is a slow process and a waiting time is required to achieve a hysteresis-free device (shown in figure 4.8a). Thicknesses (30 nm) less than metal electrodes (45 nm) are not beneficial to achieve this kind of environment, because it does not completely cover the metal-CNT contacts (figure 4.9b). The hysteresis value for 30 nm Teflon coating (figure 4.8b) of course shows a smaller value compared to values without Teflon coating. But, values of the order of 0.1 V were not achieved. The temporal evolution (blue diamonds in figure 4.8a) of 30 nm shows a similar trend of decreasing hysteresis with time.

The direction of the hysteresis loop in figure 4.8b-d is counter-clockwise and further evidence that the source of hysteresis at low gate sweeping ranges is due to water molecules and associated charges, which redistribute in response to gate voltage^[211]. At larger gate voltage sweeps hysteresis may also depend on charge traps in the dielectric, however, in light of the observed reduction of hysteresis with time it implies, that hysteresis in the devices must be caused by water-related charge traps that are mobile at room temperature and traps in h-BN are absent.

The low hysteresis of 0.1 V, observed for devices embedded in 40 nm h-BN / 45 nm Teflon and 80 nm h-BN / 80 nm Teflon on SiO₂ substrates is comparable to devices with CNTs deposited on SAM passivated oxides^{[71][74]}, devices with CNTs overgrown by a top gate oxide^[75], and devices passivation with fluoropolymers^{[81][212][8]}. Table 4.1 compares the hysteresis values of this work to the available literature.

Table 4.1: Comparison of the hysteresis values and the conditions used for achieving lower hysteresis values. The blue-colored row gives the values in this work^[190].

Gate sweep window (E)	Hysteresis (V)	Dielectric thickness	Effective Dielectric constant	CNT Condition
-3 to 3 V (3.14 MV/m)	2.2	SiO ₂ - 500nm Air- 200nm	SiO ₂ +air = 2.13	Suspended (CNT on top of electrodes) ^[69]
-5 to 5 V (2 MV/m)	<0.1	SiO ₂ – 50nm	SiO ₂ =3.9	PTFE encapsulation Dielectric Surface passivation (Electrodes on top of CNT film) ^[8]
-10 to 10 V (16.7 MV/m)	5	SiO ₂ - 200nm Parylene- 100nm	SiO ₂ + Parylene (3.15) = 3.61	Hydrophobic film on dielectric (CNT on top of electrodes) ^[62]
-1 to 1 V (16.7 MV/m)	0.1	SiO ₂ -4nm SAM-2nm	3.3	SAM on SiO ₂ (Electrodes on top of CNTs) ^[71]
-10 to 10 V (80 MV/m)	8	SiO ₂ - 100nm	SiO ₂ =3.9	PMMA passivation on top of CNT (Electrodes on top of CNT) ^[213]
-5 to 5 V (5.55 MV/m)	0.5	ZrO ₂ - 90nm	ZrO ₂ =10	PVDF- TrFE passivation on top of CNT (CNT film on top of electrodes) ^[212]
-1.5 to 3 V (10 MV/m)	0.3	TiO ₂ - 30nm	TiO ₂ =22	TiO ₂ top gate (Electrodes on top of CNT film) ^[75]
-5 to 5 V (0.263 MV/m)	0.1	h-BN- 80nm SiO ₂ - 300nm	h-BN = 3.29 h-BN+SiO ₂ = 3.75	PTFE + h-BN (CNT on top of electrodes) ^[190]

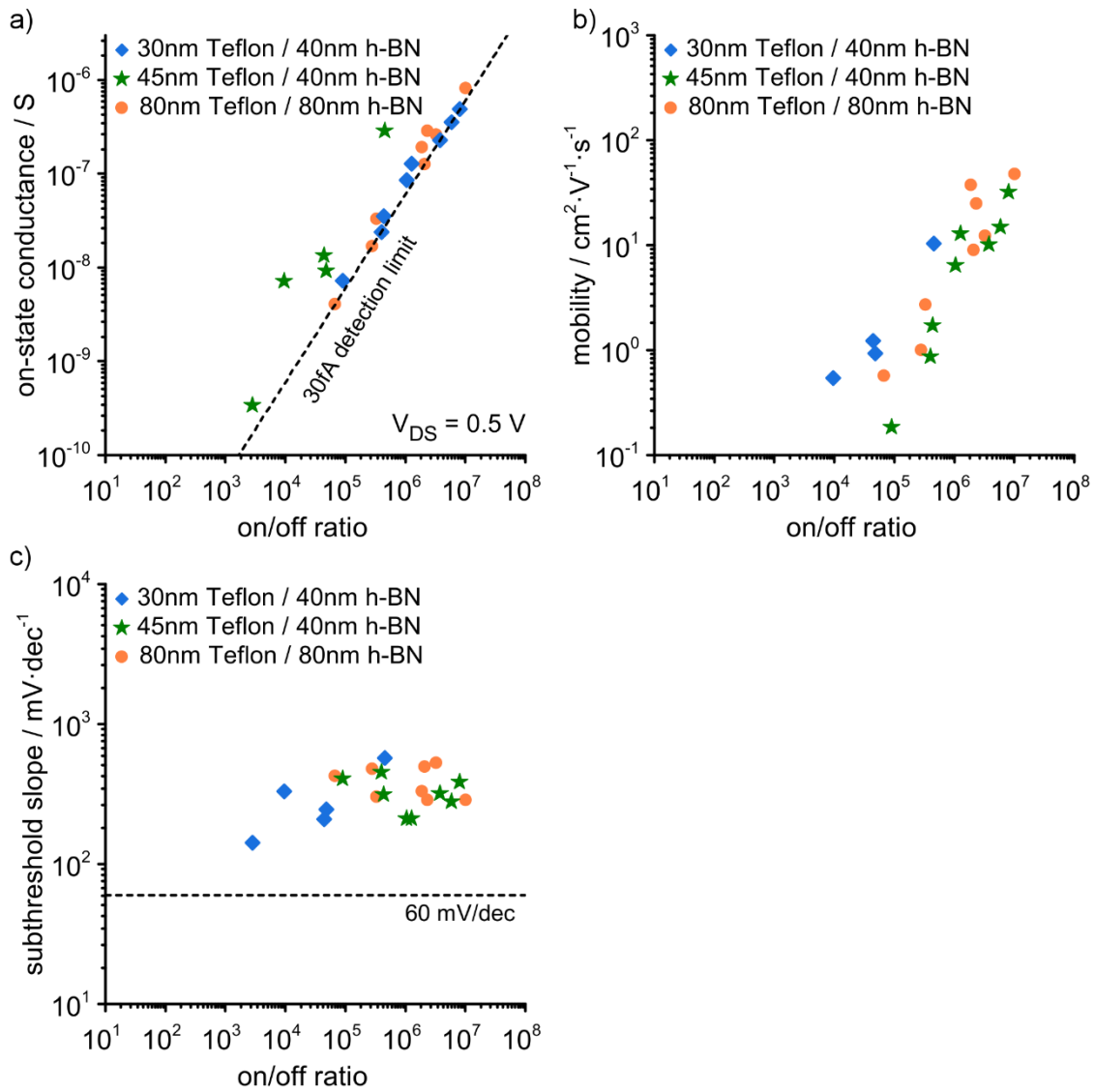


Figure 4.10: a) On-state conductance, b) mobility, and c) subthreshold slope for 21 devices. SWCNTs devices were encapsulated in three combinations of h-BN and Teflon layer thicknesses, as indicated. The data has been acquired from the transconductance curves measured after a week of storage under ambient conditions. In a) the dashed line represents 30-fA detection limit of the setup, and in c) the theoretical subthreshold slope limit at 300 K^[190].

In summary, devices with electrodes on top of CNTs placed on SAM passivated SiO_2 require additional hydrophobic packaging to remove hysteresis,^[8] whereas devices with electrodes on top of CNTs based on SAM passivated Al_2O_3 show long-term hysteresis-free behavior without additional packaging.^[214] On the other hand for devices with CNTs on top of electrodes, hydrophobic packaging seems to be mandatory to eliminate hysteresis as observed in this work as well. Transconductance curves measured after a week under ambient condition storage (final) concerning on-state conductance, on/off

ratio, mobility and subthreshold slope have also been evaluated. Figure 4.10a shows the on-state conductance values up to 10^{-6} S and on/off ratio up to 10^7 , with no correlation to the h-BN and Teflon layer thicknesses. Taking into account the small number of 1-5 SWCNTs per device and 30 fA current detection limit it can be concluded that the performance is comparable to previous devices on DEP-deposited polymer-wrapped SWCNTs.^[205] Also, field-effect mobilities^[82] up to $100 \text{ cm}^2\text{V}^{-1}\text{s}^{-1}$ and subthreshold slopes^[82] down to 140 mV dec^{-1} , shown in figure 4.10b-c, are evidence for the good performance of liquid-phase sorted, polymer-wrapped SWCNTs embedded in h-BN and Teflon. Calculations of subthreshold slopes and field-effect mobility are explained in chapter 2.

Next, the charge traps are calculated based on hysteresis values. The theory related to it has been discussed in chapter 2. The difference in threshold voltages in forward and reverse bias is plotted for different devices in figure 4.11. Taking value for one of the devices $|V_t| = 6.5 \text{ V}$,

$$Q_{\text{SiO}_2} = c_{g,\text{SiO}_2} |V_t| = 0.302 \text{ pF cm}^{-1} \times 6.5 \text{ V} = 1.2 |e| \text{ nm}^{-1} (|e| \text{ is the elemental charge})$$

For devices with h-BN+SiO₂, number of charge traps,

$$Q_{h\text{-BN}} = c_{g,h\text{-BN}} |V_t| = 0.29 \text{ pF cm}^{-1} \times 3.4 \text{ V} = 0.61 |e| \text{ nm}^{-1}$$

With $Q_{\text{SiO}_2} > Q_{h\text{-BN}}$ it can be concluded that h-BN film already reduces the number of charge traps. Since there are no contributions from the substrate, these charges should come from water adsorbed onto the metal electrodes and carbon nanotubes.

Charges after Teflon coating of 80nm ($t = 0$):

$$Q_{\text{Teflon}} = c_{g,h\text{-BN}} |V_t| = 0.29 \text{ pF cm}^{-1} \times 1.5 \text{ V} = 0.27 |e| \text{ nm}^{-1}$$

This implies $(Q_{h\text{-BN}} - Q_{\text{Teflon}}) = 0.34 |e| \text{ nm}^{-1}$ charges were removed by coating 80nm of Teflon and $0.27 |e| \text{ nm}^{-1}$ charges then contribute towards hysteresis after encapsulating the CNTs in Teflon and h-BN. These charges diffuse out through Teflon after a certain waiting time as discussed earlier.

The devices characterized in this work had subthreshold slope down to 140 mV dec^{-1} and field-effect mobility up to $100 \text{ cm}^2\text{V}^{-1}\text{s}^{-1}$ indicates the good performance of devices on h-BN. Figure 4.10 a-c summarizes device performances at room temperature for all 21 devices.

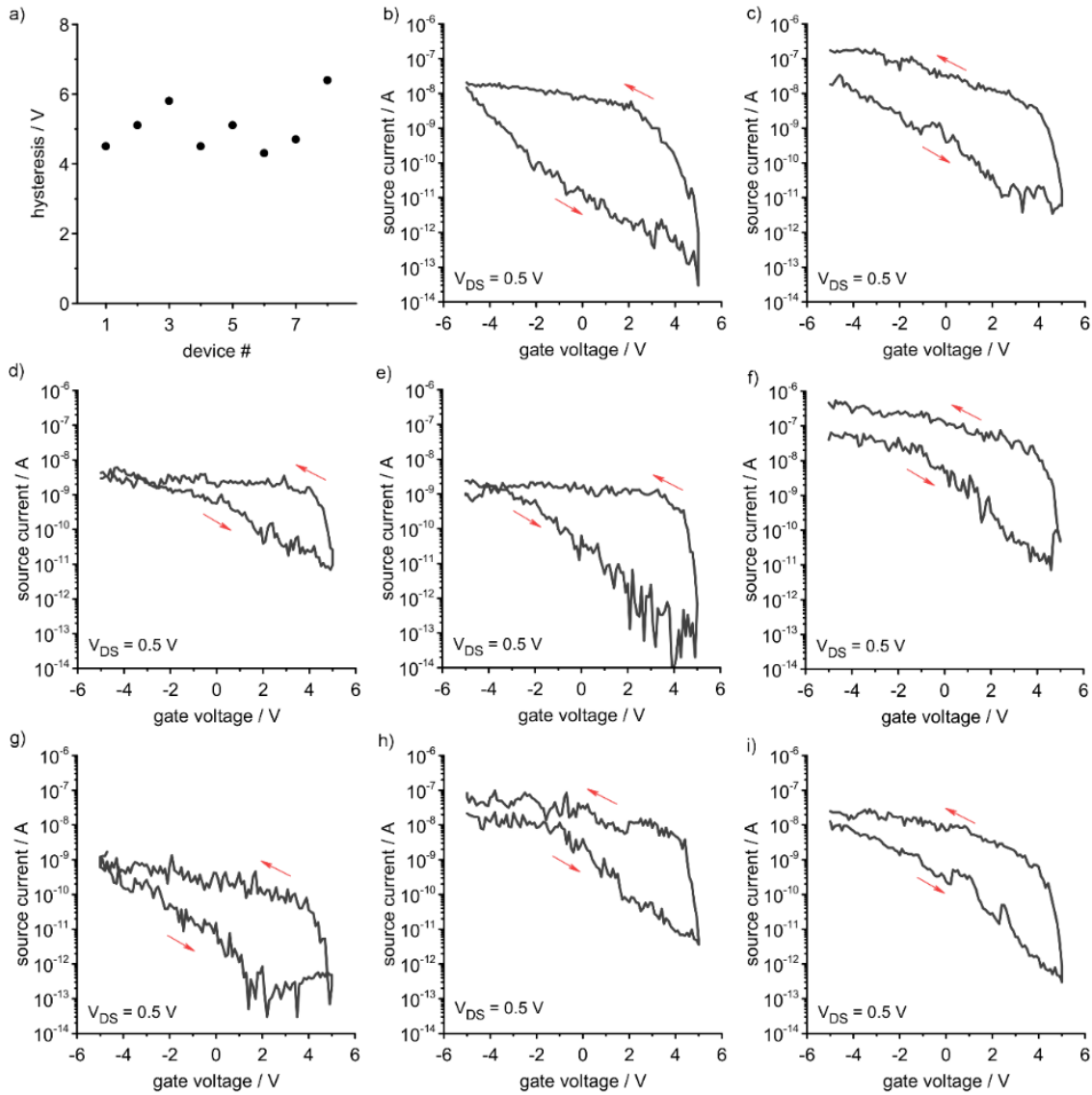


Figure 4.11: a) Hysteresis in transconductance curves for SWNCT devices on Si/SiO₂ without h-BN and PTFE encapsulation. (b-i) The corresponding transconductance curves were measured after vacuum annealing and are hence comparable to the h-BN supported devices prior to Teflon coating^[190].

4.4 Summary

To summarize, for h-BN synthesis, the two important parameters are the metal catalyst and process pressure. The presence of metal catalysts supports synthesis at lower pressures, but in its absence, synthesis only occurs at higher pressures on dielectric substrates.

Furthermore, nearly hysteresis-free transconductance curves for (9,8) single-walled carbon nanotubes embedded in h-BN / PTFE heterolayers were observed. The reduction of hysteresis after PTFE coating over a timescale of days has been explained by the slow repelling of residual water molecules that strongly adhere to the metallic electrodes onto which CNTs have been deposited under ambient conditions. Longer waiting times would eventually eliminate hysteresis. However, Teflon coating without breaking the annealing vacuum appears to be a more promising route to be explored.

5 Graphene-SURMOF Molecule Sensor

This chapter includes major parts of a research article that has been published^[215].

2D materials in the form of monolayers constitute atomically thin and extended planar structures with inherently entangled “bulk” and “surface” properties. As such, 2D materials are highly susceptible to electric fields induced by gate voltages and local charge distributions,^[10,26,216,217] to physisorption, chemisorption, and interfacial doping,^[218–221] to light, sound, and strain.^[222–225] Consequently, 2D materials are of great interest for a range of sensing applications, as has been demonstrated for the detection of gases,^[226–228] metal ions,^[229,230] strain,^[222] and pressure.^[231] A challenge for the field is the limited availability of large-area 2D materials. Currently, graphene is the only commercially available wafer-scale material with well-defined properties. Graphene has been demonstrated to be highly sensitive to interfacial doping, electric fields, and vicinal dielectrics, and for a reliable and easily accessible readout, the position of the Dirac point in the gate-voltage dependence of a GFET can be exploited. This sensing principle has already been demonstrated for pH measurements,^[232] where a dielectric oxide provides sensitivity towards hydronium ions. However, for general applicability, an interfacial layer is required that can be tailored to be highly selective to specific molecules, offering a larger versatility as compared to surface functionalization. Metal-organic frameworks are such a class of material, and a selective absorptivity for specific molecules can be tailored by specific combinations of metal ions or clusters and organic ligands. There are countless MOFs that have been synthesized and exploited for many applications related to energy harvesting^[233] and gas storage.^[234–236] Fewer examples of MOF based sensors exist for gas sensing,^[237] chemical sensing,^[238] small molecule detection by inducing stress in MOF crystal structure,^[239] and metal ions detection via a luminescent MOF.^[240] Recently a MOF with high affinity to SO₂ was grown between interdigitated electrodes, and the change in the capacitance of the structure under gas uptake was used for SO₂ detection.^[241] In this work, SURMOFs were directly grown onto GFET, to benefit from the combination of the high sensitivity, easy read-out capability of a GFET, and the high selectivity of a SURMOF. In the chapter, SURMOF/GFETs sensors based on Cu₂(BDC)₂-SURMOF-2 are presented, which yield a selective sensitivity to ethanol. It is described in detail the fabrication of the SURMOF/GFET sensor via multiple processing steps for the GFET formation. The liquid-phase synthesis of the MOF on the surface of the GFET, prepared by our collaborators at IFG, KIT, is also discussed briefly. It is shown that the SURMOF substantially changes the response of a GFET against gas

molecules in the air and common alcohols by measuring in-situ the corresponding gate-voltage dependence of the conductance. To study the performance of the ethanol sensor, sensitivity and response time are determined, and the activation and resetting schemes are described.

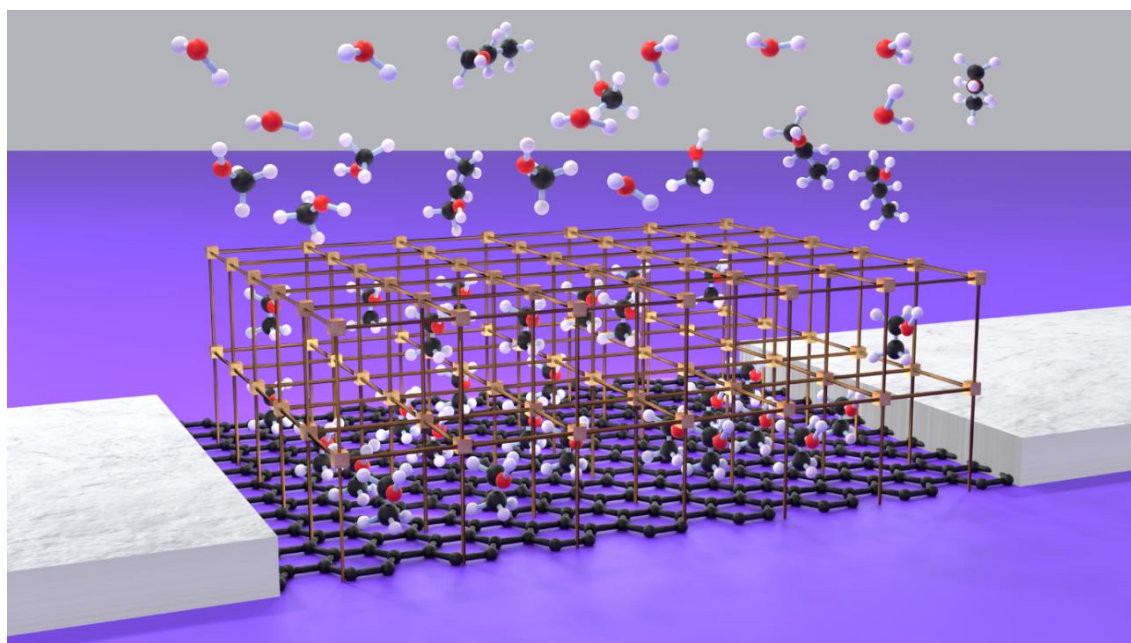


Figure 5.1: 3-D model mimicking ethanol selectivity to SURMOF. Metal linkers (brown squares) are connected to organic linkers (brown rods) grown on a hexagonal honeycomb structure of graphene.

To support these findings, the electrical transport characteristics with Raman spectroscopy are correlated. In addition, energy-dispersive X-ray, X-ray diffraction, scanning electron microscopy, adsorption, and desorption data are provided, and a model is proposed to approximate the response of the sensor. A 3-D model mimicking the selectivity of SURMOF/GFET for ethanol molecules is shown in figure 5.1.

5.1 GFET Device Fabrication

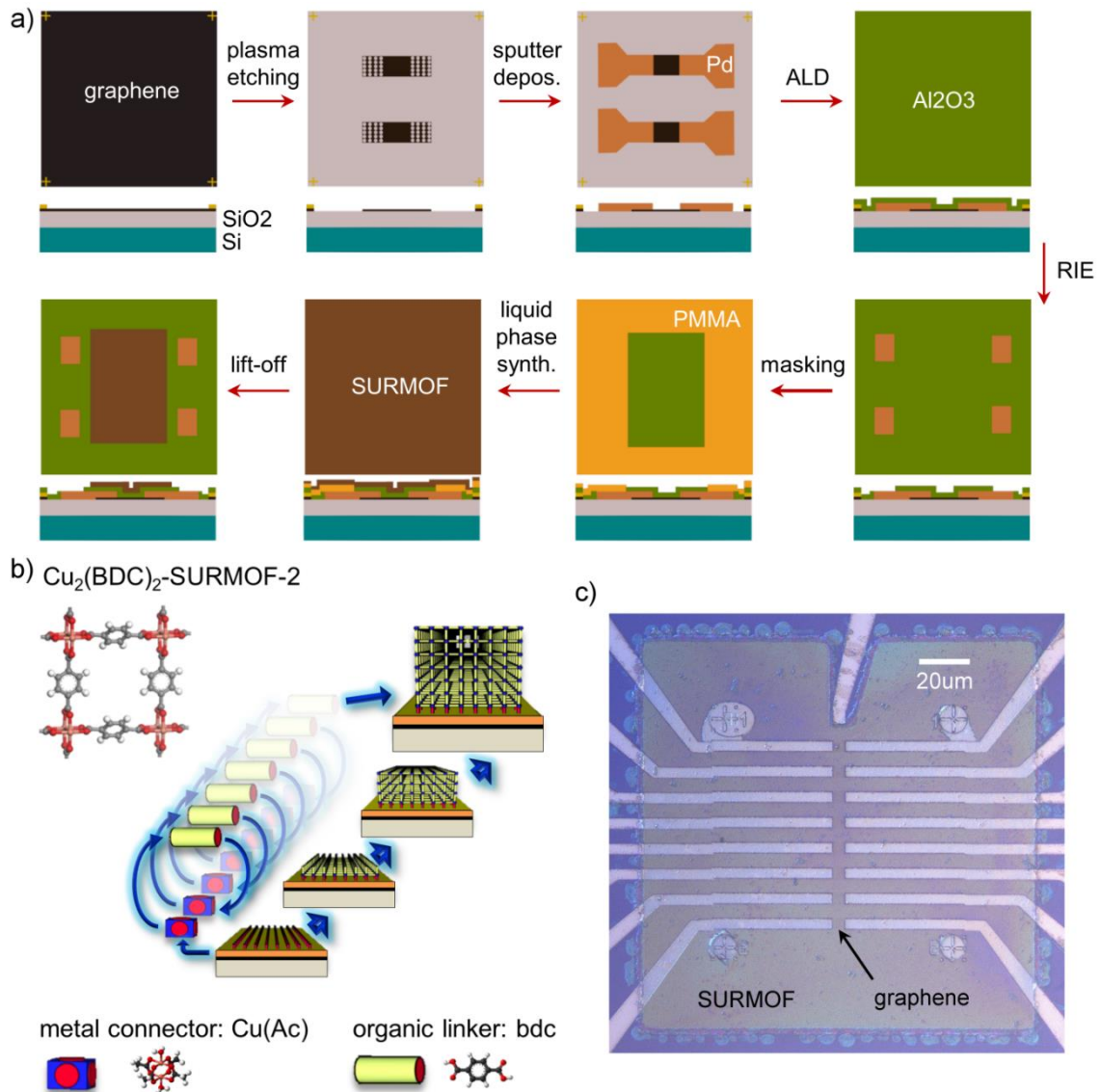


Figure 5.2: Fabrication of SURMOF/GFET devices. (a) Process flow involving multiple electron beam lithography patterning, etching, and deposition steps. (b) Liquid-phase synthesis of the SURMOF on the GFET by repeated exposure to metal connectors and organic linkers. (c) Optical micrograph of the final SURMOF/GFET devices. The sensor areas are located between the metal source-drain electrodes where graphene can be recognized due to the optical transparency of the SURMOF^[215].

Figure 5.2a shows all the steps involved in GFET fabrication. For all the steps, PMMA 950k resist (Allresist) diluted in anisole was used and prebaked at 150°C on a hot plate for 3 minutes. The e-beam exposed areas were developed in a solution of MIBK/IPA (Methyl isobutyl ketone/isopropanol) for 30 s, rinsed with IPA, and dried in a nitrogen

stream giving the required patterned structure. In the first step, markers were defined. PMMA A4.5 (4.5 % PMMA in anisole) was coated at 5000 rpm for 60 s, e-beam patterned and developed. 50 nm tungsten was deposited by sputtering (Bestec 300W DC, 60 s) and subsequently lifted off in acetone. For the second step, graphene strips of dimensions 5 μm x 100 μm were defined and perforated with holes (230 nm diameter, 640 nm lattice spacing, in total 2x(75x5) by spin coating PMMA A4.5 at 4000 rpm for 60 s, e-beam patterning, cold development at 0°C. By etching of the graphene around the PMMA protected strips and in the holes via oxygen plasma in a reactive ion etcher (RIE Oxford Plasmalab 80 plus, 15 sccm O₂, 60 mTorr, 30 W for 75 s) holes in the channel are made, leaving an unperforated area in the middle of 5 μm x 5 μm . In the third step, the source-drain electrodes and the back gate contacts were defined. A scratch through the SiO₂ was made to contact the Si gate. After spin-coating PMMA A4.5 at 6000 rpm for 60 s, e-beam exposure, and development, 3 nm Cr and 42 nm Pd were deposited by sputtering (100 W, RF, 30 s, and 70 W, DC, 45 s, respectively). On this fabricated GFET device, 5 nm of aluminum oxide was grown using trimethylaluminum (TMA) and ozone at 150°C by thermal atomic layer deposition (TMA pulse time = 0.1 s at 150 sccm flow rate, T= 25°C, purge time = 6 s, Oxygen pulse time = 0.1 s at 100 sccm flow rate, purge time = 6 s, power= 70%, 75 cycles). The Al₂O₃ layer was locally removed for electrical contacting by first spin-coating PMMA A8 (8% PMMA in anisole) at 6000 rpm, e-beam patterning, and development. Then, the aluminum oxide was etched in the RIE (40 sccm Ar, 10 sccm CHF₃, 200 W, 15 mTorr, 70 s). In the fifth and final step, the area for the SURMOF growth on top of the devices was defined by spin coating PMMA A4.5 at 5000 rpm, e-beam patterning, and development. The GFET was then used to grow SURMOF on top by our collaborators at IFG, KIT, Germany.

5.2 SURMOF synthesis

Figure 5.2b shows a schematic for the synthesis of SURMOF. The SURMOF layer was grown by the layer-by-layer (lbl) synthesis as described in Liu et al.^[242] by our collaborators from IFG, KIT. To summarize the process, first, the surface of the GFET device was activated in a UV/Ozone cleaner (Ossila, Sheffield, UK) for one minute to maximize the number of functional OH groups at the Al₂O₃ surface. Afterward, the devices were put immediately into a 1 mM of copper (2) acetate (Cu₂(OAc)₄(H₂O)₂) ethanol solution before the synthesis. Then, the devices were placed on the sample holder and subsequently sprayed with 1 mM Cu (OAc)₂ ethanolic solution for 15 s and with an 0.2 mM 1,4-benzene dicarboxylic acid (BDC) ethanol solution for 25 s at room temperature. Between both steps, the sample was thoroughly rinsed with pure ethanol

to remove under-coordinated metal nodes or organic linker molecules. This procedure was repeated in total 35 times to grow a nominally 100 nm thick layer.

5.3 Characterization parameters

1. **XRD:** X-ray diffraction (XRD) measurements were carried out in an out-of-plane geometry using a Bruker D8-Advance diffractometer equipped with a position-sensitive LynxEye detector in θ - 2θ geometry. A Cu-anode with a wavelength of $\lambda=0.154$ nm was used. The samples were investigated with an angle increment of 0.02° and a scan speed of 4 s per step.
2. **SEM / EDX:** Scanning electron micrographs were taken with a Zeiss Ultra plus SEM at 10 keV beam energy, at 45° tilt angle, and inlens detection. Energy-dispersive X-ray spectra were recorded with a Zeiss LEO 1530 SEM and an Oxford instruments X-maxN detector at 4 keV beam energy and analyzed with AZtec software from Oxford instruments.
3. **Raman:** Spectra of CVD-graphene/300nm-SiO₂/Si sample was measured before and after Al₂O₃ and SURMOF growth, under ambient conditions with a Renishaw inVia Raman microscope at 532 nm excitation wavelength, 3 mW power, 60 s integration time, and 20x magnification. SURMOF/5nm-Al₂O₃/graphene/300-nmSiO₂/Si reference sample was measured under ambient conditions after exposure to ethanol, isopropanol, and methanol vapor. Before alcohol vapor exposure, the samples were vacuum annealed at 150°C . The data were acquired at 532 nm excitation wavelength, 0.6 mW (after alcohol exposure) and 3 mW (after vacuum annealing), 60 s integration time, 20x magnification.
4. **Electrical transport and sensing measurements:** The SURMOF/GFETs were mounted to a ceramic chip carrier, wire bonded (figure 5.3d), and with the package mounted to a cavity of volume $\sim 1\text{cm}^3$ (figure 5.3b). The cavity has an inlet and outlet as part of a gas line system as described in Ganzhorn et al.^[3] A four-way valve enables instantaneous switching between gases, and the conditions were controlled by pressure gauges and flow meters (dosing valves) (figure 5.3a, b). All measurements were carried out at flow rates of 0.5 L min^{-1} and a static gas pressure of 0.25 bar above atmospheric pressure. The dynamic pressure ($<10^{-4}$ bar) is negligible. The gas in the cavity is exchanged within 0.1 s, setting the time resolution of the measurements. In the downstream, a humidity sensor (Bosch BMP280) and an alcohol sensor (NCD MQ-3) were mounted in an additional cavity and monitored with a Raspberry Pi. For exposure to alcohols and water, the liquids were filled into a steel bubbler and dry nitrogen was

passed through it at a flow rate that yields the carrier gas saturated with the corresponding liquid, as monitored by the downstream sensors. If not stated otherwise the initial starting condition was flowing dry nitrogen, and measurements were taken ~15 min after changes of conditions. Electrical transport measurements were carried out with an Agilent 4155C semiconductor parameter analyzer with TRIAX cabling, and back gate sweeps were conducted at source-drain voltages of 0.01 V, 0.02 V, and 0.03 V. Time-dependent measurements were done at zero back gate voltage and 1 s time intervals. All experiments were carried out at room temperature.

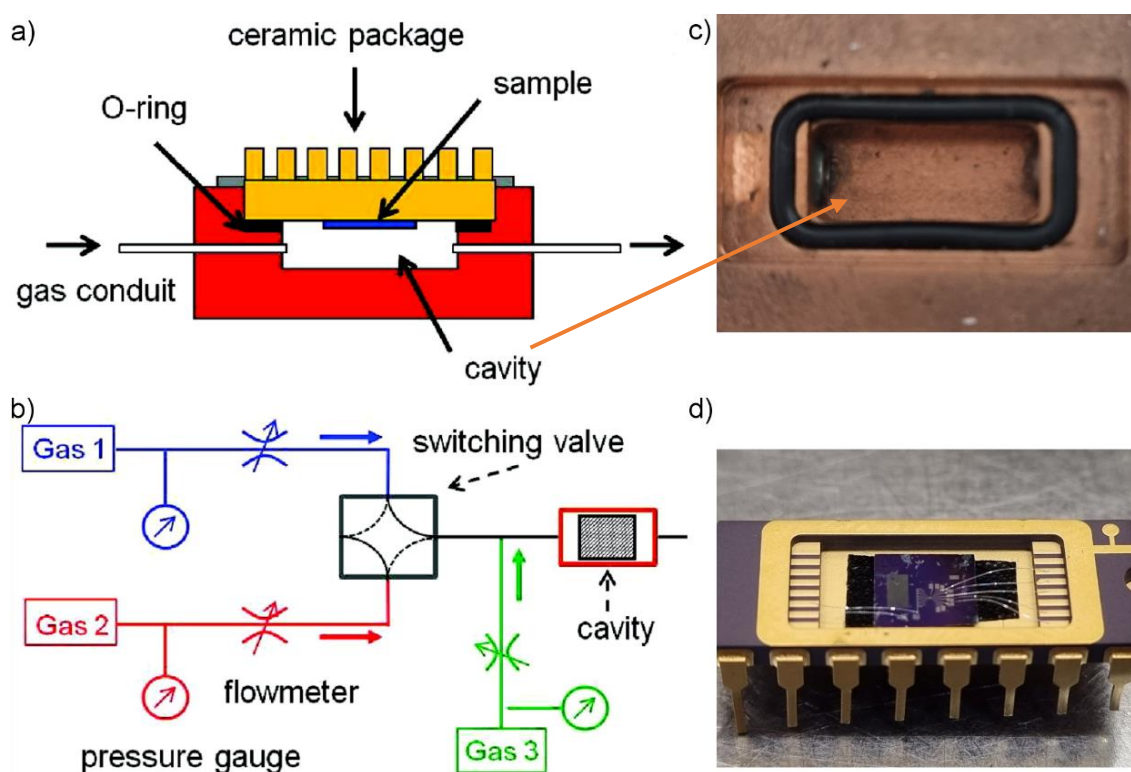


Figure 5.3: a), b) Schematic of the gas sensing setup adapted from Ganzhorn et al. ^[3] c) Cavity on which the chip carrier is loaded in inverted position d) Sample bond wired onto the chip carrier.

5. **Simulation:** A qualitative proof-of-principle simulation of the graphene carrier concentration and Dirac voltage as a function of back-gate voltage and surface charge density was conducted using a finite element partial differential equation solver (FlexPDE 6). The coupled Poisson-Drift-Diffusion equations were solved for the electrostatic potential and the quasi-Fermi potentials^[243] by solving

iteratively the Laplace equation and the Drift-Diffusion equations^{[244][245]}. The surface charge density was imposed by a natural boundary condition.

5.4 Results and discussions

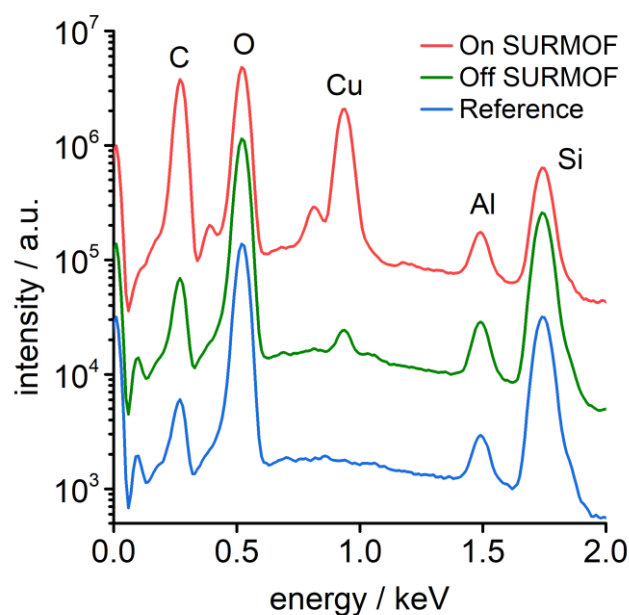


Figure 5.4: Energy-dispersive X-ray (EDX) spectra for evaluating the integrity of the ALD-grown Al_2O_3 layer. The reference is a 5nm- Al_2O_3 /graphene/300nm- SiO_2 /Si sample, on which a nominally 100 nm thick SURMOF layer was grown. The primary beam energy was 4 keV, sufficient to probe the Al_2O_3 layer underneath the top layer (On SURMOF). The upper two curves are shifted for clarity. Residues of copper from the SURMOF are detectable in lifted-off regions (Off SURMOF)^[215]. See also figure 5.6.

The SURMOF/GFET sensors were fabricated by employing several steps of electron-beam lithography, metallization, etching, coating, atomic layer deposition, and liquid-phase synthesis, as shown in the schematic process flow in figure 5.2a. Large-area monolayer graphene on $\text{p}^{++}\text{-Si}/300\text{ nm-SiO}_2$ was etched by plasma oxidation into multiple $5\text{ }\mu\text{m}$ wide and $100\text{ }\mu\text{m}$ long strips, each electrically contacted separately with Pd/Cr source-drain electrodes. The uncovered graphene channels have a length of $5\text{ }\mu\text{m}$ with an active area of $25\text{ }\mu\text{m}^2$. To minimize the contact resistance, the graphene underneath the electrodes was perforated with holes^[246]. 5 nm of Al_2O_3 was grown by thermal atomic layer deposition (ALD) by subsequent pulses of trimethylaluminum and ozone^[247] over the entire structure to provide surface hydroxyl groups required for the SURMOF growth and to electrically isolate the graphene and the electrodes. The contact

pads were opened by local etching and the area for the SURMOF growth was defined by a resist mask. A $\text{Cu}_2(\text{BDC})_2$ -SURMOF-2 with a nominal thickness of 100 nm was grown by liquid-phase synthesis (figure 5.2b),^{[248][242]} using a spray synthesis similar to Hurre et al.^[249] Afterward, the SURMOF was lifted off from outer areas with a resist mask. An optical micrograph of the complete SURMOF/GFET devices is shown in figure 5.2c. It is observed that the Al_2O_3 layer is required for the SURMOF to grow on top of graphene. With energy-dispersive X-ray spectroscopy (EDX), it is verified that the ALD-grown Al_2O_3 layer is still intact after the SURMOF synthesis (figure 5.4). Out-of-plane XRD measurements on a large-area reference sample show that the SURMOF grows on 5nm- Al_2O_3 /graphene/300nm- SiO_2 /Si with the (001) orientation parallel to the substrate surface and with a lattice constant of 1.12 nm (figure 5.5), which is comparable to the synthesis of the SURMOF on other $-\text{COOH}$ terminated surfaces^{[242][250]}. Despite the flat appearance of the SURMOF in the optical image and the (001) reflex in the XRD data, the SURMOF layer is rough on a microscopic scale. SEM images recorded under different angles reveal that the SURMOF at the interface with the Al_2O_3 layer is continuous, whereas the upper surface is uneven, with small SURMOF crystals pointing in various directions (figure 5.6), likely a consequence of the atomically uneven Al_2O_3 surface.

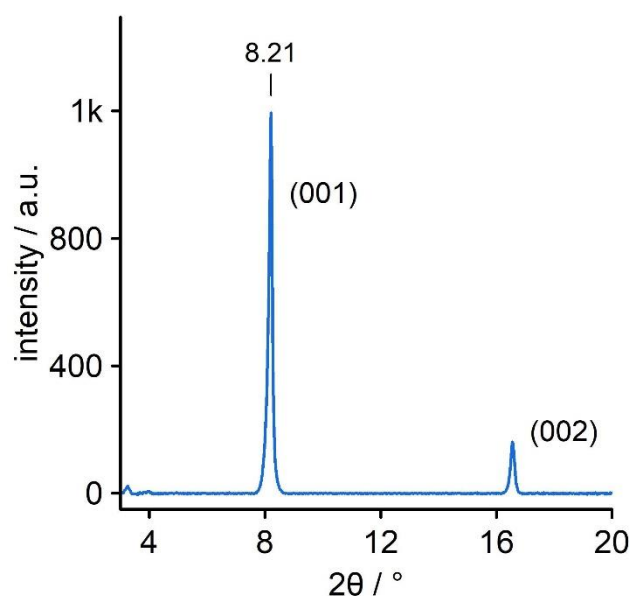


Figure 5.5: XRD measurements of SURMOF showing (001) and (002) peaks^[215].

After fabrication, the devices were wired to a ceramic package, mounted to a cavity of volume $\sim 1\text{cm}^3$, and connected to a gas line system, described in Ganzhorn et al.^[3] (figure 5.3). A four-way valve enables instantaneous switching between gases, and the conditions were controlled by pressure gauges and flow meters (dosing valves). Devices

were exposed to air, N_2 , O_2 , and CO_2 , and to molecules from liquids by purging N_2 through H_2O , methanol (CH_3OH), ethanol (C_2H_5OH), and isopropanol (C_3H_7OH). The relative humidity and alcohol concentrations were monitored downstream with commercial sensors. The gate-voltage dependencies of the device conductance were measured with a semiconductor parameter analyzer at 300 K, and the doped silicon was used as a back-gate for all devices. The details have been already discussed in the chapter 3.

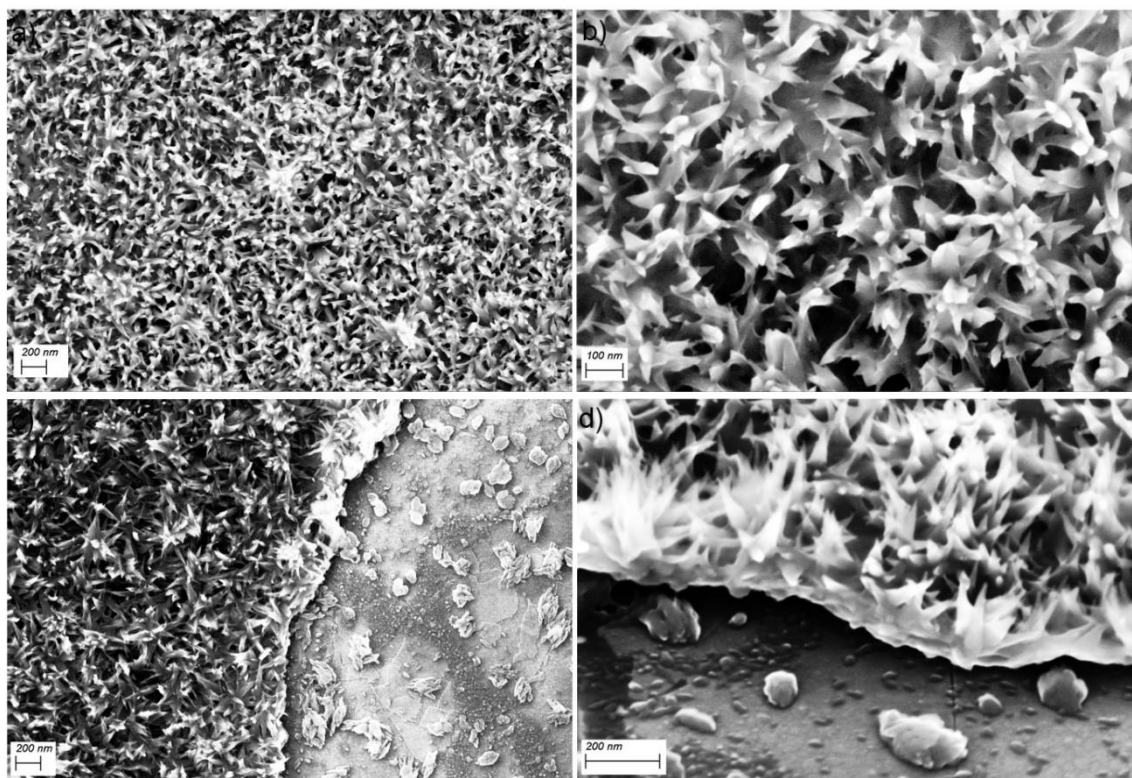


Figure 5.6: Scanning electron microscopy images of a SURMOF/5nm- Al_2O_3 /graphene/300-nm SiO_2 /Si sample, recorded at 10 keV and with in-lens detection. (a-c) measured at normal incidence, (d) under 45° angle from the front. (c-d) show the edge of the SURMOF after partial lift-off^[215].

First, the gate voltage dependence of the conductance of GFETs without SURMOF coating is discussed. As a measure for the doping, the Dirac voltage has been used, which is defined as the gate voltage that yields the minimum conductance. If the applied gate voltage is equal to the Dirac voltage, the Fermi level coincides with the charge neutrality point of graphene at the K point of the graphene band structure. The devices show significant hole doping in air, but also while purging with dry N_2 , as shown by the blue traces in figure 5.7 and figure 5.8a, respectively. The conductance decreases monotonically with increasing gate voltage and the Dirac voltage V_{Dirac} is beyond the

maximum applied gate voltage of +100 V. The corresponding doping level can be calculated from the carrier concentration n in the graphene layer, which depends on gate voltage V_{gate} , the Dirac voltage V_{Dirac} , the geometrical capacitance C formed between graphene and SiO_2/Si , and the graphene quantum capacitance, using equation 5.1. The derivations of the graphene quantum capacitance have been discussed in the chapter 2.

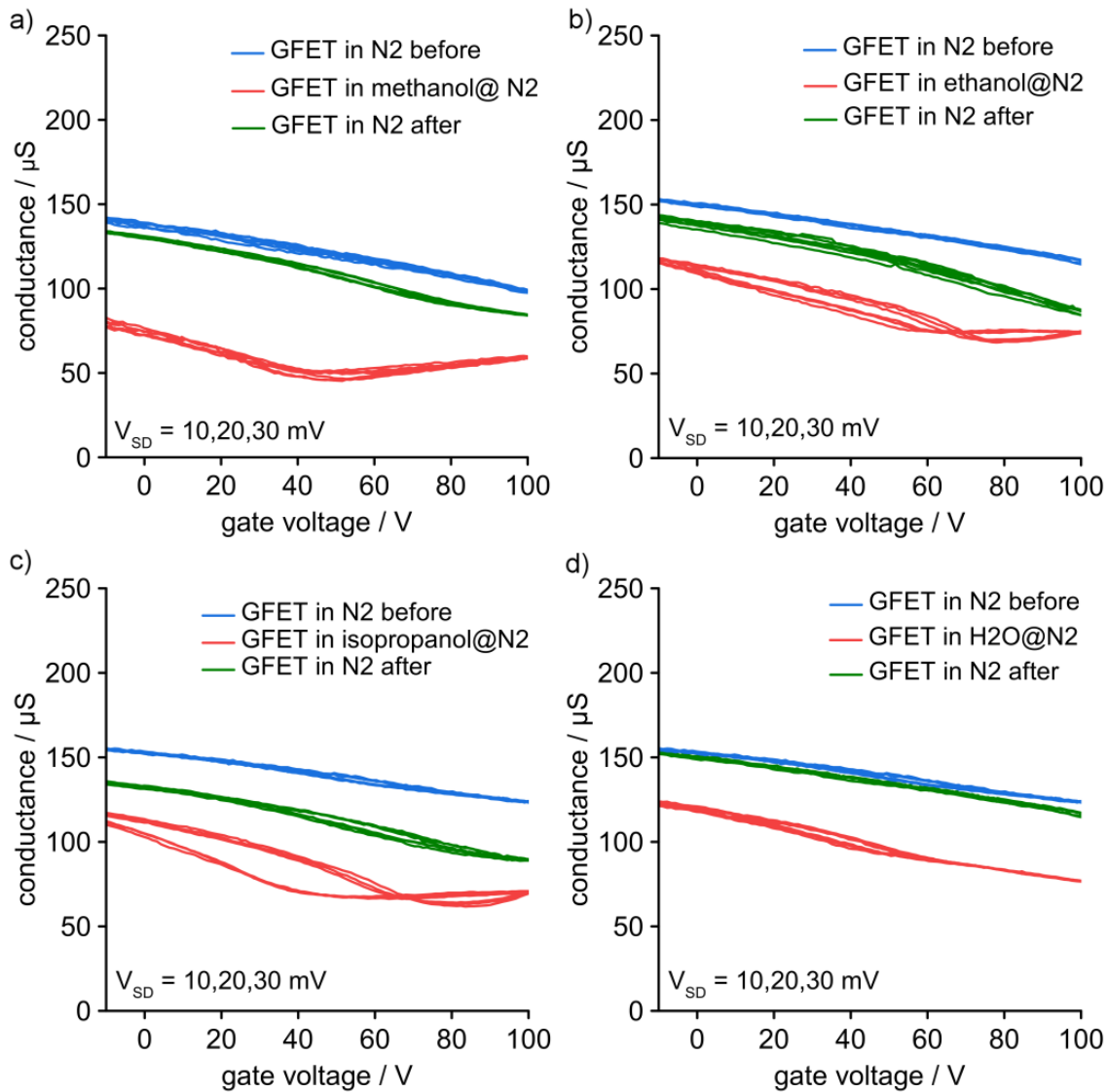


Figure 5.7: Response of the GFET without SURMOF to methanol- (a), ethanol- (b), isopropanol- (c), and water molecules in the N_2 stream. The conductance versus gate-voltage is shown for the GFET in N_2 before and after the exposure. Source-drain voltages are indicated.^[215]

$$n(V_{gate}, V_{Dirac}) = -(V_{gate} - V_{Dirac}) \left(\sqrt{\frac{|V_{gate} - V_{Dirac}|}{a + c^2}} - c \right)^2 \quad (5.1)$$

$$c = \frac{b}{2a} \quad (5.2)$$

$$a = \frac{e}{C} \quad (5.3)$$

$$b = \frac{h v_F \pi^{0.5}}{e}, v_F = 10^6 \text{ ms}^{-1} \quad (5.4)$$

$$C = 11.5 \text{ nF cm}^{-2}$$

The carrier concentration at zero gate voltage due to doping is then given as $n_{\text{doping}} = n(V_{\text{gate}}=0, V_{\text{Dirac}})$, and the value obtained is $n_{\text{doping}} > +7 \cdot 10^{12} \text{ cm}^{-2}$ for $V_{\text{Dirac}} > +100 \text{ V}$; $V_{\text{Dirac}} = +150 \text{ V}$ yields $n_{\text{doping}} = 10^{13} \text{ cm}^{-2}$. The doping level of the graphene layer was also followed by Raman spectroscopy. The spectrum of a reference CVD-graphene/300 nm-SiO₂/Si sample in figure 5.9a shows the graphene G-peak at 1596 cm^{-1} , the 2D-peak at 2686 cm^{-1} , and no visible D-peak. The peak positions were analyzed with the model of Lee et al.,^[251] by plotting our data onto the dashed grid lines, which shows how the G-peak and 2D-peak positions depend on doping and strain. Data points can then be deconvoluted into components of strain and doping by projection onto the grid lines, as demonstrated in figure 5.9b. The data is consistent with a hole-doped graphene layer which is nearly strain- and defect-free. The Raman peak in figure 5.9a at 2461 cm^{-1} is from a two-phonon combination mode in graphene, referred to as G* or D+D".^[252] The peak at 2331 cm^{-1} originates from ambient molecular nitrogen above the sample surface^{[253][254]}. After the growth of a nominally 5 nm thick Al₂O₃ layer, a small D-peak appears in figure 5.9a at 1351 cm^{-1} , and the G- and 2D-peaks are shifted down to 1589 cm^{-1} and 2682 cm^{-1} , respectively. It indicates that the growth of Al₂O₃ induces a moderate defect concentration in the graphene layer and it reduces slightly the hole doping as shown in figure 5.9b. The graphene layer though remains free of strain. Note that the Raman measurement conditions (ambient, laser irradiation) are not strictly identical with the GFET characterization conditions (gas flow system, dark), but the data is in agreement with the transport data and shows that the graphene layer underneath the Al₂O₃ layer is hole-doped.

The sensitivity of the GFET without SURMOF against the presence of alcohol and water vapors has been explored first. Figure 5.7a-c shows the response of the GFET to methanol-, ethanol-, and isopropanol molecules in the N₂ stream. It is observed that the

overall conductance is reduced in the presence of all three alcohols and the corresponding Dirac voltages could be determined. The amount of hole doping reduction is similar but most pronounced during exposure to methanol ($n_{\text{doping}} = 3.3\text{--}3.5 \cdot 10^{12} \text{ cm}^{-2}$), followed by ethanol ($n_{\text{doping}} = 4.6\text{--}5.7 \cdot 10^{12} \text{ cm}^{-2}$), and isopropanol ($n_{\text{doping}} = 4.3\text{--}6.0 \cdot 10^{12} \text{ cm}^{-2}$). Also, the exposure to water molecules reduces the hole doping when

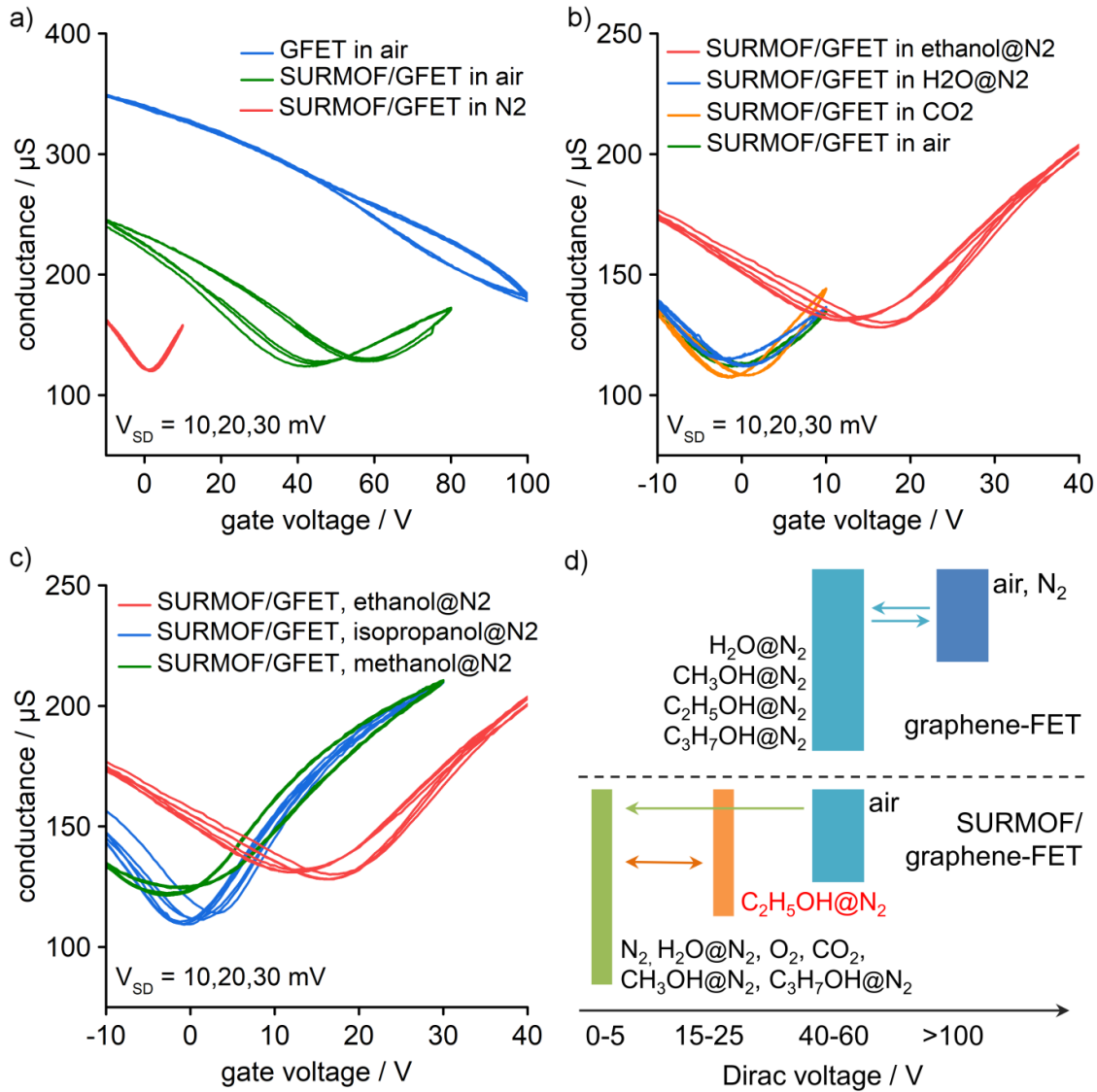


Figure 5.8: Gate-voltage dependence of SURMOF/GFET device conductance. (a) Response to air before (GFET in the air) and after SURMOF coating (SURMOF/GFET in the air), and to N_2 after SURMOF activation (SURMOF/GFET in N_2). (b) Response of SURMOF/GFETs to air and CO_2 , and N_2 purged with H_2O and ethanol. (c) Response SURMOF/GFETs to N_2 purged with ethanol, methanol, and isopropanol. (d) Schematic overview on the responses of the SURMOF/GFET and GFET devices and the Dirac voltages measured under the indicated conditions^[215].

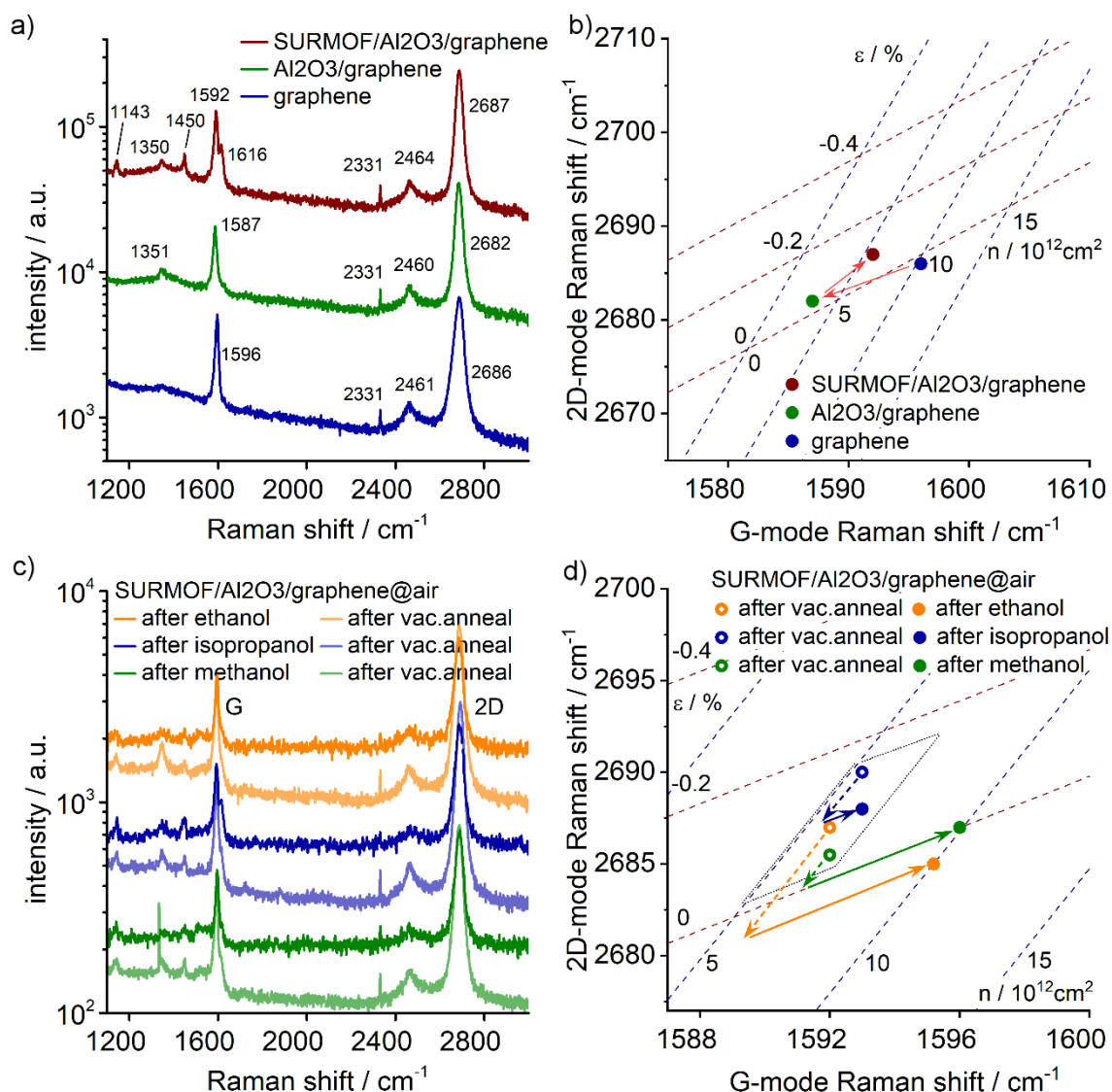


Figure 5.9: (a) Raman spectra of a CVD-graphene/300nm-SiO₂/Si sample before and after Al₂O₃ and SURMOF growth measured in air. The peak at 2331 cm⁻¹ is from N₂(g). The upper two curves are shifted for clarity. (b) Correlation between the frequencies of the G and 2D Raman modes shown in (a). The dashed lines show the effects of hole doping ($\Delta\omega_{2D}/\Delta\omega_G = 0.7$) and strain ($\Delta\omega_{2D}/\Delta\omega_G = 2.2$) on the mode frequencies of graphene using the model of Lee et al.^[145] (c) SURMOF/5nm-Al₂O₃/graphene/300-nmSiO₂/Si reference sample measured in the air after exposure to ethanol, isopropanol, and methanol vapor. Before alcohol vapor exposure, the samples were vacuum annealed at 150°C. All curves except the lowest are shifted for clarity. (d) Correlation between the frequencies of the G and 2D Raman modes is shown in (c). The dashed and full arrows show the corresponding changes in strain and doping. The dotted box encompasses the data of the vacuum annealed samples and defines the error for determining the relative changes in strain and doping^[215].

the gas flow is changed from dry N₂ to humid N₂ (~80% relative humidity, figure 5.7d). All changes are reversible and strong hole doping is reestablished when purging the

devices with dry N_2 (figure 5.7). It is important to note that GFETs without SURMOF coating always remain in the strong hole-doping regime, with the Dirac voltage above 40 V, independent of the type of alcohol exposure. This is summarized schematically in the upper part of figure 5.8d. The growth of the SURMOF changes this behavior completely. The Dirac voltage of the SURMOF/GFET in the air is at 40-60 V, whereas without SURMOF it was beyond 100 V, as shown in figure 5.8a. Also, the Raman spectrum has changed in figure 5.9a. After the growth of a nominally 100 nm thick SURMOF layer, the G and 2D peaks shifted upwards to 1592 cm^{-1} and 2687 cm^{-1} , respectively. The shifts in figure 5.9b indicate that the SURMOF growth introduces about 0.1% compressive strain in the graphene layer and a slight change in doping. After the SURMOF growth three additional Raman peaks are observed at 1143 cm^{-1} , 1450 cm^{-1} , and 1616 cm^{-1} , assigned to the ring stretch of benzene-dicarboxylate, asymmetric C-O stretch, and C= stretch in the SURMOF layer, respectively.^[256] Again, absolute strain and doping values should be taken with care.

Most interestingly, the hole doping in the air is not only significantly reduced for GFETs after the SURMOF growth, but after purging with N_2 , the device becomes undoped, and the Dirac voltage approaches zero, as shown in figure 5.8a. Also, the mobility has increased to $4640\text{ cm}^2\text{V}^{-1}\text{s}^{-1}$, which is remarkably high for CVD-graphene on SiO_2/Si without vacuum or current annealing.

The purging of SURMOF with N_2 is a common activation process step,^[257] promoting the desorption of solvent and guest molecules from MOF pores. The details of the desorption process can be rather complex. For instance, the desorption of water is inhibited in the presence of ethanol due to complex formation at the outer surface of a MOF^[256]. The activation process is important also in this work and essentially constitutes the last step in the SURMOF synthesis. The outcome of this activation process implies that ethanol captured in the SURMOF from the synthesis process diffuses out while purging with N_2 , revealing an undoped SURMOF/GFET. It is expected that ethanol can diffuse back into the structure as well.

Further tests were performed and the SURMOF/GFET devices were exposed to a flow of N_2 saturated with ethanol (ethanol@ N_2). Indeed, figure 5.8b shows that the Dirac voltage shifts from 0 V to 15 V when switching from N_2 to ethanol@ N_2 . The data also shows that the SURMOF/GFET is insensitive to H_2O molecules ($\text{H}_2\text{O}@N_2$), CO_2 , and air. Furthermore, figure 5.8c shows that the Dirac voltage of the SURMOF/GFET remains at zero and is not reacting to N_2 saturated with methanol (methanol@ N_2) or isopropanol (isopropanol@ N_2). These results are summarized schematically in the lower part of figure 5.8d.

The selectivity of the Dirac voltage to ethanol must have been imposed by the SURMOF/ Al_2O_3 interface since the adsorption and desorption properties of the SURMOF itself are very similar for the three alcohols (figure 5.12). More insights were gained by analyzing the SURMOF/GFETs transconductance curves with the model of Kim et al.^[255]. For all conditions, the mobility, residual carrier concentration, contact resistance, and Dirac voltage were determined. Figure 5.10a shows that the highest mobility has been measured in pure nitrogen ($\sim 4640 \text{ cm}^2\text{V}^{-1}\text{s}^{-1}$, @N₂) after the activation procedure. The lowest mobility is obtained for ethanol@N₂ ($1020 \text{ cm}^2\text{V}^{-1}\text{s}^{-1}$) and methanol@N₂ ($1150 \text{ cm}^2\text{V}^{-1}\text{s}^{-1}$). The mobility for isopropanol@N₂ is $3050 \text{ cm}^2\text{V}^{-1}\text{s}^{-1}$, and thereby significantly higher than for the other two alcohols. The mobility for all other conditions is between $1.6\text{--}2.6 \text{ kcm}^2\text{V}^{-1}\text{s}^{-1}$. Also, the residual carrier concentration in figure 5.10b follows a similar pattern. The lowest value is observed in pure nitrogen ($3.8 \cdot 10^{11} \text{ cm}^{-2}$), the highest values for ethanol@N₂ ($1.2 \cdot 10^{12} \text{ cm}^{-2}$) and methanol@N₂ ($9.7 \cdot 10^{11} \text{ cm}^{-2}$), and comparable to air@N₂ ($9.7 \cdot 10^{11} \text{ cm}^{-2}$) before the activation procedure. The value for isopropanol@N₂ is $4.4 \cdot 10^{11} \text{ cm}^{-2}$, and thereby significantly lower than for the other two alcohols. The other values are in between ($4.9\text{--}7.5 \cdot 10^{11} \text{ cm}^{-2}$). Furthermore, the contact resistance in figure 5.10c reproduces the different behavior of the alcohols. The lowest contact resistance is observed for ethanol@N₂ (1156 Ohm) and methanol@N₂ (1251 Ohm). For isopropanol@N₂ the value is 2175 Ohm, and thereby again significantly different from the other two alcohols. The contact resistance for all other conditions is between $1.9\text{--}2.3 \text{ kOhm}$. On the other hand, the Dirac voltage in figure 5.10d and the corresponding doping level in figure 5.10b show a different behavior among the exposure to the alcohol molecules. For ethanol@N₂ the Dirac voltage is at 12V and the doping at $8.8 \cdot 10^{11} \text{ cm}^{-2}$, whereas both values are significantly smaller for methanol@N₂ (-1.5 V , $1.07 \cdot 10^{11} \text{ cm}^{-2}$) and isopropanol@N₂ ($+0.9 \text{ V}$, $6.4 \cdot 10^{10} \text{ cm}^{-2}$).

The data thus leads to the conclusion that ethanol and methanol molecules reach the SURMOF/ Al_2O_3 interface but isopropanol does not, and only ethanol molecules induce a shift in the Dirac voltage. Therefore, it can be inferred that MOF/GFET sensing of ethanol is due to shift in Dirac voltage and not due to the changes in carrier mobility. This is shown in figures 5.10a and d where the mobility data shows similar values for both the alcohols but different Dirac voltages. This result may not be surprising given that the graphene layer is $\sim 3\text{--}5\text{nm}$ below the Al_2O_3 surface making the charge carriers in graphene less susceptible to scattering by molecules. Also, Schedin et al.^[18] reported no change in mobility despite exposing graphene directly to various gases.

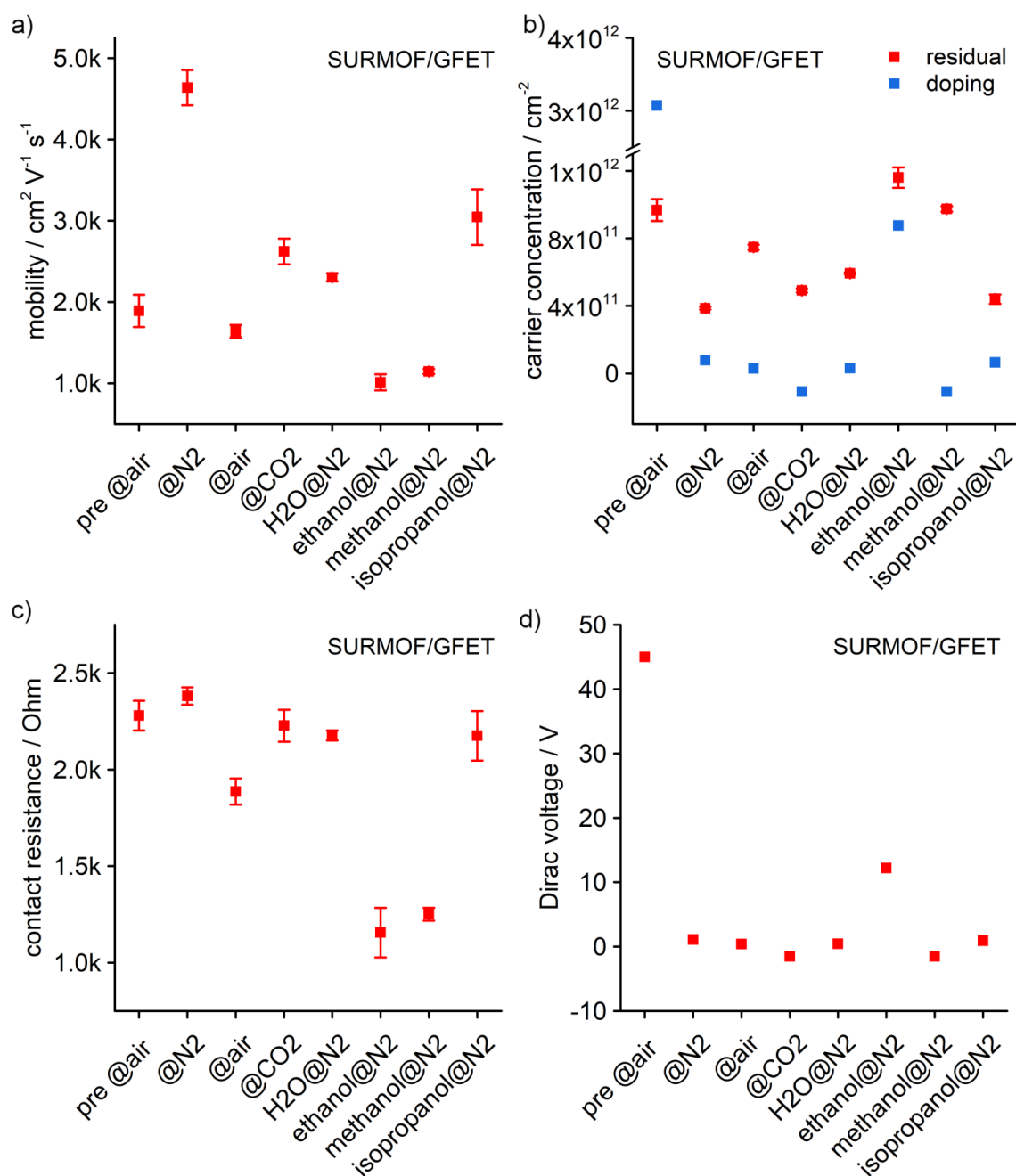


Figure 5.10: Comparison of (a) mobility, (b) residual carrier concentration, and doping, (c) contact resistance, and (d) Dirac voltage of SURMOF/GFET devices under various conditions. The values have been determined by fitting the transport measurements to the model of Kim et al.^[255] The carrier concentration due to doping in (b) has been derived from the Dirac voltage. All data were acquired after SURMOF activation, except for the measurement in the air before activation (pre @air)^[215].

Further insight into the alcohol-induced doping of graphene was gained by Raman spectroscopy on a reference SURMOF/5nm- Al_2O_3 /graphene/300nm- SiO_2 /Si sample. Figure 5.9c shows changes to the Raman spectra when exposed to ethanol, isopropanol,

and methanol vapors. Additional measurements were taken immediately after vacuum annealing at 150°C, before each alcohol exposure. Once again, the correlation between G and 2D peak positions to determine the doping and strain in the graphene layer has been used^[251]. No effect is observed after exposure to isopropanol. The changes in strain and doping are within uncertainty, as shown in figure 5.9d. This result supports the transport data, which indicates that isopropanol does not reach the SURMOF/Al₂O₃ interface. Also in agreement with the transport data is the effect due to exposure to ethanol molecules. The Raman data shows that ethanol does reach the interface and induces significant hole doping in the graphene layer. Regarding the exposure to methanol, both, Raman and transport data show that methanol reaches the SURMOF/Al₂O₃ interface. However, the transport data shows no change in doping, whereas the Raman data does. It is important to note that Raman probes the local doping and that a shift of the G peak to larger wavenumbers occurs for electron doping and hole doping^{[258][259]}. Transport measurements instead probe the average net charging by a shift of the Dirac voltage. The formation of electron-hole puddles with zero net charges, as reported in absence of charged impurities,^[260] could explain the observation with methanol, and their presence would reduce the carrier mobility and increase the residual carrier concentration without shifting the Dirac voltage. At the same time, a shift of the Raman G-peak frequency should be observable because of local doping. The different interactions of ethanol and methanol with the SURMOF/Al₂O₃ interface though must have a microscopic origin and figure 5.9d indicates a small difference in the change of strain in the graphene layer.

To further explore the sensor performance, the response time and sensitivity of the SURMOF/GFET devices were explored. Figure 5.11a shows that the Dirac voltage changes from 0 V to 15 V within seconds when switching from N₂ to ethanol@N₂. However, after switching back to pure N₂, it takes several hours until the Dirac voltage reapproaches 0 V. In the upper part of figure 5.11b, adsorption and desorption of ethanol are continuously monitored by measuring the conductance at a fixed gate-voltage of 0 V and a source-drain voltage of 30 mV. After 20 min of purging with N₂, the conductance is still 40% above the value before ethanol@N₂ exposure. Such slow desorption is a serious obstacle for sensing applications. Fortunately, there is a simple way to overcome the problem by thermally activating the desorption process, for example, by heating the device via electrical power dissipation. The lower part of figure 5.11b shows that when increasing the source-drain voltage temporarily from 30 mV to 10 V, the desorption becomes as fast as the adsorption. The corresponding increase of the power dissipation from 140 nW to 15 mW resets the sensor within 10-20 seconds. The current-driven self-heating of the graphene is estimated to increase the

temperature ΔT by ~ 150 K, determined based on $\Delta T = p/r_0$, where p is the dissipated power per area and $r_0 = 0.4 \text{ kWcm}^{-2}\text{K}^{-1}$ [261].

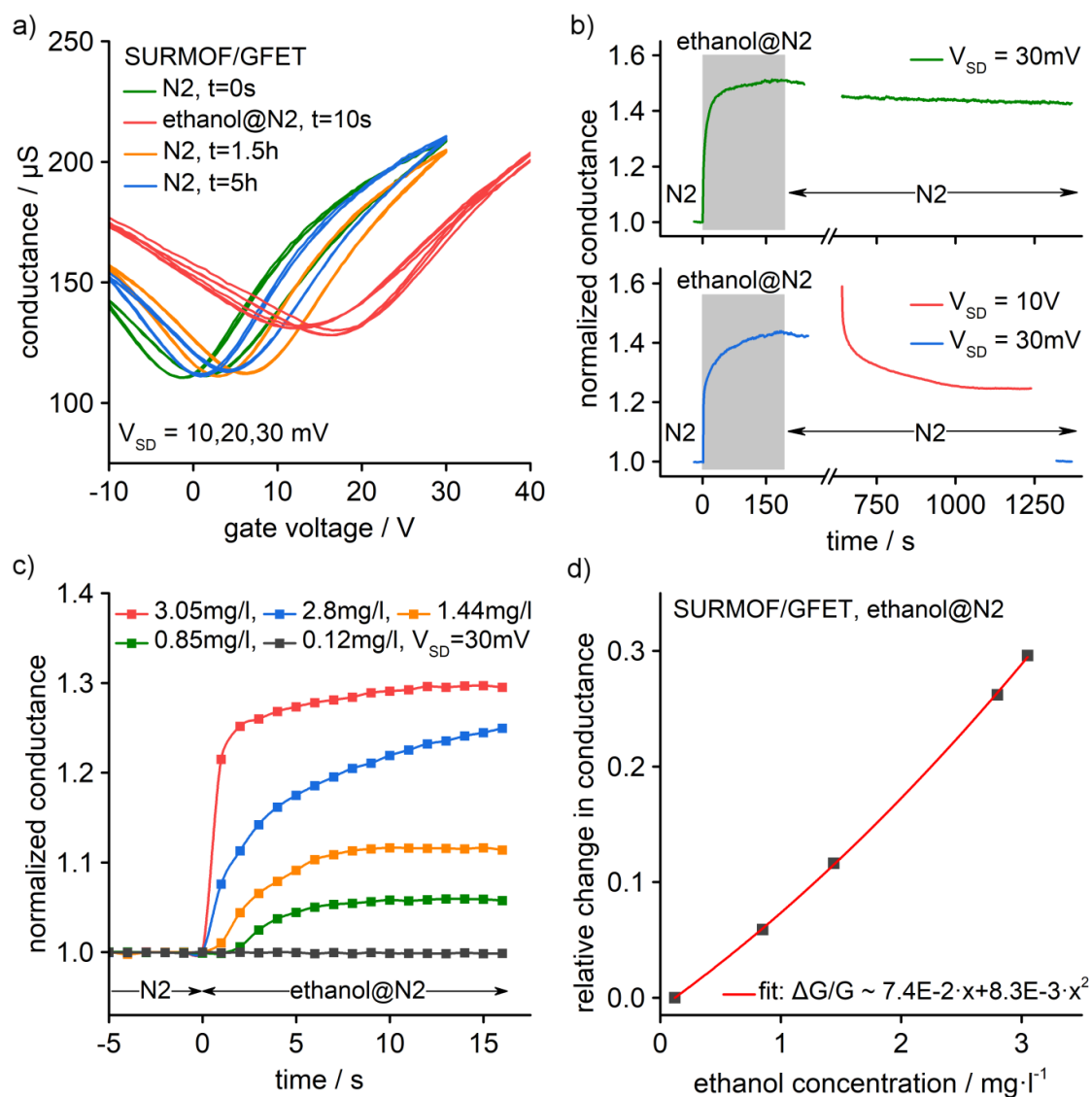


Figure 5.11: SURMOF/GFET time response and sensitivity to exposure of ethanol. (a) Time evolution of conductance versus gate-voltage measured before, after, and during ethanol exposure. Time steps and source-drain voltages V_{SD} are given. (b) In the upper panel, the corresponding change in conductance was measured at zero gate voltage and $V_{\text{SD}} = 30$ mV (green trace). The lower panel shows the reset procedure with a temporary increase of V_{SD} from 30 mV (blue trace) to 10 V (red trace). After the reset, the conductance reached the initial value. (c) SURMOF/GFET response versus ethanol concentration. The concentrations were measured with a commercial ethanol sensor. (d) Change in conductance after 15 s of ethanol exposure versus ethanol concentration. The data is fitted with a second-degree polynomial function[215].

Next in characterizing the sensors, ethanol sensitivity of the SURMOF/GFET was measured, and gauged the ethanol concentration in N₂ with a commercial alcohol sensor. The sensor-as all the commercial sensors- is based on heated metal oxide nanostructures and reacts unspecific to ethanol, methanol, and isopropanol, and many other organic molecules^[262]. The measurement results are summarized in figure 5.11c-d. The SURMOF/GFET sensor can detect ethanol concentrations larger than 0.2 mg l⁻¹ (100 ppm), and a concentration of 3 mg l⁻¹ leads to a 30 % change in conductance. This level of sensitivity is comparable to other GFET sensors responding to alcohol. However, it should be emphasized that these GFET sensors are not selective to ethanol and do not discriminate against methanol and isopropanol^[41]. In marked contrast, SURMOF/GFET in this work has high selectivity to ethanol, low detection limit, and is insensitive to humidity, and operates at room temperature. More sophisticated electrical readout schemes would enhance the sensitivity, yet with the simple tracking of the conductance applied here, the SURMOF/GFET sensor is sensitive enough to detect ethanol concentrations that are relevant for breath alcohol determination^[263].

To give a microscopic explanation for the observations made, results based on GFET without SURMOF need to be addressed first. As transport and Raman data show, the graphene layer underneath the Al₂O₃ layer in air and N₂ is strongly hole-doped. This points to negative charges located in or on the oxide layers. Regarding the Al₂O₃ layer, it has been reported that the growth by ALD can give rise to negative charge densities on the order of 10¹² cm⁻², which can be two orders of magnitude higher than what is typically observed for thermally grown SiO₂^[264]. Whereas it is unclear how many charges are located within the Al₂O₃ and SiO₂ layers, the alumina surface is certainly terminated with –OH groups after the completion of the ALD process^[265]. Exposure after growth to ambient air leads to the adsorption of water molecules on the hydrated alumina. Unlike on unhydrated alumina, molecular water is strongly bound to hydrated alumina and can only be removed when heated to 170°C^[266]. When measuring the GFET without SURMOF, therefore it is reasonable to assume that the Al₂O₃ surface is terminated with –OH groups and covered with water molecules, despite purging with N₂. How those groups get negatively charged is not clear, but probably through an electrochemical electron trapping process by the -OH groups occurring during electrical characterization. This mechanism has been verified by FTIR spectroscopy for devices on –OH terminated SiO₂ surfaces^[267]. It is reasonable to assume that hydroxyl groups on Al₂O₃ are as effective in trapping charges and that the Al₂O₃ layer is thin enough to allow the tiny tunneling current that is required to fill the traps. In any case, not all –OH groups of fully hydrated alumina will be charged as this would lead to an excessive surface charge density on the order of >10¹⁵ cm⁻¹^[268].

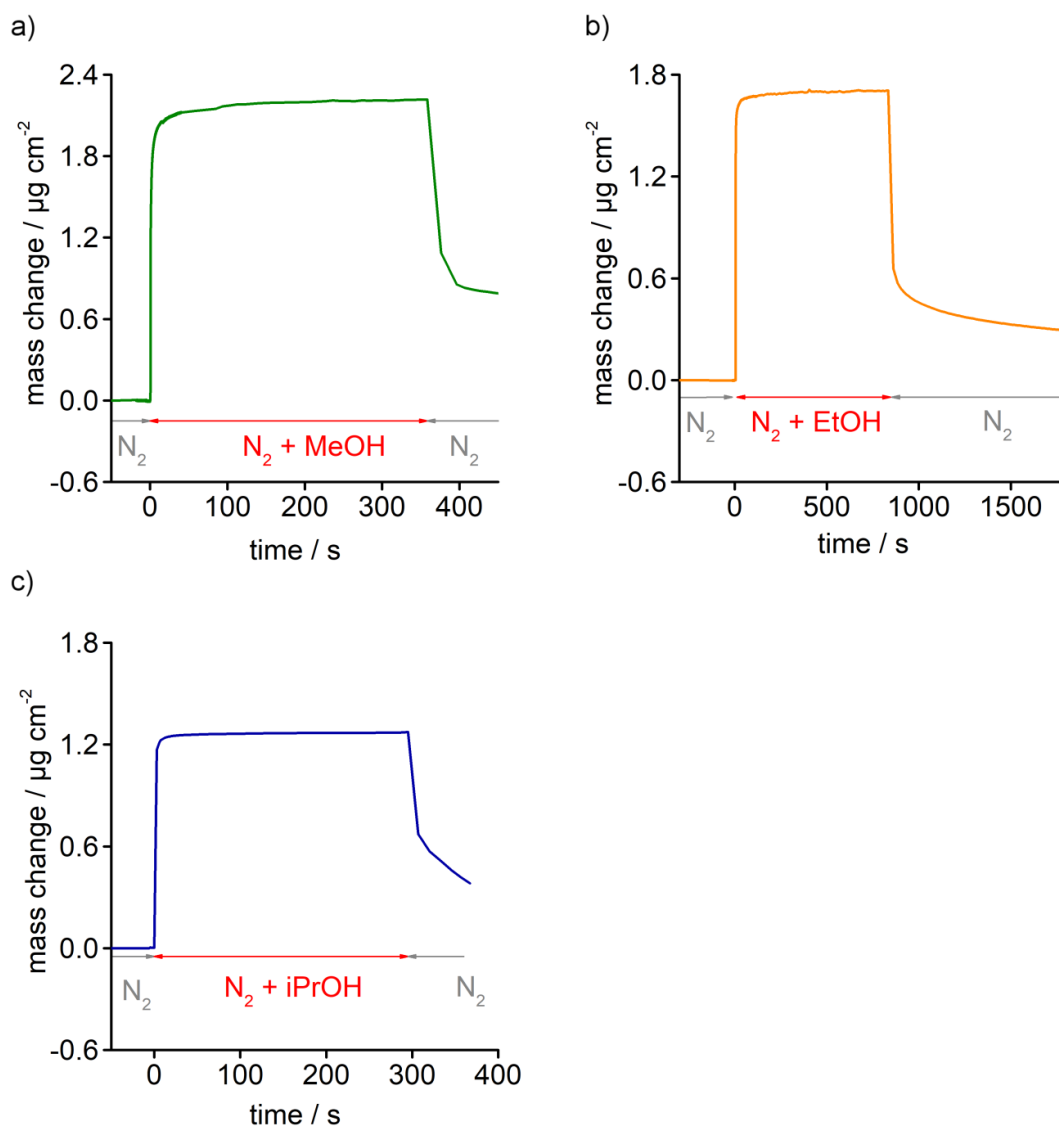


Figure 5.12: Vapor uptake by the MOF film grown Au@QCM-sensors. The vapors are a) methanol, b) ethanol and c) isopropanol. Initially, the samples are activated in an atmosphere of pure nitrogen, then the gas flow is instantaneously enriched with the vapor of the guest molecules with a vapor pressure close to saturation. After reaching equilibrium, the gas atmosphere is switched back to pure nitrogen. The gas flow rate is 100 ml per min. The temperature is 25°C ^[215].

Next, an attempt is made to understand why exposure to alcohol and water reduces the hole-doping of the GFET. There are two reasons plausible:

- Screening of charges
- Charge removal

Simulations show that monohydric alcohol interacts non-dissociative with hydrated alumina by an antiparallel alignment of the alcohol polar group to the alumina hydroxyl

group^[269]. Water molecules on hydrated alumina orient in a similar way^[268]. Both lead to a reduction of surface dipole moments. Moreover, when surface charges are covered by a polarizable medium, the electric field underneath the surface – where graphene is located – will be reduced approximately by $2\varepsilon_1/(\varepsilon_1+\varepsilon_2)$, where ε_1 and ε_2 are the effective dielectric media below and above the interface, respectively^[270]. For the devices studied above, the factor could be on the order of 0.5, which would explain the reduction of hole-doping. In this picture, the screening will disappear and the strong hole-doping will reappear as soon as a device is purged with N_2 , which experimentally occurs within minutes. The mechanism is kind of similar to the screening induced reduction of hole-doping observed for graphene devices covered with ionic liquid,^[271] or metal top gate^[272]. The physics of diffusive graphene devices can be described by coupled Poisson-Drift-Diffusion equations^{[244][245]} and a finite element partial differential equation solver to approximate the device behavior within computational limitations.

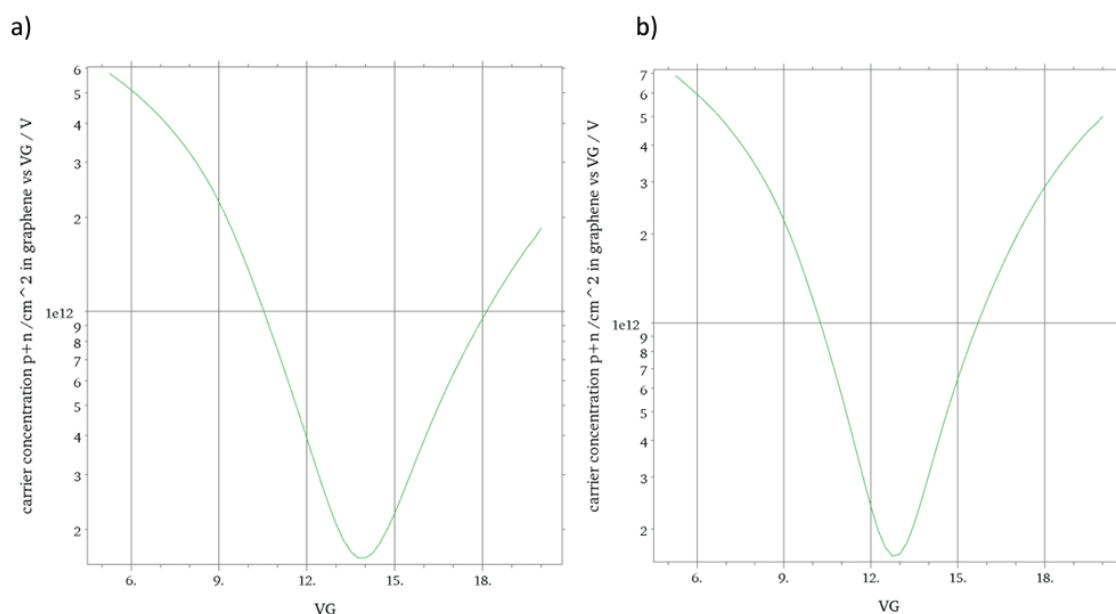


Figure 5.13: Simulated charge carrier concentration $p+n$ in graphene vs back-gate voltage V_G at 10 mV source-drain bias. Graphene was modeled as a 50 nm x 50 nm x 1 nm layer with a 30 nm back-gate dielectric (eps_SiO_2), a 3 nm top dielectric ($\text{eps_Al}_2\text{O}_3$), and a surface charge density of -10^{13} cm⁻². (a) Simulation with a 30 nm layer ($\text{eps}=1$) on top, and (b) with a 7 nm ($\text{eps}=10^3$) and a 13 nm ($\text{eps}=1$) layer on top. The data was taken from the center of the graphene layer. The high- k dielectric layer on top of the negative surface charge reduces the Dirac voltage and narrows the Dirac cone^[215].

Qualitatively, the reduction of the gate voltage when adding a polarizable dielectric on the top was reproduced. However, the effect showed to be rather small (figure 5.13). Therefore, charge removal as a possible mechanism should also be considered. A simple

hopping of negative charges from the surface is rather unlikely considering the electron affinities of alcohol (-2.1 eV), water (-1.3 eV), and hydroxyl radicals (+1.8 eV). However, a chemical reaction might take place to withdraw charges. From desorption experiments of ethanol on hydrated alumina, it is known that diethyl ether and ethene form and evaporate from the surface when heated above 180°C and 230°C,^[273] with H₂ and H₂O as byproducts. Whether charges promote reactions and lead to partial charge removal at room temperature remains unclear, but the reduction of hole-doping could be an indication for it. The re-charging in N₂ back to strong hole-doping would then have to follow the initial charging mechanism.

After the SURMOF growth, fewer hydroxyl groups are left because of the chemical reaction with the copper acetate that anchors the SURMOF to the alumina. If only a few charged -OH groups remain it would explain the close to zero doping and the high mobility that is observed after the SURMOF growth procedure. However, zero doping could also be a result of compensation of the remaining negatively charged -OH groups by positive charges. Unfortunately, the initial stages of the SURMOF growth remain elusive. In the ideal structure, there are 1.5 Cu-paddle-wheel-metal-nodes per nm², nominally bound to one OH-group per one metal node. This would affect a smaller fraction of the original -OH group density. On the other hand, the appearance of positive charges during synthesis is not known either, although the existence of charged defects in related SURMOFs structures has been reported recently^{[274][275]}. Screening and/or removal of positive charges could then lead to hole doping as observed for ethanol. At this point, a complete microscopic model cannot be provided that explains all observations, including the different behavior of the alcohols. It can be anticipated that in-situ/in-operando FTIR spectroscopy, targeted towards molecular species and processes at the interface, shall provide the necessary information to fill the voids. However, this has unfortunately not been possible during this work and remains to be explored in a future study.

5.5 Summary

In summary, a novel sensing principle by interfacing a MOF film with a graphene transistor is demonstrated. Given the countless variations of MOF films and the possibilities to chemically engineer the interface between MOF and GFET, the emergence of a whole new class of MOF/GFET sensors with tailored selectivity and sensitivity can be envisioned.

6 NCG for Sensing Applications

Graphene has been extensively studied after its discovery in 2004 but suffered due to a lack of techniques for large-area synthesis and integration with current technology. On the other hand, NCG, another form of graphene is easy to synthesize on a large area independent of substrates and with low roughness (root mean square (RMS) below 1 nm)^[99]. With nanometer crystallite size, good thermal and electrical properties, and high density of defects in form of GBs^{[2][276]}, it has been utilized in different applications (chapter 2). NCG can be classified based on the number of layers as nanocrystalline graphene (1 layer), nanocrystalline multilayer graphene (2-10 layers), and nanocrystalline graphite (more than 10 layers)^[277].

This chapter starts with the synthesis techniques of NCG explored at low temperatures (600°C). Next, the NCG thin-film transfer method used in this work is explained. Further in the chapter, NCG film is characterized based on temperature and strain. Characterization is further done by Raman spectroscopy measured under strain. Finally, an application in the form of a moisture sensor utilizing an NCG-FET is exhibited.

6.1 Low-temperature NCG synthesis

There have been several reports to synthesize NCG and described in chapter 2. Techniques such as molecular beam epitaxy, radio frequency magnetron sputtering, pulsed laser deposition, CVD, and high temperature (1000°C) pyrolysis of organic photoresist have been used^[98,111,134]. Raman spectroscopy is widely used for the characterization of such films to recognize fingerprints of C-C bond and crystallite size. G peak at 1600 cm⁻¹, D peak at 1350 cm⁻¹, and a broad 2D peak^[278] are the fingerprints of an NCG film.

In general, the synthesis of NCG is done at higher temperatures (800-1000°C). The synthesis and the characterization of NCG have been reported in detail by Riaz et al^[99]. Summarizing the method by Riaz et al., a carbon source (photoresist S1805 from Microresist) was diluted in propylene glycol methyl ether acetate (PGMEA) based on the required thickness. Next, the solution was spin-coated onto the substrate of choice which can withstand high temperatures. The spin-coated film was then loaded in a vacuum furnace and the temperature was ramped up to 1000°C at 10°C min⁻¹ heating rate. The substrate was annealed for 10 hrs and cooled down to room temperature to

obtain synthesized NCG film. However, flexible substrates are not suitable for high-temperature synthesis. Therefore, a low-temperature synthesis process is needed for synthesis on flexible substrates.

In this work, flexible glass was used as a flexible substrate. It was acquired from Schott, Germany. The technical data sheet reports glass transition temperature of 714°C and a safe operation till 600°C. Hence, a 600°C synthesis process was followed up. Higher temperature synthesis allows increased sp^2 hybridization of C-C bonds and a better electrical conductivity^[279]. One of the techniques to measure hybridization is using Raman spectroscopy. The comparison of the intensity ratio of the D peak and G peak of graphene films can give qualitative insight into the levels of hybridization in the film. Different low-temperature routes were studied to achieve a good quality NCG film that can be applied for synthesis on glass substrates.

PMMA depolymerizes, and long chains are broken which eventually evaporate when heated at 420°C in a vacuum^[280]. However, providing a metal capping layer allows the graphitization to occur. The advantage of using a metal as a capping layer is two-folds. First, the metals with melting points greater than graphitization temperature can remain in their pristine condition making it easier to remove. Secondly, the role of catalyst metals like copper has been studied for graphene synthesis at low temperatures^[281].

PMMA and S1805 were used as carbon sources for NCG synthesis. 5 substrates of 300nm SiO₂/Si were cut of dimensions 10 mm X 10 mm. Two of them were spin-coated with PMMA (5% in Anisole) at 5000 RPM and the three with S1805 (diluted to 1:21 in PGMEA) at 8000 RPM. PMMA coated samples were post-annealed at 150°C and the S1805 coated samples at 110°C. One of each substrate from the two groups was covered by a capping layer of copper (30 nm) and the one from each group with aluminum (30 nm) using MBE. One of the substrates with S1805 film was used as a reference sample. The samples with metal capping layers were loaded in the vacuum chamber at 10⁻⁶ mbar pressure and heated to 600°C at a 10°C min⁻¹ heating rate. The samples were allowed to heat at 600°C for 10 hours and then cooled down to room temperature. The sample without the metal capping layer (reference sample) was heated at 1000°C for 10 hours.

Raman spectra were recorded for all these samples and are plotted in figure 6.2a. The ratio of peak intensities of D and G mode is plotted in figure 6.2c. I_D/I_G was calculated by using integrated intensities of the D and G peaks. The values of all the ratios are in the range of 0.7-1.6. S1805 graphitization at 1000°C, which is the reference sample, has a ratio of 1.59. For 532 nm excitation wavelength, the ratio values for complete sp^2 hybridization should be in the range of 2-3 (figure 6.1a). Hence, it can be concluded that there is approximately 10% of sp^2 hybridization for the NCG synthesis at 1000°C.

Comparable amorphization exists for the condition Al_PMMA (ratio = 1.46). For all the other conditions the sp^3 hybridized carbon content was higher.

FWHM of D peak was used to calculate the crystallite sizes for different conditions by using the relation by Concado et al. as discussed in chapter 2^[148]. The crystallite sizes for S1805@1K°C (3.94 nm) and Al_PMMA (4.02 nm) are comparable (figure 6.2d). All the other synthesized films have smaller crystallite sizes. Lower I_D/I_G ratios and smaller crystallite sizes imply highly disordered graphene formed as in the case of Cu_S1805.

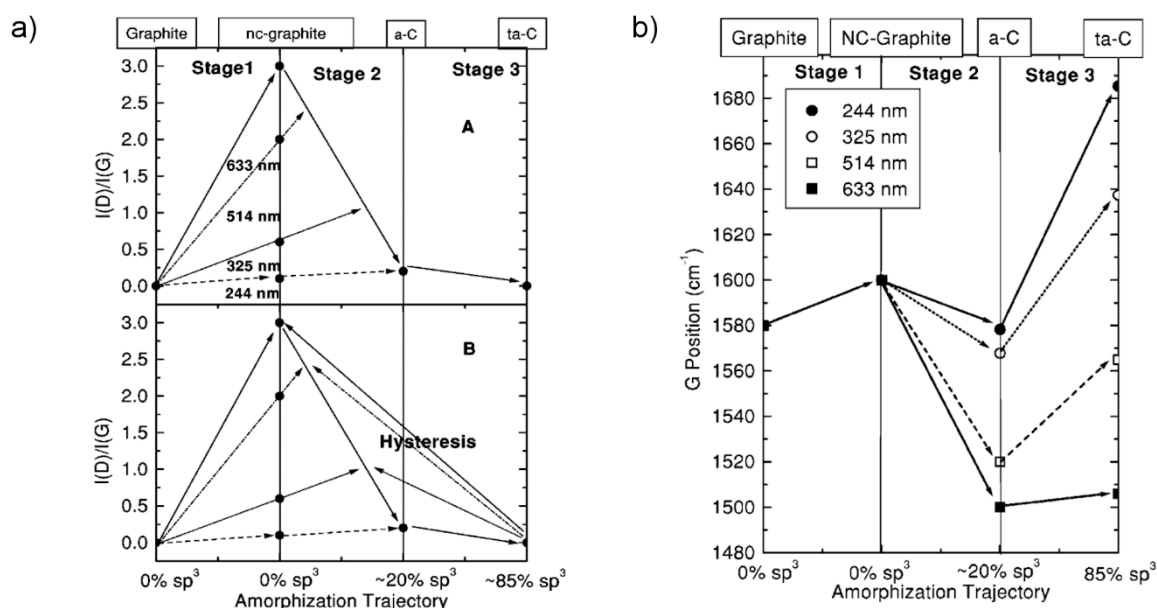


Figure 6.1: a) Amorphization trajectory based on the intensity of ratio D and G peak and b) G peak position for different excitation wavelengths. Adopted from ^[282].

G and D peak positions have been plotted for all the conditions in figure 6.2b. The peak positions can also be linked to the percentage of sp^3 amorphization present in the film. For NCG, the G peak is at 1600 cm^{-1} independent of excitation wavelength as described by Ferrari et al. in figure 6.1b. Similar to I_D/I_G ratio and crystallite size, the G-peak position also confirms that Cu_S1805 has the most sp^3 amorphization compared to other synthesis conditions. S1805@1k°C has a peak position at 1599 cm^{-1} and sample Al_PMMA has a peak position at 1597 cm^{-1} and therefore the least sp^3 amorphization compared to other conditions. In summary, NCG synthesized using S1805@1k°C route had the least amorphization and crystal size of 3.94 nm. Nevertheless, synthesis route in preparation of sample Al_PMMA demonstrates a promising synthesis technique at a lower temperature (600°C) with a comparable crystallite size (4.02 nm). This technique could be beneficial to grow NCG on substrates that cannot withstand higher

temperatures. However, the GBs density still remains high. Nevertheless, such a high defect density can be useful in some contexts like gas sensing and piezoresistivity^{[23][24]}.

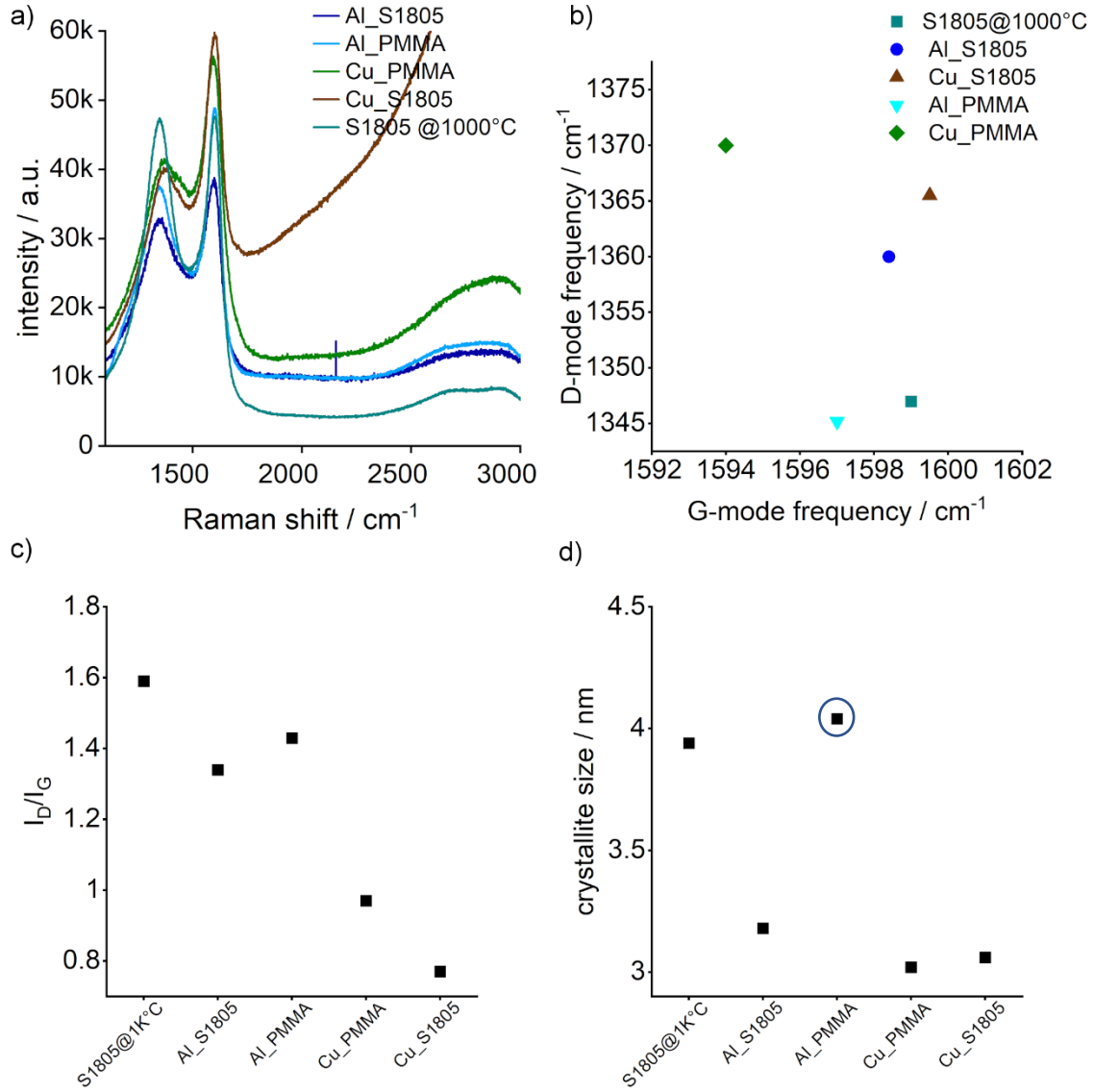


Figure 6.2: Comparison of a) Raman spectra b) D and G modes c) I_D/I_G and d) crystallite size L_a of the NCG samples fabricated under different conditions. The crystallite sizes have been calculated using Concado's relation utilizing the FWHM of D peak^[148]. All the measurements were done using a 532nm laser with 100x objective (NA= 0.85) at 0.3 mW laser power.

6.2 Patterning and graphitization of PMMA

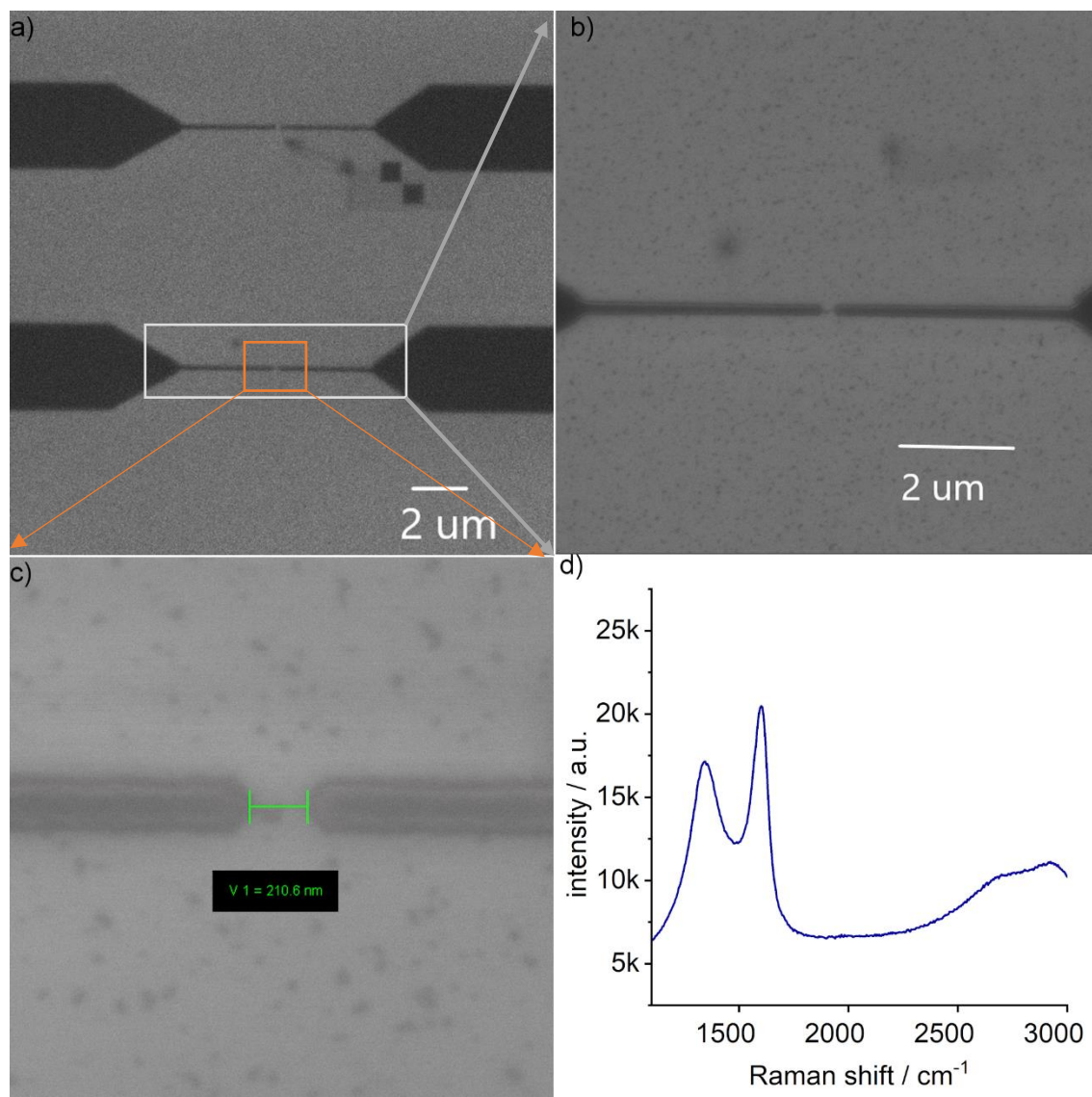


Figure 6.3: a-c) Scanning electron micrographs of the patterned structure before graphitization at different magnifications. Structures as small as few hundred nanometers were achieved based on the required application d) Raman spectra of the graphitized film using 532 nm laser at 0.06 mW power with an integration time of 10 s.

PMMA is an electron-beam resist that is widely used for patterning and fabrication of nanoscale structures. It is chemical resistant and UV stable. Therefore, it can find its use in many applications like a protective coating, shatterproof windows, etc. In this work, an attempt has been made to first pattern and then synthesize NCG using PMMA as a carbon source. Duan et al. demonstrated the process to convert PMMA nanofibers into

graphene nanoribbons by in-situ e-beam electron radiation^[283]. A similar technique has been used here to fabricate an NCG pattern with a potential application of electrodes for carbon nanotube transistors.

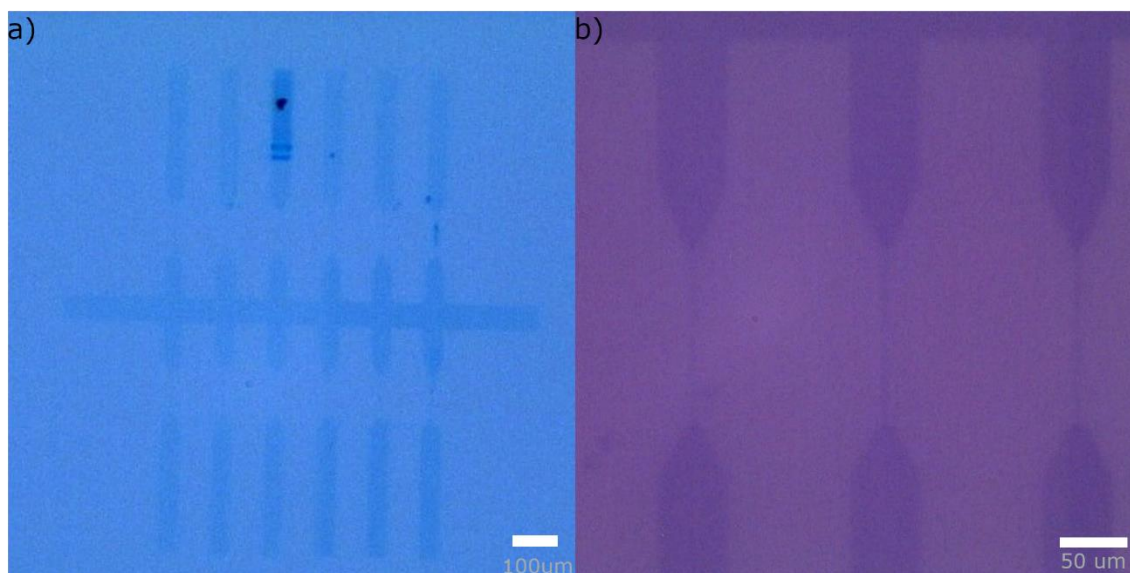


Figure 6.4: Optical micrograph of NCG film synthesized by cross-linking PMMA at a) 20x and b) at 50x magnifications.

PMMA A4.5 was spin-coated at 5000 RPM and post-annealed at 150°C on 300 nm SiO₂/Si substrates. Next, the structure was patterned and exposed with a high dose of 8260 $\mu\text{C cm}^{-2}$. Due to the high dose, PMMA was cross-linked, and contrary to its behavior, does not dissolve in acetone or MIBK/IPA solution as shown in SEM images in figure 6.3a-c. The remaining PMMA was dissolved in acetone and the patterned structure was heated at 800°C for 2 hrs in 10⁻⁶ mbar pressure to allow graphitization. Figure 6.3d shows the Raman spectra of heated film and confirms the synthesis of NCG.

Figure 6.4a, b shows the optical micrographs of the graphitized pattern on 300 nm SiO₂/Si substrate. Structures as small as 200 nm were successfully patterned which can be used to replace metal electrodes in CNT devices. This technique of device patterning and NCG synthesis can reduce several steps of electron beam writing and etching steps and make overall device fabrication easy. The quality of the synthesized film was not studied electrically and would be the vital next step to realize this technique. From Raman measurements, the crystallite size was calculated in the range of 3-5 nm which is similar to the synthesized NCG with the technique mentioned in the previous section. One of the demerits of this process is overexposure due to the proximity effect in e-beam lithography^[284], which leads to comparatively larger dimensions. Therefore, proximity correction of the large doses is needed to achieve precise results.

6.3 Transfer process

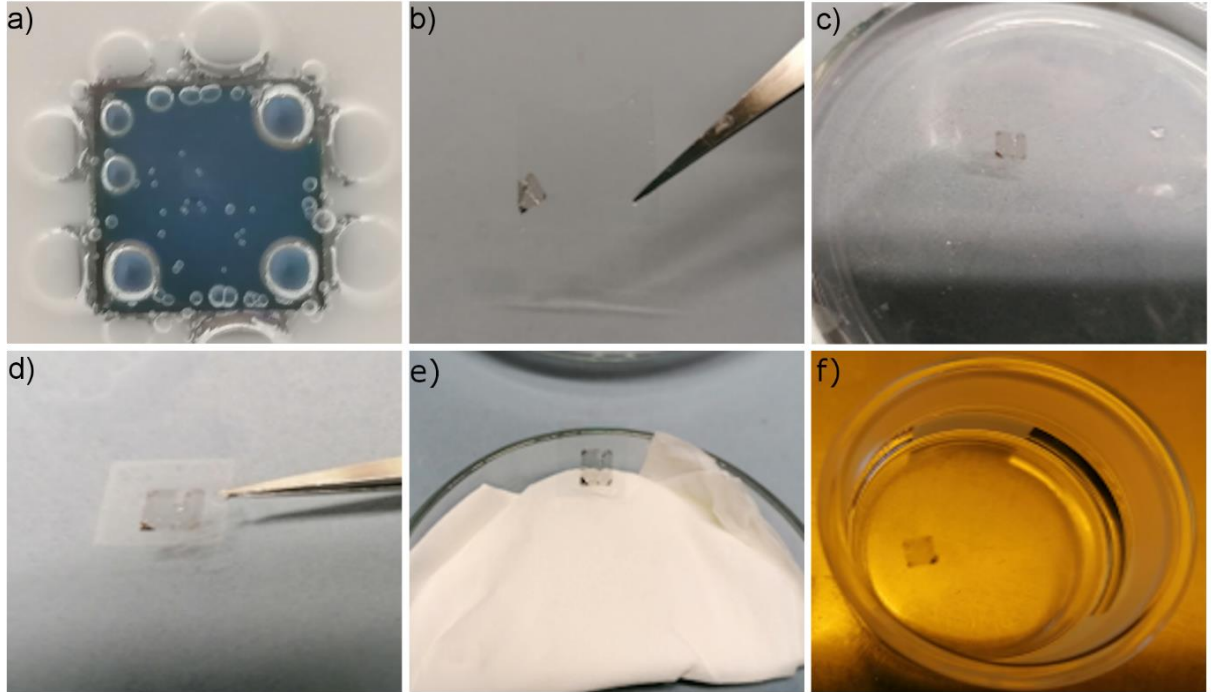


Figure 6.5: a) PMMA coated NCG/SiO₂ sample in 5M solution of NaOH/H₂O b) PMMA/NCG film picked up using a transfer glass slide c) PMMA/NCG film in distilled water d) PMMA/NCG transferred on desired substrate e) drying in air f) PMMA lift-off in acetone.

Transferring 2D films onto the desired substrate without losing its properties is essential. Hence, an adequate process with immense control is significant. For graphene synthesis, metal substrates like copper is chosen by the research community^{[285][286]}. However, application-dependent substrates are desired and a transfer process is inevitable to further investigate the synthesized film^[287]. Few of the commonly observed defects appearing during transfer processes are cracks, wrinkles, and chemical or polymer residues used during the transfer process. Few ways these defects can originate are^{[288][289]}

- Sacrificial substrate
- Etchant to dissolve the substrate
- Polymer transfer layer (for example PMMA)

The impurities generated are detrimental as they can dope graphene and create charge scattering sites^[290]. As the film thickness is few nm, cracks can easily form and propagate due to applied mechanical stress during transfer and cleaning processes. To counter

these transfer issues, numerous good processes have been developed and reported in recent years. They can be categorized in following categories:

- a) **Wet transfer:** In the wet transfer process, the film remains in a liquid until the final transfer step. The grown film on a substrate is coated with a transfer layer. The growth substrate is then dissolved in an etching solution and the film (with transfer layer) is cleaned in an aqueous solution. The final step of transfer is performed in the cleaning solution. PMMA supported transfer of graphene grown on copper is the most extensively used transfer technique due to its straightforward approach and ease of chemical availability. But to prevent p-doping from PMMA, different transfer layers like naphthalene^[291] and camphor^[292] have been used because of their easy removal by sublimation with minimal residues. Gold as a transfer layer has also been used to prevent contamination from the organic polymers and demonstrated better quality graphene film compared to PMMA assisted transferred film^[293]. Paraffin as a support layer for transfer provides two-fold benefits. First, there are no covalent interactions with graphene. Second, paraffin expands at very low temperatures (~40°C). This helps in avoiding wrinkles if the transfer is made in water which is at a slightly higher temperature. As paraffin expands, graphene is stretched, and wrinkles are flattened before transferring onto the substrate^[290]. Removal of paraffin is easy because there are no chemical interactions with graphene.
- b) **Dry transfer:** This technique has an immense advantage over the wet transfer technique in terms of the level of contamination and defects induced in graphene. A lifting layer with low binding energy is used so it can be washed away using water. Molybdenum oxide is one of the examples of such a lifting layer and gives high-quality graphene film transfer^[294]. Delamination of graphene from the copper substrate can also be achieved by a thermal release tape (TRT). Graphene on copper is allowed to sit in the water near the boiling point (90-95°C). This step forms a copper oxide between copper and graphene and allows easy delamination using TRT and with no effect on graphene^[295].
- c) **Support free transfer:** The first two methods are conventional methods to transfer graphene onto the target substrate and require support. However, the defects are inevitable in both of them. Thus, a process where the support layer can be avoided would be ideal. It reduces the number of steps involved and the cost incurred. One of the examples is by using an electrostatic generator, where the target substrate is charged and then used to pick copper/graphene. Copper is then etched away^[296]. In another attempt, graphene is hot-pressed onto the target substrate to achieve a high-quality film^[297].

In this work, PMMA assisted wet transfer process was used to transfer NCG thin films onto different substrates. AFM images were then recorded to examine the quality of transferred NCG film on the target substrate.

NCG was grown on $10 \times 10 \text{ mm}^2$, 300nm SiO_2/Si substrate (as discussed previously) using 1:4 diluted solution. The NCG-grown substrate was then spin-coated using A4.5 PMMA at 5000RPM and post-baked at 150°C for 3 minutes. Simultaneously, a 5M solution of NaOH in water was prepared and kept on a hot plate at 80°C . The PMMA coated substrate was then put in the NaOH solution for SiO_2 etching as shown in figure 6.5a. After the SiO_2 etching, PMMA/NCG film floats on the top of the liquid. A clean transfer glass was used to pick up the floating film (figure 6.5b) and put it into distilled water (figure 6.5c) for 1 hour to dissolve the NaOH impurities. Water trapped between the transfer glass and the PMMA/NCG film prevents any damage to the NCG film. This process is repeated 3 times to remove any NaOH residues on the bottom part of NCG. Finally, the target substrate is used to fish the floating film (figure 6.5d) and allowed to dry (figure 6.5e) for 3 hours. On the dried PMMA/NCG film sitting on the target substrate, $10 \mu\text{l}$ PMMA is gently drop cast and left in air for drying. This step drastically reduces the number of wrinkles and gives comparatively better films^[298]. Finally, the substrate is put into acetone to remove PMMA (figure 6.5f).

PMMA is not a good polymer for its use in transfer processes as discussed earlier. If used, a strong solvent like acetic acid should be utilized to completely remove the residues of PMMA^[299]. Therefore, to avoid PMMA, a paraffin-assisted transfer was explored as well. But, due to the requirement of higher temperature for SiO_2 etching and low melting point of paraffin, the process could not be completed till the final transfer step. One important observation to be mentioned is that 300 nm SiO_2/Si substrates with NCG films synthesized at 1000°C , when etched, did not give continuous NCG films. However, NCG films synthesized at 800°C had a good quality and continuous film after etching. Note that it is just an observation based on numerous etching and transfer attempts made in our laboratory. The reason for this is not clear. Therefore, for transferring films, 800°C synthesis temperature was used.

AFM images were recorded for the films transferred on different substrates. An area of $50 \mu\text{m} \times 50 \mu\text{m}$ was measured to analyze the quality of films transferred over a larger area. Figure 6.6a shows AFM of an NCG film transferred on glass using conventional PMMA supported transfer. The film consisted large density of wrinkles. Drop casting $10 \mu\text{l}$ of PMMA and allowing it to dry flattens the wrinkles as shown in figure 6.6b. Similar observations were observed for film transfer done on a PET substrate. Figure 6.6d shows a large number of particles due to the poor quality of PET substrate used. The substrate itself had many scratches and non-removable particles stuck on the surface. A good

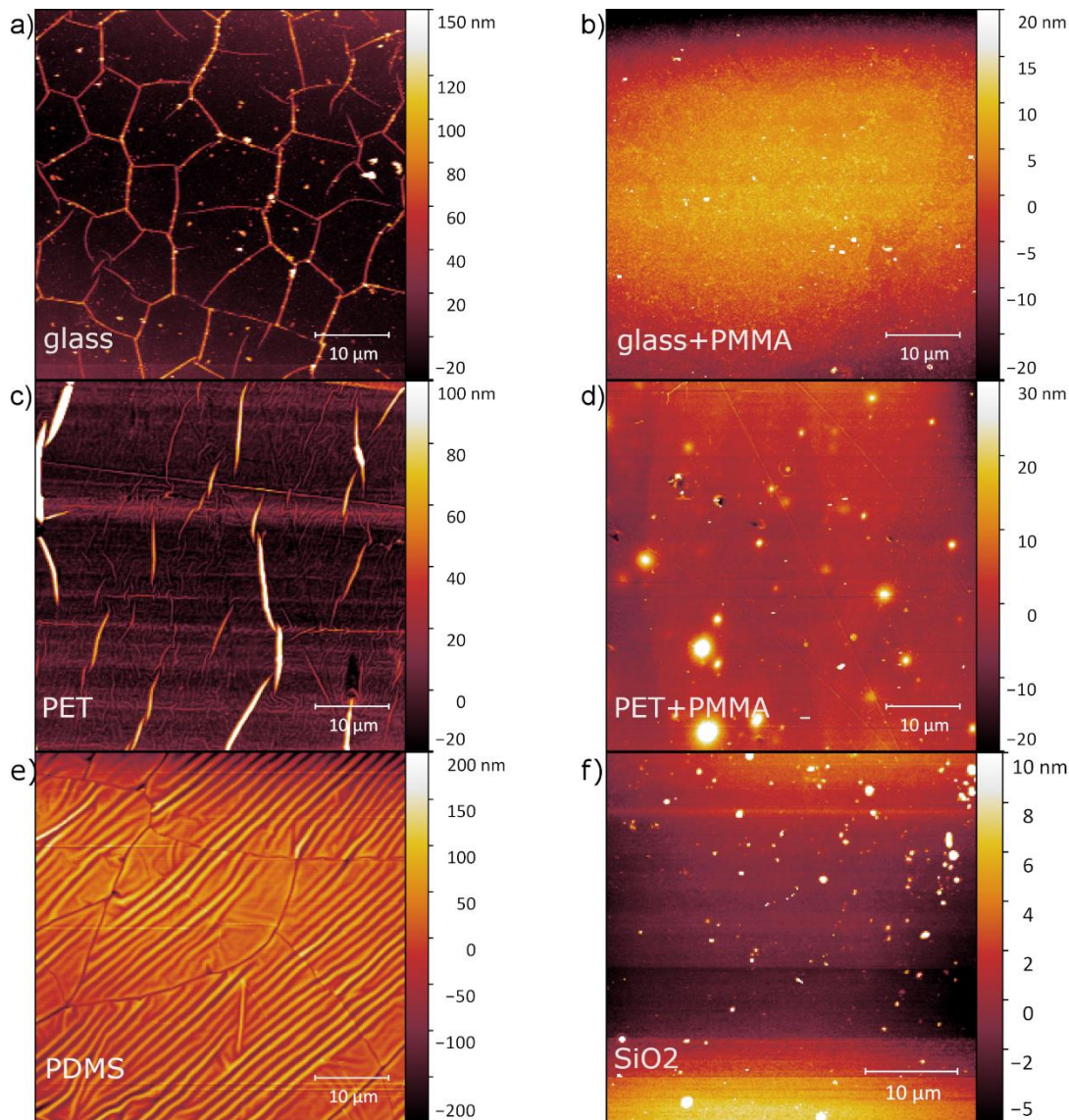


Figure 6.6: AFM images of a) NCG film transferred on glass without drop-casting PMMA on a glass substrate b) with drop-casting PMMA drop on a glass substrate c) without drop-casting PMMA on a PET substrate d) with drop-casting PMMA on a PET substrate e) without drop-casting on a PDMS substrate f) with drop-casting on Si/SiO₂ substrate. All the images have been measured after the removal of the drop cast PMMA layer.

quality NCG film for transfer on glass (figure 6.6b) with few particles and wrinkles was confirmed by the AFM image. PDMS is not a good substrate for transferring a thin film onto it. The film contained a high density of wrinkles as shown in figure 6.6e. Figure 6.6f shows NCG film on Si/SiO₂ surface. PMMA residues are visible on the surface and can be removed with a heating step of 400°C. Wrinkles on Si/SiO₂ are also minimal. Therefore, it can be concluded that wrinkles are reliably eliminated using a top PMMA drop cast layer after the transfer step on the target substrate. However, PMMA residues are still

present when dissolved in acetone, and using different sacrificial polymer support or a strong solvent for PMMA could be beneficial to eradicate the issue. All the images reported in figure 6.6 have been recorded after removal of the drop cast PMMA layer.

6.4 Dependence of sheet resistance of NCG on temperature

Sheet resistance (R_s) is a measure to express resistance for thin (sheet) films used out of convenience. It depends on the resistivity (ρ) and thickness (t) of the material. It has the unit of $\Omega \text{ sq}^{-1}$. It can be altered by changing external environments like temperature^[300] and strain^[24].

Mathematically, the sheet resistance is given by

$$R_s = \frac{\rho}{t} \quad (6.1)$$

There are several techniques to measure sheet resistance like the two-point, four-point, and Van der Pauw methods. These have been discussed in chapter 3. For the measurement of sheet resistance, in this case, the four-point or Kelvin method was used. The advantage of using the four-point method is, it directly measures the sheet resistance and is independent of contact resistances. Four contacts were made numbered 1-4 on the patterned structure as shown in figure 6.7a. The measurement scheme was made such that a constant current is applied across contacts 1 and 3 (main lines) and the voltage drop was measured across points 2 and 4 (sense lines). Resistance and hence, the resistivity of the device under test (DUT) of area 1 mm x 1 mm was calculated using the values of voltage drop and current applied using equation 6.1.

NCG for the device was synthesized by spin coating S1805 with a dilution of 1:4 in PGMEA on 300 nm SiO_2/Si substrates. The sample was then heated to 1000°C for 10 hrs and then cooled down to room temperature. The thickness of the film was measured as 5 nm. Next, the structure (figure 6.7a) was patterned on the synthesized NCG. For patterning, NCG film was spin-coated with PMMA A4.5 at 5000 RPM and post-annealed at 150°C. The structure was written using e-beam and developed (MIBK: IPA in the ratio 1:3 for 30 s) and etched in RIE using oxygen plasma. The patterned substrate was wire bonded onto a substrate holder and loaded in the cryostat and pumped to 10^{-6} mbar (refer Gaulke et al. for cryogenic setup details^[99]). Liquid nitrogen was used to reach the temperature of 77 K and the temperature was controlled by the integrated heater. The starting temperature was 77 K. Measurements were done by sweeping current values from 100 nA to 200 nA with a step size of 1 nA. Lower values of current were used to

avoid any heating due to power dissipation in the channel which can heat the material and alter the actual temperature.

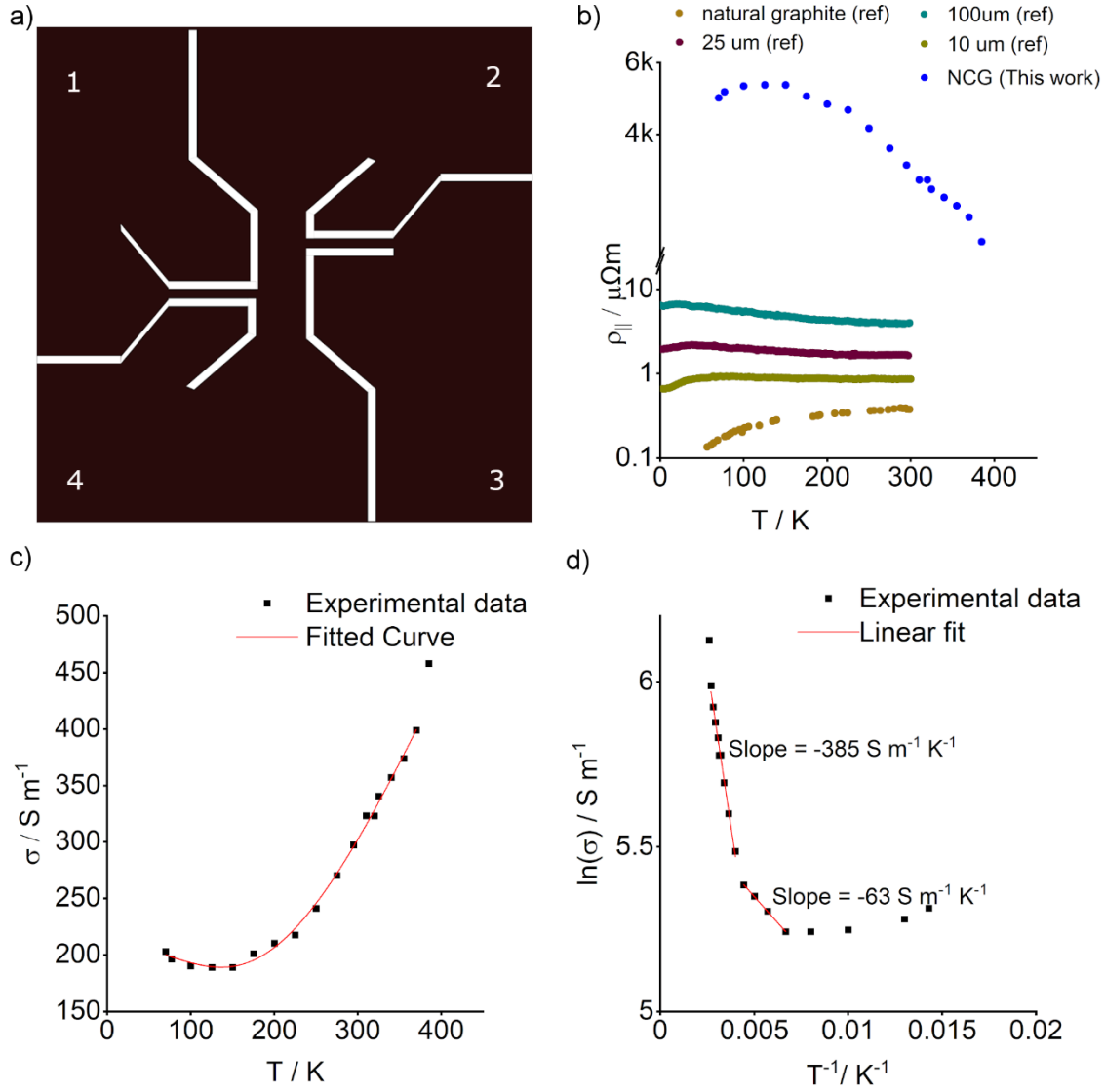


Figure 6.7: a) Schematic of structure used for the four-probe study of sheet resistance dependence on temperature. The white area indicates the etched area (no NCG) and the black area indicates NCG. b) Dependence of in-plane resistivity on the temperature of an NCG film grown at 1000°C in comparison with data from ref^[190]. c) Fitting of experimental data based on the model of variable range hopping (VRH). d) two different slopes for temperature indicating two activation energies of the processes involved.

The measurement shows the inverse dependence of sheet resistance of NCG on temperature. Similar results have been observed for thin pyrolytic graphite films, where the resistance first increases and then decreases with an increase in temperature.

Metallic behavior dominates at lower temperature and variable range hopping (VRH) at higher temperatures^[301].

In figure 6.7b, in-plane resistivity of the measured sample with reference to data from a study done by Nakamura et al.^[301] is plotted. Their study focuses on the dependence of resistivity of pyrolytic graphite sheets on temperature. Two resistivities, in-plane ($\rho_{||}$) and out of plane (ρ_{\perp}) were defined. Nakamura et al. inferred that with increasing thickness of graphite sheets, the in-plane resistivity increases. Also, for each thickness, the in-plane resistivity first increases with the temperature and reaches a peak. Further increase in temperature leads to a decrease in resistivity. Similar observations were recorded in the case of NCG in this work. The thickness of the film is 5 nm and the measured resistivity is in-plane resistivity. The peak lies at ~130 K. Two different regions in resistivity vs temperature plots indicate two different mechanisms. The first mechanism is similar to a metallic resistance which is dominated at lower temperatures. At higher temperatures VRH mechanism becomes dominant. The model is given for temperature below 150 K as^[301]:

$$\sigma = \frac{1}{\rho_0 + AT} + \sigma_0^h \exp\left(-\frac{T_0}{T}\right)^\alpha \quad (6.2)$$

In equation 6.2, the first term corresponds to the metallic mechanism and the second term corresponds to the VRH mechanism. This model agrees with the NCG data and fits as shown in figure 6.7c up to 400 K. For the fitting, $\alpha = 1$ was used which corresponds to simple Arrhenius type conduction. All the other variables were kept as fitting parameters. To look closely at the activation energies in the VRH mechanism, $\ln(\sigma)$ was plotted against T^{-1} as shown in figure 6.7d. Two linear regimes were found with different activation energies E_a , and therefore, two different VRH processes. Utilizing the slope of the linear fit lines, at lower temperature close to conductance dip, E_a was calculated as ~5 meV. With the increase in temperature, E_a increases and was calculated as ~33 meV. Conductivity in NCG can be understood by the resistance model shown in figure 6.8. There are two VRH mechanisms (VRH₁ and VRH₂) and one metallic process controlling the conductive pathway in NCG. All three mechanisms are in parallel connection. At a lower temperature ($T < 130$ K), VRH₁ and VRH₂ channels are highly resistive and therefore conductance in the material follows metallic behavior. With a further increase in temperature, VRH mechanisms start activating. However, the metallic channels become highly resistive and contribute negligibly to conductance at higher temperatures. For temperatures $225 \text{ K} > T > 130 \text{ K}$, VRH₁ channels resistance decreases and is the main contributor towards conductance. Hence, more current flows through VRH₁ channels. Nevertheless, a second process (VRH₂) starts contributing for $T > 225 \text{ K}$.

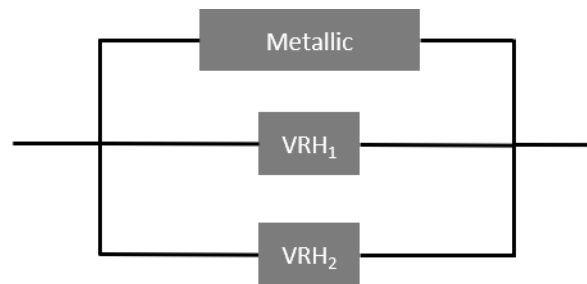


Figure 6.8: Conduction model in NCG

Table 6.1: Temperature-dependent behavior of conduction model in NCG

Temperature	Resistance of VRH ₁ ($E_a = 5$ meV)	Resistance of VRH ₂ ($E_a = 33$ meV)	Resistance of Metallic channel	Mode of conductance
$T < 130$ K	High	High	Low	Metallic
225 K $> T > 130$ K	Low	High	High	VRH ₁
$T > 225$ K	Low (Saturated)	Low	High	VRH ₁ + VRH ₂ (VRH ₁ < VRH ₂)

To see contributions from the VRH₂ process, two conditions should be fulfilled. First, VRH₁ remains low resistive, but the conductance does not increase further with increase in temperature and saturates (completely open). Second, more channels in the material follow the VRH₂ mechanism compared to VRH₁, and are activated at this higher temperature. Therefore, a dominant contribution to conductance is observed for VRH₂. With a further increase in temperature, VRH₂ becomes less resistive, and the overall conductance of the material increases. Table 6.1 summarizes the conduction model behavior at different temperature ranges.

6.5 Strain dependent measurements

Figure 6.9 shows the circuit diagram of the Piezoresistance measurement setup which was built in-house. The two stepper motors are attached at the two ends of the flexible substrate.

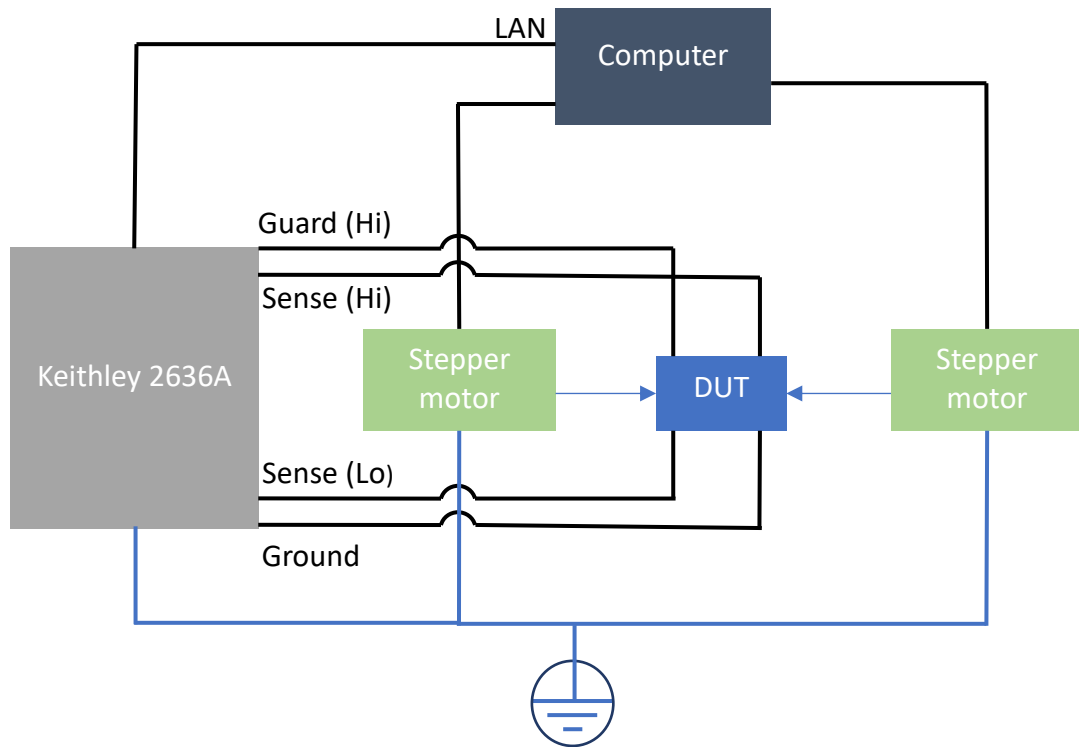


Figure 6.9: Circuit diagram of Piezoresistance measurement setup.

The connections are made from the DUT to Keithley SMUs using BNC cables. Keithley and the stepper motors are controlled by a python code using a computer. The building of bending setup is explained in detail in chapter 3.

In this section device design and fabrication, and the measured results are discussed. Schematics of different structures are explained later with the measurements. The applied strain on the film based on the movement of the stepper motor can be calculated as described in the next section.

6.5.1 Strain calculation

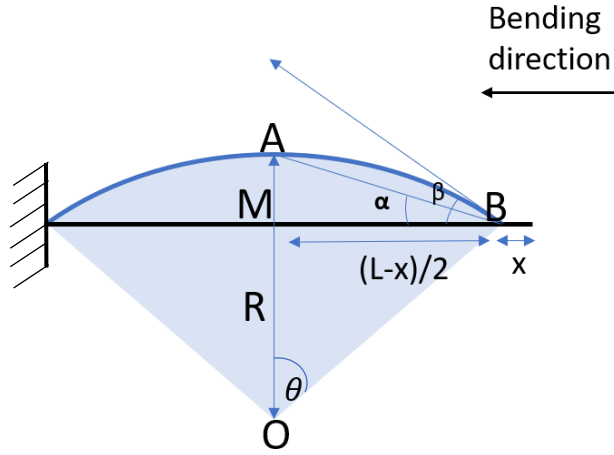


Figure 6.10: Initial (black) and final (blue) curvature of the substrate when the stepper motor moves a distance x .

L and D are the length and thickness of the substrate respectively.

x corresponds to the distance moved by the stepper motor to impart strain to the film on top of the substrate. The value of x is the only known quantity, hence strain has to be calculated based on x . It is assumed that the thickness of the film $t \ll D$.

From figure 6.10, for a circular arc AB with center at O

$$\theta = L/2R \quad (6.3)$$

In $\triangle MBO$,

$$R \sin \theta = \frac{L-x}{2} \quad (6.4)$$

Binomially expanding $\sin \theta$:

$$\sin \theta = \theta - \frac{\theta^3}{3!} + \frac{\theta^5}{5!} - \dots \quad (6.5)$$

Combining equations 6.3, 6.4 and 6.5 gives,

$$2R \left[\frac{\left(\frac{L}{2R}\right)^3}{3!} - \frac{\left(\frac{L}{2R}\right)^5}{5!} + \frac{\left(\frac{L}{2R}\right)^7}{7!} \right] = x \quad (6.6)$$

The equation 6.6 is solved recursively using a MATLAB code which converges at a solution for R at each value of x .

Finally, strain is calculated using

$$\varepsilon = \frac{D}{2R} \quad (6.7)$$

6.5.2 Piezoresistance in NCG

Piezoresistance is a property of materials wherein the electrical resistance of the material changes due to an externally applied mechanical stress. William Thomson (Lord Kelvin) was the first to report on change in resistance with strain in iron and copper in the year 1856. This material property has many applications like strain sensors, pressure sensors, etc. Graphene has already been used in such applications^[302,303]. For flexible displays, graphene has an advantage due to its transparency and minimal piezoresistance effect^[304]. However, the piezoresistance effect in graphene is small. The reason for such a diminished piezoresistance effect in graphene is that the displacement of the Dirac cone occurs in continuous k-space and there are no changes in band structure due to strain-induced lattice distortions up to 20% strain^[305]. On the contrary, the band gap in carbon nanotubes can be controlled by uniaxial strain due to displacement of Dirac point in quantized k-space^[306].

There are few reports to understand piezoresistance in graphene and it was concluded that grain boundaries could enhance this effect. The symmetric grain boundaries remain metallic whereas the asymmetric grain boundaries bandgap can be altered by providing an external strain^[307].

NCG intrinsically has a high density of grain boundaries and therefore, might have an enhanced piezoresistance effect. Zhao et al. have shown a tunable strain sensor based on nanographene by tailoring crystallite sizes^[24]. Preliminary work done in our lab in this direction was reported by Riaz et al^[99]. Higher GFs in comparison to graphene was demonstrated for NCG at lower strain values. However, the strain sensor was fabricated on rigid substrates, and therefore, higher strain values could not be achieved. In this work, piezoresistivity in NCG was studied on a flexible substrate to allow measurements at higher strain values. Therefore, Ultra-thin glass (AF 32 eco) from Schott as a flexible substrate was chosen due to certain merits. First, as reported in Schott datasheet, it can withstand higher temperatures for synthesis ($T_g=740^\circ\text{C}$). Second, small thicknesses (~ 50 μm) allow the glass to be highly flexible with a minimum radius of curvature up to 2 mm.

Third, the glass is transparent in the visible and IR region, suitable to study for transparent strain sensors.

The fabrication of the structure started with the growth of NCG by spin-coating the glass substrate by 1:4 diluted S1805 and heating the substrate. The heating temperature was kept at 600°C, below the glass transition temperature of the glass. NCG was successfully grown at 600°C on the glass, which was confirmed by Raman spectroscopy. But, the flexibility of the glass was completely impaired. The details have been discussed in the next section and a solution to this problem has been explored. Also, the wet transfer technique could not be used to transfer NCG film on ultra-thin glass substrate due to corrosion of glass substrate by water^[308].

Owing to the problems with the flexible glass, NCG film was then grown at 800°C on 300 nm SiO₂/Si and transferred on a flexible polymer substrate PET. Transfer steps are already discussed in the previous section. After the successful transfer of the film, the four-probe structure was patterned for sheet resistance measurements. The structure was patterned such that NCG itself provided a large area for contact (figure 6.11). Unfortunately, soldering was not possible as the solder does not stick on the NCG surface. Therefore, an alternative was required to make copper wire contacts on NCG. To solve this issue, a thermally curable silver epoxy (Elecolit 3653, Panacol) was used to make four contacts on the substrate. The epoxy has conductive silver particles and is liquid at room temperature. The epoxy solidifies at higher temperature (5 min at 150°C) and provides robust contacts for bending experiments. The other ends of copper wires were soldered to BNC connectors. BNC connectors were then connected to the Keithley 2636A SMUs as shown in the wire diagram (figure 6.11).

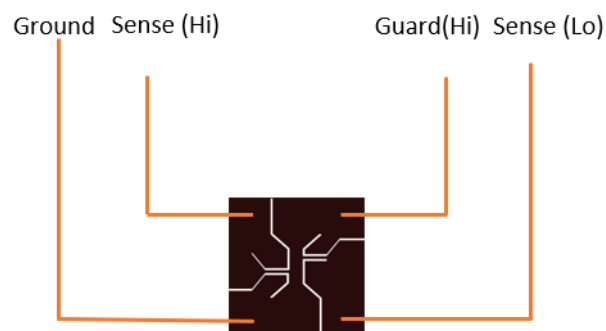


Figure 6.11: Wire diagram of the connections made from the substrate to Keithley 2636A for four-probe sheet resistance measurements.

A Keithley 2636A has two channels (A and B) allowing different configurations for measurements. Here, four terminals of one channel were used for four-probe

measurement. Guard (Hi) and the ground were connected at the ends of the device (DUT) where a constant current is maintained while measuring sheet resistance. Sense (Hi and Lo) lines were used to measure the voltage drop across the other two connected terminals. Thin NCG lines were used to connect the voltage drop points to ensure that the potential measured is not of an extended area. Four-wire mode (or sense mode) was selected from the settings in Keithley to perform four-point measurements. Here, that was automated using a python code. The movement of stepper motors was also controlled simultaneously using the code. The measurement scheme was such that for each movement of the stepper motor, the potential drop across the DUT was measured, whilst maintaining a constant current through DUT. The value of current was chosen to be few nanoamps to avoid any heating due to power loss and change in temperature which can correspondingly change resistance.

Figure 6.12a shows the normalized change in resistance vs strain plot for NCG film patterned on PET substrate. The strain is varied to 2% and swept forward and backward. Therefore, it was confirmed that NCG is piezoresistive. As already discussed previously, resistance in NCG films is contributed by two resistances: grain resistance, and GB resistance. For the films grown in this study with 2-5 nm domain size, the resistance from GBs is a dominant contributor. Zhao et al. attributed the piezoresistive effect in NCG to change in GB resistance^[24]. They inferred that charge carriers have to tunnel through grain boundaries to display conductance in NCG. Therefore, as the strain is increased, the tunneling distance between the two domains increases. This is similar to grains (conductor) and grain boundaries (polymer) in NCG.

In NCG used in this work, it was observed that GF changes from 24 to 52 at around 0.35% strain (figure 6.12a). Till 0.35%, increase in GF indicates that the tunneling distance increased (see Raman measurements in next section). Consequently, the change of resistance of the film with strain increased. Around 0.7% strain, GF drops to 39 indicating that the rate of change in resistance decreased. GF then drops further till 1.5% strain and again an increase of GF to 40 and then to 230 is observed. The complete behavior can be explained by the tunneling and tunneling + destruction model. Till 0.35% strain, the tunneling model is applicable where resistance is dependent mainly on tunneling distance.

The derivation of the tunneling and tunneling + destruction model has been discussed in Chapter 2^[127]. To understand the results, it is included here briefly. Resistance in the material can be expressed by Simmons function^[109] based on tunneling distance s as^[24]:

$$R = \frac{V}{a^2 J} = \frac{8\pi h s}{3a^2 \gamma e^2} \exp(\gamma s) \quad (6.8)$$

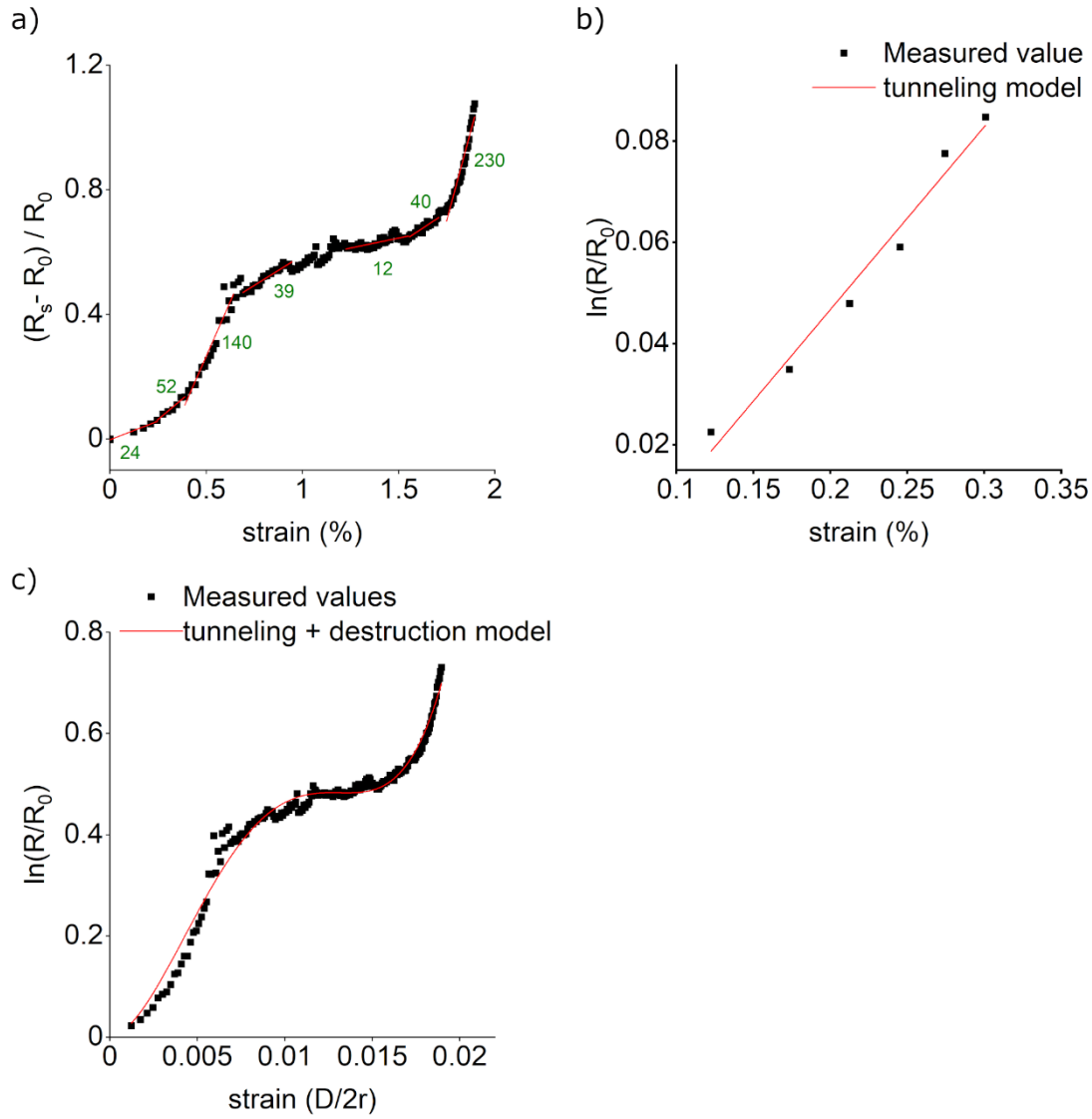


Figure 6.12: a) Dependence of normalized change in resistance with strain. Different regions with different GFs have been identified. b) $\ln(R/R_0)$ vs strain curve fitted with tunneling model (red curve) c) tunneling + destruction model (red curve)

For smaller strain values $< 0.35\%$, the tunneling model is applicable and follows the relationship between change in resistance and strain as

$$\ln \frac{R}{R_0} = \ln(1 + \varepsilon) + \gamma s_0 \varepsilon \quad (6.9)$$

The equation was used to linearly fit the measured experimental data as shown in figure 6.12b and the value of $\gamma s_0 = 36.14$ was extracted from the slope of the fitted line. Using empirical value of $A = 10 \text{ nm}^{-1[131]}$, initial tunneling distance $s_0 = 3.6 \text{ nm}$ was calculated.

Zhao et al. (3.4 nm) for nanographene films^[126] reported comparable results of initial tunneling distance.

Further increase in strain ($> 0.35\%$) causes the exponential decrease in the number of conductive paths, N , according to the following equation

$$N = N_0 \exp[-(\alpha\varepsilon + \beta\varepsilon^2 + \gamma\varepsilon^3 + \lambda\varepsilon^4)] \quad (6.10)$$

And the change in resistance as a function of strain can be rewritten as

$$\ln \frac{R}{R_0} = \ln(1 + \varepsilon) + \alpha\varepsilon + \beta\varepsilon^2 + \gamma\varepsilon^3 + \lambda\varepsilon^4 \quad (6.11)$$

Using this equation, the complete measurement data up to $\sim 2\%$ strain was fitted as shown in figure 6.12c. The values of the fitting parameter are tabulated in table 6.2. The good fit with the model indicates that the mechanism of piezoresistance in NCG is indeed tunneling + destruction at higher values of strain.

Table 6.2: Fitting equation and parameters of tunneling + destruction model with errors used in figure 6.12.

Equation	$\ln(1+\varepsilon) + \alpha\varepsilon + \beta\varepsilon^2 + \gamma\varepsilon^3 + \delta\varepsilon^4$
α	5
β	$1.55\text{E}4 \pm 1.8\text{E}2$
γ	$-1.63\text{E}6 \pm 2.5\text{E}4$
δ	$4.6\text{E}7 \pm 8.6\text{E}5$

In the reverse sweep of strain, the same trend is not observed as in the forward sweep. This could be due to the mechanical delay of the substrate in recovering from applied strain. Mechanical delay implies that even after removal of externally applied strain, the substrate takes an extended time (or delay) to recover. Additionally, the initial value of resistance (at zero strain in a forward sweep) was not achieved when returned to zero strain in the reverse sweep, indicating a plastic deformation of the substrate and/or fracture of the NCG at GBs which increases the resistance permanently.

FTIR measurements accompanied with strain will be the next step to get more insights into such dependence of GF on strain. In-situ study of the optical and electrical property of NCG based on external strain can help identify correlations between piezoresistivity and structural properties in NCG. Measuring the transmission spectrum in FTIR

microscope, Fermi level movement in NCG can be followed with respect to strain and subsequently, the piezoresistivity origin can be understood.

In addition, it was inferred from Raman measurements under the strain that at lower strain values ($< 0.35\%$) there are no shifts in Raman D and G peaks. This supports the observation of piezoresistance measurement that the GBs move apart with strain and there is no stretching of C-C bonds within a domain (grains) in NCG. Therefore, an increase in the tunneling distance between two grains is the main contributor of piezoresistance in NCG for strain values less than 0.35% . Consequently, there is no distortion of the hexagonal lattice.

One point to note is that GF is dependent on initial tunneling distance s_0 (equation 2.36). Therefore, to fabricate a highly sensitive piezoresistor, s_0 should be maximized and not increase the initial resistance. At higher temperatures, there is a higher nucleation density of nanographene grains^[24] in the PECVD process of NCG growth. This reduces the grain size but the tunneling distance increases. By utilizing the property of controlling initial tunneling distance, Zhao et al. fabricated a sensitive tunable GF piezoresistor^[24].

6.5.3 Raman spectroscopy measured under strain

Raman spectroscopy is a non-destructive technique to gain useful information on carbon-nano systems. The peak position, intensity, and FWHM of G, D, and 2D bands are used to extract various information. It is used to determine the doping level in graphene, the stress in the film, the number of layers, disorders or defects in the film, and many more^{[309][140][310]}. Details of Raman spectroscopy have been discussed in chapter 3. This section focuses on studying Raman spectroscopy of NCG film measured under applied strain.

Due to issues with ultra-thin glass, NCG films were transferred on polymer substrates. However, the transferred film on polymer substrates had a very large background and no Raman signal from the film was resolved. Water and high temperature (600°C) were detrimental to flexible glass; therefore, another approach was needed to grow NCG film and keeping the flexibility of the glass unimpaired.

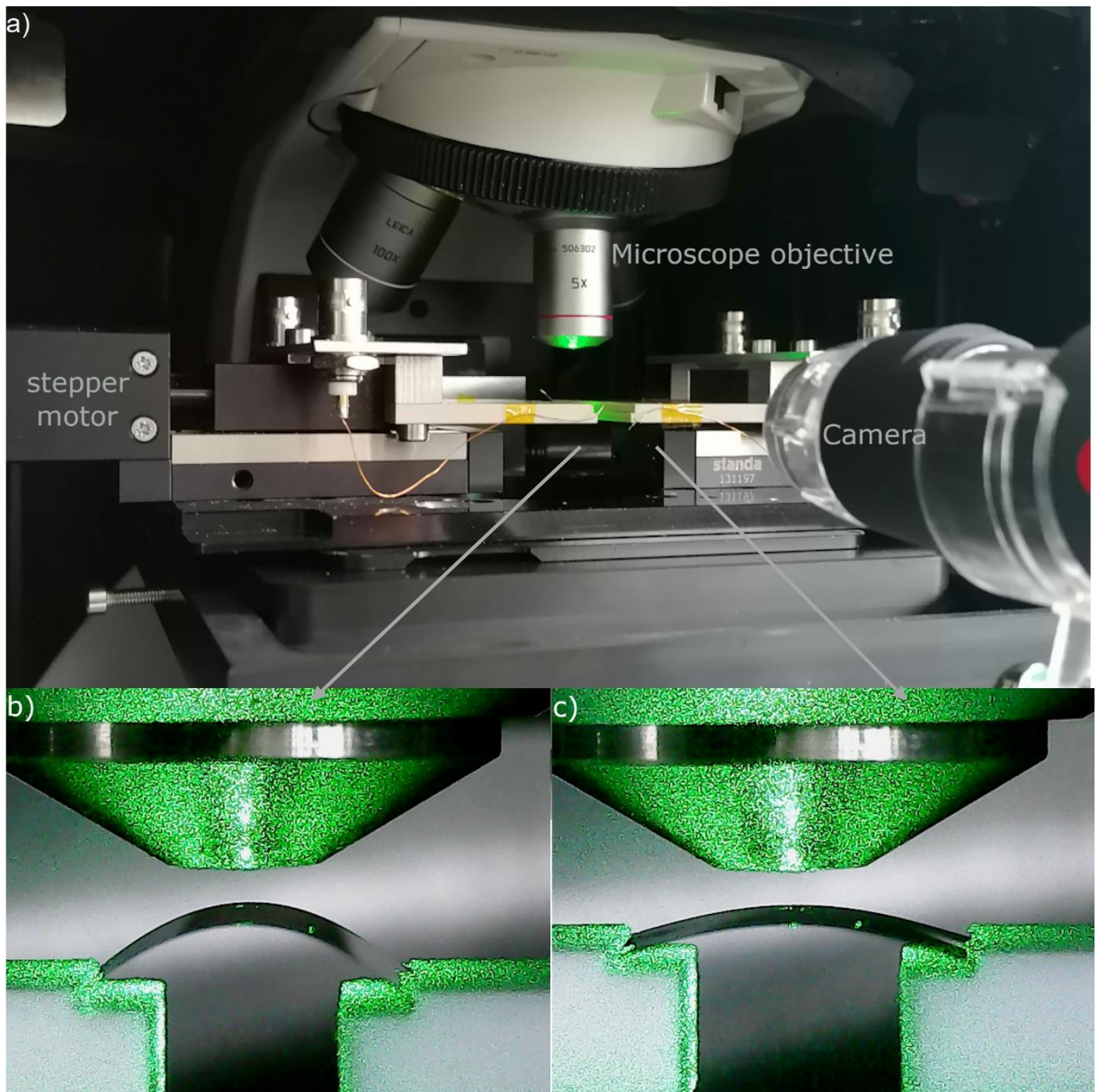


Figure 6.13: a) Two-point bending setup compatible with Renishaw in-Via microscope. b) and c) Raman measurements at different strain values using 532nm laser at 0.3mW with 10s integration time.

6.5.3.1 Process induced loss of flexibility of ultra-thin glass

Looking at the production process of flexible glasses, it is understood that the glass is under immense compressive stress. At high temperatures, as the atoms become more mobile, the stress in the glass can be easily released which reduces the flexibility. On the other hand, water corrodes glass and also affects its overall flexibility^[308]. Therefore, the growth of NCG at 600°C or transferring NCG film in aqueous media was not possible. One possible solution could be to use an encapsulating material for glass which has a small thermal expansion coefficient and inhibits the expansion and release of stress at a

higher temperature. An important point to note here is that the side used for cutting the substrates using a diamond cutter should be always on the compressive side while bending. This is because cracks are generated while scratching and cutting the substrate and may propagate to premature failure of glass if kept on tensile side.

Graphite and graphene have negative thermal expansion coefficients^[311,312] and are resistant to chemicals. The negative thermal coefficient of NCG allows keeping the inherited cracks in the glass intact. Therefore, encapsulating glass with NCG was deemed reasonable. Hence, the glass substrate was coated on both sides with S1805 and heated at 600°C for 10 hrs. This allows the NCG film to grow on both sides of the glass covering the edges of the 10 mm x 10 mm substrate. The benefit of this NCG film is three-fold. First, due to its negative thermal expansion coefficient, it prevents the release of stress present in the glass. Second, the film protects the glass from any corrosion from water if the transfer is required on glass in an aqueous media. Third, the NCG fills in the cracks present at the edges and reduces its propagation during the bending of the substrate.

To investigate the effect of the NCG layer on the flexibility of ultra-thin glass, glass substrates were single side coated, double side coated, and compared with uncoated glass samples. All of them were subjected to similar conditions of temperature at 600°C for 10 hrs. The nominal minimum radius of curvature that can be achieved is approximately 2 mm for the flexible glass from Schott (AF 32 eco). The minimum radius of curvatures achieved for different conditions was compared and has been tabulated in table 6.3.

Table 6.3: Comparison of the radius of curvatures for different processes of coating ultra-thin glass

Substrate	Uncoated	Single side NCG	Double side NCG
Radius of curvature (mm)	8.1	7.6	5.3

The results tabulated in table 6.3 show that the substrate with double side coated NCG was able to achieve the smallest radius of curvature compared to the other two samples for the same thickness of NCG on one side. The uncoated glass substrate flexibility was impaired completely at 600°C. Therefore, it confirms that the NCG film reinforces the glass substrate.

Next, to understand the role of the thickness of NCG, different thicknesses of NCG were grown with similar conditions, and the minimum radius of curvature achieved by them was compared.

Table 6.4: Comparison of the radius of curvatures for two thicknesses of S1805 resist

Dilution	1:10 at 8000 RPM	1:4 at 8000 RPM
Radius of curvature (mm)	5.3	4.1

From table 6.4, it may be concluded that with a thicker film (1:4) of NCG encapsulating the glass, a smaller bending radius was achieved compared to a thinner film. This can be attributed to the fact that a thicker NCG film provides a stronger reinforcement. Further increase in thickness may allow reaching the limit of bending and could be beneficial for use in the synthesis of film at higher temperature (600°C) without losing the flexibility of the substrate.

For Raman measurements, the bending setup was modified to be used with the inVia Renishaw Raman microscope (figure 6.13a). The NCG films for the Raman study were synthesized by spin coating 1:4 resist at 8000 RPM for 30s on both sides and heated at 600°C for 10 hrs. The bending setup was attached to the Raman microscope and the sample was loaded onto it.

Figure 6.13b-c shows two instances of Raman measurements with laser light on and film under strain. The Raman measurements were recorded for each strain value and are plotted as a waterfall plot in figure 6.14a-b. No shifts in Raman G and D peaks are observed as the value of tensile strain is increased from 0% to 0.39%. Figure 6.14c-d is shown as zoom-in of the spectra in figure 6.14a-b, with focus on D and G peaks plotted versus y-scale in logarithmic scale. The 2D peak of NCG is broad and difficult to observe any shifts. It should be emphasized that there is no probable slip movement between the substrate and the grown film. The observation needs a microscopic picture of the NCG film to be addressed.

GBs and TJs are the most common defects present in nanocrystalline graphene. They are comprised of pentagon-heptagon or five-seven defects^[307]. Stress is concentrated on these defects. Therefore, the fracture originates at these defects when an external strain is applied to the film and may propagate intergranular or intragranular. The number of such defect scales with parameter L^2/D^2 where L is the length of the NCG strip and D is the grain size^[2]. NCG in this work has a grain size between 2-5 nm and therefore possesses a huge number of GBs and TJs defects. This implies the density of such stress concentrators is huge and the strength of the film is diminished. Another parameter is strain rate that needs to be considered. The survival probability of the film reduces with decreasing strain rate. This is because, with a lower strain rate, thermal nucleation of fracture at more defects is possible, a similar concept to dislocation nucleation in plastic

materials^{[313][314]}. Hence, based on the background, two reasons could lead to such type of behavior of NCG:

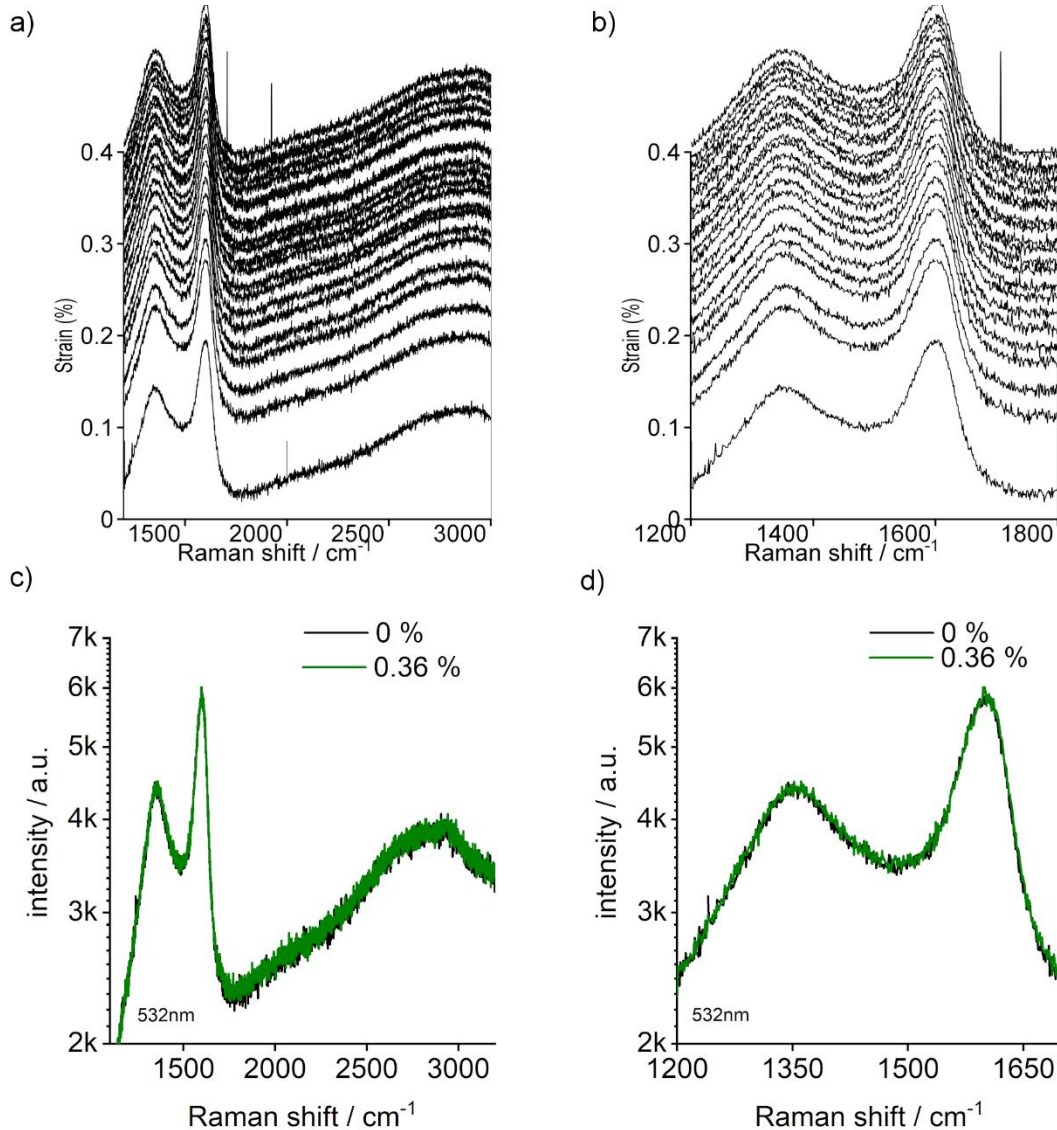


Figure 6.14: a) Water fall plot of complete Raman spectra with varying strain values b) Waterfall plot of Raman spectra till 1700 cm^{-1} for clarity in showing D and G peaks c) and d) Comparing Raman spectra for strain values 0% (black) and 0.36% (green) on a logarithmic y-scale.

- 1) Due to the large density of defects present, the strength of the film is reduced drastically. Accordingly, when the tensile strain is applied to the film, rupture and crack propagation through GBs occur before phonon hardening or softening. This suggests that the strain is not imparted to the lattice and the energy is utilized in cracks generation at the defects. Since the Raman G peak measures the vibrational frequency of phonons and with no change in vibrational frequency

no shift in peak is observed. In addition, from piezoresistance experiments, it was inferred that for lower values of strain (0.3 - 0.4%) the distance between the grains (at GBs) increases.

- 2) Strain rate plays a crucial role in determining nucleation of fracture at the defect sites and hence the overall fracture of the film. A lower strain rate can lead to a premature fracture of the NCG film. Fracture at GBs or TJ occurs as soon as the defects become unstable^[314]. Therefore, in this case, a possible fracture could initiate due to a lower strain rate and lead to fracture while straining the film.

6.6 NCG field-effect transistors as a humidity sensor

NCG, as already discussed, is a highly defective graphene film. Nevertheless, it finds its way in many applications as sensors and FETs. There have been reports showing the increased potential of ions and gas sensing^[23,315]. With good electrical properties and high transparency, NCG has shown a promising application in photodetectors^[25]. In this section, an ionic liquid gated NCG field-effect transistor was fabricated, gated by the top ionic liquid, (IL) to demonstrate its potential application as a humidity sensor. IL can manifest high capacitances due to the formation of an electrical double layer (EDL) as shown in figure 6.15.

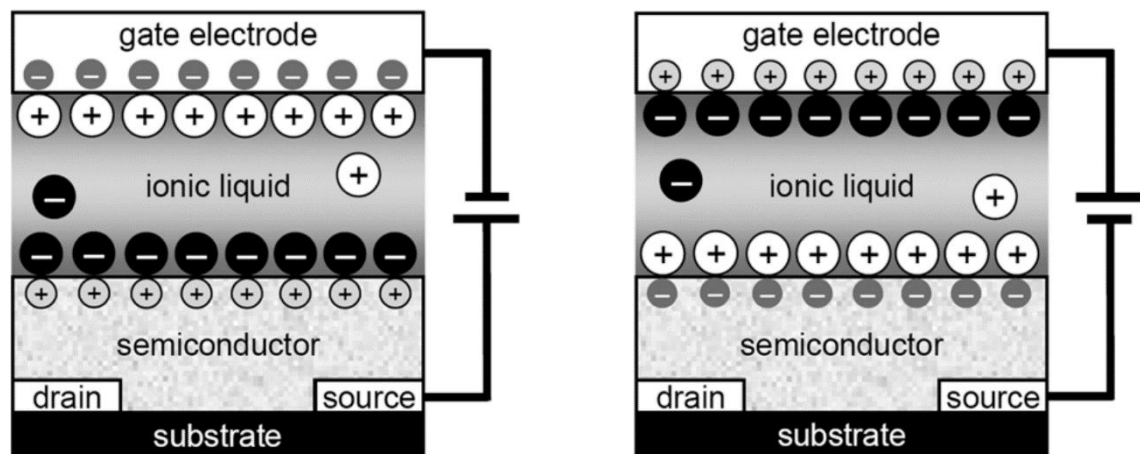


Figure 6.15: EDL formation while gating in ionic liquid, adapted from ^[316].

The EDL comprises holes in the channel and electrons in ionic liquid and vice versa depending on the gate configuration. Large capacitance values allow high-density charge carriers injection compared to a 300 nm SiO₂^[317]. These devices can achieve fast

operation of FETs. The ultra-thin (1 nm) EDL of the IL gate permits the low voltage operation of such devices.

For fabrication of NCG-FET, 1 nm thick NCG film was grown on 300 nm Si/SiO₂ using the technique discussed previously. Next, PMMA was coated and markers were patterned by e-beam lithography. Tungsten markers were then deposited using sputtering (45s). In the next step, NCG strips of dimensions 100 μm x 1 μm were patterned, and NCG was etched from the undesired surface using oxygen plasma. For the third and last step, electrodes were patterned and 45 nm thick tungsten was deposited by sputtering (45s). The active device area was 5 μm x 1 μm . 5 layers of Lithium per-chlorate (IL) were printed on top of the FET devices using an inkjet printer. The device structure with printed ionic liquid is shown in figure 6.16a. For gas sensing experiments, the devices were wire bonded onto the chip carrier as already discussed in previous chapters (Chapter 5).^[3] Distilled water was filled into the bubbler and nitrogen was bubbled through water. The rate of flow of nitrogen in the bubbler was kept low to allow saturation with water molecules. Another line of flow of dry nitrogen was kept as the reference. Different levels of water saturation were achieved by mixing these two lines in different ratios.

A small gate voltage sweep window (-1 V to 1 V) was used to prevent the breakdown of the IL gate. In the transconductance curves (figure 6.16b, black curve), it was observed that there is no doping on the NCG channel and the conductance minima (Dirac point) is close to 0 V. At the Dirac voltage, the Fermi level coincides with charge neutrality point of graphene at the K point of the graphene band structure. If the Dirac voltage is zero, it implies the NCG channel is undoped. The devices were then exposed to water-saturated nitrogen mixed with dry nitrogen in ratio 1:1. The green curve in figure 6.16b shows the transconductance characteristics in presence of a 1:1 gas mixture. The Dirac voltage moves beyond 1 V, and due to limitations of ionic liquid, could not be measured. This indicates that the NCG channel was p-doped. In the humid nitrogen environment, water gets adsorbed onto the IL and p- dopes the channel. This in turn shifts the Dirac voltage to positive values and the conductivity of the channel at zero gate voltage increases. The devices were then exposed to different concentrations of water to investigate their sensitivity. Figure 6.16c shows the response of the FETs at different water concentrations at $V_G = 0$ V and $V_{SD} = 0.1$ V. At 1:3 mixture, devices are non-responsive and a flat line was observed. For the 1:1 mixture of dry and humid nitrogen, the device response showed a 40% change in conductance. Response for water-saturated nitrogen was maximum and a 400% change in conductance was observed.

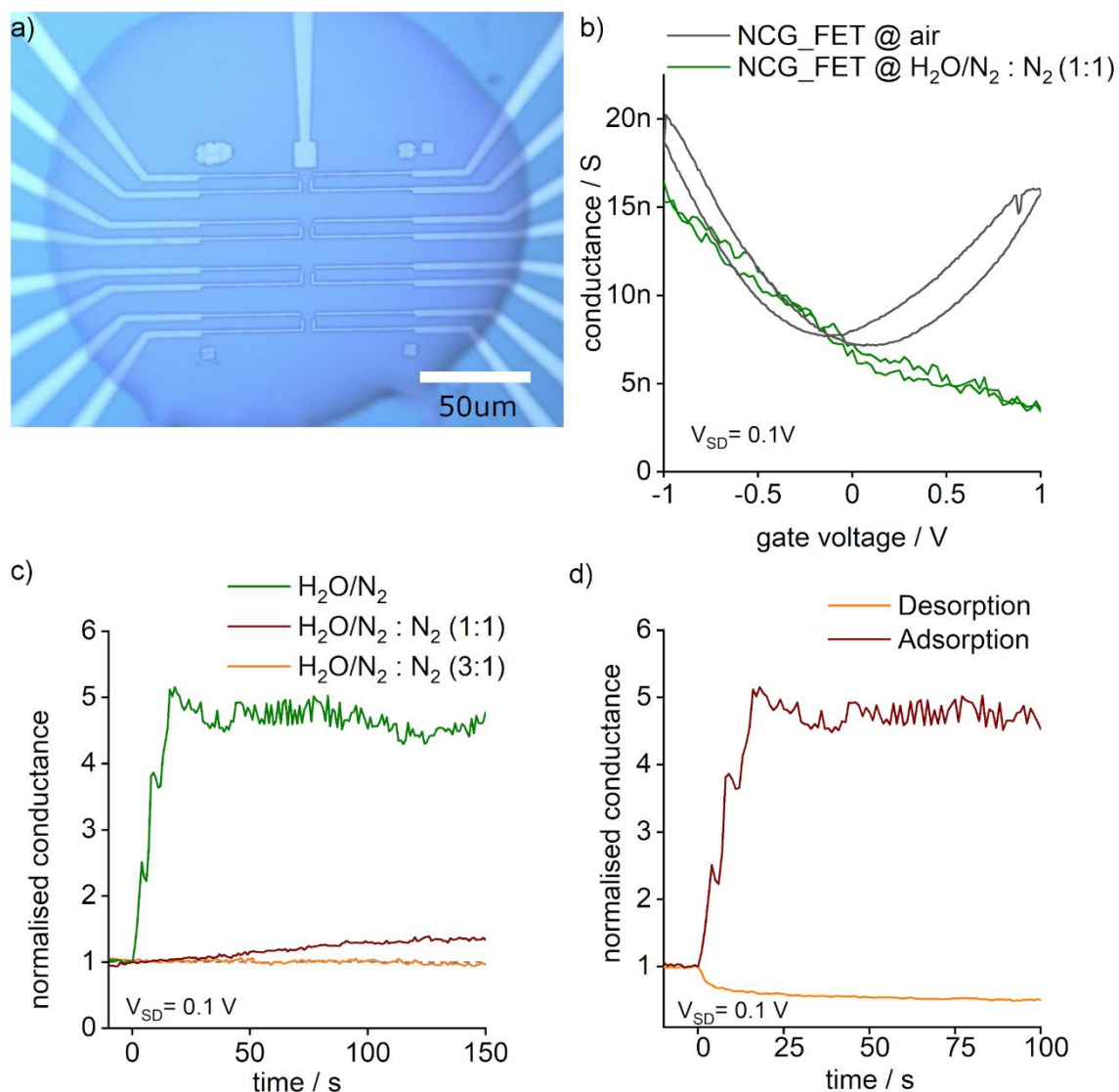


Figure 6.16: a) Optical micrograph of the device structure with ionic liquid gate printed as top gate b) Comparison of transconductance curves of the device in the air (black) and a mixture of N₂ and H₂O/N₂ (1:1) (green) c,) Device response vs water concentration at $V_G = 0$ V d) Time scale showing different rates of adsorption and desorption of water molecules at $V_G = 0$ V.

To further investigate the response, adsorption and desorption experiments were done. Figure 6.16d shows adsorption and desorption curves at room temperature and $V_g = 0$ V. Adsorption was quick and takes few seconds to reach the maximum conductance for completely saturated nitrogen with water. For resetting the devices, the desorption rate should be faster. However, in this case, desorption in completely dry nitrogen was slower. Hence, a mild heating step should be required to bring devices back to their original state. It can be achieved by performing high bias current annealing, similar to the method discussed in chapter 5. However, current annealing was not studied for

these devices. Nevertheless, NCG gated with IL demonstrated a potential application as a moisture sensor. This device structure can also be exploited for fabricating different gas sensors, for example, a CO₂ or ammonia gas sensor.

6.7 Summary

In conclusion, in this chapter, different routes for NCG synthesis were discussed at low temperatures (600°C). PMMA as a carbon source was used for NCG synthesis via cross-linking at a high dose e-beam and subsequent heating. Next, the transfer technique was discussed and the problems associated with it and solutions were developed. In the characterization, temperature and strain-dependent studies were done on NCG. Raman as a probing technique with strain was applied to gain insights into piezoresistance characteristics of NCG. An ionic liquid gated NCG-FET was fabricated and its usage as a humidity sensor was explored.

7 Conclusion and Outlook

Conclusion

In summary, devices based on carbon nano-systems were studied. The prime objective of the thesis was to improve the device's performance. First, the long-term problem of hysteresis in CNTs was encountered and a possible solution was explored. Second, molecule-specific sensitivity in graphene FET was demonstrated by utilizing a porous structure of SURMOF. Third, NCG was then investigated as a material and its utilization in different device applications was explored.

In chapter 4, the mechanism of hysteresis in CNT-FETs was studied and a possible route was explored to solve the long-term prevalent issue. Therefore, a large area h-BN was chosen as the substrate. The direct growth synthesis route on the dielectric substrate was explored to grow h-BN using borazine as a precursor. CNT-FETs were fabricated on the h-BN and hysteresis in the transconductance curves were studied and compared with the FETs fabricated on SiO₂/Si substrate. It was found that the main contributor is water molecules in the environment and therefore a hydrophobic film Teflon was required on the top of the channel. Utilizing this polymer film to encapsulate CNT and CNT-metal contacts completely eradicated hysteresis, after a waiting time of several days. The time scale of the reduction of hysteresis suggested a diffusion process of water molecules.

In chapter 5, a novel concept of sensing molecules was demonstrated using GFETs and SURMOF. The sensitivity of graphene to detect changes in its surrounding was the tool for sensing. The problem of selectivity in GFET was resolved by growing SURMOF on top of GFET. With the help of shifts in Dirac voltage in the transport data, it was shown that without SURMOF, GFET reacts with all the alcohols and as well as water, but after growing SURMOF over the GFET, it becomes selective to just ethanol. In addition, Raman spectroscopy was performed to understand and give insights into the doping and strain levels when exposed to different alcohols. Raman and transport data implied that both methanol and ethanol go at the interface of graphene and SURMOF, but only ethanol provides global doping detected by the shift in the Dirac voltage in the transport.

In the final experimental chapter, chapter 6, NCG was explored. The investigation starts with a low temperature (600°C) synthesis route compared to the conventional high temperature (1000°C) technique by using a metal capping layer. It was found that NCG

film with comparable crystallite size can be synthesized at lower temperatures by using a capping layer of metal. Also, it was possible to graphitize PMMA if encapsulated with metal, which is otherwise not possible. Next, the thin-film transfer technique was demonstrated by using PMMA as a support layer. Problems encountered and possible solutions were discussed. NCG was then characterized based on temperature and strain. NCG sheet resistivity showed decreasing behavior with an increase in the temperature. Variable range hopping mechanism as possible charge transfer technique was deduced. Next, piezoresistivity in the NCG thin films was studied. For this study, a piezoresistance setup was built in-house using two stepper motors and a Keithley. Piezoresistance in NCG was explained by a tunneling and destruction model similar to a matrix of conductive nanoparticles dispersed in an insulator polymer separated by a tunneling distance. Further investigation with Raman spectroscopy measurement based on strain did not show any peak shifts as a function of strain. This suggested that the vibrational frequency of C-C bonds does not change for NCG with strain and only the grains move apart at the grain boundaries. Further explaining the versatility of NCG, an application as a moisture sensor was exhibited.

Outlook

In chapter 4, synthesized h-BN was amorphous and had rough morphology due to the absence of catalyst and low (1000°C) synthesis temperature^[318]. This limits its application as a gate dielectric for 2D materials. To improve the crystallinity of the film, h-BN synthesis should be done at temperatures higher than 1500°C or in presence of a metal catalyst^[319]. Therefore, in relation to the h-BN growth process used in this work, further investigation needs to be done to achieve a high-quality 2D film of h-BN with a controlled growth rate.

Hysteresis in carbon nanotube transistors can be eliminated if the environment around the tubes is free from charge traps^[190]. Hence, providing an encapsulant layer at the top and a charge trap-free layer at the bottom makes the environment charge-free, as already discussed in chapter 4 of the thesis. However, coating the polymer layer in an ambient environment leads to the trapping of water molecules which is not desirable. Hence, coating the nanotube devices in a vacuum or an inert atmosphere could prevent the trapping of water. Furthermore, encapsulating nanotubes from both the bottom and top by growing h-BN could be an alternative approach.

Findings in chapter 5 of the thesis explained a novel gas sensing technique which is exciting and opened up a whole new class of sensors. However, the sensor could not achieve lower detection levels (in ppb) due to the absence of off-state in graphene. Therefore, combining SURMOF with the material possessing a distinct off-state would

enhance the performance and lower the limits of detection. For example, CNTs could be the material to be tested by replacing graphene. Next, to understand the mechanism of sensing in more depth, FTIR measurements combined with molecules adsorption and desorption need to be done.

In chapter 6 NCG synthesis routes at low temperatures (600°C) was explored. Although, achieving a synthesis temperature to facilitate the growth of NCG directly on flexible substrates would be desirable. Strain-dependent sheet resistance measurements confirmed piezoresistive property in NCG. The results were explained using a tunneling and destruction model^[24]. However, an in-depth study is required to understand the complete mechanism. In-situ FTIR measurements in the infrared region would give an insight into how the doping and defect levels change with strain. With a combination of the electrical and optical measurements, the correlation between the structure of NCG and piezoresistivity could be established.

8 List of abbreviations

2DEG : 2 dimension electron gas
AFM : Atomic force microscopy
ALD : Atomic layer deposition
CNT : Carbon nanotubes
CVD : Chemical vapor deposition
DEP : Dielectrophoresis
DUT : Device under test
EBL : Electron beam lithography
EDL : Electrical double layer
EDX : Energy-dispersive X-ray
FEM : Finite element method
FET : Field-effect transistor
FWHM : Full width at half maximum
GB : Grain boundary
GF : Gauge factor
GFET : Graphene field-effect transistor
IL : Ionic liquid
lbl : Layer-by-layer
MBE : Molecular beam epitaxy
MFC : Mass flow controller
MIBK : Methyl iso butyl ketone
MOF : Metal-organic frameworks
NCG : Nanocrystalline graphene
PECVD : Plasma-enhanced chemical vapor deposition
PEEK : Polyether ether ketone
PGMEA : Propylene glycol methyl ether acetate
PMMA : Polymethylmethacrylate
PTFE : Polytetrafluoroethylene

PVC : Polyvinyl chloride
RDS : Rate determining step
RMS : Root mean square
SAM : Self-assembled monolayer
SAW : Surface acoustic wave
SEM : Scanning electron microscopy
SERS : Surface-enhanced Raman scattering
SMU : Source measure unit
STM : Scanning tunneling microscope
SURMOF : Surface-mounted metal-organic frameworks
SWCNT : Single-walled carbon nanotube
TJ : Triple junction
TRT : Thermal release tape
VC-SEM : Voltage-contrast scanning electron micrography
VRH : Variable range hopping
XPS : X-ray photoelectron spectroscopy
XRD : X-ray diffraction

9 List of Figures

Figure 1.1: Number of publications per year.....	1-1
Figure 2.1: Unit cell and Reciprocal space of graphene	2-7
Figure 2.2: Conduction and Valence Band of graphene	2-8
Figure 2.3: Transconductance curve of GFET	2-9
Figure 2.4: Equivalent capacitance of GFET.....	2-10
Figure 2.5: Graphene sheet to CNT	2-14
Figure 2.6: Band diagram of metallic and zig-zag CNTs.....	2-15
Figure 2.7: Transconductance curve of CNT-FET	2-16
Figure 2.8: Time dependent VC-SEM for a metallic nanotube	2-17
Figure 2.9: Hysteresis in CNT-FET due to water molecules	2-18
Figure 2.10: Mechanism of hysteresis	2-20
Figure 2.11: Capacitance model of CNT on h-BN and SiO ₂ /Si.....	2-21
Figure 2.12: Transconductance curve of NCG-FET	2-26
Figure 2.13: Stress concentrators in NCG film.....	2-27
Figure 2.14: Resistance of a system.....	2-28
Figure 2.15: Piezoresistance principle in a conductor filled polymer composite.....	2-29
Figure 2.16: Raman spectra of graphene.....	2-32
Figure 2.17: 2D vs G peak frequency of graphene at different strain and doping	2-34
Figure 2.18: 2D vs G peak frequency of graphene at different strain and doping	2-35
Figure 2.19: Plot of ratio of peak intensities vs crystallite size.....	2-36
Figure 2.20: Plots of FWHM of D and G peaks vs crystallite size	2-37
Figure 2.21: Two point bending test.....	2-40
Figure 2.22: Stress profile in ultra-thin glass	2-41
Figure 3.1: Schematic of the h-BN and NCG synthesis setup	3-45
Figure 3.2: Device structure for four-point sheet resistance measurement.....	3-48
Figure 3.3: Measurement configuration in Van der Pauw method.....	3-50

Figure 3.4: Raman Stokes and Anti-Stokes principle	3-51
Figure 3.5: Schematic of a Raman microscope	3-52
Figure 3.6: Images of Piezoresistance setup	3-54
Figure 3.7: Schematic of spring contact holder	3-54
Figure 3.8: Schematic of substrate holder	3-55
Figure 3.9: Schematic of motor connector	3-55
Figure 3.10: Schematic of BNC connector holder	3-56
Figure 3.11: Images of substrate holder in gas sensing setup	3-57
Figure 3.12: Schematic of the connection diagram of the gas sensing setup	3-58
Figure 4.1: Raman and XPS spectroscopy of h-BN film	4-60
Figure 4.2: Optical and AFM image of h-BN film.....	4-61
Figure 4.3: SEM image of h-BN film	4-62
Figure 4.4: Comparison of Raman spectra in different conditions of h-BN synthesis	4-63
Figure 4.5: Process flow and fabricated device structure for CNT-FET	4-64
Figure 4.6: Optical images of CNT-FET	4-66
Figure 4.7: Reflectance spectra of a stack of Teflon/ h-BN /SiO ₂ / Si	4-67
Figure 4.8: Transconductance curves for different stacks of h-BN and Teflon.....	4-68
Figure 4.9: Schematic of diffusion of water trapped at CNT-metal contacts	4-69
Figure 4.10: Performance characteristics of CNT-FET on h-BN/SiO ₂ /Si.....	4-72
Figure 4.11: Transconductance curve of CNT-FET on Si/SiO ₂	4-74
Figure 5.1: 3-D model mimicking ethanol adsorbed into SURMOF	5-78
Figure 5.2: GFET/SURMOF device fabrication.....	5-79
Figure 5.3: Schematic of the gas sensing setup	5-82
Figure 5.4: EDX spectra of Al ₂ O ₃ /graphene/SiO ₂ /Si	5-84
Figure 5.5: XRD measurements of SURMOF	5-85
Figure 5.6: Scanning electron microscopy images of a SURMOF.....	5-86
Figure 5.7: Response of the GFET without SURMOF to different alcohols.....	5-87
Figure 5.8: Transconductance curves of GFET under alcohols and gas exposures.....	5-89
Figure 5.9: Raman spectra of graphene to deconvolute strain and doping levels	5-90

Figure 5.10: Comparison of mobility, residual carrier concentration, doping, contact resistance of GFET/SURMOF	5-93
Figure 5.11: SURMOF/GFET time response and sensitivity to exposure of ethanol ...	5-95
Figure 5.12: Vapor uptake by the MOF film grown Au@QCM-sensors	5-97
Figure 5.13: Simulated charge carrier concentration p+n in graphene vs back-gate .	5-98
Figure 6.1: Amorphization and G peak position for different excitation laser.....	6-103
Figure 6.2: Comparison of crystallite sizes and levels of amorphization for different synthesis routes	6-104
Figure 6.3: SEM image of cross-linked PMMA structure.....	6-105
Figure 6.4: Optical micrograph of NCG film synthesized by cross-linking PMMA.....	6-106
Figure 6.5: Thin film transfer process using PMMA top layer	6-107
Figure 6.6: AFM images of transferred thin films.....	6-110
Figure 6.7: Temperature dependence of sheet resistance of NCG	6-112
Figure 6.8: Conduction model in NCG	6-114
Figure 6.9: Circuit diagram of Piezoresistance measurement setup.....	6-115
Figure 6.10: Calculation of radius of curvature	6-116
Figure 6.11: Wire diagram of the connections from the substrate to Keithley	6-118
Figure 6.12: Piezoresistance measurements in NCG and curve fitting with tunneling and destruction model.....	6-120
Figure 6.13: Two-point bending setup compatible with Raman microscope	6-123
Figure 6.14: Water fall plot of complete Raman spectra with varying strain values	6-126
Figure 6.15: EDL formation while gating in ionic liquid.....	6-127

10 List of Tables

Table 2.1: Linear fit parameters for D and G peaks obtained experimentally	2-33
Table 2.2: Important properties of ultra-thin glass	2-36
Table 2.3: Properties of Teflon AF2400..	2-38
Table 3.1: Few Parameters of Standa 8MT173-20 translation stage.	3-48
Table 4.1: Comparison of the hysteresis values from literature to this work.	4-65
Table 6.1: Temperature-dependent behavior of conduction model in NCG	6-106
Table 6.2: Fitting equation and parameters of tunneling + destruction model	6-113
Table 6.3: Comparison of the radius of curvatures for different processes	6-116
Table 6.4: Comparison of the radius of curvatures for two thicknesses	6-117

11 Bibliography

- [1] S. Reich, C. Thomsen, J. Maultzsch, *Carbon Nanotubes: Basic Concepts and Physical Properties*, Wiley-VCH, **2003**.
- [2] A. Shekhawat, R. O. Ritchie, *Nat. Commun.* **2016**, 7, 10546.
- [3] M. Ganzhorn, A. Vijayaraghavan, S. Dehm, F. Hennrich, A. A. A. Green, M. Fichtner, A. Voigt, M. Rapp, H. von Löhneysen, M. C. Hersam, M. M. Kappes, R. Krupke, *ACS Nano* **2011**, 5, 1670.
- [4] A. Riaz, A. Alam, P. B. Selvasundaram, S. Dehm, F. Hennrich, M. M. Kappes, R. Krupke, *Adv. Electron. Mater.* **2019**, 5, 1800265.
- [5] M. Gaulke, A. Janissek, N. A. Peyyety, I. Alamgir, A. Riaz, S. Dehm, H. Li, U. Lemmer, B. S. Flavel, M. M. Kappes, F. Hennrich, L. Wei, Y. Chen, F. Pyatkov, R. Krupke, *ACS Nano* **2020**, 14, 2709.
- [6] R. S. Park, M. M. Shulaker, G. Hills, L. Suriyasena Liyanage, S. Lee, A. Tang, S. Mitra, H. S. P. Wong, *ACS Nano* **2016**, 10, 4599.
- [7] W. Kim, A. Javey, O. Vermesh, Q. Wang, Y. Li, H. Dai, *Nano Lett.* **2003**, 3, 193.
- [8] T. J. Ha, D. Kiriya, K. Chen, A. Javey, *ACS Appl. Mater. Interfaces* **2014**, 6, 8441.
- [9] M. Muoth, T. Helbling, L. Durrer, S. W. Lee, C. Roman, C. Hierold, *Nat. Nanotechnol.* **2010**, 5, 589.
- [10] C. R. Dean, A. F. Young, I. Meric, C. Lee, L. Wang, S. Sorgenfrei, K. Watanabe, T. Taniguchi, P. Kim, K. L. Shepard, J. Hone, *Nat. Nanotechnol.* **2010**, 5, 722.
- [11] K. K. Kim, A. Hsu, X. Jia, S. M. Kim, Y. Shi, M. Hofmann, D. Nezich, J. F. Rodriguez-Nieva, M. Dresselhaus, T. Palacios, J. Kong, *Nano Lett.* **2012**, 12, 161.
- [12] S. Nakhaie, J. M. Wofford, T. Schumann, U. Jahn, M. Ramsteiner, M. Hanke, J. M. J. Lopes, H. Riechert, *Appl. Phys. Lett.* **2015**, 106, 213108.
- [13] X. Du, I. Skachko, A. Barker, E. Y. Andrei, *Nat. Nanotechnol.* **2008**, 3, 491.
- [14] M. C. Lemme, *Solid State Phenom.* **2009**, 156–158, 499.
- [15] K. S. Novoselov, A. K. Geim, S. V. Morozov, D. Jiang, Y. Zhang, S. V. Dubonos, I. V. Grigorieva, A. A. Firsov, *Science (80-.)*. **2004**, 5, 1.
- [16] A. A. Balandin, S. Ghosh, W. Bao, I. Calizo, D. Teweldebrhan, F. Miao, C. N. Lau, *Nano Lett.* **2008**, 8, 902.

-
-
- [17] C. Lee, X. Wei, J. W. Kysar, J. Hone, *Science* (80-.). **2008**, 321, 385.
- [18] F. Schedin, A. K. Geim, S. V. Morozov, E. W. Hill, P. Blake, M. I. Katsnelson, K. S. Novoselov, *Nat. Mater.* **2007**, 6, 652.
- [19] C. W. Chen, S. C. Hung, M. D. Yang, C. W. Yeh, C. H. Wu, G. C. Chi, F. Ren, S. J. Pearton, *Appl. Phys. Lett.* **2011**, 99, 243502.
- [20] J. Hong, S. Lee, J. Seo, S. Pyo, J. Kim, T. Lee, *ACS Appl. Mater. Interfaces* **2015**, 7, 3554.
- [21] L. Huang, Z. Zhang, Z. Li, B. Chen, X. Ma, L. Dong, L. Peng, *ACS Appl. Mater. Interfaces* **2015**, 7, 9581.
- [22] X. Xu, J. Zhou, Y. Xin, G. Lubineau, Q. Ma, L. Jiang, *Sci. Rep.* **2017**, 7, 4317.
- [23] M. V. S. Chandrashekar, J. Lu, M. G. Spencer, M. Qazi, G. Koley, in *2007 IEEE Sensors*, IEEE, **2007**, pp. 1–4.
- [24] J. Zhao, G. Wang, R. Yang, X. Lu, M. Cheng, C. He, G. Xie, J. Meng, D. Shi, G. Zhang, *ACS Nano* **2015**, 9, 1622.
- [25] Q. Zhang, L. Tang, J. Luo, J. Zhang, X. Wang, D. Li, Y. Yao, Z. Zhang, *Carbon N. Y.* **2017**, 111, 1.
- [26] K. S. Novoselov, *Science* (80-.). **2004**, 306, 666.
- [27] A. A. Balandin, S. Ghosh, W. Bao, I. Calizo, D. Teweldebrhan, F. Miao, C. N. Lau, *Nano Lett.* **2008**, 8, 902.
- [28] N. D. Aschcroft, N.W and Mermin, *Solid State Physics*, **1976**.
- [29] https://www.wikiwand.com/en/Electronic_properties_of_graphene, **n.d.**
- [30] J. E. Proctor, D. A. M. Armada, V. A, *An Introduction to Graphene and Carbon Nanotubes*, **2017**.
- [31] R. Saito, G. Dresselhaus, *Phys. Rev. B - Condens. Matter Mater. Phys.* **2000**, 61, 2981.
- [32] R. Saito, G. Dresselhaus, M. S. Dresselhaus, *Physical Properties of Carbon Nanotubes*, ICP, London, **1998**.
- [33] S. Kim, K. Lee, E. Tutuc, *Phys. Rev. Lett.* **2011**, 107, 1.
- [34] S. Kim, **2012**.
- [35] Y.-J. Yu, Y. Zhao, S. Ryu, L. E. Brus, K. S. Kim, P. Kim, *Nano Lett.* **2009**, 9, 3430.
- [36] S. Luryi, *Appl. Phys. Lett.* **1988**, 52, 501.

-
-
- [37] S. Kim, J. Nah, I. Jo, D. Shahrjerdi, L. Colombo, Z. Yao, E. Tutuc, S. K. Banerjee, *Appl. Phys. Lett.* **2009**, *94*, 2007.
- [38] J. M. Raimond, M. Brune, Q. Computation, F. De Martini, C. Monroe, K. S. Novoselov, *Science (80-.)*. **2004**, *306*, 666.
- [39] J. H. Choi, J. Lee, M. Byeon, T. E. Hong, H. Park, C. Y. Lee, *ACS Appl. Nano Mater.* **2020**, *3*, 2257.
- [40] F. Vivaldi, A. Bonini, B. Melai, N. Poma, A. Kirchhain, D. Santalucia, P. Salvo, F. Di Francesco, in *2019 41st Annu. Int. Conf. IEEE Eng. Med. Biol. Soc.*, IEEE, **2019**, pp. 1563–1566.
- [41] T. Wang, D. Huang, Z. Yang, S. Xu, G. He, *Nano-Micro Lett.* **2016**, *8*, 95.
- [42] M. Gautam, A. H. Jayatissa, *Solid State Electron.* **2012**, *78*, 159.
- [43] F. Yavari, E. Castillo, H. Gullapalli, P. M. Ajayan, N. Koratkar, *Appl. Phys. Lett.* **2012**, *100*, 203120.
- [44] Y. Seekaew, S. Lokavee, D. Phokharatkul, A. Wisitsoraat, T. Kerdcharoen, C. Wongchoosuk, *Org. Electron.* **2014**, *15*, 2971.
- [45] H. Choi, H. Y. Jeong, D. Lee, C.-G. Choi, S. Choi, *Carbon Lett.* **2013**, *14*, 186.
- [46] R. Pearce, T. Iakimov, M. Andersson, L. Hultman, A. L. Spetz, R. Yakimova, *Sensors Actuators B Chem.* **2011**, *155*, 451.
- [47] K. R. Nemade, S. A. Waghuley, *J. Electron. Mater.* **2013**, *42*, 2857.
- [48] H. Joong, D. Han, J. Ho, Z. Zhou, *Sensors Actuators B. Chem.* **2011**, *157*, 310.
- [49] W. Fu, C. Nef, O. Knopfmacher, A. Tarasov, M. Weiss, M. Calame, C. Schönenberger, *Nano Lett.* **2011**, *11*, 3597.
- [50] M. Huang, T. A. Pascal, H. Kim, W. A. Goddard, J. R. Greer, *Nano Lett.* **2011**, *11*, 1241.
- [51] X.-W. Fu, Z.-M. Liao, J.-X. Zhou, Y.-B. Zhou, H.-C. Wu, R. Zhang, G. Jing, J. Xu, X. Wu, W. Guo, D. Yu, *Appl. Phys. Lett.* **2011**, *99*, 213107.
- [52] Y. Kim, J. Young, H. Ham, H. Huh, D. So, I. Kang, *Curr. Appl. Phys.* **2011**, *11*, S350.
- [53] K. Kneipp, Y. Wang, H. Kneipp, L. T. Perelman, I. Itzkan, R. R. Dasari, M. S. Feld, *Phys. Rev. Lett.* **1997**, *78*, 1667.
- [54] J. Li, L. Chen, T. Lou, Y. Wang, *ACS Appl. Mater. Interfaces* **2011**, *3*, 3936.
- [55] X.-G. Gao, L.-X. Cheng, W.-S. Jiang, X.-K. Li, F. Xing, *Front. Chem.* **2021**, *9*, 1.

-
- [56] H. Lai, F. Xu, Y. Zhang, L. Wang, *J. Mater. Chem. B* **2018**, 6, 4008.
- [57] Q. Ye, J. Wang, Z. Liu, Z.-C. Deng, X.-T. Kong, F. Xing, X.-D. Chen, W.-Y. Zhou, C.-P. Zhang, J.-G. Tian, *Appl. Phys. Lett.* **2013**, 102, 021912.
- [58] F. Xing, G. X. Meng, Q. Zhang, L. T. Pan, P. Wang, Z. B. Liu, W. S. Jiang, Y. Chen, J. G. Tian, *Nano Lett.* **2014**, 14, 3563.
- [59] J.-C. Charlier, X. Blase, S. Roche, *Rev. Mod. Phys.* **2007**, 79, 677.
- [60] <https://de.wikipedia.org/wiki/Kohlenstoffnanoröhre#/media/File:CNTnames.svg>, n.d.
- [61] R. Saito, M. Fujita, G. Dresselhaus, M. S. Dresselhaus, *Phys. Rev. B* **1992**, 46, 1804.
- [62] A. Vijayaraghavan, C. W. Marquardt, F. Hennrich, R. Krupke, S. Dehm, *Carbon N. Y.* **2009**, 48, 494.
- [63] W. Kim, A. Javey, O. Vermesh, Q. Wang, Y. Li, H. Dai, *Nano Lett.* **2003**, 3, 193.
- [64] S. H. Jin, A. E. Islam, T. Kim, J. Kim, M. A. Alam, J. A. Rogers, *Adv. Funct. Mater.* **2012**, 22, 2276.
- [65] J. S. Lee, S. Ryu, K. Yoo, I. S. Choi, W. S. Yun, J. Kim, *J. Phys. Chem. C* **2007**, 111, 12504.
- [66] S. A. McGill, S. G. Rao, P. Manandhar, P. Xiong, S. Hong, *Appl. Phys. Lett.* **2006**, 89, 163123.
- [67] L. T. Zhuravlev, *Colloids Surfaces A Physicochem. Eng. Asp.* **2000**, 173, 1.
- [68] B. Diamond, V. Chakrapani, J. C. Angus, A. B. Anderson, S. D. Wolter, B. R. Stoner, G. U. Sumanasekera, *Science (80-.)*. **2007**, 318, 1424.
- [69] Y. Pascal-Levy, E. Shifman, M. Pal-Chowdhury, I. Kalifa, T. Rabkin, O. Shtempluck, A. Razin, V. Kochetkov, Y. E. Yaish, *Phys. Rev. B* **2012**, 86, 115444.
- [70] Z. Xu, Y. Gao, C. Wang, H. Fang, *J. Phys. Chem. C* **2015**, 119, 20409.
- [71] R. T. Weitz, U. Zschieschang, F. Effenberger, H. Klauk, M. Burghard, K. Kern, *Nano Lett.* **2007**, 7, 22.
- [72] M. Ganzhorn, A. Vijayaraghavan, A. A. Green, S. Dehm, A. Voigt, M. Rapp, M. C. Hersam, R. Krupke, *Adv. Mater.* **2011**, 23, 1734.
- [73] J. Lefebvre, J. Ding, Z. Li, F. Cheng, N. Du, P. R. L. Malenfant, *Appl. Phys. Lett.* **2015**, 107, 243301.
- [74] R. T. Weitz, U. Zschieschang, A. Forment-Aliaga, D. Kälblein, M. Burghard, K. Kern,

- H. Klauk, *Nano Lett.* **2009**, *9*, 1335.
- [75] R. S. Park, G. Hills, J. Sohn, S. Mitra, M. M. Shulaker, H.-S. P. Wong, *ACS Nano* **2017**, *11*, 4785.
- [76] T. Haeberle, F. Loghin, U. Zschieschang, H. Klauk, P. Lugli, in *2015 IEEE 15th Int. Conf. Nanotechnol.*, IEEE, **2015**, pp. 160–163.
- [77] K. Grigoras, M. Y. Zavodchikova, A. G. Nasibulin, E. I. Kauppinen, V. Ermolov, S. Franssila, *J. Nanosci. Nanotechnol.* **2011**, *11*, 8818.
- [78] S. P. Schießl, N. Fröhlich, M. Held, F. Gannott, M. Schweiger, M. Forster, U. Scherf, J. Zaumseil, *ACS Appl. Mater. Interfaces* **2015**, *7*, 682.
- [79] C. Cao, J. B. Andrews, A. D. Franklin, *Adv. Electron. Mater.* **2017**, *3*, 1700057.
- [80] S. Selvarasah, X. Li, A. Busnaina, M. R. Dokmeci, *Appl. Phys. Lett.* **2010**, *97*, 153120.
- [81] S. Jang, B. Kim, M. L. Geier, P. L. Prabhumirashi, M. C. Hersam, A. Dodabalapur, *Appl. Phys. Lett.* **2014**, *105*, 122107.
- [82] T. Dürkop, S. A. Getty, E. Cobas, M. S. Fuhrer, *Nano Lett.* **2004**, *4*, 35.
- [83] P. Zhang, Y. Yang, T. Pei, C. Qiu, L. Ding, S. Liang, Z. Zhang, L. Peng, *Nano Res.* **2015**, *8*, 1005.
- [84] L. Chico, V. H. Crespi, L. X. Benedict, S. G. Louie, M. L. Cohen, *Phys. Rev. Lett.* **1996**, *76*, 971.
- [85] F. Pyatkov, V. Fütterling, S. Khasminskaya, B. S. Flavel, F. Hennrich, M. M. Kappes, R. Krupke, W. H. P. Pernice, *Nat. Photonics* **2016**, *10*, 420.
- [86] S. Berber, Y. Kwon, D. Tománek, *Phys. Rev. Lett.* **2000**, *84*, 4613.
- [87] M. S. Fuhrer, T. Brintlinger, T. Dürkop, T. Brintlinger, *Nano Lett.* **2002**, *2*, 755.
- [88] J. B. Cui, R. Sordan, M. Burghard, K. Kern, *Appl. Phys. Lett.* **2002**, *81*, 3260.
- [89] V. Derycke, R. Martel, J. Appenzeller, P. Avouris, *Nano Lett.* **2001**, *1*, 453.
- [90] D. J. Yang, Q. Zhang, S. G. Wang, G. F. Zhong, *Diam. Relat. Mater.* **2004**, *13*, 1967.
- [91] J. Kong, *Science (80-.)*. **2000**, *287*, 622.
- [92] C. S. Huang, B. R. Huang, Y. H. Jang, M. S. Tsai, C. Y. Yeh, *Diam. Relat. Mater.* **2005**, *14*, 1872.
- [93] J. U. Lee, P. P. Gipp, C. M. Heller, *Appl. Phys. Lett.* **2004**, *85*, 145.
- [94] L. Yang, S. Wang, Q. Zeng, Z. Zhang, T. Pei, Y. Li, L.-M. Peng, *Nat. Photonics* **2011**, *5*, 672.

-
- [95] Z. Zhang, B. Ge, Y. Guo, D. Tang, X. Wang, F. Wang, *Chem. Commun.* **2013**, 49, 2789.
- [96] A. Turchanin, D. Weber, M. Büenfeld, C. Kisielowski, M. V Fistul, K. B. Efetov, T. Weimann, R. Stosch, J. Mayer, A. Götzhäuser, *ACS Nano* **2011**, 5, 3896.
- [97] T. Zhao, C. Xu, W. Ma, Z. Liu, T. Zhou, Z. Liu, S. Feng, M. Zhu, N. Kang, D. Sun, H. Cheng, W. Ren, *Nat. Commun.* **2019**, 10, 4854.
- [98] R. Yekani, E. Rusak, A. Riaz, A. Felten, B. Breitung, S. Dehm, D. Perera, J. Rohrer, C. Rockstuhl, R. Krupke, *Nanoscale* **2018**, 10, 12156.
- [99] A. Riaz, F. Pyatkov, A. Alam, S. Dehm, A. Felten, V. S. K. Chakravadhanula, B. S. Flavel, C. Kübel, U. Lemmer, R. Krupke, *Nanotechnology* **2015**, 26, 325202.
- [100] D. Noll, P. Hönicke, Y. Kayser, S. Wagner, B. Beckhoff, U. Schwalke, *ECS J. Solid State Sci. Technol.* **2018**, 7, Q3108.
- [101] V. A. Krivchenko, A. A. Pilevsky, A. T. Rakhimov, B. V. Seleznev, N. V. Suetin, M. A. Timofeyev, A. V. Besspalov, O. L. Golikova, *J. Appl. Phys.* **2010**, 014315, 014315.
- [102] M. H. Oliveira, T. Schumann, R. Gargallo-caballero, F. Fromm, T. Seyller, M. Ramsteiner, A. Trampert, L. Geelhaar, J. Marcelo, J. Lopes, H. Riechert, *Carbon N. Y.* **2013**, 56, 339.
- [103] Q. Yu, L. A. Jauregui, W. Wu, R. Colby, J. Tian, Z. Su, H. Cao, Z. Liu, D. Pandey, D. Wei, T. F. Chung, P. Peng, N. P. Guisinger, E. A. Stach, J. Bao, S.-S. Pei, Y. P. Chen, *Nat. Mater.* **2011**, 10, 443.
- [104] K. W. Clark, X.-G. Zhang, I. V Vlassiouk, G. He, R. M. Feenstra, A. Li, *ACS Nano* **2013**, 7, 7956.
- [105] L. Tapasztó, P. Nemes-Incze, G. Dobrik, K. Jae Yoo, C. Hwang, L. P. Biró, *Appl. Phys. Lett.* **2012**, 100, 053114.
- [106] J. C. Koepke, J. D. Wood, D. Estrada, Z. Y. Ong, K. T. He, E. Pop, J. W. Lyding, *ACS Nano* **2013**, 7, 75.
- [107] A. W. Cummings, D. L. Duong, V. L. Nguyen, D. Van Tuan, J. Kotakoski, J. Eduardo, B. Vargas, Y. H. Lee, S. Roche, *Advanced Mater.* **2014**, 26, 5079.
- [108] J. Ryu, Y. Kim, D. Won, N. Kim, J. S. Park, E.-K. Lee, D. Cho, S. Cho, S. J. Kim, G. H. Ryu, H. Shin, Z. Lee, B. H. Hong, S. Cho, *ACS Nano* **2014**, 8, 950.
- [109] J. G. Simmons, *J. Appl. Phys.* **1963**, 34, 1793.
- [110] J. Lu, W. Weng, X. Chen, D. Wu, C. Wu, G. Chen, *Adv. Funct. Mater.* **2005**, 15, 1358.
- [111] Z. Zhang, B. Ge, Y. Guo, D. Tang, X. Wang, F. Wang, *Chem. Commun.* **2013**, 49,

2789.

- [112] R. Grantab, V. B. Shenoy, R. S. Ruoff, *Science* (80-.). **2010**, 330, 946.
- [113] Y. Wei, J. Wu, H. Yin, X. Shi, R. Yang, M. Dresselhaus, *Nat. Mater.* **2012**, 11, 759.
- [114] Z. Song, V. I. Artyukhov, B. I. Yakobson, Z. Xu, *Nano Lett.* **2013**, 13, 1829.
- [115] M. A. Meyers, A. Mishra, D. J. Benson, *Prog. Mater. Sci.* **2006**, 51, 427.
- [116] T. William, *Proc. R. Soc. London* **1857**, 8, 546.
- [117] J. W. Cookson, *Phys. Rev.* **1935**, 47, 194.
- [118] C. S. Smith, *Phys. Rev.* **1954**, 94, 42.
- [119] W. P. Mason, R. N. Thurston, *J. Acoust. Soc. Am.* **1957**, 29, 1096.
- [120] W. G. Pfann, R. N. Thurston, *J. Appl. Phys.* **1961**, 32, 2008.
- [121] K. E. Petersen, in *Micromechanics MEMS*, IEEE, **2009**, pp. 58–95.
- [122] H. Rolnick, *Phys. Rev.* **1930**, 36, 506.
- [123] W. A. Brantley, *J. Appl. Phys.* **1973**, 44, 534.
- [124] I. S. Sokolnikoff, *Mathematical Theory of Elasticity*, McGraw-Hill, New York, **1956**.
- [125] C. Kittel, *Introduction to Solid State Physics.*, Wiley John + Sons, **2004**.
- [126] J. Zhao, C. He, R. Yang, Z. Shi, M. Cheng, W. Yang, G. Xie, D. Wang, D. Shi, G. Zhang, *Appl. Phys. Lett.* **2012**, 101, 063112.
- [127] X. W. Zhang, Y. Pan, Q. Zheng, X. S. Yi, *J. Polym. Sci. Part B Polym. Phys.* **2000**, 38, 2739.
- [128] G. R. Ruschau, S. Yoshikawa, R. E. Newnham, *J. Appl. Phys.* **1992**, 72, 953.
- [129] K. Ohe, Y. Naito, *Jpn. J. Appl. Phys.* **1971**, 10, 99.
- [130] P. Sheng, *Phys. Rev. B* **1980**, 21, 2180.
- [131] J. Herrmann, K. H. Müller, T. Reda, G. R. Baxter, B. Raguse, G. J. J. B. De Groot, R. Chai, M. Roberts, L. Wieczorek, *Appl. Phys. Lett.* **2007**, 91, 1.
- [132] F. R. Al-solamy, A. A. Al-ghamdi, W. E. Mahmoud, *Polym. Adv. Technol.* **2012**, 23, 478.
- [133] P. Yasaei, B. Kumar, R. Hantehzadeh, M. Kayyalha, A. Baskin, N. Reppin, C. Wang, R. F. Klie, Y. P. Chen, P. Král, A. Salehi-Khojin, *Nat. Commun.* **2014**, 5, 1.
- [134] Z. Zhang, Y. Guo, X. Wang, D. Li, F. Wang, S. Xie, *Adv. Funct. Mater.* **2014**, 24, 835.

-
- [135] S. J. Fishlock, S. H. Pu, G. Bhattacharya, Y. Han, J. McLaughlin, J. W. McBride, H. M. H. Chong, S. J. O'Shea, *Carbon N. Y.* **2018**, *138*, 125.
- [136] R. Narula, S. Reich, *Phys. Rev. B - Condens. Matter Mater. Phys.* **2008**, *78*, 1.
- [137] P. Venezuela, M. Lazzeri, F. Mauri, *Phys. Rev. B - Condens. Matter Mater. Phys.* **2011**, *84*, 1.
- [138] M. Lazzeri, F. Mauri, *Phys. Rev. Lett.* **2006**, *97*, 266407.
- [139] D. Abdula, T. Ozel, K. Kang, D. G. Cahill, M. Shim, *J. Phys. Chem. C* **2008**, *112*, 20131.
- [140] Z. H. Ni, T. Yu, Y. H. Lu, Y. Y. Wang, Y. P. Feng, Z. X. Shen, *ACS Nano* **2008**, *2*, 2301.
- [141] F. Tuinstra, J. L. Koenig, *J. Chem. Phys.* **1970**, *53*, 1126.
- [142] M. Huang, H. Yan, T. F. Heinz, J. Hone, *Nano Lett.* **2010**, *10*, 4074.
- [143] D. Yoon, Y. Son, H. Cheong, *Phys. Rev. Lett.* **2011**, *106*, 155502.
- [144] J. Yan, Y. Zhang, P. Kim, A. Pinczuk, *Phys. Rev. Lett.* **2007**, *98*, 166802.
- [145] J. E. Lee, G. Ahn, J. Shim, Y. S. Lee, S. Ryu, *Nat. Commun.* **2012**, *3*, 1024.
- [146] T. P. Mernagh, R. P. Cooney, R. A. Johnson, *Carbon N. Y.* **1984**, *22*, 39.
- [147] L. G. Cançado, K. Takai, T. Enoki, M. Endo, Y. A. Kim, H. Mizusaki, A. Jorio, L. N. Coelho, R. Magalhães-Paniago, M. A. Pimenta, *Appl. Phys. Lett.* **2006**, *88*, 163106.
- [148] L. G. Cançado, A. Jorio, M. A. Pimenta, *Phys. Rev. B - Condens. Matter Mater. Phys.* **2007**, *76*, 1.
- [149] R. M. Martin, L. M. Falicov, *Light Scattering in Solids I: Introductory Concepts*, Springer, Berlin, **1983**.
- [150] L. Song, L. Ci, H. Lu, P. B. Sorokin, C. Jin, J. Ni, A. G. Kvashnin, D. G. Kvashnin, J. Lou, B. I. Yakobson, P. M. Ajayan, *Nano Lett.* **2010**, *10*, 3209.
- [151] K. Zhang, Y. Feng, F. Wang, Z. Yang, J. Wang, *J. Mater. Chem. C* **2017**, *5*, 11992.
- [152] M. Yankowitz, Q. Ma, P. Jarillo-Herrero, B. J. LeRoy, *Nat. Rev. Phys.* **2019**, *1*, 112.
- [153] G. Giovannetti, P. A. Khomyakov, G. Brocks, P. J. Kelly, J. Van Den Brink, *Phys. Rev. B - Condens. Matter Mater. Phys.* **2007**, *76*, 2.
- [154] K. S. Novoselov, D. Jiang, F. Schedin, T. J. Booth, V. V. Khotkevich, S. V. Morozov, A. K. Geim, *Proc. Natl. Acad. Sci. U. S. A.* **2005**, *102*, 10451.
- [155] W. Q. Han, L. Wu, Y. Zhu, K. Watanabe, T. Taniguchi, *Appl. Phys. Lett.* **2008**, *93*, 1.

-
-
- [156] A. Ismach, H. Chou, D. A. Ferrer, Y. Wu, S. McDonnell, H. C. Floresca, A. Covacevich, C. Pope, R. Piner, M. J. Kim, R. M. Wallace, L. Colombo, R. S. Ruoff, *ACS Nano* **2012**, *6*, 6378.
- [157] L. Ci, L. Song, C. Jin, D. Jariwala, D. Wu, Y. Li, A. Srivastava, Z. F. Wang, K. Storr, L. Balicas, F. Liu, P. M. Ajayan, *Nat. Mater.* **2010**, *9*, 430.
- [158] K. H. Lee, H. J. Shin, J. Lee, I. Y. Lee, G. H. Kim, J. Y. Choi, S. W. Kim, *Nano Lett.* **2012**, *12*, 714.
- [159] D. Golla, K. Chattrakun, K. Watanabe, T. Taniguchi, B. J. LeRoy, A. Sandhu, *Appl. Phys. Lett.* **2013**, *102*, 161906.
- [160] L. Wang, I. Meric, P. Y. Huang, Q. Gao, Y. Gao, H. Tran, T. Taniguchi, K. Watanabe, L. M. Campos, D. A. Muller, J. Guo, P. Kim, J. Hone, K. L. Shepard, C. R. Dean, *Science (80-.)*. **2013**, *342*, 614.
- [161] P. Blake, E. W. Hill, A. H. Castro Neto, K. S. Novoselov, D. Jiang, R. Yang, T. J. Booth, A. K. Geim, *Appl. Phys. Lett.* **2007**, *91*, 063124.
- [162] M. Okada, T. Sawazaki, K. Watanabe, T. Taniguchi, H. Hibino, H. Shinohara, R. Kitaura, *ACS Nano* **2014**, *8*, 8273.
- [163] N. Fang, K. Otsuka, A. Ishii, T. Taniguchi, K. Watanabe, K. Nagashio, Y. K. Kato, *ACS Photonics* **2020**, *7*, 1773.
- [164] A. Baumgartner, G. Abulizi, K. Watanabe, T. Taniguchi, J. Gramich, C. Schönenberger, *Appl. Phys. Lett.* **2014**, *105*, 023111.
- [165] J. Huang, C. Pan, S. Tran, B. Cheng, K. Watanabe, T. Taniguchi, C. N. Lau, M. Bockrath, *Nano Lett.* **2015**, *15*, 6836.
- [166] S. T. Gulati, J. Westbrook, S. Carley, H. Vepakomma, T. Ono, *SID Symp. Dig. Tech. Pap.* **2011**, *42*, 652.
- [167] M. J. MATTHEWSON, C. R. KURKJIAN, S. T. GULATI, *J. Am. Ceram. Soc.* **1986**, *69*, 815.
- [168] I. Pinnau, L. G. Toy, *J. Memb. Sci.* **1996**, *109*, 125.
- [169] L. Heinke, C. Wöll, *Adv. Mater.* **2019**, *31*, 1806324.
- [170] I. Stassen, N. Burtch, A. Talin, P. Falcaro, M. Allendorf, R. Ameloot, *Chem. Soc. Rev.* **2017**, *46*, 3185.
- [171] S. Kitagawa, R. Kitaura, S. I. Noro, *Angew. Chemie - Int. Ed.* **2004**, *43*, 2334.
- [172] G. Férey, *Chem. Soc. Rev.* **2008**, *37*, 191.
- [173] C. G. Silva, A. Corma, H. García, *J. Mater. Chem.* **2010**, *20*, 3141.

-
- [174] X. Zhao, S. Liu, Z. Tang, H. Niu, Y. Cai, W. Meng, F. Wu, J. P. Giesy, *Sci. Rep.* **2015**, *5*, 11849.
- [175] Y. Cui, J. Zhang, H. He, G. Qian, *Chem. Soc. Rev.* **2018**, *47*, 5740.
- [176] Y. Kobayashi, B. Jacobs, M. D. Allendorf, J. R. Long, *Chem. Mater.* **2010**, *22*, 4120.
- [177] M. Yoon, K. Suh, S. Natarajan, K. Kim, *Angew. Chemie - Int. Ed.* **2013**, *52*, 2688.
- [178] G. K. H. Shimizu, J. M. Taylor, S. R. Kim, *Science (80-.).* **2013**, *341*, 354.
- [179] B. M. Wiers, M. L. Foo, N. P. Balsara, J. R. Long, *J. Am. Chem. Soc.* **2011**, *133*, 14522.
- [180] M. E. Foster, J. D. Azoulay, B. M. Wong, M. D. Allendorf, *Chem. Sci.* **2014**, *5*, 2081.
- [181] D. Jonckheere, E. Coutino-Gonzalez, W. Baekelant, B. Bueken, H. Reinsch, I. Stassen, O. Fenwick, F. Richard, P. Samorì, R. Ameloot, J. Hofkens, M. B. J. Roefsaers, D. E. De Vos, *J. Mater. Chem. C* **2016**, *4*, 4259.
- [182] S. Saha, S. Chandra, B. Garai, R. Banerjee, *Indian J. Chem. - Sect. A Inorganic, Phys. Theor. Anal. Chem.* **2012**, *51*, 1223.
- [183] Z. Chen, P. Li, R. Anderson, X. Wang, X. Zhang, L. Robison, L. R. Redfern, S. Moribe, T. Islamoglu, D. A. Gómez-Gualdrón, T. Yildirim, J. F. Stoddart, O. K. Farha, *Science (80-.).* **2020**, *368*, 297.
- [184] M. Hatzakis, *J. Electrochem. Soc.* **1969**, *116*, 1033.
- [185] D. Grientschnig, W. Sitte, *Meas. Sci. Technol.* **1991**, *2*, 118.
- [186] W. Li, F. Hennrich, B. S. Flavel, S. Dehm, M. Kappes, R. Krupke, *Nano Res.* **2021**, *14*, 2188.
- [187] R. Krupke, F. Hennrich, M. M. Kappes, H. v. Löhneysen, *Nano Lett.* **2004**, *4*, 1395.
- [188] R. Krupke, F. Hennrich, H. v. Löhneysen, M. M. Kappes, *Science (80-.).* **2003**, *301*, 344.
- [189] C. V. RAMAN, K. S. KRISHNAN, *Nature* **1928**, *121*, 501.
- [190] S. Kumar, D. Dagli, S. Dehm, C. Das, L. Wei, Y. Chen, F. Hennrich, R. Krupke, *Phys. status solidi – Rapid Res. Lett.* **2020**, *14*, 2000193.
- [191] S. K. Jang, J. Youn, Y. J. Song, S. Lee, *Sci. Rep.* **2016**, *6*, 30449.
- [192] H. Oh, J. Jo, Y. Tchoe, H. Yoon, H. Hwi Lee, S.-S. Kim, M. Kim, B. Sohn, G. Yi, *NPG Asia Mater.* **2016**, *8*, e330.
- [193] K. Ahmed, R. Dahal, A. Weltz, J.-Q. Lu, Y. Danon, I. B. Bhat, *Appl. Phys. Lett.* **2016**, *109*, 113501.

-
- [194] S. Behura, P. Nguyen, S. Che, R. Debbarma, V. Berry, *J. Am. Chem. Soc.* **2015**, *137*, 13060.
- [195] Y. Gong, G. Shi, Z. Zhang, W. Zhou, J. Jung, W. Gao, L. Ma, Y. Yang, S. Yang, G. You, R. Vajtai, Q. Xu, A. H. MacDonald, B. I. Yakobson, J. Lou, Z. Liu, P. M. Ajayan, *Nat. Commun.* **2014**, *5*, 3193.
- [196] Y. Shi, C. Hamsen, X. Jia, K. K. Kim, A. Reina, M. Hofmann, A. L. Hsu, K. Zhang, H. Li, Z. Y. Juang, M. S. Dresselhaus, L. J. Li, J. Kong, *Nano Lett.* **2010**, *10*, 4134.
- [197] P. J. Fazen, E. E. Remsen, J. S. Beck, P. J. Carroll, A. R. McGhie, L. G. Sneddon, *Chem. Mater.* **1995**, *7*, 1942.
- [198] P. J. Fazen, J. S. Beck, A. T. Lynch, E. E. Remsen, L. G. Sneddon, *Chem. Mater.* **1990**, *2*, 96.
- [199] J. C. Koepke, J. D. Wood, Y. Chen, S. W. Schmucker, X. Liu, N. N. Chang, L. Nienhaus, J. W. Do, E. A. Carrion, J. Hewaparakrama, A. Rangarajan, I. Datye, R. Mehta, R. T. Haasch, M. Gruebele, G. S. Girolami, E. Pop, J. W. Lyding, *Chem. Mater.* **2016**, *28*, 4169.
- [200] S. Behura, P. Nguyen, S. Che, R. Debbarma, V. Berry, *J. Am. Chem. Soc.* **2015**, *137*, 13060.
- [201] S. Frueh, R. Kellett, C. Mallery, T. Molter, W. S. Willis, C. King'Ondu, S. L. Suib, *Inorg. Chem.* **2011**, *50*, 783.
- [202] H. Cho, S. Park, D.-I. Won, S. O. Kang, S.-S. Pyo, D.-I. Kim, S. M. Kim, H. C. Kim, M. J. Kim, *Sci. Rep.* **2015**, *5*, 11985.
- [203] H. Wang, B. Wang, X.-Y. Quek, L. Wei, J. Zhao, L.-J. Li, M. B. Chan-Park, Y. Yang, Y. Chen, *J. Am. Chem. Soc.* **2010**, *132*, 16747.
- [204] H. Wang, L. Wei, F. Ren, Q. Wang, L. D. Pfefferle, G. L. Haller, Y. Chen, *ACS Nano* **2013**, *7*, 614.
- [205] F. Hennrich, W. Li, R. Fischer, S. Lebedkin, R. Krupke, M. M. Kappes, *ACS Nano* **2016**, *10*, 1888.
- [206] V. Karre, P. D. Keathley, Jing Guo, J. T. Hastings, *IEEE Trans. Nanotechnol.* **2009**, *8*, 139.
- [207] M. K. Yang, *J. Micro/Nanolithography, MEMS, MOEMS* **2008**, *7*, 033010.
- [208] S. Lee, T. Jeong, S. Jung, K. Yee, *Phys. status solidi* **2019**, *256*, 1800417.
- [209] R. Gholami, M. Alyani, K. Smith, *Catalysts* **2015**, *5*, 561.
- [210] N. Rungraeng, Y. Cho, S. Hoo, S. Jun, *J. Food Eng.* **2012**, *111*, 218.

-
- [211] M. Shlafman, T. Tabachnik, O. Shtempluk, A. Razin, V. Kochetkov, Y. E. Yaish, *Appl. Phys. Lett.* **2016**, *108*, 163104.
- [212] S. Jang, B. Kim, M. L. Geier, P. L. Prabhumirashi, M. C. Hersam, A. Dodabalapur, *Appl. Phys. Lett.* **2014**, *105*, 122107.
- [213] H. Shimauchi, Y. Ohno, S. Kishimoto, T. Mizutani, *Jpn. J. Appl. Phys.* **2006**, *45*, 5501.
- [214] R. T. Weitz, U. Zsehiesehang, A. Forment-Aliaga, D. Kälblein, M. Burghard, K. Kern, H. Klauk, *Nano Lett.* **2009**, *9*, 1335.
- [215] S. Kumar, Y. Pramudya, K. Müller, A. Chandresh, S. Dehm, S. Heidrich, A. Fediai, D. Parmar, D. Perera, M. Rommel, L. Heinke, W. Wenzel, C. Wöll, R. Krupke, *Adv. Mater.* **2021**, 2103316.
- [216] A. K. Geim, K. S. Novoselov, *Nat. Mater.* **2007**, *6*, 183.
- [217] B. Radisavljevic, A. Radenovic, J. Brivio, V. Giacometti, A. Kis, *Nat. Nanotechnol.* **2011**, *6*, 147.
- [218] B. Liu, L. Chen, G. Liu, A. N. Abbas, M. Fathi, C. Zhou, *ACS Nano* **2014**, *8*, 5304.
- [219] A. N. Abbas, B. Liu, L. Chen, Y. Ma, S. Cong, N. Aroonyadet, M. Köpf, T. Nilges, C. Zhou, *ACS Nano* **2015**, *9*, 5618.
- [220] M. Sajjad, G. Morell, P. Feng, *ACS Appl. Mater. Interfaces* **2013**, *5*, 5051.
- [221] S. Prezioso, F. Perrozzi, L. Giancaterini, C. Cantalini, E. Treossi, V. Palermo, M. Nardone, S. Santucci, L. Ottaviano, *J. Phys. Chem. C* **2013**, *117*, 10683.
- [222] Y. Wang, L. Wang, T. Yang, X. Li, X. Zang, M. Zhu, K. Wang, D. Wu, H. Zhu, *Adv. Funct. Mater.* **2014**, *24*, 4666.
- [223] M. Park, Y. J. Park, X. Chen, Y. Park, M. Kim, J.-H. Ahn, *Adv. Mater.* **2016**, *28*, 2556.
- [224] F. Zhou, J. Chen, X. Tao, X. Wang, Y. Chai, *Research* **2019**, *2019*, 1.
- [225] Y. Wang, T. Yang, J. Lao, R. Zhang, Y. Zhang, M. Zhu, X. Li, X. Zang, K. Wang, W. Yu, H. Jin, L. Wang, H. Zhu, *Nano Res.* **2015**, *8*, 1627.
- [226] B. Cho, J. Yoon, S. K. Lim, A. R. Kim, D. Kim, S. Park, J. Kwon, Y.-J. Lee, K.-H. Lee, B. H. Lee, H. C. Ko, M. G. Hahm, *ACS Appl. Mater. Interfaces* **2015**, *7*, 16775.
- [227] R. Pearce, T. Iakimov, M. Andersson, L. Hultman, A. L. Spetz, R. Yakimova, *Sensors Actuators B Chem.* **2011**, *155*, 451.
- [228] N. H. Ha, C. T. Long, N. H. Nam, N. T. Hue, N. H. Phuong, H. S. Hong, *J. Electron. Mater.* **2017**, *46*, 3353.
- [229] X. Guo, B. Du, Q. Wei, J. Yang, L. Hu, L. Yan, W. Xu, *J. Hazard. Mater.* **2014**, *278*,

- [230] R. Sitko, E. Turek, B. Zawisza, E. Malicka, E. Talik, J. Heimann, A. Gagor, B. Feist, R. Wrzalik, *Dalt. Trans.* **2013**, 5682.
- [231] G. Y. Bae, S. W. Pak, D. Kim, G. Lee, D. H. Kim, *Advacned Mater.* **2016**, 28, 5300.
- [232] W. Fu, C. Nef, O. Knopfmacher, A. Tarasov, M. Weiss, M. Calame, C. Schönenberger, *Nano Lett.* **2011**, 11, 3597.
- [233] M. C. So, G. P. Wiederrecht, J. E. Mondloch, J. T. Hupp, O. K. Farha, *Chem. Commun.* **2015**, 51, 3501.
- [234] M. P. Suh, H. J. Park, T. K. Prasad, D. W. Lim, *Chem. Rev.* **2012**, 112, 782.
- [235] Y. Li, R. T. Yang, *Langmuir* **2007**, 23, 12937.
- [236] J. A. Mason, M. Veenstra, J. R. Long, *Chem. Sci.* **2014**, 5, 32.
- [237] C. Bartual-Murgui, A. Akou, C. Thibault, G. Molnár, C. Vieu, L. Salmon, A. Bousseksou, *J. Mater. Chem. C* **2015**, 3, 1277.
- [238] L. E. Kreno, K. Leong, O. K. Farha, M. Allendorf, R. P. Van Duyne, J. T. Hupp, *Chem. Rev.* **2012**, 112, 1105.
- [239] M. D. Allendorf, R. J. T. Houk, L. Andruszkiewicz, A. A. Talin, J. Pikarsky, A. Choudhury, K. A. Gall, P. J. Hesketh, *J. Am. Chem. Soc.* **2008**, 130, 14404.
- [240] Q. Tang, S. Liu, Y. Liu, J. Miao, S. Li, L. Zhang, Z. Shi, Z. Zheng, *Inorg. Chem.* **2013**, 52, 2799.
- [241] V. Chernikova, O. Yassine, O. Shekhah, M. Eddaoudi, K. N. Salama, *J. Mater. Chem. A* **2018**, 6, 5550.
- [242] J. Liu, B. Lukose, O. Shekhah, H. K. Arslan, P. Weidler, H. Gliemann, S. Bräse, S. Grosjean, A. Godt, X. Feng, K. Müllen, I.-B. Magdau, T. Heine, C. Wöll, *Sci. Rep.* **2012**, 2, 921.
- [243] S. Selberherr, *Analysis and Simulation of Semiconductor Devices*, Springer Vienna, Vienna, **1984**.
- [244] M. G. Ancona, *IEEE Trans. Electron Devices* **2010**, 57, 681.
- [245] J. G. Champlain, *J. Appl. Phys.* **2011**, 109, 084515.
- [246] L. Anzi, A. Mansouri, P. Pedrinazzi, E. Guerriero, M. Fiocco, A. Pesquera, A. Centeno, A. Zurutuza, A. Behnam, E. A. Carrion, E. Pop, R. Sordan, *2D Mater.* **2018**, 5, 025014.
- [247] B. Lee, S. Park, H.-C. Kim, K. Cho, E. M. Vogel, M. J. Kim, R. M. Wallace, J. Kim,

-
- Appl. Phys. Lett.* **2008**, 92, 203102.
- [248] O. Shekhah, H. Wang, D. Zacher, R. A. Fischer, C. Wöll, *Angew. Chemie Int. Ed.* **2009**, 48, 5038.
- [249] S. Hurre, S. Friebe, J. Wohlgemuth, C. Wöll, J. Caro, L. Heinke, *Chem. - A Eur. J.* **2017**, 23, 2294.
- [250] Z. Wang, J. Liu, B. Lukose, Z. Gu, P. G. Weidler, H. Gliemann, T. Heine, C. Wöll, *Nano Lett.* **2014**, 14, 1526.
- [251] J. E. Lee, G. Ahn, J. Shim, Y. S. Lee, S. Ryu, *Nat. Commun.* **2012**, 3, 1024.
- [252] P. May, M. Lazzeri, P. Venezuela, F. Herziger, G. Callsen, J. S. Reparaz, A. Hoffmann, F. Mauri, J. Maultzsch, *Phys. Rev. B - Condens. Matter Mater. Phys.* **2013**, 87, 1.
- [253] H. A. Hyatt, J. M. Cherlow, W. R. Fenner, S. P. S. Porto, *J. Opt. Soc. Am.* **1973**, 63, 1604.
- [254] P. G. Spizzirri, J.-H. Fang, S. Rubanov, E. Gauja, S. Prawer, *arXiv 1002.2692* **2010**.
- [255] S. Kim, J. Nah, I. Jo, D. Shahrjerdi, L. Colombo, Z. Yao, E. Tutuc, S. K. Banerjee, *Appl. Phys. Lett.* **2009**, 94, 062107.
- [256] A. C. Elder, A. B. Aleksandrov, S. Nair, T. M. Orlando, *Langmuir* **2017**, 33, 10153.
- [257] J. E. Mondloch, O. Karagiari, O. K. Farha, J. T. Hupp, *CrystEngComm* **2013**, 15, 9258.
- [258] S. Pisana, M. Lazzeri, C. Casiraghi, K. S. Novoselov, A. K. Geim, A. C. Ferrari, F. Mauri, *Nat. Mater.* **2007**, 6, 198.
- [259] Y. Zhao, L. Du, W. Yang, C. Shen, J. Tang, X. Li, Y. Chu, J. Tian, K. Watanabe, T. Taniguchi, R. Yang, D. Shi, Z. Sun, G. Zhang, *Phys. Rev. B* **2020**, 102, 165415.
- [260] M. Gibertini, A. Tomadin, F. Guinea, M. I. Katsnelson, M. Polini, *Phys. Rev. B* **2012**, 85, 201405.
- [261] M. Engel, M. Steiner, A. Lombardo, A. C. Ferrari, H. V. Löhneysen, P. Avouris, R. Krupke, *Nat. Commun.* **2012**, 3, 906.
- [262] A. Ponzoni, C. Baratto, N. Cattabiani, M. Falasconi, V. Galstyan, E. Nunez-Carmona, F. Rigoni, V. Sberveglieri, G. Zambotti, D. Zappa, *Sensors* **2017**, 17, 714.
- [263] A. W. Jones, *Forensic Sci. Rev.* **2000**, 12, 23.
- [264] R. Kotipalli, R. Delamare, O. Poncelet, X. Tang, L. A. Francis, D. Flandre, *EPJ Photovoltaics* **2013**, 4, 45107.

-
- [265] D. N. Goldstein, J. A. McCormick, S. M. George, *J. Phys. Chem. C* **2008**, *112*, 19530.
- [266] N. G. Petrik, P. L. Huestis, J. A. LaVerne, A. B. Aleksandrov, T. M. Orlando, G. A. Kimmel, *J. Phys. Chem. C* **2018**, *122*, 9540.
- [267] L. Chua, J. Zaumseil, J. Chang, E. C.-W. Ou, P. K.-H. Ho, H. Sirringhaus, R. H. Friend, *Nature* **2005**, *434*, 194.
- [268] D. Argyris, T. Ho, D. R. Cole, A. Striolo, *J. Phys. Chem. C* **2011**, *115*, 2038.
- [269] G. Feng, C.-F. Huo, C.-M. Deng, L. Huang, Y.-W. Li, J. Wang, H. Jiao, *J. Mol. Catal. A Chem.* **2009**, *304*, 58.
- [270] D. T. Edmonds, *Eur. Biophys. J.* **1988**, *16*, 255.
- [271] S. Wang, P. K. Ang, Z. Wang, A. L. L. Tang, J. T. L. Thong, K. P. Loh, *Nano Lett.* **2010**, *10*, 92.
- [272] B. Lee, G. Mordì, M. J. Kim, Y. J. Chabal, E. M. Vogel, R. M. Wallace, K. J. Cho, L. Colombo, J. Kim, *Appl. Phys. Lett.* **2010**, *97*, 043107.
- [273] P. Clayborne, *Appl. Catal. A Gen.* **2004**, *257*, 225.
- [274] W. Wang, D. I. Sharapa, A. Chandresh, A. Nefedov, S. Heißler, L. Heinke, F. Studt, Y. Wang, C. Wöll, *Angew. Chemie Int. Ed.* **2020**, *59*, 10514.
- [275] K. Müller, N. Vankova, L. Schöttner, T. Heine, L. Heinke, *Chem. Sci.* **2019**, *10*, 153.
- [276] A. Isacson, A. W. Cummings, L. Colombo, L. Colombo, J. M. Kinaret, S. Roche, *2D Mater.* **2016**, *4*, 012002.
- [277] O. Simionescu, R. C. Popa, A. Avram, G. Dinescu, *Plasma Process. Polym.* **2020**, *17*, 1900246.
- [278] A. C. Ferrari, J. Robertson, *Phys. Rev. B* **2000**, *61*, 14095.
- [279] C. N. S. Kumar, V. S. K. Chakravadhanula, A. Riaz, S. Dehm, D. Wang, X. Mu, B. Flavel, R. Krupke, C. Kübel, *Nanoscale* **2017**, *9*, 12835.
- [280] P. Gałka, J. Kowalonek, H. Kaczmarek, *J. Therm. Anal. Calorim.* **2014**, *115*, 1387.
- [281] U. Narula, C. M. Tan, C. S. Lai, *Sci. Rep.* **2017**, *7*, 1.
- [282] A. C. Ferrari, J. Robertson, *Phys. Rev. B - Condens. Matter Mater. Phys.* **2001**, *64*, 1.
- [283] H. Duan, E. Xie, L. Han, Z. Xu, *Adv. Mater.* **2008**, *20*, 3284.
- [284] Liming Ren, Baoqin Chen, in *Proceedings. 7th Int. Conf. Solid-State Integr. Circuits Technol. 2004.*, IEEE, **2007**, pp. 579–582.

-
-
- [285] X. Li, L. Colombo, R. S. Ruoff, *Adv. Mater.* **2016**, *28*, 6247.
- [286] S.-M. Kim, J.-H. Kim, K.-S. Kim, Y. Hwangbo, J.-H. Yoon, E.-K. Lee, J. Ryu, H.-J. Lee, S. Cho, S.-M. Lee, *Nanoscale* **2014**, *6*, 4728.
- [287] J. W. Suk, A. Kitt, C. W. Magnuson, Y. Hao, S. Ahmed, J. An, A. K. Swan, B. B. Goldberg, R. S. Ruoff, *ACS Nano* **2011**, *5*, 6916.
- [288] I. A. Kostogrud, E. V Boyko, D. V Smovzh, P. E. T. Eva, *Mater. Chem. Phys.* **2018**, *219*, 67.
- [289] M. Hassanpour Amiri, J. Heidler, A. Hasnain, S. Anwar, H. Lu, K. Müllen, K. Asadi, *RSC Adv.* **2020**, *10*, 1127.
- [290] W. S. Leong, H. Wang, J. Yeo, F. J. Martin-Martinez, A. Zubair, P. Shen, Y. Mao, T. Palacios, M. J. Buehler, J. Hong, J. Kong, *Nat. Commun.* **2019**, *10*, 867.
- [291] M. Chen, D. Stekovic, W. Li, B. Arkook, R. C. Haddon, E. Bekyarova, *Nanotechnology* **2017**, *28*, 255701.
- [292] M. Chen, R. C. Haddon, R. Yan, E. Bekyarova, *Mater. Horizons* **2017**, *4*, 1054.
- [293] M. Jang, T. Q. Trung, J. Jung, B. Kim, N. Lee, *Phys. Chem. Chem. Phys.* **2014**, *16*, 4098.
- [294] J. Moon, S. Kim, S. Son, S. Kang, J. Lim, D. K. Lee, B. Ahn, D. Whang, H. K. Yu, J. Lee, *Adv. Mater. Interfaces* **2019**, *6*, 1900084.
- [295] J. Kim, J. Yeon, S. Jo, J. Ho, W. Hong, B. Chul, *Appl. Surf. Sci.* **2020**, *508*, 145057.
- [296] D.-Y. Wang, I. Huang, P. Ho, S. Li, Y. Yeh, D. Wang, W.-L. Chen, Y. Lee, Y. Chang, C.-C. Chen, C. Liang, C. Chen, *Adv. Mater.* **2013**, *25*, 4521.
- [297] G. J. M. Fechine, I. Martin-Fernandez, G. Yiapanis, R. Bentini, E. S. Kulkarni, R. V. Bof de Oliveira, X. Hu, I. Yarovsky, A. H. Castro Neto, B. Özyilmaz, *Carbon N. Y.* **2015**, *83*, 224.
- [298] X. Li, Y. Zhu, W. Cai, M. Borysiak, B. Han, D. Chen, R. D. Piner, L. Colomba, R. S. Ruoff, *Nano Lett.* **2009**, *9*, 4359.
- [299] H. Park, C. Lim, C. Lee, J. Kang, J. Kim, M. Choi, H. Park, *Nanotechnology* **2018**, *29*, 415303.
- [300] J. Heo, H. J. Chung, S. Lee, H. Yang, D. H. Seo, J. K. Shin, U. Chung, S. Seo, E. H. Hwang, S. Das Sarma, *Phys. Rev. B* **2011**, *84*, 035421.
- [301] S. Nakamura, D. Miyafuji, T. Fujii, T. Matsui, H. Fukuyama, *Cryogenics (Guildf)*. **2017**, *86*, 118.
- [302] A. D. Smith, F. Niklaus, A. Paussa, S. Schröder, A. C. Fischer, M. Sterner, S. Wagner,

-
- S. Vaziri, F. Forsberg, D. Esseni, M. Östling, M. C. Lemme, *ACS Nano* **2016**, *10*, 9879.
- [303] M. Šiškins, M. Lee, D. Wehenkel, R. van Rijn, T. W. de Jong, J. R. Renshof, B. C. Hopman, W. S. J. M. Peters, D. Davidovikj, H. S. J. van der Zant, P. G. Steeneken, *Microsystems Nanoeng.* **2020**, *6*, 102.
- [304] S. Bae, H. Kim, Y. Lee, X. Xu, J. Park, Y. Zheng, J. Balakrishnan, T. Lei, H. Ri Kim, Y. Il Song, Y.-J. Kim, K. S. Kim, B. Özyilmaz, J.-H. Ahn, B. H. Hong, S. Iijima, *Nat. Nanotechnol.* **2010**, *5*, 574.
- [305] V. M. Pereira, A. H. Castro Neto, N. M. R. Peres, *Phys. Rev. B* **2009**, *80*, 045401.
- [306] S. Sreekala, X.-H. Peng, P. M. Ajayan, S. K. Nayak, *Phys. Rev. B* **2008**, *77*, 155434.
- [307] S. B. Kumar, J. Guo, *Nano Lett.* **2012**, *12*, 1362.
- [308] G. S. Frankel, J. D. Vienna, J. Lian, J. R. Scully, S. Gin, J. V Ryan, J. Wang, S. H. Kim, W. Windl, J. Du, *npj Mater. Degrad.* **2018**, *2*, 15.
- [309] C. Neumann, S. Reichardt, P. Venezuela, M. Drögeler, L. Banszerus, M. Schmitz, K. Watanabe, T. Taniguchi, F. Mauri, B. Beschoten, S. V. Rotkin, C. Stampfer, *Nat. Commun.* **2015**, *6*, 8429.
- [310] M. Bayle, N. Reckinger, A. Felten, P. Landois, O. Lancry, B. Dutertre, J. Colomer, A. Zahab, L. Henrard, J. Sauvajol, M. Paillet, *J. Raman Spectrosc.* **2018**, *49*, 36.
- [311] E. G. STEWARD, B. P. COOK, E. A. KELLETT, *Nature* **1960**, *187*, 1015.
- [312] N. Mounet, N. Marzari, *Phys. Rev. B* **2005**, *71*, 205214.
- [313] T. Zhu, J. Li, A. Samanta, A. Leach, K. Gall, *Phys. Rev. Lett.* **2008**, *100*, 025502.
- [314] A. L. Sellerio, A. Taloni, S. Zapperi, *Phys. Rev. Appl.* **2015**, *4*, 024011.
- [315] T. Y. Ling, S. J. Fishlock, M. S. Shamsudin, S. M. Sultan, H. M. H. Chong, S. H. Pu, in *2017 IEEE SENSORS*, IEEE, **2017**, pp. 1–3.
- [316] T. Fujimoto, K. Awaga, *Phys. Chem. Chem. Phys.* **2013**, *15*, 8983.
- [317] A. I. Kingon, J. Maria, S. K. Streiffer, *Nature* **2000**, *406*, 1032.
- [318] J. G. Kho, K. T. Moon, J. H. Kim, D. P. Kim, *J. Am. Ceram. Soc.* **2000**, *83*, 2681.
- [319] S. Park, T. H. Seo, H. Cho, K. H. Min, D. S. Lee, D. Il Won, S. O. Kang, M. J. Kim, *Sci. Rep.* **2017**, *7*, 1.
- [320] C. Herring, E. Vogt, *Phys. Rev.* **1956**, *101*, 944.
-

Acknowledgements

The study included in this thesis was conducted at Institute of nanotechnology (INT) at Karlsruhe institute of technology (KIT), campus North and Department of Materials and Geosciences at Technical University, Darmstadt.

I am grateful to everyone who supported me scientifically and morally during my stay at INT, KIT:

First and foremost, I am extremely thankful to Professor Dr. Ralph Krupke for giving me an opportunity to work under his supervision. Conversations with him are always enlightening about science as well as about life. This thesis wouldn't have been possible without his constant motivation and guidance.

I am grateful to Professor Dr. Jan Philipp Hofmann to become a co-referee for the thesis. I am thankful to Professor Dr. Jörg Schneider and Professor Dr. Robert Stark to examine my doctoral examination.

Sincere gratitude to Simone Dehm for all the help with device fabrication and scientific advices.

Many thanks to members of Krukpe-Unit to create an amazing and helpful atmosphere for research. I specially cherished time spent with my friends and colleagues Vibhuti, Anirudh, Devang, Navid, Min-Ken, Dr. Pranaav and Dr. Twinkle. It was fun to have long scientific discussions with Anirudh. I would like to thank my previous colleague Adnan, who made me feel comfortable in the initial phase of my PhD. Special thanks to Marco for his valuable insights and help into building the Piezoresistance setup.

I would like to thank few of my close friends Divya, Akanksha and Rashmi who continuously supported me morally and motivated me.

Last but not least, I am lucky to have my family: my brother Pradeep, my sisters Mausam and soon to be Dr. Sandhya, and my parents, who have been with me eternally and constantly support and push me to extend my limits.